FABRICATION OF SiC-B_4C–Si AND SiC-B_4C–Al CERMETS BY POWDER METALLURGY ROUTE

PANKAJINI SAHANI

Department of Metallurgical and Materials Engineering
National Institute of Technology Rourkela, Odisha, India

FABRICATION OF SiC-B_4C–Si AND SiC-B_4C–Al CERMETS BY POWDER METALLURGY ROUTE

Dissertation submitted in partial fulfillment

of the requirements of the degree of

Doctor of Philosophy

in

Metallurgical and Materials Engineering

by

Pankajini Sahani

(Roll Number: 510MM102)

based on research carried out

under the supervision of

Prof. Debasis Chaira

April, 2017

Department of Metallurgical and Materials Engineering
National Institute of Technology Rourkela

Department of Metallurgical and Materials Engineering
National Institute of Technology Rourkela

April, 2017

Certificate of Examination

Roll Number: *510MM102*

Name: *Pankajini Sahani*

Title of Dissertation: *Fabrication of SiC-B_4C–Si and SiC-B_4C–Al cermets by powder metallurgy route*

We the below signed, after checking the dissertation mentioned above and the official record book (s) of the student, hereby state our approval of the dissertation submitted in partial fulfilment of the requirements of the degree of *Doctor of Philosophy* in *Metallurgical and Materials Engineering* at *National Institute of Technology Rourkela*. We are satisfied with the volume, quality, correctness, and originality of the work.

Debasis Chaira
Principal Supervisor

Anindya Basu
Member, DSC

Syed Nasimul Alam
Member, DSC

Simanchala Panigrahi
Member, DSC

Subash Chandra Mishra
Chairman, DSC

Smarajit Sarkar
Head of the Department

External Examiner

Department of Metallurgical and Materials Engineering
National Institute of Technology Rourkela

Prof. Debasis Chaira
Assistant Professor

April, 2017

Supervisor's Certificate

This is to certify that the work presented in the dissertation entitled *Fabrication of SiC-B_4C–Si and SiC-B_4C–Al cermets by powder metallurgy route* submitted by *Pankajini Sahani*, Roll Number 510MM102, is a record of original research carried out by her under my supervision and guidance in partial fulfilment of the requirements of the degree of *Doctor of Philosophy* in *Metallurgical and Materials Engineering*. Neither this dissertation nor any part of it has been submitted earlier for any degree or diploma to any institute or university in India or abroad.

Debasis Chaira
Assistant Professor

"Dedicated to my parents, brother and my husband"

Signature

Declaration of Originality

I, *Pankajini Sahani*, Roll Number *510MM102* hereby declare that this dissertation entitled *Fabrication of SiC-*B_4C*–Si and SiC-*B_4C*–Al cermets by powder metallurgy route* presents my original work carried out as a doctoral student of NIT Rourkela and, to the best of my knowledge, contains no material previously published or written by another person, nor any material presented by me for the award of any degree or diploma of NIT Rourkela or any other institution. Any contribution made to this research by others, with whom I have worked at NIT Rourkela or elsewhere, is explicitly acknowledged in the dissertation. Works of other authors cited in this dissertation have been duly acknowledged under the sections "Reference" or "Bibliography". I have also submitted my original research records to the scrutiny committee for evaluation of my dissertation.

I am fully aware that in case of any non-compliance detected in future, the Senate of NIT Rourkela may withdraw the degree awarded to me on the basis of the present dissertation.

April, 2017
NIT Rourkela

Pankajini Sahani

Acknowledgment

I would like to acknowledge my institute and many people who have made this wonderful PhD journey possible. First of all, it is my immense privilege to express my profound gratitude and indebtedness to my supervisor Dr. Debasis Chaira, Department of Metallurgical and Materials Engineering, National Institute of Technology Rourkela. He has been an inextinguishable fire of inspiration and a wonderful mentor for me. Without his great efforts and effective guidance this work could not have been possible. He has guided me at all stages during this research work. He has been a real idol for me and I will always remember him for his unconditional support to complete my PhD work.

I would like to acknowledge Prof. A. Basu, Prof. S.N. Alam, and Prof. S.Panigrahi my doctoral scrutiny committee members for fulfilling their duties of assessing my PhD work without fail.

I would like to convey my sincere gratitude to Prof. S.C. Mishra, Head of the Department, Metallurgical and Materials Engineering, National Institute of Technology Rourkela, for constant support, guidance and encouragement.

I take this opportunity to thank Dr. Anindya Basu, Department of Metallurgical and Materials Engineering, National Institute of Technology Rourkela for allowing me to conduct wear measurements. I am very much indebted to Prof. P. N. Viswakarma, Department of Physics, National Institute of Technology Rourkela for providing the technical facilities and necessary discussions specially in electrical conductivity study. I am grateful to Dr. D. Chakravarty, Scientist D, ARCI, Hyderabad for conducting spark plasma sintering of the cermet samples. I thank Dr. B. Mishra, Deputy Director, DISIR, Rajgangpur, Odisha for supplying materials for my research work. I would like to thank CSIR-National Metallurgical Laboratory (NML), Jamshedpur, for providing facilities for conducting high temperature conventional sintering. I also would like to thank Dr. P. Das, Central Glass Ceramic Research Institute, Kolkata for allowing me to conduct spark plasma sintering of some of my cermet samples.

Further my appreciation goes to the entire Metallurgical and Materials Engineering faculty and staff of NIT Rourkela for all their help along the way. I would like to thank Dr. S. Bal, Scientific officer, Department of Metallurgical and Materials Engineering, National Institute of Technology Rourkela and our laboratory members U.K. Sahu, S. Pradhan, G. Dash, S. Hembram, R. Pattnaik, R. Tanti, and A. Acharya for constant practical assistance and help whenever required.

I would like to acknowledge my friends Arpna Kujur, Geetanjali Parida, Shashank R, Mohan Nuthalapati, Narsimha Chary for their unconditional help and support during my research work.

I would like to especially thanks to my parents for their unconditional love, motivation and assisting me throughout my life. I am blessed to have them beside me all the time that gave me the moral power to move further. Without their help, support, love and encouragement it would not have been possible for me to undertake this work. I am very grateful to my sweet brother Parthasarathi for his love, care, affection and support along the way.

Finally my special thanks to the special person of my life my beloved husband Swaraj Jena for his kind support, understanding, dedication, encouragement, sacrifice and for all he has done in this concluding year of my PhD. Thank you so much my dearest husband for being a part of my whole life.

All errors and limitations remaining in this thesis are exclusively by me.

April, 2017
NIT Rourkela

Pankajini Sahani
Roll Number: 510MM102

Abstract

Cermets are unique that combines the characteristic properties of metals and ceramics. These superior properties make cermet a promising material for use in several aero-engine components, turbo pumps, heat exchangers, fusion reactors, armour plates, wear resistant components as blast nozzles and wheels dressing tools, seal rings, valve components and bearings, oxidation resistant material as refractory lining, coating to protect materials from corrosive environments and combustion engines. SiC-B_4C based cermets are being developed as remarkable engineering materials for their outstanding physical and mechanical properties, including high hardness, lightweight, high wear resistance, high melting point, oxidation resistance and great resistance to chemical attack. Fabrication of highly dense SiC-B_4C based ceramic composite is quite difficult due to its high melting point and strong covalent bond. Properties of these materials can be improved by reducing initial particle size of powders and incorporation of metallic elements into ceramic matrix. The fine and disordered structure produced by mechanical milling increases the molecular diffusion channel during sintering and enhance the densification. Incorporation of Si and Al into SiC-B_4C ceramic matrix improves the properties since it acts as a binder, enhances densification, and lowers the sintering temperature.

In the present study, SiC-B_4C (60:40 wt. %) ceramic composite powder, SiC-B_4C–Si (2, 5, 10 and 20 wt. % of Si) and SiC-B_4C–Al (2, 5, 10 and 20 wt. % of Al) cermet powders of various compositions were prepared separately by mechanical milling for 10 h in a planetary mill. An average particle size of 3–4 µm was obtained after 10 h milling for all the compositions. XRD, SEM and particle size analysis reveal the particle size reduction and homogeneous distribution of Si, Al, in the respective SiC-B_4C composite matrix.

All the compositions were consolidated by both conventional sintering at 1950 °C and spark plasma sintering (SPS) methods at different temperatures respectively. The SPS was carried out at 1500 and 1600 °C for high melting SiC-B_4C ceramic composite. SPS temperature was optimized to 1350 °C and 1300 °C for SiC-B_4C–Si and SiC-B_4C–Al cermets. Higher density, microhardness, indentation fracture toughness, and compressive strength values were achieved for all the compositions consolidated by SPS than conventional sintering. Cermets containing 10 wt. % Si and 10 wt. % Al exhibit optimum mechanical properties than other compositions. There is an enhancement of Vickers microhardness from 18±2.23 to 28±2.12 GPa for the cermet sample containing 10 wt. % Si when the sintering condition was changed from conventional sintering to SPS. The relative density, microhardness, indentation fracture toughness and compressive strength of SiC-B_4C–10 wt. % Si composition fabricated by SPS are 98%, 28±2.12 GPa, 3.8 MPa $m^{1/2}$, and 1387 MPa respectively. Similarly, the optimum relative density, microhardness and indentation fracture toughness of SiC-B_4C–10 wt. % Al consolidated by SPS are 97%, 23±2.29 GPa and 3.28 MPa.$m^{1/2}$, respectively.

Un-lubricated sliding wear behavior of SPS and conventional sintered samples against diamond indenter were compared at different loads (20, 40, 60 and 80N for SPS samples; 20 and 40N for conventional sintered samples). It has been observed that wear resistance decreases with increasing applied load for both cases. Minimum wear depth with high wear resistance, lowest wear rate and lowest volume of wear debris were obtained for the SPS samples containing 10 wt. % Si and 10 wt. % Al. The possible wear mechanisms are abrasive grooves, delamination, and formation of crack.

High temperature oxidation study was performed to understand the tendency of varying Si amount (0–20 wt. %) in SiC-B_4C ceramic matrix and the effect of different oxidation temperatures. Isothermal oxidation study was performed at 800, 1000 and 1200 °C for all the compositions. The cermets with 10 and 20 wt. % Si show more oxidation resistance than the other compositions. At 1200 °C, the SiO_2 glassy phase formed as an oxidation protective layer over the sample surface and prevented from further oxidation.

Finally, after performing all characterizations and analyzing results it was concluded that mechanical milling followed by SPS technique was more efficient and advanced technique to produce SiC-B_4C based cermet with better physical, mechanical, wear and oxidation properties. Moreover, metallic reinforcement improved the key properties needed for structural and oxidation applications.

Keywords: Cermets$_1$; Powder Metallurgy$_2$; Mechanical Milling$_3$; Spark Plasma Sintering$_4$; Mechanical Properties$_5$; Wear$_6$; Oxidation$_7$

Contents

List of Figures

List of Tables

Abbreviations

SiC	Silicon Carbide
B_4C	Boron Carbide
Si	Silicon
Al	Aluminium
Fe	Iron
Pt	Platinum
ASTM	American Society for Testing of Materials
wt. %	Weight percent
at.%	Atomic percent
vol.%	Volume percent
BSE	Back Scattered Electron
CTE	Co-efficient of thermal expansion
EDS	Energy Dispersive Spectrometry
FESEM	Field Emission Scanning Electron Microscopy
HIP	Hot Isostatic Pressing
HV	Vickers Pyramid Number
P/M	Powder Metallurgy
PCA	Process Control Agent
SE	Secondary Electron
BSE	Back Scattered Electron
SEM	Scanning Electron Microscopy
SPS	Spark Plasma Sintering
XRD	X-Ray Diffraction
MH	Microhardness
FT	Fracture toughness
CS	Compressive strength
FS	Flexural strength

Nomenclature

ρ	Relative density
MPa	Mega pascal
°C	Degree in Celsius
KI_c	Indentation fracture toughness
gm_f	Gram force
nm	Nano meter
µm	Micro meter
α-SiC	Silicon Carbide (hexagonal structure)
β-SiC	Silicon Carbide (cubic structure)
σ	Flexural strength
σ	Electrical conductivity
Ω	Atomic volume
λ	Wavelength of the Cu target
M	Grain boundary mobility
C_o	Concentration of solute atoms
G_L	Grain size
D_b	Diffusion co-efficient across boundary
k	Boltzmann constant
Q	Partition co-efficient between the boundary and lattice
Q	Volume of wear debris

Chapter 1

Introduction and Literature review

1.1 Introduction

In last few decades, efforts have been made to develop structural **cermets** for industrial applications and scientific research. Cermets are “a heterogeneous combination of metal(s) or alloy(s) with one or more ceramic phases in which the latter constitutes approximately 15 to 85 percent by volume and there is relatively little solubility between metallic and ceramic phases at the preparation temperature” [1]. In fact, cermets are unique in the way that combines the characteristic properties of metals and ceramics. Cermets are being developed as remarkable materials for working under different critical conditions due to their outstanding physical and mechanical properties, including high hardness, lightweight, high wear resistance, high melting point, oxidation resistance and great resistance to chemical attack. These superior properties of cermet make it a promising engineering material for use in several aero-engine components, turbo pumps, cutting tools, heat exchangers, heat engine parts, fusion reactors, armour plates etc [2–9]. Since metals and ceramics have their own limitations for the use of different industrial applications, interest has been given to cermet materials. During high speed application, heat generated from friction creates problems for metals. Metals might corrode or rust when used in wet environment. Whereas, ceramics are chemical resistant and heat resistant; use of ceramics can reduce these problems. But brittleness of ceramic materials leads to crack generation and give catastrophic failures to the ceramic equipment.

Carbide based cermet materials have potential for extreme high temperature resistance, and high hardness. SiC and B_4C are mainly used for the preparation of ceramic armour, cockpits of military airplanes, and high speed applications [8, 9]. Materials with high melting point like SiC (2700 °C) and B_4C (2445 °C) require high temperature and pressure for densification during consolidation. Unfortunately, the processing of pure B_4C and SiC components to obtain sufficiently dense products have proved quite difficult, mainly due to the strong covalent bonding, which is responsible for the inherently low diffusion mobility [10]. B_4C and SiC are intrinsically super-hard, but hardly sinterable and relatively brittle, highly resistance to grain boundary sliding, of low diffusion co-efficient, Exhibit exaggerated grain growth at high temperature, and very low fracture toughness limit their applications as structural materials [10–12].

There are three conditions for producing dense products [8].

(a) Reaction sintering gives porous structure. Mixture of SiC and B_4C powders are preferred over reaction sintering of SiB_6 and graphite to produce dense SiC+B_4C because reaction sintering of SiB_6 and graphite give porous SiC and B_4C.

(b) Secondly, the grain size must be as low as possible i.e. < 3µm. In many studies it has been observed that powder size greater than 10 µm cannot be sintered properly even at high temperatures.

(c) Last but not least, high temperature sintering near the melting point of SiC and B_4C (> 2300 °C) is needed.

Several strategies have been developed to overcome these disadvantages, such as reduction of initial particle size of powders, and combining it with sintering aids for example, Al, Si, and Fe to obtain the dense SiC-B_4C based cermets under low temperature. Incorporation of metallic elements into SiC-B_4C based ceramic matrix improves the properties since they acts as a binder and lowers the sintering temperature [13–18]. Addition of low temperature melting metal like Al (660 °C) not only enhances densification but also favours β to α phase transformation of SiC [19, 20]. It imparts high strength and fracture toughness to the matrix. Si (1414 °C) addition into B_4C and SiC is also very useful in improving the sinterability and properties of sintered products [21–26]. Boron carbide can act as an alternative source of carbon in the presence of Si to form secondary SiC particles and is beneficial for the improvement of properties [5–21, 22, 24].

In addition, modern investigations have shown that disorder-order transformation during sintering promotes the densification process and lowers the sintering temperature. Many processes are in commercial use like rapid solidification, mechanical alloying/milling, plasma processing, and vapour deposition for better control of the structure and constitution of advanced materials under non-equilibrium conditions. Mechanical milling is one of the simple, widely used, economically variable but powerful ways to synthesize disordered ultrafine ceramic/ composite powders. Repeated collision, crushing and extruding of powder particles in between balls during milling reduces the diameter of powder particles. Thus a large number in lattice defects are formed and atomic disorder of the powder increased. This disordered structure increases the molecular diffusion channel during sintering and enhance the densification. Therefore, dense samples are obtained at low sintering temperature [26].

Several approaches have been made to fabricate SiC and B_4C for better densification and improved mechanical properties by conventional sintering, hot pressing and spark plasma sintering (SPS) techniques. It is very difficult to achieve fully dense materials with monolithic SiC and B_4C by conventional sintering technique and there is a chance of phase transformations at high temperature sintering [27, 28]. Pressure assisted high temperature sintering is essential for densification of such kind of carbide cermet materials. From the available literatures it has been observed that, the monolithic B_4C and SiC powders can be densified completely by SPS method at comparatively low temperatures without sintering additives [29, 30]. The sintering conditions applied for SPS is helpful for obtaining harder B_4C and SiC ceramics with high density and limited grain growth. To increase the toughness and maintain the refined microstructure for better hardness and improved strength in final products is a processing challenge. The sinterability and toughness of highly refractory ceramics has been improved by using sintering additives. So the needs can be fulfilled by a combination of SPS process and addition of reinforcing secondary phases into the main constituent material [31–34].

The main part of this thesis is to prepare fine and homogeneous SiC-B_4C based cermets powders by mechanical milling in lesser time that can be easily fabricated and consolidated by pressure-less sintering and SPS methods. The fine particle sizes with higher surface area of milled powders have potential to sinter faster at low temperature. The retention of finer grain size in the final sintered product after consolidation has put a great challenge. High porosity coupled with poor mechanical strength is found when sintered by conventional sintering even at high temperature. Conventional pressure-less sintering cannot eliminate all the pores and there is a rapid grain growth. Spark plasma sintering is regarded as a rapid sintering method that generates highly sintered products in less sintering time with finer grain size.

Although there are some reports on the fabrication of SiC-B_4C ceramics by pressure assisted sintering technique, limited work has been carried out on the addition of a metal (namely Al and Si) into SiC-B_4C during pressure-less sintering. Moreover, no reports are available on the synthesis of SiC-B_4C–Si and SiC-B_4C–Al cermets by SPS process. Hence, the present study attempts to prepare SiC-B_4C–Si and SiC-B_4C–Al cermets by both pressures-less sintering and SPS and also study the effect of Si and Al addition on their microstructures and mechanical properties. The weight percentage of Al and Si metal addition were kept to 0, 2, 5, 10, and 20 wt. % because the metal addition in greater amount could result in a formation of additional phases and hence deteriorate the mechanical properties. The effect of sintering temperatures, and sintering methods (conventional and SPS) on microstructure, density, hardness, phase analysis, flexural strength, fracture toughness and un-lubricated sliding wear resistance properties were evaluated. In addition to this, oxidation resistance and electrical conductivity of SiC-B_4C based cermets were also conducted which has not been previously investigated.

1.2 Literature review

This portion has been divided into four sections and enlightens the available research work that has been done in the area of improving the properties of SiC-B_4C based cermets. The first section summarizes the fabrication methods of cermets by powder metallurgy route. This section has been divided into four sub-sections where it covers composite powder preparation and processing by mechanical milling, shape-forming process by die compaction and finally consolidation. Consolidation process comprises sintering mechanism, stages of sintering, grain growth and coarsening, control of grain growth, liquid phase sintering, and different sintering techniques. Special emphasis is placed on conventional sintering and SPS process. The second section describes the structure and properties of SiC and B_4C materials. The third section presents the recent literatures on fabrication of SiC-B_4C, SiC-B_4C–Si and SiC-B_4C–Al cermets. In the fourth section a general overview on the wear mechanism and existing literatures on oxidation properties of these cermet materials are illustrated.

1.2.1 Fabrication methods of cermets

Cermets can be processed by various processing techniques. Some of the important processing techniques are as follows [33, 34]:

1. Cold pressing and sintering
2. Hot pressing
3. Reaction bonding
4. Infiltration

5. In-situ chemical reaction techniques
6. Sol-gel technique
7. Electrophoretic deposition
8. Self-propagating high temperature synthesis
9. Powder metallurgy.

Amongst them ***powder metallurgy*** is the most diverse manufacturing technique to fabricate high quality, homogeneous, complex parts with improved properties, coupled with low cost and productivity. Powder metallurgy is the study of the processing of powders, including the fabrication, characterization and conversion of powders into useful engineering components. In the powder metallurgy route, required powders could be fabricated below melting temperature of the materials. This eliminates segregation and other defects associated with casting route. Many applications rely on the economical production of complex parts and which are quite difficult to process by other techniques. Components for automotive industry represents good example of this area. The unique property and microstructure of oxide dispersion strengthen alloys, cermets and cemented carbides are very difficult to fabricate by other techniques, which contributes to the growth of powder metallurgy [26, 33].

Powder metallurgy route requires five steps to complete materials synthesis. It includes, (I) powder preparation, (II) powder processing, (III) shape-forming operations, (IV) sintering or consolidation and (V) finally finishing of the fully dense specimens [33, 34].

1.2.1.1 Powder preparation

Ceramic powders can be prepared by various techniques namely, electrolytic deposition, chemical reaction, atomization and mechanical process like grinding or comminution. These techniques permit mass production of ceramic and metal powders with fine grain size. The main benefit of electrolytic process is to form metal powders with high purity. In this process dissolution of the anode begins under an applied voltage in an electrolytic cell. The powder formed by electrolytic process is often dendrite or sponge in shape. Chemical methods are generally used to prepare most advanced ceramic materials from synthetic materials or naturally occurring raw materials, and undergone a considerable degree of chemical refinement to have higher purity. In case of atomization process, from molten metal the powder formation is possible using a spray of droplets. Both metal powders and pre-alloyed powders can be processed by this method. It involves gas atomization, water atomization and centrifugal atomization techniques. Mechanical process involves preparing traditional ceramics from naturally occurring raw materials. There are four fundamental mechanical processes: impaction, attritioning, shearing and compression. Powders produced by mechanical process are typically irregular in shape [33, 34].

1.2.1.2 Powder processing

Powder processing is a very important step for powder metallurgy. It involves the weighing and mixing of powder according to desired composition. The chosen elements for powder processing will influence the structure and properties of the final product. Some of the important characteristics of powders which define the quality of final ceramics or cermets are taken into consideration: chemical composition, phase composition, particle size, particle size distribution, particle shape, and agglomeration. Blending is a very necessary step to provide a uniform distribution of the required composition powder by mixing two or more powder constituents [33]. Blending is usually done by mechanical milling. Mechanical milling uses the mechanical force to break the agglomerates and reduce the sizes of the individual particles. Milling can be done in dry or wet environment. Wet milling has advantage over dry milling because the energy utilisation is higher in wet milling and it increases the production of higher fraction of finer particles. There are various mills available to reduce the size of the particles for research and industrial purposes. These are mainly, SPEX shaker mills, planetary ball mills, attritor mills and commercial mills. SPEX shaker mills are used for only laboratory uses to mill about 10-20 gm of powers at a time. Planetary ball mills can generate even up to 1200 RPM. A large quantity of powder can be milled by attritor mill and commercial ball mill for industrial purposes [26].

Mechanism of milling: During high energy ball milling the powder particles are subjected to repeated flattening, cold welding, fracturing, and rewelding to produce controlled microstructure of powder particles. During milling, collision occurs among ball to ball, ball to powder and ball to vial. During collision, some amount of powder is entrapped in between balls and the impact force plastically deforms the powder particles. This leads to work hardening and fracture of the powder particles. In case of ductile metals, the powder get flattened and work hardened in the initial stages of milling. This causes the increase of particle size of the starting particles. On the other hand, in case of brittle ceramic materials (SiC, B_4C) fracturing takes place. With continuous milling, the particles get work hardened and fracture with continuous deformation by fatigue failure. Constant milling causes the fracture predominates over the cold welding and refined the particle size. High energy mechanical alloying introduced heavy plastic deformation. This plastic deformation causes crystal defects such as dislocations, vacancies, stacking faults, and increased the surface area by increasing number of grain boundaries [26]. Figure 1.1 shows the schematic diagram of ball-powder-ball collision and mechanism during mechanical milling.

Contamination is a problem in mechanical milling. While the particle size is being reduced, the mill walls and milling media also get wear. Contamination can be controlled by careful selection of milling media and vials.

Various milling process variables are there to optimize the milling parameter for production of contamination free fine powders with required size. Some of the important parameters are [26]:

(a) Type of mill
(b) Milling container
(c) Milling speed
(d) Milling time
(e) Grinding medium
(f) Ball to powder weight ratio
(g) Extent of filling the vial
(h) Milling atmosphere
(i) Process control agent and
(j) Temperature of milling

All these parameters should be carefully chosen for producing ultrafine powders in minimal contamination.

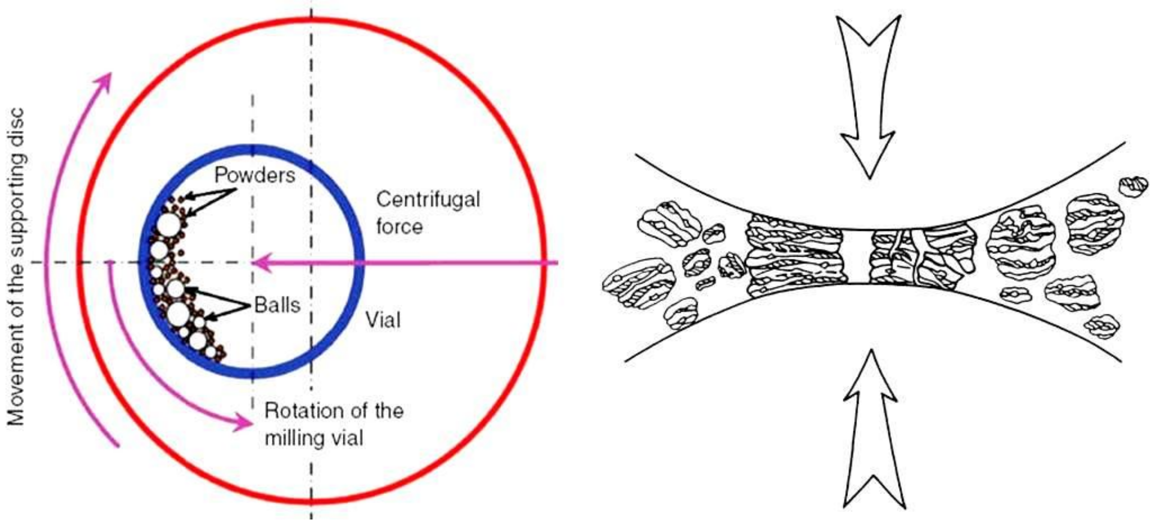

Figure 1.1 Schematic diagrams of ball-powder-ball collisions of powder mixture and mechanism during mechanical milling [26].

1.2.1.3 Shape-forming process

Table 1.1 *Various forming methods of pre-consolidated powders [34].*

Forming methods	**Feed material**	**Shape of green body**
	Pressing	
Uniaxial pressing (Die compaction)	Powder or free-flowing granules	Small, simple shapes
Isostatic pressing	Powder or fragile granules	Larger, more intricate shapes
	Casting of a slurry	
Slip casting	Free-flowing slurry with low binder content	Thin, intricate shapes
Tape casting	Free-flowing slurry with high binder content	Thin sheets
	Deformation of a plastic mass	
Extrusion	Moist mixture of powder and binder solution	Elongated shapes with uniform cross section
Injection moulding	Granulated mixture of powder and solid binder	Small, intricate shapes

The common forming methods of pre-consolidated powders are summarized in Table 1.1. The formed ceramic body is an un-sintered, low density powder compact (green body) having very little mechanical strength. The main forming method includes, mechanical pressing, slip or tape casting, and plastic forming. Mechanical pressing is the only process used for this research and will be explained further in this section.

Die compaction involves the pressing of dry (< 2 wt. % water) or semidry (5 to 20 wt. % water) powders in a die. It is a most widely used method for ceramic powder compaction which forms simple shapes rapidly with accurate dimensions. The height to diameter ratio for die pressing should be ≤ 0.5. The overall process of compaction consists of three steps: filling of the die, powder compaction, and the ejection of compacted powder. In uniaxial pressing, ceramic powders poured into a rigid die and loaded along a single axial direction through a rigid punch until the applied pressure achieved the given pressure. The upper and lower punches simultaneously compress the powders. The density of the compact increased within the die and good particle-to-particle contact is achieved in this process. After pressing the green compact get ejected from the die body.

There are some problems that can be encountered in uniaxial pressing. The density obtained in uniaxial pressing is non-uniform. Here, the applied pressure is not transmitted uniformly because of the friction between the particles and friction generated between the die walls and particles. The stress variation limits the uniform degree of packing and creates density variations in the green body. Applied pressure decreases exponentially with the increase in axial distance from the punch. This pressing can leave large pores that cannot be eliminated by sintering and hence reduce the mechanical properties of the specimen. Often cracks initiates at the top edge of the green compact during release of pressure or ejection of the compact. Due to improper die design, air entrapment, and die wall friction, the materials rebounds near the top centre of the compact. During ejection also material rebounds to a larger cross section. Tensile stress is generated in the material just above the top of the die and results in a series of lamellar cracks [34, 35].

These problems can be avoided by considering the following steps:

(a) Use of lubricant to reduce die–wall friction;

(b) Proper binder selection to improve the green strength;

(c) Minimizing rebound; and

(d) Maintaining a hold-down pressure on the upper punch during ejection.

The good green strength with minimum rebound can be achieved by a suitable binder addition into the powder prior to pressing. Binders reduce the die-wall friction and particle-particle friction and thus reduce density variation in the compact. Generally organic binders are used. They coat the powder particles, provide lubrication during pressing, and increase the temporary bonding after pressing. The amount of binder required for pressing is quite low and varies from 0.5 to 5 wt. %. These organic binders decompose during high temperature sintering and evolved as gases. Waxes, wax emulsions and some gums produce soft granules and called as soft binders. The soft binders have a tendency to stick and reduce the homogeneous density distribution or rate of production. Some binders are hard and they produce hard granules. These granules have the advantages that they are dimensionally stable, free-flowing and good for high volume production. These are not generally self-lubricating. They require small amount of lubricant and moisture prior to pressing. Dextrin, lignin, acrylates and starches are the example of hard granules. Polyvinyl alcohol (PVA) and methyl cellulose are slightly softer granules and hence are widely use as binder in production of many ceramic compacts. In the present research, PVA is being used as binder for the compaction of cermet powders [34, 35].

Green body can be subjected to additional compaction by the process called isostatic pressing or cold isostatic pressing (CIP). Here, the pressure applied from all direction instead of one or two direction. Here, the compact is placed in a mold made from rubber or some type of elastomer and all the assembly dropped into a chamber filled with fluid. Generally, 400 to 1000 MPa pressure is applied through the fluid.

1.2.1.4 Sintering

Sintering is a processing technique used to produce dense solid materials or components from metal and/or ceramic powders by applying thermal energy. From 1940s, the sintering was studied scientifically and remarkable developments have been made. In modern research, sintering is the most important part for all kind of materials fabrication, including powder metallurgical parts and bulk ceramic components. Basically, sintering process is categorized into four types depending on the composition being fired and the extent of second phase formed during heat treatment.

Solid state sintering: In this sintering process, powder compact is densified in a solid state at the sintering temperature. The shaped green body is heated to a temperature that is typically 0.5– 0.9 of the melting point. Atomic diffusion in the solid state produces joining of particles and reduces the porosity.

Liquid phase sintering: In this sintering process, liquid phase is present in the powder compacts during sintering. This is an important method for industrial fabrication of ceramics. Liquid phase present during sintering enhanced the densification at lower sintering temperature.

Vitrification: In this process, the large volume of liquid that is typically greater than 25% of the original solid volume is formed on heating. Here the dense product is achieved by flow of liquid into the pores and either crystallization or vitrification (glass formation) of the liquid during cooling. It is important for the production of ceramics from naturally available raw materials such as clays.

Viscous sintering: In this process, a consolidated mass of the glass particles is heated above the softening temperature. Here, densification occurs by viscous flow of glass under the influence of surface tension.

1.2.1.4.a Mechanisms of sintering

Sintering of crystalline materials can occur by six different mechanisms as shown schematically in Figure 1.2. A distinction commonly made between densifying and non-densifying mechanisms. The mechanisms 1, 2, and 3 i.e., surface diffusion, lattice diffusion from the particle surface to the neck, and vapour transport lead to neck growth without densification and called as non-densifying mechanisms. Grain boundary diffusion, lattice diffusion from the grain boundary to the pore (mechanism 4, and 5) is the most important densifying mechanisms. Diffusion from grin boundary to the pore permits neck growth as well as densification. Plastic flow by dislocation motion (mechanism 6) also leads to neck growth and densification but it is more common for metal powders [36, 37].

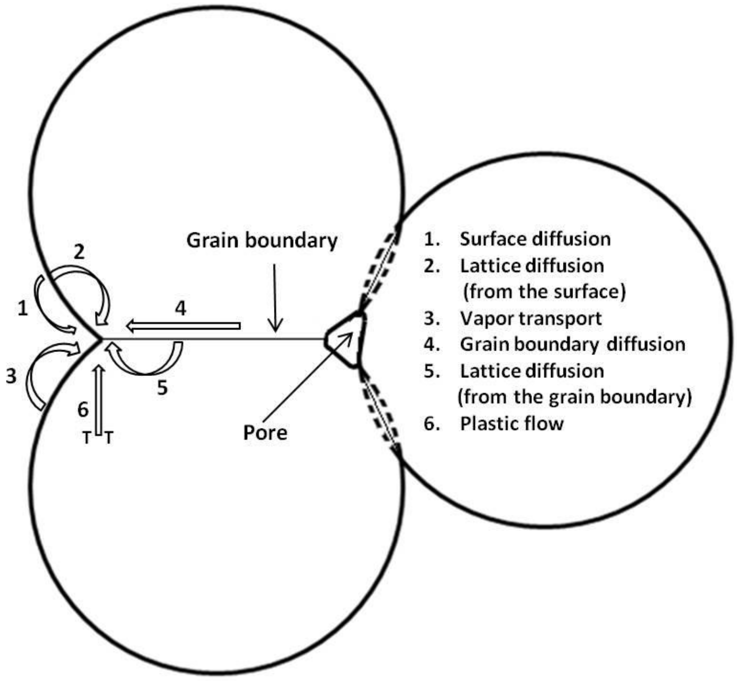

Figure 1.2 Six mechanisms contribute to the sintering of porous powder compact where mechanisms 4 and 6 lead to densification and all cause the necks to grow and influence the rate of densification [36, 37].

1.2.1.4.b Stages of sintering

There are three stages of sintering; (1) initial stage, (2) intermediate stage and (3) final stage as shown in Figure 1.3. During the initial stage of sintering, concave neck forms between the individual particles and rapid growth of the inter-particle neck takes place. The amount of densification is small and this stage ends when relative density reaches 65% with linear shrinkage of 3–5%. In intermediate stage, the pore structure becomes smooth and interconnected. Pore radius decreases with increase in densification and grain growth. This stage ends when relative density reaches 90% with relative shrinkage of 5–20%. Final stage of sintering is a slow process, pores become isolated at the grain corners and spherical pores shrink by bulk diffusion mechanism. Continuous pore shrinkage occurred in this stage and gradually disappears altogether. The relative density ≥ 95% could be reached after final stage of sintering. However, pores that are larger than grain shrink relatively slowly. As the final stage of sintering is prolonged process, the grains increase their size rapidly while the pores within the larger grains shrink slowly [33–36].

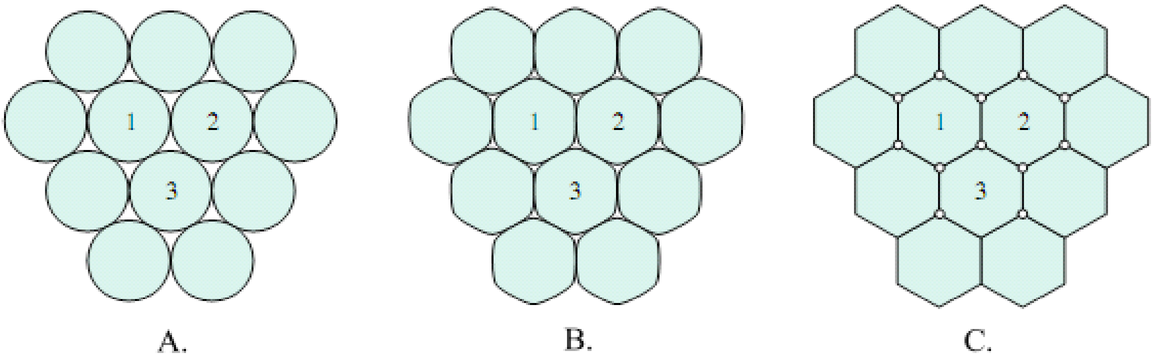

Figure 1.3 The sintering process: A. Initial stage; B. Intermediate stage; C. Final stage.

1.2.1.4.c Grain growth and coarsening

The average grain size of polycrystalline materials increases as the annealing time increases or heated at elevated temperatures. Grain growth is the term describes the increase in the average grain size of polycrystalline materials. In the process of grain growth, the convex grains lose atoms while the concave grains gain atoms. Therefore, the grain boundary moves towards the centre of curvature. Grain growth is divided into two types (i) normal grain growth and (ii) abnormal (exaggerated) grain growth. In the normal grain growth, the average grain size increase with time but the grain size distribution remains self-similar. In case of abnormal grain growth, a few numbers of large grains grow rapidly at the expense of smaller grains. It gives bimodal grains size distribution. Anisotropic grain growth is an example of abnormal grain growth in which abnormal grains grow in an elongated manner. Abnormal grain growth must be avoided if high density is to be achieved [38–40].

The coarsening is a process where the increase in average grain size accompanied by an increase in the average pore size. Coarsening reduces the driving force for sintering and increases the diffusion distance for mass transport; thereby reduce the rate of sintering. Therefore, suppression of coarsening mechanism is the key requirement for reaching high density. Coarsening of particles in solid or liquid medium is commonly known as Ostwald ripening [39, 40]. Schematic diagram of Ostwald ripening is shown in Figure 1.4. As large size grains are more energetically stable than small grains, therefore, small grains loose atoms to larger grains. The grains smaller than the critical size continues to shrink and larger grains grow further, at the expense of small grains. This is the process of Ostwald ripening described by Wilhelm Ostwald in 1896.

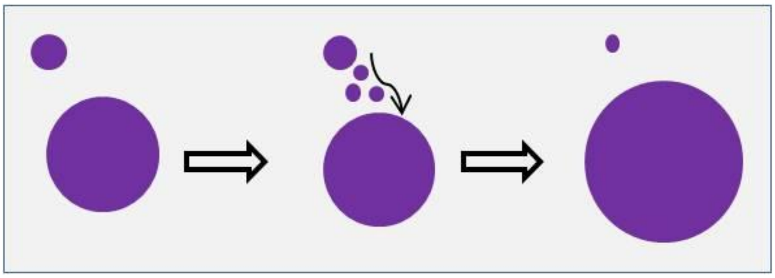

Figure 1.4 Schematic diagram of Ostwald ripening

1.2.1.4.d Control of grain growth

The most effective approach for inhibiting grain growth is the incorporation of additives in the powder to form solid solution. The concentration of dopant is believed to reduce its solid solubility limit in the ceramic. The effectiveness of dopant in suppressing grain growth depends on its ability to grain boundary segregation. The grain growth is inhibited by the mechanism of solute drag. Here, strong interactions occur in between the segregated atoms and the grain boundary so that the solute must be carried along the moving grain boundary. The solute drag theory put forward by Cahn [41], and the grain boundary mobility of the doped material is given by

$$M'_b = \frac{D_b \Omega}{4\mathrm{kT}\delta_{gb}\mathrm{Q}C_o} \qquad (1.1)$$

Where D_b is the diffusion co-efficient of the solute atoms across the boundary of width δ_{gb}, Ω is the atomic volume of the host atoms, k is the Boltzmann constant, C_o is the concentration of the solute atoms in the lattice, and Q is the partition co-efficient (< 1) between the boundary and lattice, and T is the absolute temperature. According to eq. (1) the boundary mobility is directly proportional to the diffusivity of the solute across the boundary and inversely proportional to the segregated concentration of the solute(QC_o). This indicates that the aliovalent solutes with larger ionic radii than the host would be effective for suppressing grain growth.

Another effective approach for grain growth control involves the fine, inert second phase particles at the grain boundaries. The precipitates inhibit grain growth by pinning mechanism suggested by Zener in a communication to Smith. According to Zener, the matrix reaches a limiting grain size given by

$$G_L = \frac{2\alpha r}{3f} \qquad (1.2)$$

Where α is the geometrical constant depends on shape of the matrix grains (e.g., α = 2 for spherical grain), r is the radius of the inclusion (precipitates) and f is the volume fraction of inclusions in the solid. Stearns *et al.* [42, 43] indicates that the pinning particles are not distributed as randomly as assumed by Zener model, so eq. (1.2) requires some modification by incorporating the observed fraction of pinning particles at the grain boundaries.

1.2.1.4.e Functions of fine grains on sintering

It is evident that ball milling is a useful technique to reduce the particle size of the raw ceramic materials to 0.1–1.0 µm. These smaller particles have a high surface energy. The large surface energy increases the driving force of sintering. The small size particles compact properly during pressing by particle rearrangement. Therefore, at lower sintering temperature the compactness of the powder sample increases. At early stage of sintering, many connective pores distribute at the boundaries and their shapes are irregular. With rise in temperature, the heat would eliminate pores and accelerate the grains to grow up. At the end, the minor round shape closed pores are present at the boundaries or in the grains. Special efforts are undertaken to densify the fine grained materials and suppress the grain growth. Pressure assisted sintering methods like hot pressing and spark plasma sintering (SPS) are mainly used to promote densification over sintering. High density with limited grain growth can be achieved by long time sintering at intermediate temperature (rate control sintering) or at high temperature with short sintering time (fast firing). The activation enthalpy for lattice diffusion is larger than the activation enthalpy for grain boundary diffusion and surface diffusion. Therefore, short sintering time at high temperature is beneficial in producing fine grained dense ceramics. So, the grain growth can be restricted and ultrafine sintered grains (≤ 5 µm) can be produced [10, 34].

1.2.1.4.f Liquid phase sintering

Liquid phase sintering is effective for SiC, B_4C, and Si_3N_4 those have a high covalent bonding. Therefore, densification by solid state sintering of these materials is very difficult. This process is important when the use of solid state sintering is very expensive and requires very high fabrication temperature. In liquid phase sintering, the liquid phase wets and spreads to cover the solid surfaces. The solid particles will be separated by liquid bridge, so the friction between the particles reduced. Hence, the particles rearrange more easily under the compressive capillary stress exerted by the liquid [34].

Generally, liquid phase sintering is performed by four main stages:

(a) Melting and redistribution of liquid forming particles;

(b) Rearrangement of solid matrix phases driven by capillary stress gradient;

(c) Diffusivity in the liquid dominates, densification and shape accommodation of the solid phase involving solution–precipitation;

(d) Final densification driven by residual porosity in the liquid phase as shown in Figure 1.5.

The liquid additive should have some qualities for better densification,

(i) Low contact angle for good wetting of the solid

(ii) An appropriate solubility for the solid

(iii) Low viscosity for rapid matter transport through the liquid.

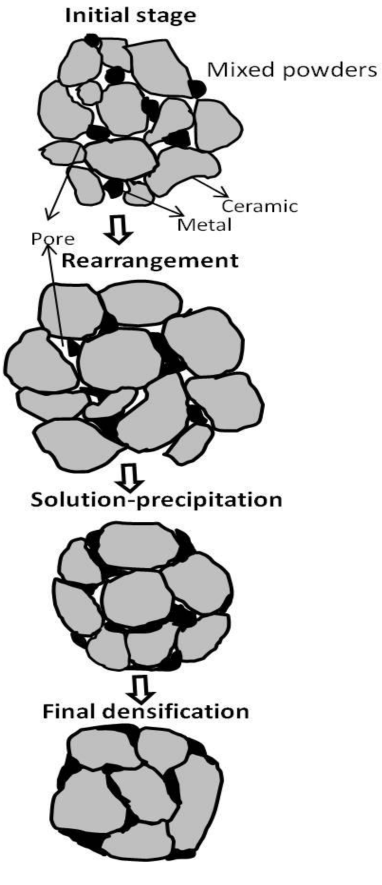

Figure 1.5 Schematic diagram showing microstructure changes during liquid phase sintering.

1.2.1.4.g Sintering techniques

A wide variety of sintering techniques have been developed to obtain dense ceramics with a desired density, microstructure, and phase composition for the required application. In general, pressure-less sintering and pressure assisted sintering are two main methods of sintering for a ceramic and cermet powder compact. Pressure assisted sintering includes spark plasma sintering (SPS), hot pressing, hot isostatic pressing (HIPing) and sinter forging. In the following section the details of pressure-less sintering and SPS are being discussed.

(i) Conventional pressure-less sintering

Conventional pressure-less sintering uses only heat energy, no external pressure is applied to the compact. This sintering method is the preferred method because it is economical, can be sintered geometrically complicated shape and large number of compacts can be sintered at one time. The powder can be compacted to green body and then can be machined, if necessary, into final green shape before sintering. The pressure-less sintering avoids density variation in the final component, which may occur with pressure-assisted sintering. Control of sintering atmosphere is also an important factor. The heating schedule is manipulated to enhance the densification rate relative to the coarsening rate. The activation energy for densification should be greater than that for coarsening rate. Hence, the final product of high density and fine grain size can be obtained by using rapid heating and the short sintering time at the high temperature. Conventional process involves higher temperature and longer holding times, which results in grain growth and thereby a reduced grain boundary area, are the main causes for lower mechanical properties. Magnani *et al.* [24] depicted that pressure-less sintering at 2150 °C of α-SiC–B_4C composite improved the density up to 96% with increasing hardness, fracture toughness and flexural strength.

(ii) Spark plasma sintering (SPS)

SPS is a rapid sintering method that uses heat energy, electric current and pressure simultaneously. The benefit of SPS over conventional pressure-less sintering is derived from the applied pressure, intense joule heating and a high current density at the particle contact surface rise the temperature rapidly causing surface melting and facilitating various diffusion processes which reduces the sintering time, temperature and inhibits the grain growth. In the SPS process, the graphite dies or tungsten carbide dies are being used. The stacked powder materials experience direct heating by the large spark pulse current, under an applied pressure of 30 to 500 MPa. An external uniaxial pressure is applied to the compact in order to accelerate the sintering process and facilitate a sufficient current path through the powder compact. This gives very high thermal efficiency compared to pressure-less conventional sintering. The plasma spark on the contact point or in the gap between the particles generates a local high temperature of several thousand degrees of centigrade. This is the main cause of evaporation and melting of surface powder particles and neck formation around contact area between particles in SPS process [26–28]. The specimen temperatures are difficult to assess and are measured by using an optical pyrometer focused on the graphite die wall. The ON-OFF DC pulse voltage and current produces spark plasma, spark impact pressure, joule heating, and an electric field diffusion effect [28]. Also high-temperature sputtering phenomena are generated by spark plasma and spark impact pressure and are responsible for eliminating adsorptive gas and impurities existing on the surface of powder particles [28]. This enables the powder particles on the surface to be purified and activated than in conventional sintering process. The electrical power generates joule heating; the applied pressure promotes plastic flow in materials, and the action of the electric field gives high-speed ion migration between contacts particles. These are believed to be the main factors promoting sintering. It creates high-speed diffusion, high-speed material transfer at micro and macro level. The schematic diagram of the SPS process is shown in the Figure 1.6. Most ceramic materials processed by conventional sintering are not able to achieve the theoretical density higher than 85%; however, it is possible to acquire density higher than 98% by spark plasma sintering (SPS) processing technique [44]. Hulbert *et al.* [29] stated that SPS is a promising potential technique to synthesize refractory hard materials. Hayun *et al.* [30] used plasma sintering (SPS) to prepare sufficient dense B_4C without any sintering aids with improved mechanical properties. According to Sahin *et al.* [45], an addition of 5 wt. % Y_2O_3 into B_4C–SiC composite sintered by SPS at 1700 °C and 1750 °C under a pressure of 40 MPa increased the density of B_4C–SiC composite to 99%. Hence, the SPS method has been used for the successful fabrication of poorly sintering materials such as borides, carbides and nitrides.

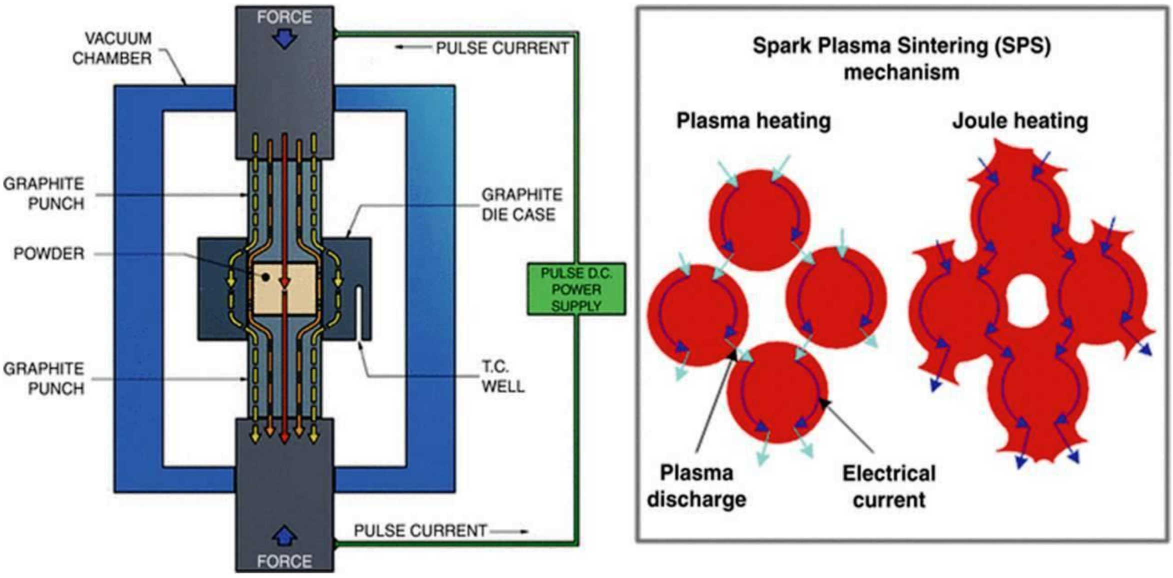

Figure 1.6 Schematic diagrams of SPS furnace and sintering mechanism.

1.2.2 Properties of SiC and B_4C ceramics

The structures of ceramics are more complicated than those of metals and generally be classified as crystalline and non-crystalline or amorphous ceramics. Some of the properties of crystalline solids depend on the crystal structure of the material. The following sections discuss the crystalline structure of ceramics and show the physical states of SiC and B_4C at different conditions of temperature and pressure with the help of phase diagrams.

1.2.2.1 Silicon carbide

Silicon carbide is a compound of silicon and carbon with the net formula SiC. The crystalline structure of the material varies because it exhibits polytypism. Around, 200 polytypes have been found for SiC, and some have the stacking periods of several hundred layers. Among the large number of SiC polytypes, only handfuls are considered as thermodynamically stable. The cubic structure β-SiC poly type 3C, the hexagonal structure polytypes such as 2H, 4H, and 6H polytypes α-SiC, along with the rhombohedra polytype 15R are most common as shown in Figure 1.7. The 6H-SiC polytype is most widely used in industrial purpose [46, 47].

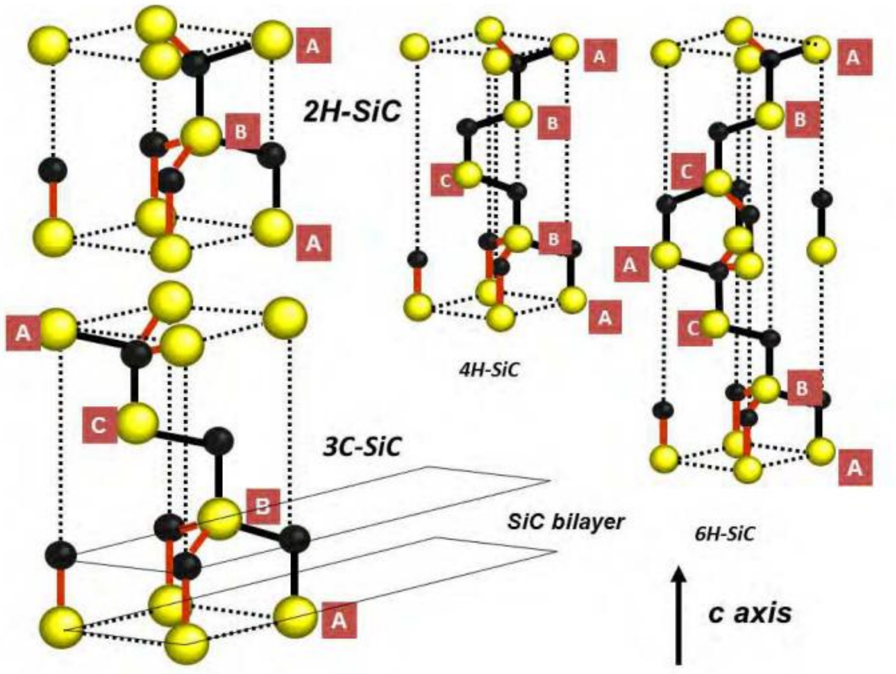

Figure 1.7 Three dimensional ball and stick representation of different polytypes of SiC. In the chains structures the stacking sequence are in dark colour and Si-C bonds are in red colour [48, 49].

The equilibrium phase diagram of the Si-C system is shown in Figure 1.8. The diagram indicates that there is a eutectic transformation at 1402 ± 5 °C at a composition of 0.75 ± 0.5 atomic percent carbon. The peritectic transformation occurs at 2545 ± 40 °C where SiC melts incongruently at a composition of 27 atomic percent carbon. A gaseous phase is formed at temperature above 3200 °C. β-SiC shows stability up to 1750 °C and phase transformation starts to take place above that temperature where β to α transformation was observed with 4H and 6H (α-SiC) polytypes. Nearly at 1900 °C, β-SiC transforms to α-SiC (4H with small amount 6H). As per literature β-SiC powder is prone to grain growth whereas α-SiC powders showed much less grain growth as function of temperature [46, 47].

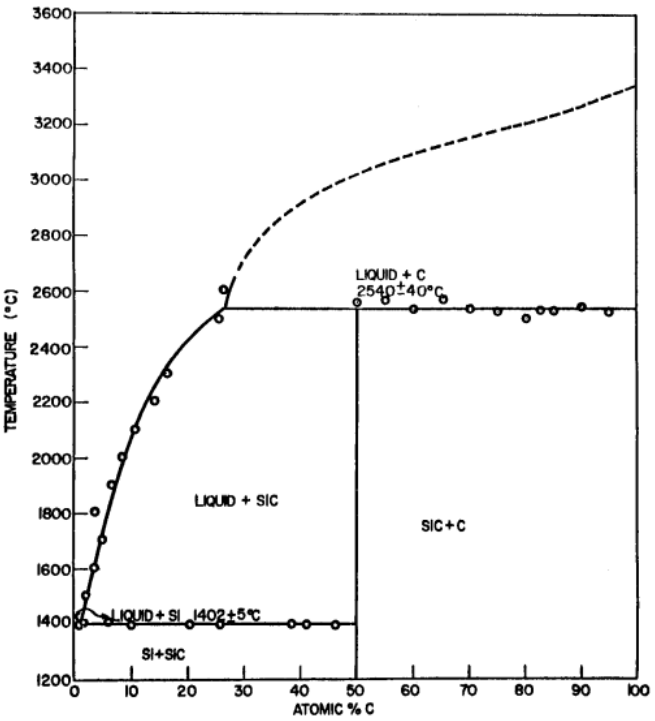

Figure 1.8 An equilibrium phase diagram of Silicon-Carbon [50].

Among the various hard materials, SiC containing materials have potential for aero engines, refractories and tribological applications due to high hardness, low relative density (light weight), low thermal expansion, high elastic modulus, and superior chemical inertness. Table 1.2 represents the summary of mechanical properties of SiC at room temperature.

Table 1.2 *Mechanical properties of SiC and B_4C*

Mechanical properties	**Silicon carbide (SiC)**	**Boron carbide (B_4C)**
Density [gm/cm^3]	3.16	2.52
Vickers hardness (1000 g_f load) [GPa]	30-35	28-30
Elastic modulus [GPa]	415	360-460
Flexural strength [MPa]	359	300-450
Fracture toughness [MPa.m$^{1/2}$]	3.1	2.9-3.7
Thermal expansion co-efficient [10^{-6}.K^{-1}]	2.5	3.1

1.2.2.2 Boron carbide

Boron carbide occupies a specific space in the group of most important non-metallic hard materials. The crystalline structure of boron carbide is a rhombohedral unit cell having 12-atom ecosahedral structures at the corner of cell. The centre of these ecosahedra are located on each of the corners of the rhombohedra cells and the 3- atom linear chains that link the ecosahedra along the rhombohedral axis as shown in Figure 1.9. A rhombohedron has axes of equal length and equal axial angles, while an ecosahedron is a polyhedron with 20 faces, 12 equivalent vertices, and various planes of symmetry. Boron carbide can exist as one phase with a large variation in carbon concentrations. This is possible by the boron and carbon atoms substitution for one another within both the ecosahedra and inter-ecosahedral chains. From the crystal symmetry consideration, two stoichimetries of boron carbide has the stable phase: (i) carbon rich boron carbide (B_4C or $B_{12}C_3$) with idealized structural formula (B12)CCC represents the 12 icosahedral boron atoms and 3 carbon chain atoms (C-C-C chain), and (ii) the $B_{13}C_2$ or ($B_{6.5}C$) compound with idealized structural configuration (B12)CBC represents the central chain carbon atom is replaced by boron atom (C-B-C chain). The mechanism of $B_{13}C_2$ formation and phase transition has become a subject of extensive studies [51–54].

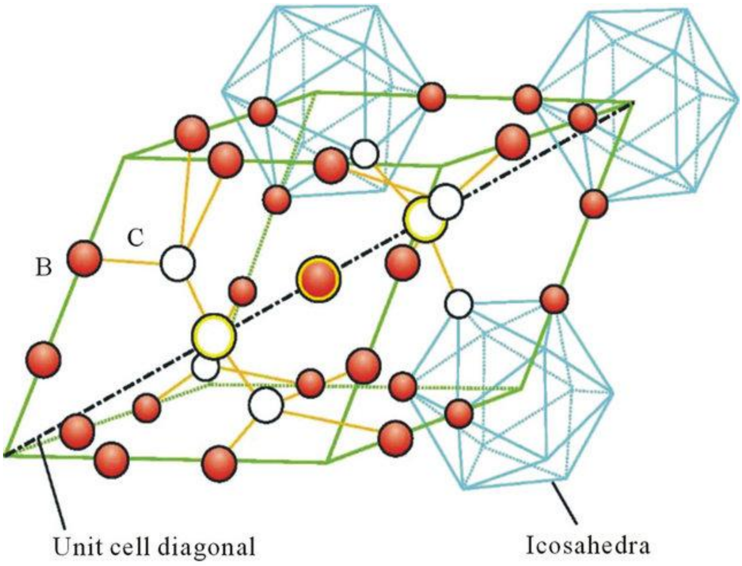

Figure 1.9 Schematic representation of crystalline structure of boron carbide [55].

The rhombohedral crystal structure of boron carbide has wide phase homogeneity range from B_4C (20 at.% carbon) to $B_{10.5}C$ (8.8 at.% Carbon) as shown in boron-carbon phase diagram in Figure 1.10. With increase in carbon content in the boron carbide the hardness value increases. For 10.6 at.% C content, the hardness in Knoop hardness tester was 29.1 GPa whereas, for 20 at.% C content, the hardness of 37.7 GPa was recorded [8]. The carbon saturated boron carbide and carbon mixture melt eutectically at 2390 ± 20 °C at a carbon concentration of about 27 atomic percent. The boron saturated boron carbide and β-rhombohedral boron melts peritectically at about 2075 °C. In between these two temperature limits, maximum solid solubility limit reached where B_4C melts congruently at 2470 ± 20 °C. The maximum melting temperature placed at a composition of 13.3 atomic percent carbon and in sometimes it placed at a compositions as high as 18.4 atomic percent carbon in some phase diagrams [50]. The exact composition at this point is not well known.

The hardest covalent solid substance after diamond and cubic boron nitride is B_4C which has a hardness of about 30 GPa. B_4C has been extensively used for its attractive properties, including high hardness, high melting point, low specific weight, great resistance to chemical agent, and neutron absorption capability. Therefore, B_4C has potential use in fast breed light weight armours, high temperature thermoelectric conversion and nuclear energy. Table 1.2 represents the summary of mechanical properties of B_4C at room temperature.

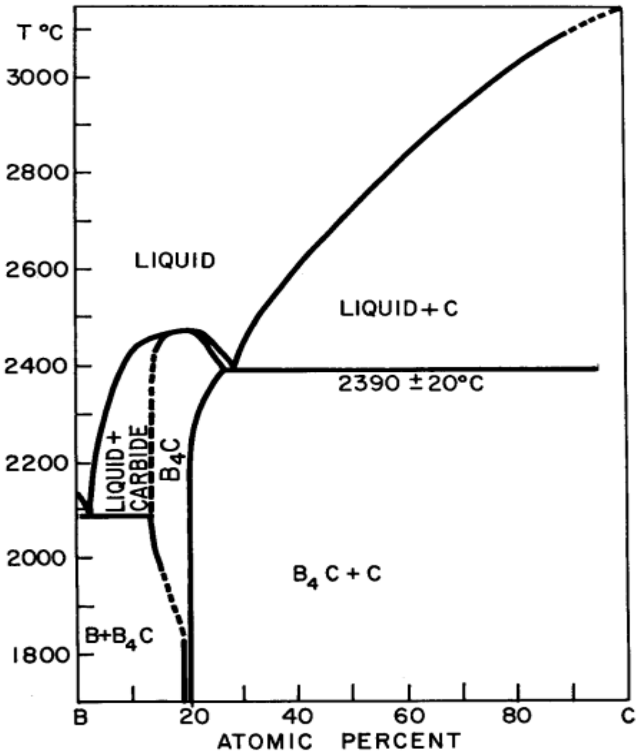

Figure 1.10 An equilibrium phase diagram of Boron-Carbon [50].

Figure 1.11 shows the ternary phase diagram of Silicon-Boron-Carbon system for the high carbon region. The line joining the SiC and B_4C has been drawn arbitrarily to define the area of research. The ternary system results that, there is a eutectic transformation between SiC, B_4C and carbon at 2250 ± 20 °C at the approximate composition of 15 atomic percent

Si, 30 atomic percent carbon and 55 atomic percent of boron. There is no compound formation at the high carbon region of the ternary system.

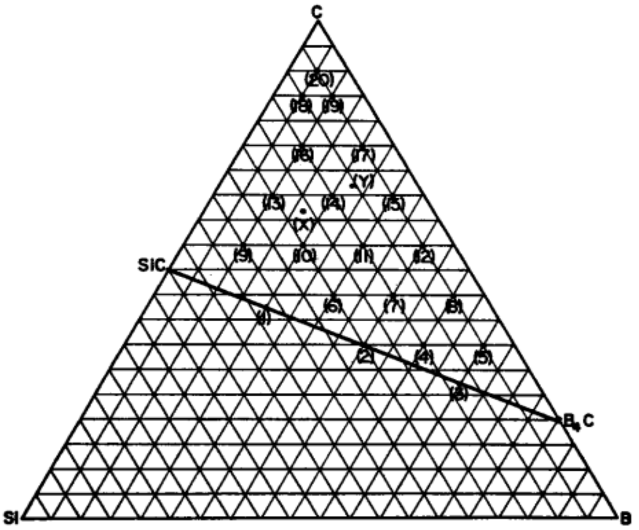

Figure 1.11 Silicon-Boron-Carbon ternary phase diagram [50].

1.2.3 Synthesis and characterization of SiC-B_4C composite ceramics

According to Mallick [56], preparation of dense β-SiC is difficult as there is a phase transformation from β-SiC to α-SiC in between 1900–2000 °C, that entraps porosity between grains. Addition of secondary phases to B_4C and SiC matrix improve their mechanical properties (fracture toughness and flexural strength) while reduce sintering temperature [57, 58]. Omori *et al.* [27, 28] reported rare earth oxides combined with Al_2O_3 and boron could be used to obtain highly dense SiC through liquid phase sintering. In various studies, Al_2O_3, CaO, and Y_2O_3 were added in SiC for liquid phase sintering. These oxides react with SiO_2 present at the surface of SiC to form the liquid phase at low temperature [59–62]. Alumina and yttria systems were not useful for high temperature application in heat exchanger manufacture due to the grain boundary oxidation phases which caused decreasing mechanical properties. One suitable material to improve the mechanical properties of SiC is B_4C. In order to control the phase transformation, grain growth and enhancement of mechanical properties, B_4C is used with SiC in various applications. Prochazka *et al.* [5] first used boron (B) and carbon (C) in SiC as sintering aids at a temperature of 2000 °C for better densification. SiC and B_4C are recognized as important structural ceramic materials for its unique combination of properties. Magnani *et al.* [24] studied the effects of B_4C addition on SiC properties. Sintering was performed by graphite element furnace at the temperature range of 1950–2220 °C. They obtained very interesting materials properties like high hardness, high flexural strength and fracture toughness compared to other SiC based materials for application in which high oxidation resistance is required. Moshtaghioun *et al.* [63] prepared ultra-fine grained B_4C–15 wt. % SiC and B_4C–15 wt. % SiC–2 wt. % C composites by mechanical milling followed by SPS technique at 1650 °C for 5 min or at 1700 °C for 3 min. They reported that B_4C–SiC composite ceramic has possessed high hardness and better toughness than pure B_4C ceramic. They observed that SiC grains formed crack bridging where cracks start to propagate and induce the toughening effect to the composite ceramic.

1.2.4 Synthesis and characterization of SiC-B_4C–Si cermets

Si addition in the B_4C and SiC is very useful in improving the sinterability and properties of sintered products [64]. Du *et al.* [64] studied the effect of Si addition on B_4C-SiC composites prepared from polycarbosilane-coated B_4C powder and found an enhancement of hardness, flexural strength and fracture toughness value by forming liquid phase at 11.4 wt. % Si. Feng *et al.* [65] also studied the effect of Si on densification and strengthening of B_4C consolidated by SPS. They observed maximum hardness, fracture toughness and flexural strength at 8 wt. % of Si. Boron carbide acts as an alternative source of carbon in the presence of Si to form secondary SiC particles and is beneficial for the improvement in properties [64–67]. Telle *et al.* [68] studied the B_4C-B–Si system and reported that the solid solubility of Si in boron carbide was 2.5 at.% after pressure-less sintering at 2250 °C. Higher amounts of Si reinforcement increased the residual Si contents in the sintered product and deteriorated the mechanical properties of the final product [30, 67].

1.2.5 Synthesis and characterization of SiC-B_4C–Al cermets

To aid sintering, a low melting metallic phase such as aluminium has been added and the effects of Al addition on the microstructure and mechanical properties of SiC-B_4C based cermets have been studied by Glasson *et al.* [13]. Ductile Al addition into SiC and B_4C acts as a binder and lowers the sintering temperature. Al metal addition also improves the toughness of the ceramic matrix without impairing the hardness of the carbide phase. Zhou et *al.* [69] studied pressure-less sintering of α- SiC by adding Al_4C_3-B_4C-C and observed the addition of these materials to enhance density and toughness. Cho *et al.* [15] also used Al, B and C additives to enhance densification in SiC. They found that grain growth rate decreases with increase in Al-B-C content in SiC. Gilbert et *al.* [19] used Al, B and C as additives into β-SiC to produce dense SiC by hot pressing. Williams et *al.* [23, 24] added Al, B and C to produce dense SiC by pressure-less sintering techniques. The addition of Al not only enhances densification but also favours β to α phase transformation of SiC. It imparts high strength and fracture toughness to the matrix. Mashhadi et *al.* [14] studied the effect of Al addition on pressure-less sintering of B_4C and found that density and grain size depend on the Al amount.

Viala *et al.* [70, 71] studied the stable and meta-stable phase equilibria of Al-Si-C and Al-B-C ternary systems under atmospheric pressure and temperatures up to 1627 °C. They found that Al does not react with SiC and B_4C in the solid state. However, liquid Al reacts with SiC and B4C and the reactions mainly took place in two couples like Al/SiC and Al-B_4C.

The Al/SiC couple

Figure 1.12 represents the Al-Si-C ternary system in the isothermal section at 1000 °C and 727 °C. At 650 ± 3 °C, Al reacts with SiC and produces Al_4C_3 and L, where L is liquid ternary phase containing Al, SiC (1.5±0.4 at.%) and C (< 1 ppm). At temperatures greater than 660 °C, SiC reacts with molten Al, and produces Al_4C_3 and Si.

$$\mathrm{SiC + Al \leftrightarrow Al_4C_3 + L_o} \tag{1.3}$$

$$\mathrm{3SiC + 4Al \rightarrow Al_4C_3 + 3Si} \tag{1.4}$$

At temperatures above 1377 °C, Al-SiC mixture produces Al_4SiC_4 instead of Al_4C_3. At higher temperatures, Al_8SiC_7 is formed.

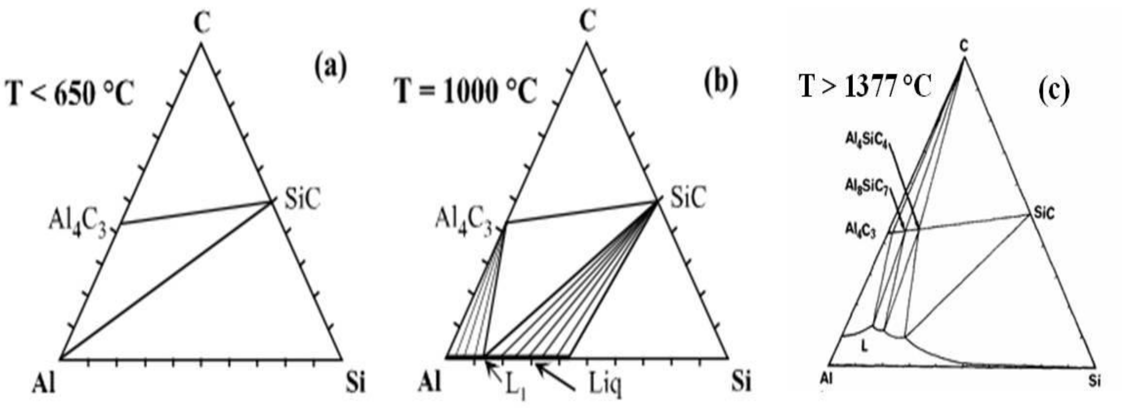

Figure 1.12 Isothermal sections of the Al-Si-C phase diagram; (a) at T < 650 °C, (b) at 1000 °C and (c) at T >1377 °C [70, 71].

The Al/B_4C couple

Figure 1.13 represents the Al-B-C ternary system in the isothermal section at 1000 °C and 727 °C. Viala *et al.* [71] studied the Al-B-C ternary system. At temperatures higher than (868 ± 4 °C), Al melts and decomposes to produce ternary carbide Al_3BC, diboride AlB_2 or complex boro carbide $Al_3B_{48}C_2$ (β-AlB_{12}).
At 868 ± 4 °C, quasi-peritectic reaction takes place:

$$Al_3B_{48}C_2 + L \leftrightarrow AlB_2 + Al_3BC \tag{1.5}$$

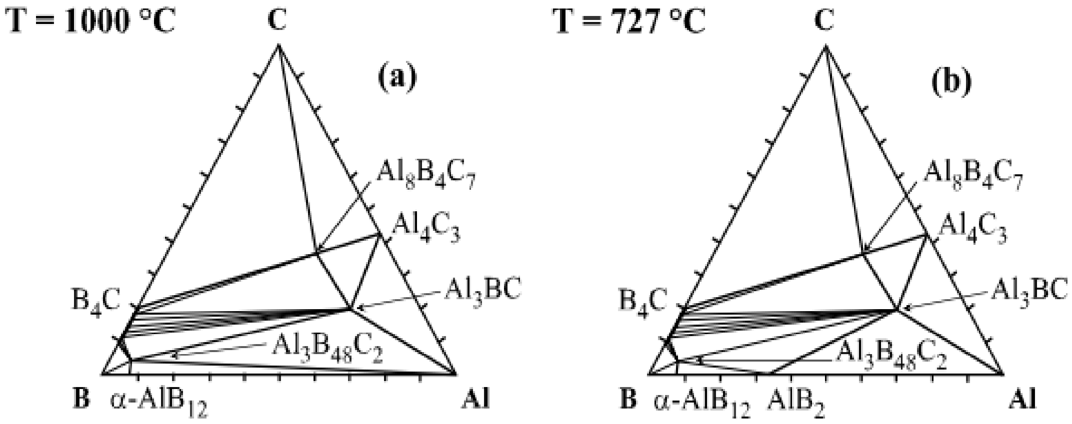

Figure 1.13 Isothermal sections of the Al-B-C phase diagram; (a) at 1000 °C and (b) at 727 °C [71].

1.2.6 Wear behaviour study of SiC-B_4C based cermets

Components made of B_4C and SiC ceramics have been used extensively in abrasive media for grinding and lapping, polishing media for hard materials, wear resistance components as blast nozzles and wheels dressing tools, valve components and bearings, seal rings, and heat engine parts etc. [8, 9, 72, 73]. Keeping in mind the versatile applications of SiC-B_4C based ceramics and cermets as wear and abrasion components, it is extremely important to study the wear behaviour of such material. It has also been observed that few literatures are available on wear behaviour of SiC materials at high temperatures [74]. Wear mechanism, effect of load, temperature, sliding speed on SiC materials were also studied [75–77]. Many researchers studied the wear and friction behaviour on carbide-boride systems [78–82]. Despite of many tribological studies, there is a lack of knowledge on sliding wear mechanisms of SiC-B_4C based ceramic composites. Yang *et al.* [83] studied

SiC–TiB_2 system and obtained a specific wear rate of 71.0 x 10^{-6} mm^3/Nm by carrying out wear experiment under pressure of 0.8 MPa at 0.2 m/sec. Daoud *et al.* [84] also investigated the effects of load and speed on the wear and friction behaviour of sand cast brake rotor (A359–20 vol.% SiC particle composites) sliding against automobile friction material. They observed that the wear rate of the composite increases with increasing applied load from 50 to 100 N. Zorzi *et al.* [85] studied the effect of C, B, TiB_2 and SiC addition on hardness and wear resistance properties of B_4C consolidated by pressure-less sintering at 2250 °C. They observed greater improvement in hardness and wear co-efficient of B_4C ceramic for 4 wt. % SiC, and also for 4 wt. % TiB_2 addition than that of only B_4C. We have seen that no report is available till today on wear behaviour of SiC-B_4C ceramic composites with metallic Si and Al reinforcement. Hence, we have attempted to give a fresh look on un-lubricated sliding wear behavior and mechanism of SiC-B_4C–Si and SiC-B_4C–Al cermets fabricated by pressure-less and SPS techniques.

1.2.7 Oxidation behaviour of SiC-B_4C based cermets

Oxidation resistance of SiC and B_4C is an important matter for its practical application at high temperatures. SiC based materials are widely used as refractory materials [86]. This material is also used in coating to protect materials from corrosive environments and combustion engines [87, 88]. SiC and B_4C are non-oxide but it has the tendency to get oxidize at high temperature in the presence of oxygen or oxidizing agents. Oxidation of SiC depends upon the type of atmosphere, oxygen partial pressure, and in coating purpose it depends on the nature of the substrate used. Fan *et al.* [89] studied the oxidation behavior of fine grained and course grained hot pressed SiC-B_4C/C composites at 800, 1200 and 1400 °C and found that fine grained composites had higher oxidation resistance with self-healing properties at 1400 °C. The effect of nanoparticle size SiC upon the oxidation behavior of C-B_4C-SiC composites was studied by Zhang *et al.* [90]. They performed the oxidation test from 500 to 1300 °C and found a very little mass change at different temperature due to self-protection process of SiC from oxidation. Narushima *et al.* [91] studied the oxidation behavior of B_4C-SiC composite at 800 to 1500 °C. They found mass gain at 800 °C due to formation of boron oxide (B_2O_3) liquid phase and mass loss at 1000 °C due to the vaporization of B_2O_3 in liquid borosilicate and showed that increase of SiC phase in B_4C-SiC composite can improve the oxidation resistance of the materials.

As SiC-B_4C based cermet material with a ductile binder metal imparts a certain degree of toughness to the material and lowers the sintering temperature. The improved toughness of these composite materials gives high thermal and mechanical shock resistance which is higher than the monolithic ceramic material. As cermet materials withstand higher shock than ceramic, cermet tools with less damage can replace the metal and ceramic tools [13, 16–18, 92–94]. In the present investigation, we have attempted to prepare the SiC-B_4C based cermets with varying Si and Al amount (0–20 wt. %) by conventional pressure-less sintering and SPS methods to improve the materials properties for specific applications.

1.2.8 Objectives

Based on the literature presented above, the salient objectives of the present study are:

- Fabrication of SiC-B_4C ceramic composite powder, SiC-B_4C–Si (2, 5, 10 and 20 wt. % of Si) and SiC-B_4C–Al (2, 5, 10 and 20 wt. % of Al) cermet powders of various compositions separately by mechanical milling for 10 h in a planetary mill.

- To prepare fine and homogeneous SiC-B_4C based cermets powders by mechanical milling in lesser time that can be easily fabricated and consolidated by pressure-less sintering and SPS methods.

- Retention of finer grain size in the final sintered product after consolidation is our main goal. Hence, optimization of SPS temperature to produce highly sintered products in less sintering time with finer grain size.

- Investigation of physical and mechanical properties (density, hardness, indentation fracture toughness, flexural strength and compressive strength) of the sintered products for various applications of SiC-B_4C based cermets.

- Investigation of wear resistant properties of all sintered products of SiC-B_4C–Si and SiC-B_4C–Al cermets at different applied loads.

- To study the oxidation resistance properties of all the cermets at different temperatures.

1.2.9 Scope of the thesis

Chapter 1 discusses about introduction and literature review. A detailed experimental procedure is provided in Chapter 2. All the synthesis and characterization techniques used for as received powder, milled powders and consolidated products of all the compositions are provided in this chapter.

Chapter 3 includes the major part of the thesis. This chapter is divided into two sections. In chapter 3.1, a description of the effect of milling on the dispersion, microstructure, and properties of the SiC-B_4C–Si and SiC-B_4C–Al composite powders have been discussed in details. Chapter 3.2 is again divided into three sub sections. In first subsection (Chapter 3.2b) we have discussed the fabrication of high melting SiC-B_4C ceramic composite by both conventional sintering and SPS techniques. The microstructure, density, hardness, indentation fracture toughness, compressive strength of all the samples fabricated by SPS and conventional sintering methods were compared. Second subsection (Chapter 3.2c) explains the effect of milling, variation of wider range of Si (2, 5, 10, and 20 wt. %) amount, and consolidation methods on physical and mechanical properties of the SiC-B_4C–Si cermet samples are studied. In third subsection (Chapter 3.2d) a detail description of the effects of 2, 5, 10, and 20 wt. % Al addition and consolidation methods on physical and mechanical properties of the SiC-B_4C–Al cermet samples has been discussed.

Chapter 4 explains the un-lubricated sliding wear bahaviour against a diamond indenter and electrical conductivity study by four-point probe measurement method of SiC-B_4C–Si and SiC-B_4C–Al fabricated through conventional sintering and SPS methods. This chapter provides the detail investigation of effect of different applied loads, wear mechanisms, wear depth, wear rate, volume of wear debris on the variation of Si and Al amount in SiC-B_4C–Si and SiC-B_4C–Al cermets separately (Chapter 4.2 and Chapter 4.3). Chapter 4.3 explains the electrical conductivity study with composition variation.

Chapter 5 describes the effect of high temperature oxidation behavior of the SiC-B_4C ceramic composite, and SiC-B_4C–Si cermets containing 2, 5, 10, and 20 wt. % Si prepared by both SPS and conventional sintering methods. This study was executed to understand the added Si amount (0–20 wt. %) in SiC-B_4C ceramic matrix and the effect of temperatures on oxidation behaviour.

Chapter 6 is devoted to summary of the main findings and conclusions to the present study.

Chapter 2

Experimental procedure

2.1 Characterization of as received powder

The elemental powders of SiC, B_4C, Si, and Al (purity > 99%, and an initial average particle size < 40 µm) were selected as starting materials. The raw materials are supplied from DISIR, Rajgangpur are Analar grade with high purity (impurity < 1%). For SiC and Si, the common impurity is SiO_2 (< 1%). For B_4C, impurities are B_2C, B_8C, and a trace amount of graphite (< 1%). Scanning electron microscopy (SEM) was carried for all the powders to verify the size and morphology of powders. From Figure 2.1 it has been observed that, as received powders of SiC, B_4C, Si and Al are irregular in shape with sharp edges. SiC, B_4C, Si and Al were blended to obtain nominal compositions of 60SiC40B_4C, 60SiC38B_4C2Si, 60SiC35B_4C5Si, 60SiC30B_4C10Si, 60SiC20B_4C20Si, 60SiC38B_4C2Al, 60SiC35B_4C5Al, 60SiC30B_4C10Al, and 60SiC20B_4C20Al (all in wt. %) respectively.

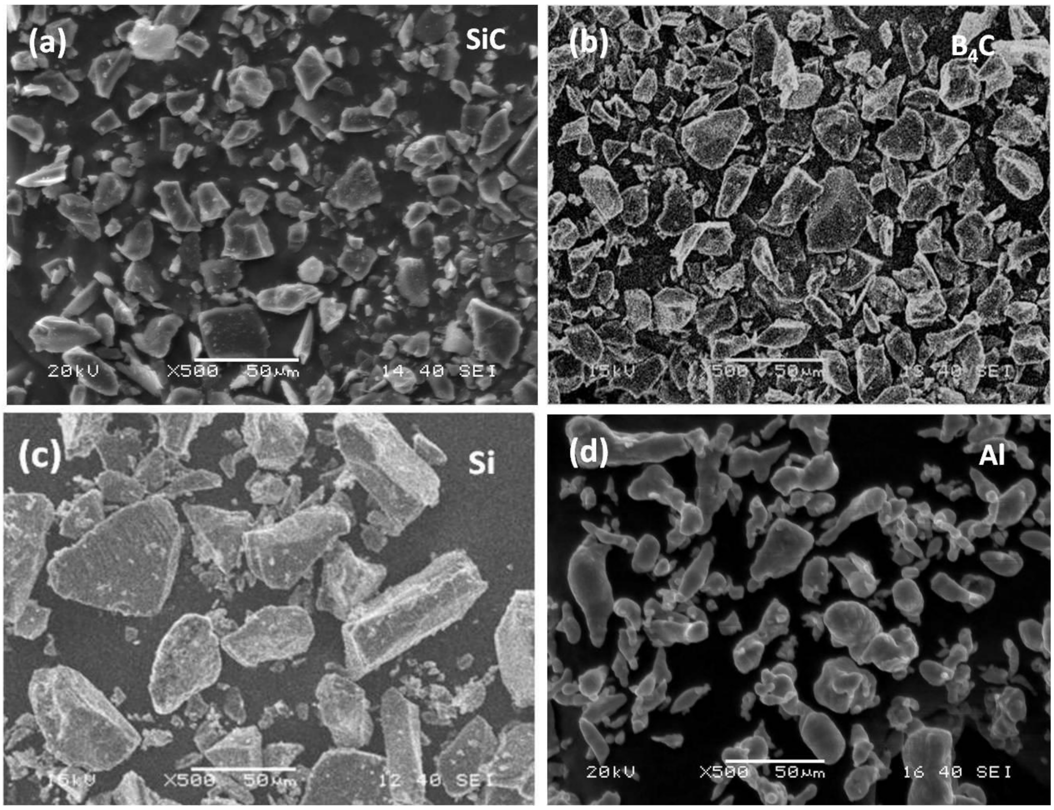

Figure 2.1 SEM micrographs of as received powders: (a) SiC, (b) B_4C, (c) Si, and (d) Al respectively.

Particle size of as received SiC, B_4C, Si, and Al powders was measured by using Malvern, Mastersizer laser scattering particle size analyzer as shown in Figure 2.2. The median size (d_{50}) of all the as received powders was found to be ≤ 25 µm.

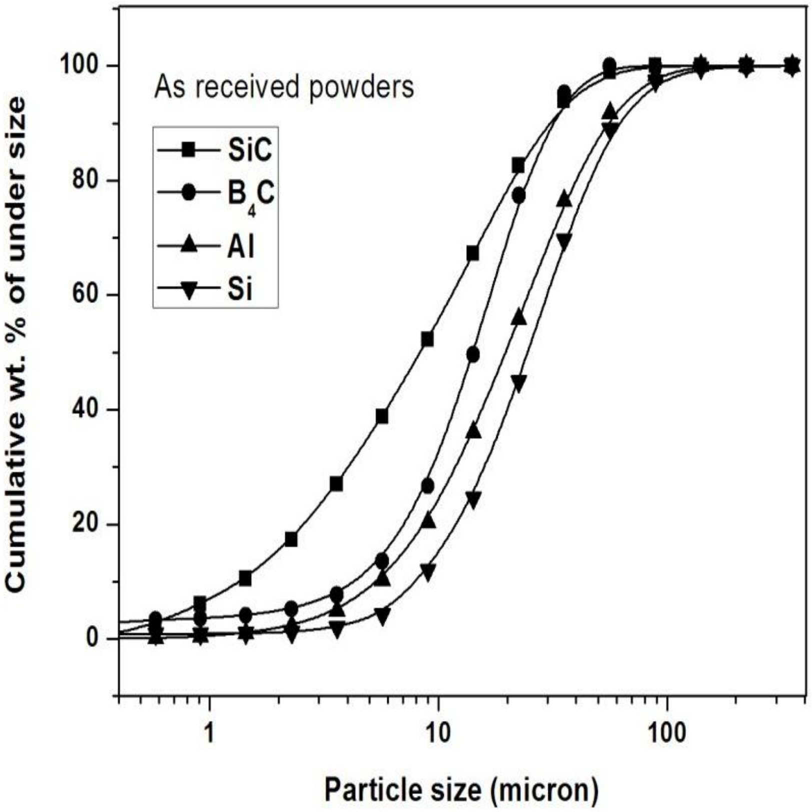

Figure 2.2 Particle size distribution of as received SiC, B_4C, Si, and Al powders respectively.

Figure 2.3 shows the XRD pattern of as received SiC, and B_4C powders. XRD patterns show the peaks correspond to α-SiC and B_4C. From the XRD analysis trace amount of carbon phase was also observed with B_4C phase.

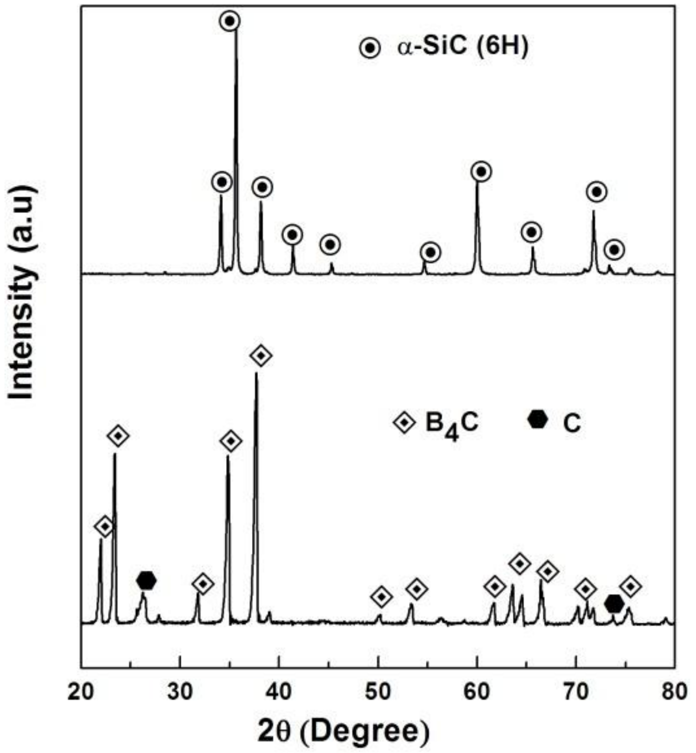

Figure 2.3 XRD pattern of as received SiC, and B_4C powders.

2.2 Synthesis of composite powder mixture by mechanical milling

2.2.1 Synthesis and characterization of SiC-B_4C composite powder mixture

Silicon carbide (SiC) of 60 wt. % and boron carbide (B_4C) of 40 wt. % powders of 99% purity were used as starting materials for mechanical milling. 60SiC-40B_4C powder composition was milled in a Fritsch planetary (P5) mill at a speed of 300 rpm for 10 h. A 180 gm of high carbon chrome steel balls (AISI 52100) of diameter 10 mm were filled with 40 vol.% in each steel jar (volume 500 ml). In the jar, ball to powder weight ratio was maintained 6:1 and milling was carried out under toluene to prevent oxidation. The milled powders were collected at the intervals of 0, 2, 5, and 10 h of milling. The phase, surface morphology and particle size distribution of the milled powders were studied by X-ray diffraction (XRD), scanning electron microscopy (SEM) and particle size analyzer (Malvern, Mastersizer) respectively. After 10 h of milling, the initial powder size (around 15–25 µm) reduced to nearly 3–4 µm.

2.2.2 Synthesis and characterization of SiC-B_4C–Si cermet powder mixture

SiC, B_4C, and Si of 99% purity were used as the starting powder materials. SiC-B_4C with varying Si amount (2, 5, 10, and 20 wt. %) were taken for mechanical milling in a Fritsch planetary (P5) ball mill. The SiC-B_4C–Si cermet powders with nominal compositions are 60SiC38B_4C2Si, 60SiC35B_4C5Si, 60SiC30B_4C10Si and 60SiC20B_4C20Si (all in wt. %). The steel jar containing 30 gm of powders were milled at the speed of 300 rpm for 10 h. The ball to powder weight ratio was 6:1 and wet milling was carried out in the presence of toluene. Powder samples were collected at the interval of 0, 2, 5, and 10 h and phase transformation, morphology and particles size were analyzed by using XRD, SEM and particle size analyzer.

2.2.3 Synthesis and characterization of SiC-B_4C–Al cermet powder mixture

The SiC-B_4C-Al cermets were fabricated using Analar grade raw elemental powders of SiC, B_4C, and Al. The powders were blended to make the nominal compositions of 60SiC38B_4C2Al, 60SiC35B_4C5Al, 60SiC30B_4C10Al and 60SiC20B_4C20Al (all in wt. %). These compositions were milled in a Fritsch planetary (P5) mill at a speed of 300 rpm for 10 h. The mill was run continuously at the interval of 30 min and then left to cool for 30 min. Each steel jar containing 30 gm of powder with ball to powder weight ratio was 6:1. Milling was carried out in toluene to prevent oxidation. The jar was opened at the intervals of 0, 2, 5, and 10 h of milling and small amount of the milled powders was taken from the jar for the analysis.

2.3 Cold compaction

The milled powder compositions of SiC-B_4C with Si and Al of 0, 2, 5, 10, and 20 wt. % respectively were compacted into pellets in a hydraulic press (SoiLab) with applied pressure of 1500 MPa for 3 min. Specimens for 3-point bend test (flexural strength) measurement were compacted using a rectangular die of dimension (31.5 x 12.5 x 6.35 mm^3). For compressive strength measurement, the samples were prepared using cylindrical die of 10 mm diameter and 8 mm height. Before compaction, 3 wt. % poly vinyl alcohol (PVA) binder was mixed with the powder to provide the lubrication and temporary bonding during compaction. Compacted powders were conventionally sintered at 1950 °C for 30 min in a high temperature resistance furnace under argon atmosphere. SPS was carried out at a pressure of 50 MPa and at different temperatures for SiC-B_4C composite, SiC-B_4C–Si and SiC-B_4C–Al cermets for 5 minutes in a 20 mm diameter graphite die.

2.4 Consolidation of SiC-B_4C, SiC-B_4C–Si and SiC-B_4C–Al cermets

In the present thesis two methods of sintering are mainly used to dansify the cermet materials by using conventional sintering and spark plasma sintering techniques.

2.4.1 Conventional pressure-less sintering

To optimize the sintering temperature, conventional sintering was carried out at 1400, 1600, and 1950 °C for SiC-B_4C–10 wt. % Si and SiC-B_4C–10 wt. % Al samples. After optimization of sintering temperature, conventional sintering was performed at 1950 °C for SiC-B_4C–0, 2, 5, 10, and 20 wt. % Si and Al compositions. Poor sintering with porous structure and low density were obtained when sintering was conducted at 1400, and 1600 °C. Hence, conventional sintering of all the cermets was conducted at 1950 °C.

The as-milled powders (SiC-B_4C, SiC-B_4C–Si and SiC-B_4C–Al) were compacted into pellets in a hydraulic press followed by conventional sintering in a high temperature furnace having graphite heating element at 1950 °C for 30 min. The sintering was carried out in a commercial flowing argon gas atmosphere. From room temperature to 1100 °C the heating rate was 20 °/min with holding time of 10 min. Then temperature rose to 1500 °C with heating rate of 10 °/min and hold for 5 min. Subsequently, with the same heating rate temperature was increased to 1850 °C and hold for 10 min. Finally, with the heating rate of 5°/min, temperature was increased to 1950 °C and hold for 30 min. After completion of sintering, all the samples were furnace cooled to room temperature.

2.4.2 Spark plasma sintering (SPS)

In another set of experiment, the as milled powders were loaded into a 20 mm diameter graphite die. Spark plasma sintering (SPS) was carried out at different temperatures for different composition depending on the melting point of additive (Si, and Al) materials.

SPS was performed at a heating rate of 100 K /min and held for 5 min under 50 MPa pressure using *DR SINTER* Model *1050* (Sumitomo Coal Mining Co. Ltd. (SCM), Japan). In Table 2.1, all the materials compositions, sintering methods adopted and respective sintering temperature have shown.

Table 2.1 *shows all the materials compositions, sintering methods adopted and respective sintering temperature.*

<table>
<tr><th rowspan="2">Compositions</th><th colspan="5">Sintering temperature and techniques</th></tr>
<tr><th>Conventional sintering (°C), holding time 30</th><th colspan="4">Spark plasma sintering (°C), holding time 5 min, pressure 50 MPa, heating</th></tr>
<tr><td>SiC-B_4C</td><td>1950</td><td colspan="2">1500</td><td colspan="2">1600</td></tr>
<tr><td>SiC-B_4C–2 wt. % Al</td><td>1950</td><td>1100</td><td colspan="2">1200</td><td>1300</td></tr>
<tr><td>SiC-B_4C–2 wt. % Si</td><td>1950</td><td>1100</td><td colspan="2">1300</td><td>1350</td></tr>
<tr><td>SiC-B_4C–5, 10, and 20 wt. % Al</td><td>1950</td><td colspan="4">1300</td></tr>
<tr><td>SiC-B_4C–5, 10, and 20 wt. % Si</td><td>1950</td><td colspan="4">1350</td></tr>
</table>

SiC-B_4C ceramic composite: High melting SiC-B_4C ceramic composite was spark plasma sintered at two different temperatures of 1500 and 1600 °C with 5 min holding time.

SiC-B_4C–Si cermets: As the melting point of Si is around 1400 °C, spark plasma sintering was carried out at 1100, 1300, and 1350 °C for SiC-B_4C–2 wt. % Si to optimize the sintering temperature for SiC-B_4C–Si. After optimization of sintering temperature, SPS was performed at 1350 °C for SiC-B_4C–5, 10, and 20 wt. % Si compositions.

SiC-B_4C–Al cermets: Al is used as additive for SiC-B_4C–Al cermet which has low melting point of 660 °C. Therefore, SiC-B_4C–2 wt. % Al composition was spark plasma sintered at 1100, 1200, and 1300 °C to optimize the sintering temperature. Optimum result was obtained at 1300 °C. Hence for the compositions of SiC-B_4C–5, 10, and 20 wt. % Al, SPS was carried out at 1300 °C.

2.5 Characterization of milled powders and sintered products

2.5.1 X-ray diffraction (XRD)

The phases developed in the milled powders and sintered pellets were analyzed by Rigaku Japan model: Ultima IV multipurpose X-ray diffraction system using Cu-K_α (λ=1.54 Å) radiation.

2.5.2 Particle size analysis

Particle size distribution of powders milled for different time was conducted by using Malvern, MicroP, Mastersizer laser scattering particle size analyzer. Milled powders were dispersed in a solution of 500 ml distilled water and 25 ml of sodium hexa metaphosphate (1 liter distilled water + 2 gm of Sodium hexa metaphosphate powder) before particle size measurement.

2.5.3 Optical microscopy

Microstructure was revealed by means of Murakami's etching by attacking the grain boundary phases. Murakami etchant was prepared by mixing 10 gm KNO_3 and 10 gm $K_3Fe(CN)_6$ into a solution of 100 ml distilled water and10 ml HNO_3.

Microstructural study of conventionally sintered and SPS samples after prior etching were carried out by Carl Zeiss, Germany/Axiotech, 100HD-3D optical microscopy. The volume fraction of different phases of all the cermet samples were calculated by using an inbuilt Axio Vision Release 4.8.2 SP3 (08-2013) software.

2.5.4 Scanning electron microscopy (SEM)

For structural and morphological analysis, JEOL JSM-6480 LV scanning electron microscopy (SEM) was used to investigate the milled powder and sintered cermet samples. The images were taken both in secondary electron (SE) and back scattered electron (BSE) mode according to the requirement. The elemental detection analysis (EDS) was carried out to know the various elements present in the samples.

2.5.5 Field emission scanning electron microscopy (FESEM)

Field emission scanning electron microscopy (FESEM) of NOVA NANOSEM 450 was used to investigate the morphology of the milled powder and sintered specimens. EDS and elemental mapping of various compositions were also carried out.

2.5.6 Differential scanning calorimetry (DSC)

Thermal analysis of the cermet powder samples were carried out in differential scanning calorimetry (DSC) (Netzsch, STA409C, Germany). The milled powders were heat treated from room temperature to 1200 °C at the heating rate of 10 °C / min under argon atmosphere. DSC was carried out for SiC-B_4C–Al cermet powders of various compositions.

2.6 Mechanical property study

2.6.1 Density measurement

After sintering, the bulk density was measured by the Archimedes' method using distilled water as immersion media. Bulk density of the samples was calculated using following formula:

$$\text{Bulk density} = W_D/(W_S - W_{Su}) \tag{2.1}$$

Where, W_D, W_S and W_{Su} are the dry weight, soaked weight and suspended weight of the specimens respectively. Bulk density of all the SiC-B_4C ceramic composite, SiC-B_4C–Si and SiC-B_4C–Al cermets of various compositions sintered by conventional sintering and SPS methods were performed.

2.6.2 Microhardness study

Microhardness of sintered samples was measured by Vickers microhardness tester (Leco Microhardness tester LM248AT) at an indentation load of 300 gmf for a dwell time of 10 seconds. Minimum of fifteen hardness measurement were taken for each sample and average values were reported.

The Vickers microhardness value of all the samples were calculated using the relation

$$H_v = 1.8544\ (P/d^2) \tag{2.2}$$

Where, P is the applied load (gmf) and d (mm) is the diagonal length of the indentation.

Microhardness test was carried out for SiC-B_4C ceramic composite, SiC-B_4C–Si and SiC-B_4C–Al cermets of various compositions sintered by conventional sintering and SPS techniques.

2.6.3 Compression strength study

Compressive strength was carried out in a universal hydraulic machine (Instron- SATEC series 600 KN servohydraulic machine). The strain rate of 2×10^{-3} was maintained throughout the experiment. Samples of diameter 10 mm and L/D = 0.8 were prepared as per ASTM standard E9-89.

Compressive strength test was carried out for SiC-B_4C ceramic composite, SiC-B_4C–Si and SiC-B_4C–Al cermets of various compositions sintered by conventional sintering at 1950 °C. But for SPS samples, compressive strength test were carried out for SiC-B_4C ceramic composite, and 10 wt. % Si added SiC-B_4C cermet specimens. As optimum physical and mechanical properties were obtained for 10 wt. % Si and Al added compositions, SPS samples (for 10 wt. % Si and 10 wt. % Al cermet) of dimension as per compressive strength test were prepared.

2.6.4 Flexural strength study

Figure 2.4 shows the experimental setup of flexural test machine. Flexural test/ transverse rupture strength test (TRS) was measured by three point bend test in Instron-1195 machine. Specimens as bars of dimension (31.5x 12.7x 6.35 mm^3) were prepared as per ASTM B 925-08 at compaction pressure of 600 MPa. Flexural strength measurement was performed using a three-point-bend fixure with a span of 30 mm.

The TRS/ flexural strength of specimens were measured by using following formula:

$$\text{Flexural strength}(\sigma) = 3PL/2bd^2 \qquad (2.3)$$

Where P = maximum load required to rupture the specimen (N), L = span length or distance between two supporting rods (mm), b = width of specimen (mm) and d = thickness of specimen (mm).

Flexural strength test was carried out for SiC-B_4C ceramic composite, SiC-B_4C–Si and SiC-B_4C–Al cermets of various compositions sintered by conventional sintering at 1950 °C. But flexural strength could not be performed for the SPS samples. This is because of the dimension (bar shape) of the specimens required for flexural strength test was not available for SPS samples.

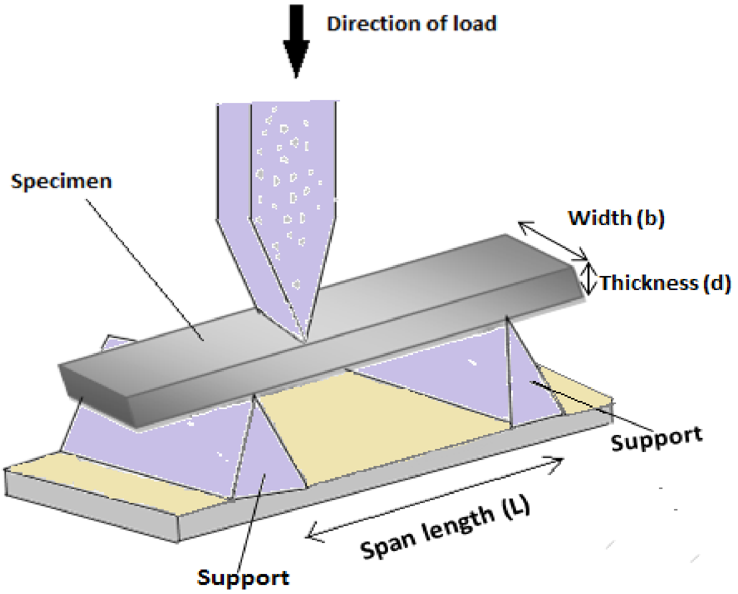

Figure 2.4 Schematic diagram of experimental setup for flexural test.

2.6.5 Fracture toughness study

Indentation fracture toughness of sintered samples was calculated by Vickers indentation method using Niihara equation as follows:

$$K_{IC} = 0.067\left(\frac{E}{H_v}\right)^{0.4} H_v a^{0.5} (c/a)^{-1.5} \tag{2.4}$$

Where E = Elastic modulus (MPa), Hv = Vickers hardness (MPa), c = average length of the cracks obtained in the tips of the Vickers marks (micron), and a = half average length of the diagonal of the Vickers marks (micron) [95]. Figure 2.5 shows the schematic diagram of the Vickers indentation mark and crack propagation in cermet samples. Fracture toughness test was carried out for SiC-B_4C ceramic composite, SiC-B_4C–Si and SiC-B_4C–Al cermets of various compositions consolidated by conventional sintered and SPS methods.

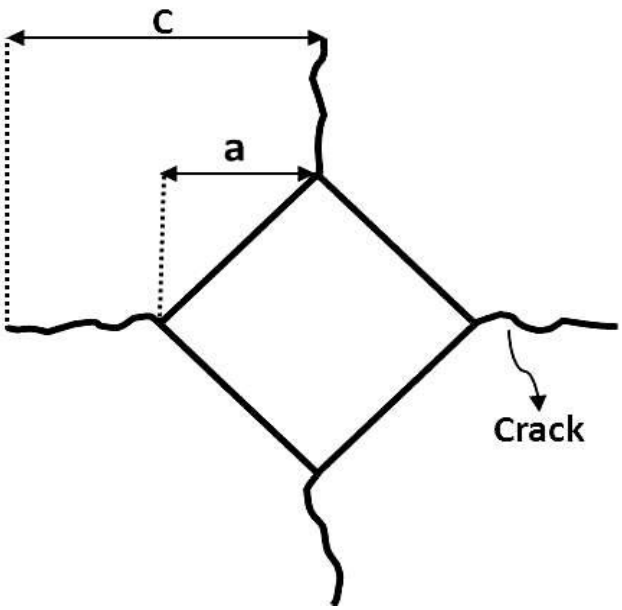

Figure 2.5 Schematic diagram of indentation fracture.

2.6.6 Un-lubricated sliding wear study

Pin-On-Disc wear tester (TR-208-M1) was used to investigate the un-lubricated sliding wear behaviour of all the conventional sintered and SPS samples against a Rockwell diamond indenter. Figure 2.6 shows the schematic diagram of wear testing set up. The wear test was carried out with normal loads of 20, 40, 60 and 80N. Uni-directional sliding between test samples and indenter take place with a speed of 6.28 mm sec^{-1} where sliding distance of 3.77 m was covered in 10 minutes. Depth of worn surface was measured by stylus surface profilometer (Veeco Dektak 150). The phase evolution of the wear debris was analyzed by Rigaku Japan model: Ultima IV multipurpose X-ray diffraction system using Cu-K$_\alpha$ (λ=1.54 Å).

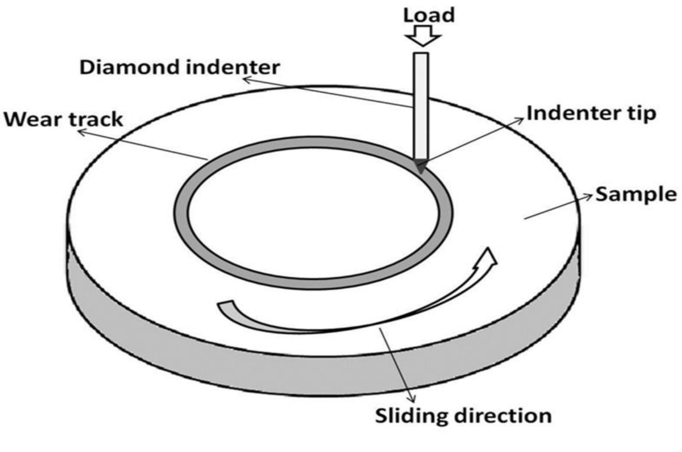

Figure 2.6 Schematic diagram of wear testing set up.

Wear rate for all the specimens was obtained by using the following equation:

$$W = \frac{M}{\rho D} \tag{2.5}$$

Where W is the wear rate (mm^3/m); M denotes the mass loss (gm); the density is represented by ρ (gm/mm^3) and D denotes the sliding distance (m) respectively [84].

Volume of the wear debris was evaluated by using Archard equation. It is proposed that the wear volume as a function of normal load, sliding velocity and hardness of the material as follows:

$$Q = \frac{KWD}{H} \tag{2.6}$$

Where Q is the total volume of wear debris produced (mm^3); K represents a dimensionless constant (used 10^{-7} for SiC-B_4C based cermets); W indicates the total normal load (gm_f); D and H are the sliding distance (m) and hardness of the softest contacting surfaces (gm/cm^2), respectively [96, 97].

2.7 Electrical conductivity study

Figure 2.7 shows the schematic diagram of four-point probe electrical resistance measurement system. Four-probe resistance measuring instrument is used to measure the resistance of the sample in which two probes are connected with ammeter (Keithly 6221, DC) and another two probes are connected with the voltmeter (Keithly 2182A). Resistance (R) of the sample was calculated from the slope of I-V curve which was plotted by using Labview program 488.2 interface.

Electrical conductivity of the cermet was calculated by using the following formula:

$$\sigma = \frac{1}{R}\frac{L}{A} \tag{2.7}$$

Where, σ is the electrical conductivity; R represents resistance of cermet; L is the length of the cermet and A represents the cross-sectional area of cermet.

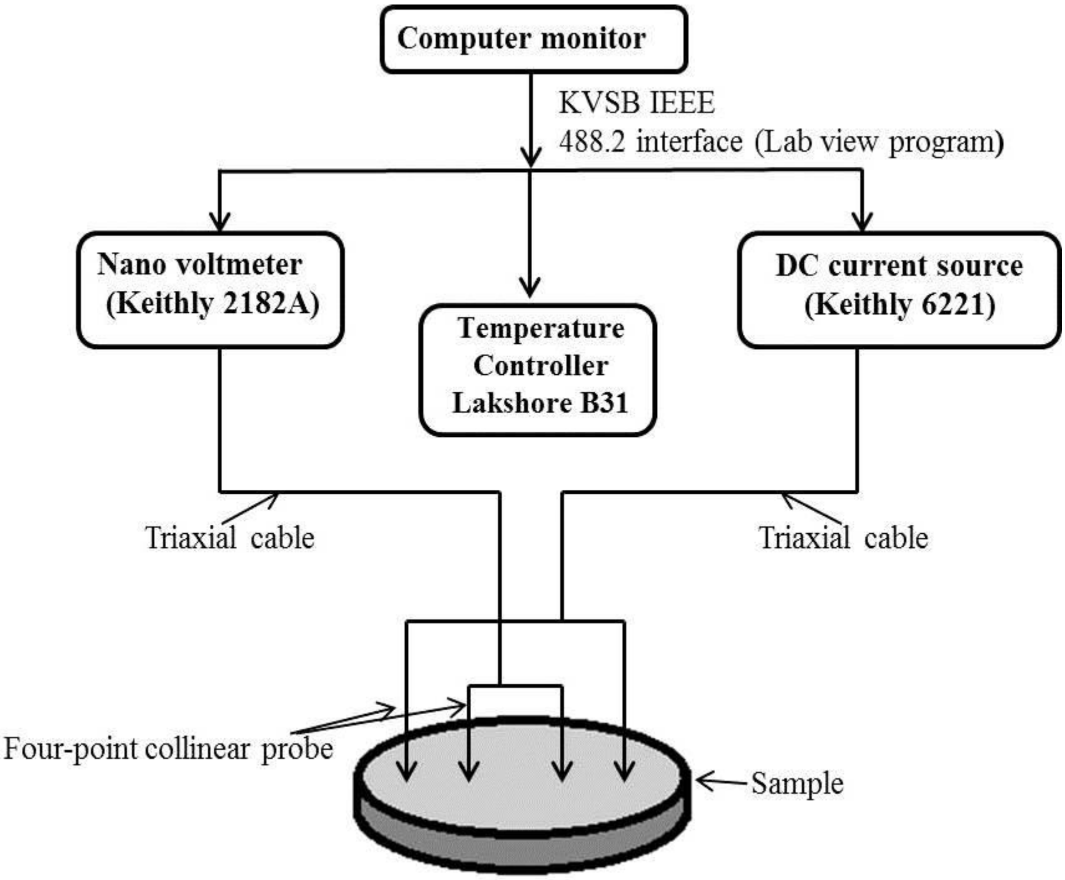

Figure 2.7 Schematic diagram of four-point probe measurement system.

2.8 Oxidation behaviour study

All the specimens prior to oxidation were rinsed and cleaned with acetone. The isothermal oxidation test was conducted in a tube furnace of capacity to withstand higher temperature up to 1400 °C and provision of flow of excess air. The high temperature oxidation was carried out at 800, 1000 and 1200 °C for 10 h holding time. During oxidation test, the mass of the specimens were recorded using an electronic balance (sensitivity = 0.01 mg). The mass of the specimens were taken during oxidation at the intervals of 0 h, 1 h, 5 h and 10 h. For all the intervals of taking weight, the samples were air cooled rapidly and took mass of the cooled sample then again placed into the furnace for further heating time.

Chapter 3

Results and discussion

3.1 Synthesis of SiC-B_4C based composite powders by mechanical milling

3.1.1 Scope and objectives of the work

SiC and B_4C have received great attention as promising high temperature resistant materials with light weight, high hardness, and high oxidation resistance. Incorporation of B_4C in SiC controls the phase transformation, grain growth and enhances mechanical properties of the composite powder. During preparation of cermet, homogeneous dispersion of reinforcement into the ceramic matrix is always a great challenge. Mechanical milling is widely used for refinement and homogeneous distribution of second phase in the matrix. Incorporation of metallic Al and Si phase into the SiC-B_4C matrix enhances the mechanical properties of the material as well as reduces the sintering time and improves bond strength. Powder samples of SiC-B_4C ceramic composite, SiC-B_4C–Si (2, 5, 10 and 20 wt. %) and SiC-B_4C–Al (2, 5, 10 and 20 wt. %) cermet of various compositions were prepared by mechanical milling for 10 h. The progress of milling and the continuous refinement of cermet powders were confirmed by X-ray diffraction, particle size analysis and scanning electron microscopy.

3.1.2 Characterization of milled powders

3.1.2.1 X-ray diffraction study

Figure 3.1(a) shows the typical XRD patterns of powder composition of 10 wt. % Si milled up to 10h. From phase analysis, it can be seen that SiC, B_4C and Si peaks are intact after milling. It is also noticed that no reaction takes place between SiC, B_4C and Si after 10 h of milling. The XRD pattern of 10 wt. % Al milled powder with varying milling time is shown in Figure 3.1 (b). The peak intensity gradually decreases with progress in milling time and becomes broad for all the compositions due to reduction in particle size and introduction of lattice strain during milling. During planetary milling, collision takes place between ball-powder, powder-powder and powder-jar surface reducing the particle size and inducing lattice strain. From XRD analysis it can be seen that the SiC, B_4C, and Al peaks are intact after milling. After 10 h of milling, there are no detectable contamination phases as evidenced by XRD peaks.

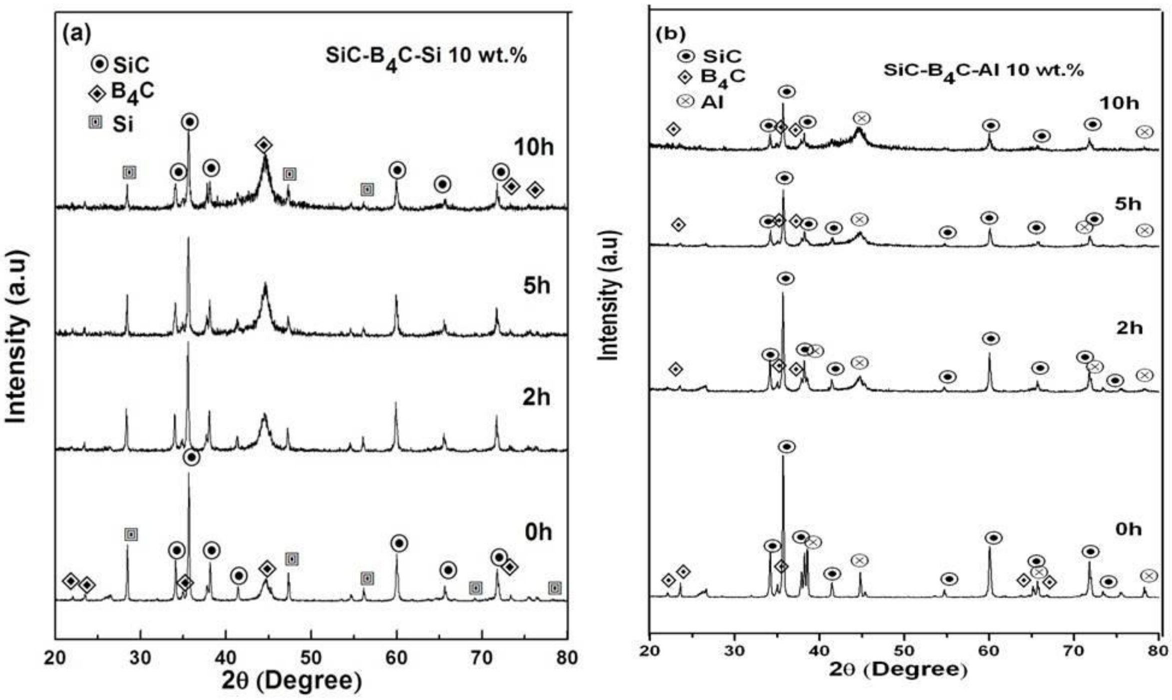

Figure 3.1 XRD spectra of cermet containing (a) 10 wt. % Si and (b) 10 wt. % Al powder samples at different milling times (0, 2, 5 and 10 h).

3.1.2.2 Particle size analysis

The progress of mechanical milling process continuously changes the size and morphology of powder sample. Figure 3.2 (a) shows the particle size distribution of milled powder containing 10 wt. % Si. It is observed that with the progress of milling time from 0 to 10 h, the particle size gradually decreased. Variations of average particle size of powder sample containing 10 wt. % Si with the progress of milling from 0 to 10 h is shown in Figure 3.2 (b). It is evident from the figure that the median size (d_{50}) has been reduced from 10 µm to ~ 3 µm after 10 h of milling. The presence of harder and brittle SiC and B_4C particles get fragmented and refine the size of the particle by a repetitive collision of powder particles in between balls and vial during the milling process.

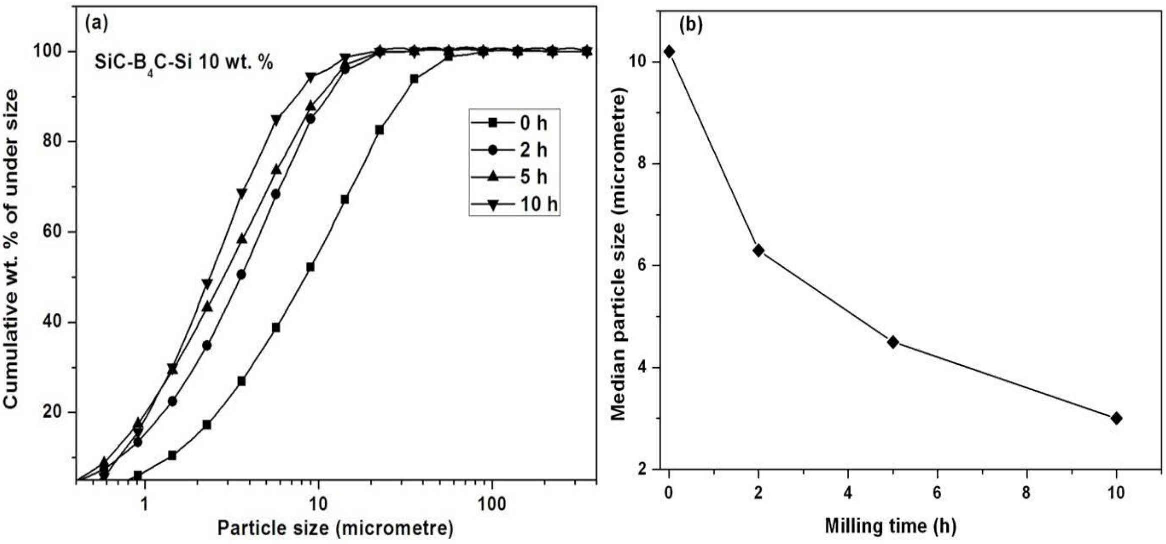

Figure 3.2 (a) Particle size distribution of sample containing 10 wt. % Si at different intervals, (b) variation of average particle size of 10 wt. % Si with progress of milling time.

Figure 3.3 (a) shows the particle size distribution of 10 wt. % Al milled powder with progress of milling time from 0 to 10 h. The particle size gradually decreases with the progress of milling and the size and morphology of powder sample changes continuously. Variation of average particle size of 10 wt. % Al with the progress of the milling from 0 to 10 h is shown in Figure 3.3 (b). It is evident from the figure that median size (d_{50}) has been reduced from 9 µm to ~ 3 µm after 10h of milling.

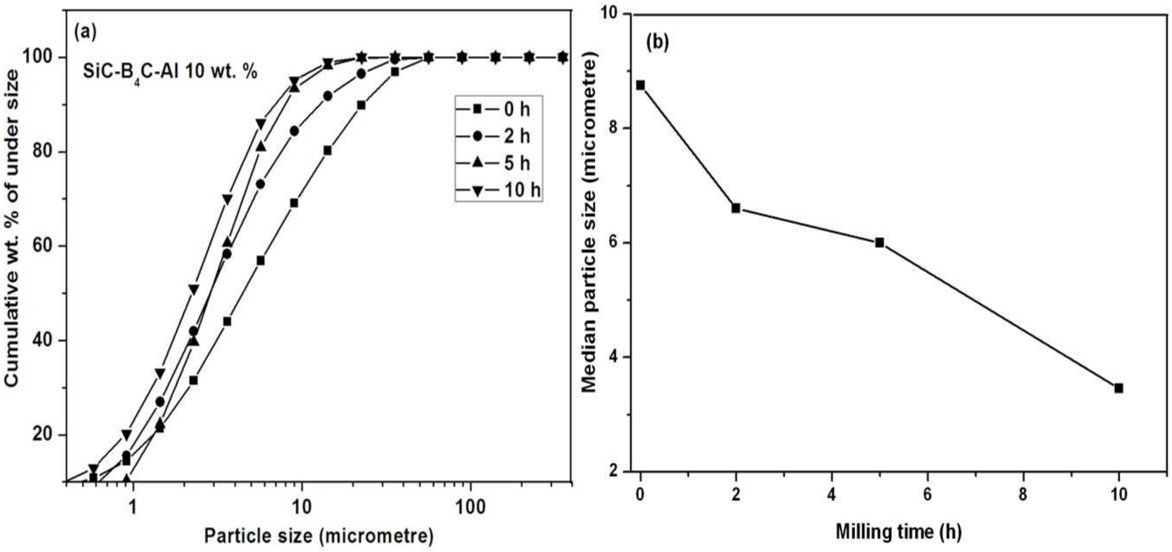

Figure 3.3 (a) Particle size distribution of sample containing 10 wt. % Al at different intervals, (b) variation of average particle size of 10 wt. % Al with progress of milling time.

3.1.2.3 Scanning electron microscopy

The size and morphology of milled powder at different intervals are investigated by scanning electron microscopy. Figure 3.4 shows SEM micrographs that reveal a gradual refinement of powder particles for the cermet containing 10 wt. % of Si with milling. During milling, the particles get fragmented, and the particle size reduced continuously. The initial powder size was around 25–40 µm and after 10 h of milling, it was reduced to nearly ~ 3–4 µm. It is also corroborated by particle size analysis as shown in Figure 3.2.

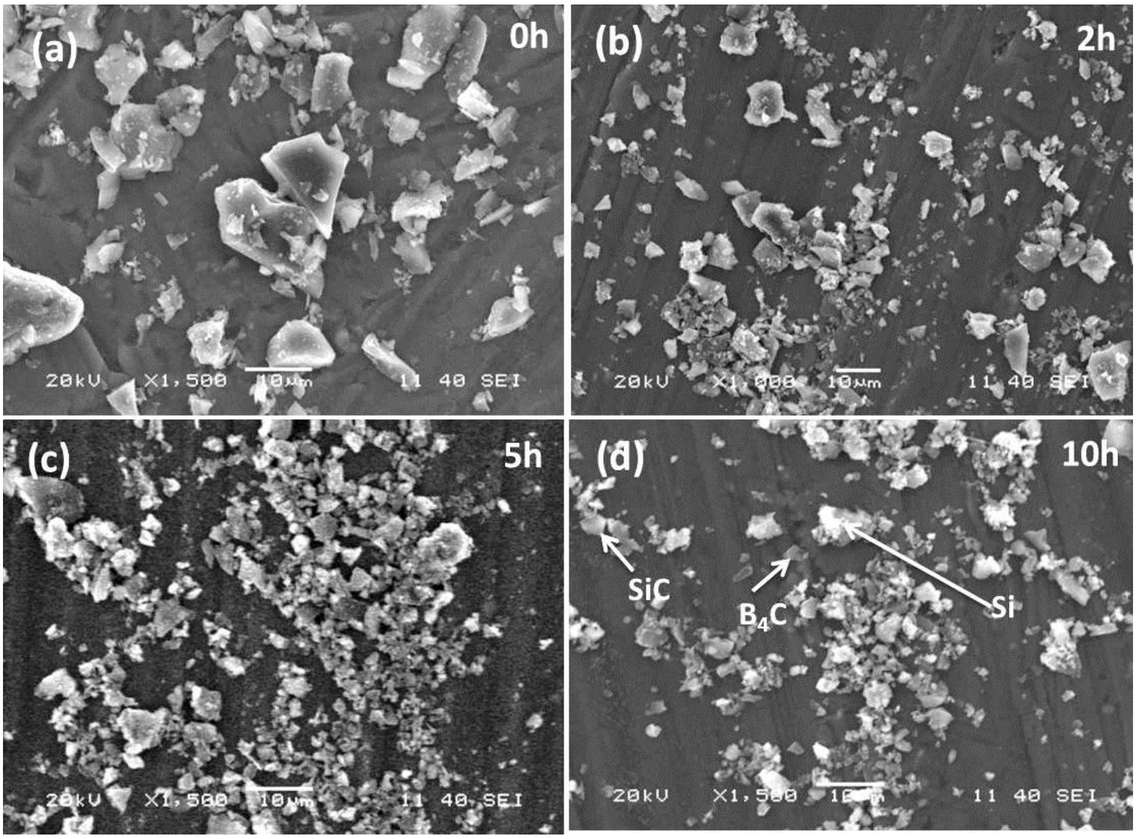

Figure 3.4 SEM micrographs of the sample with 10 wt. % Si milled for 0h to 10h in planetary ball mill which shows gradual refinement of particles size.

Figure 3.5 shows the SEM micrographs of 10 wt. % Al powder particles with milling time. SEM analysis shows the size and morphology of milled powder at different intervals of milling. As expected, the particles get fragmented and the particle size reduces continuously. The initial powder size was around 25–45 µm and after 10 h of milling it reduced to ~ 3–4 µm, also supported by the particle size analysis in Figure 3.3.

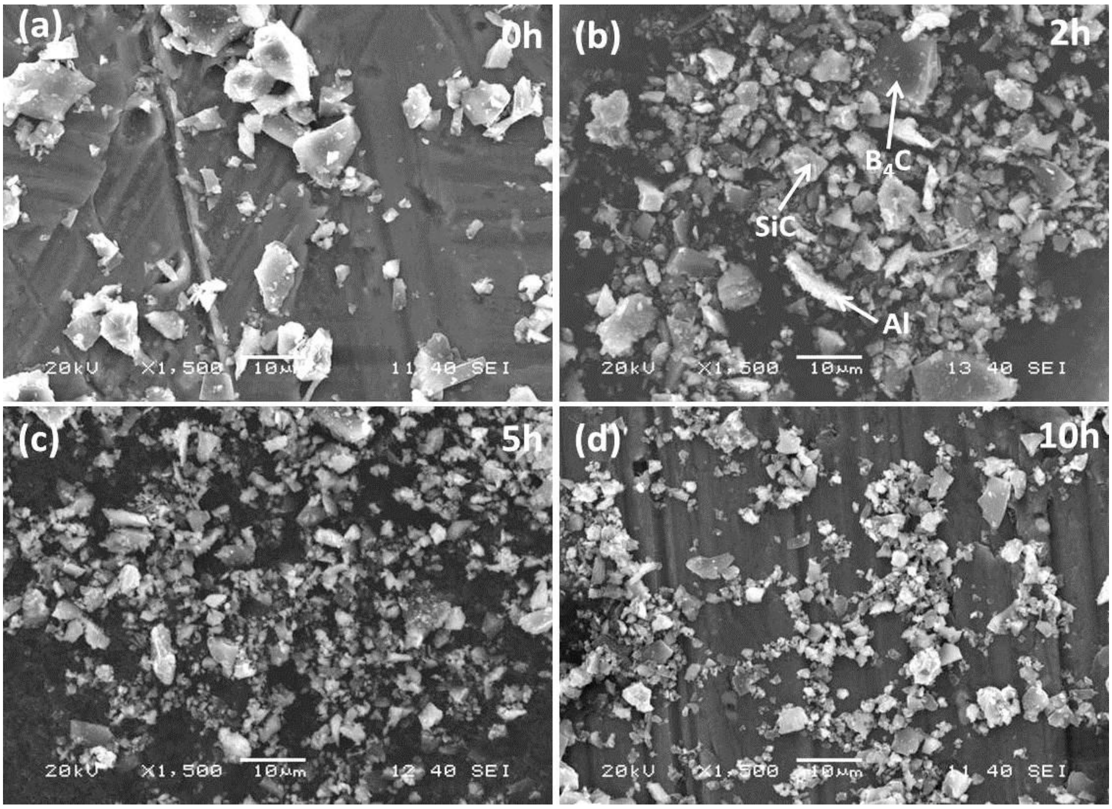

Figure 3.5 SEM micrographs of 10 wt. % Al milled for 0h to 10h in planetary ball mill which shows gradual refinement of particles size.

3.1.2.4 Thermal analysis

Figure 3.6 shows the DSC plot of milled 5 wt. % Al powder during heating from room temperature to 1200 °C at the heating rate of 10 °C / min under argon atmosphere. The figure shows a strong exothermic peak at 730 °C, and a relatively weaker peak at 1100 °C. The exothermic peak corresponds to crystal growth, crystalline phase transition and lattice strain release at this temperature. The exothermic peaks at around 700 °C and 1100 °C indicates the formation of $Al_8B_4C_7$ and AlB_{12} phases respectively, which is also supported by the XRD results (will be further discussed in Figure 3.28). Arslan *et al.* [98] studied B_4C-Al composites and reported the interfacial oxide film breakage and interaction at the Al/B_4C interface after melting of Al and an initial incubation period. The Al metal rapidly saturates in boron and carbon by the dissolution of carbides. The solubility of carbon and boron in Al is very small about 10 and 100 at. ppm for C and B at 727 °C. This process nucleates Al_3BC and AlB_2 at around 700 °C, and then the growth of these phases takes place below 870 °C. Above 1000 °C, AlB_2 decomposes and generates free Al. At this temperature, $AlB_{24}C_4$ with Al_4C_3 phases are formed. These phases are composed of boron and carbon resulting in B_4C depletion [71].

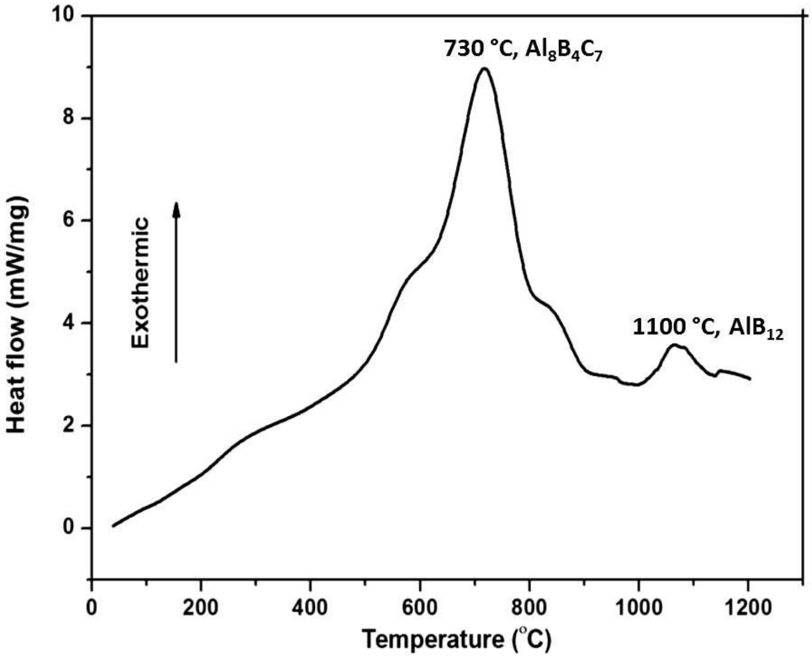

Figure 3.6 DSC graph of 5 wt. % Al added composition.

3.1.3 Summary

- In the present investigation, fine structured SiC-B_4C ceramic composite, SiC-B_4C–Si (2, 5, 10 and 20 wt. %) and SiC-B_4C–Al (2, 5, 10 and 20 wt. %) cermet powders of various compositions were successfully prepared by 10 h of high energy mechanical milling.

- Milling reduces the particle size of all the compositions to 3–4 µm. XRD, SEM and particle size analysis reveals the particle size reduction and homogeneous distribution of Si, Al, in the respective SiC-B_4C composite matrix.

- XRD spectrum of different hours milled powder shows no phase transformation in the composition during milling. Shape of the cermet powders is irregular as shown in SEM micrographs.

- Thermal analysis of SiC-B_4C–Al cermet powders shows the exothermic peak, which represent crystalline phase transition and lattice strain release during heating. The exothermic peaks at around 730 °C and 1100 °C indicate the formation of $Al_8B_4C_7$ and AlB_{12} phases respectively in the Al added cermet samples.

3.2 Synthesis of SiC-B_4C composite ceramic, SiC-B_4C–Si and SiC-B_4C–Al cermet through conventional sintering and spark plasma sintering methods

3.2a Scope and objectives of the work

The objective of the present study is to development of SiC-B_4C, SiC-B_4C–Si and SiC-B_4C–Al based cermet samples with wide variation of composition (2, 5, 10 and 20 wt. % of Si and Al) of mechanical milled powders and subsequent consolidation by conventional sintering and spark plasma sintering (SPS) routes. Conventional sintering of all the compositions was done at 1950 °C. present study is divided into three sections. In first section, high melting SiC-B_4C ceramic composite was spark plasma sintered at two different temperatures of 1500 and 1600 °C with 5 min holding time. Reason behind two sintering temperature is to study the effect of temperature on the progress of sinterability and properties of the ceramic composite. The microstructure, density, hardness, indentation fracture toughness, compressive strength of all the samples fabricated by SPS and conventional sintering methods were compared. In second section, mechanically milled SiC-B_4C–Si cermet with varying Si (2, 5, 10, and 20 wt. %) content were consolidated by conventional sintering and SPS route. The effects of wider composition range and consolidation methods on physical and mechanical properties of the cermet samples were studied. For optimization of SPS temperature for SiC-B_4C–Si cermet samples, SPS was performed at 1100, 1300 and 1350 °C for SiC-B_4C–2 wt. % Si composition. SPS was carried out at 1350 °C for SiC-B_4C–5, 10, and 20 wt. % Si compositions. The third section describe the effects of wider composition range (2, 5, 10, and 20 wt. % Al) and consolidation methods on physical and mechanical properties of the SiC-B_4C–Al cermet samples. For optimization of SPS temperature for SiC-B_4C–Al cermet samples, SPS was performed at 1100, 1200 and 1300 °C for SiC-B_4C–2 wt. % Al composition. SPS was carried out at 1300 °C for SiC-B_4C–5, 10, and 20 wt. % Al compositions.

3.2b Characterization of SiC-B_4C ceramic composite

3.2b.1 X-ray diffraction (XRD)

Figure 3.7 shows the XRD patterns of 60SiC40(B_4C) composition sintered by conventional and spark plasma techniques at different temperatures. In conventional sintering, peak intensity decreased for B_4C phase. Due to the decomposition and elimination of carbon from boron, the peak intensity reduces. Some peaks of free Si are also present in SPS samples. Clear diffraction peaks corresponds to α-SiC, B_4C and $B_{13}C_2$ are observed in conventional sintered (1950 °C) samples of $SiC_{60}(B_4C)_{40}$ composition. The limits of rhombohedral boron carbide phase are: B_4C (20 at.% C) to $B_{10.5}C$ (8.8 at.% C). Carbon rich boron carbide has the lowest viscosity and is densified easily than the boron rich materials. The mechanism of $B_{13}C_2$ formation and phase transition has become a subject of extensive studies [51]. The existence of C-B-C chains in $B_{13}C_2$, instead of C-C-C chain in B_4C is the only difference [51, 53, 99]. B_4C phase is unstable above 327 °C. With increasing sintering temperature as C eliminates and B_4C phase changes to $B_{13}C_2$. There is no phase change until the melting point of B_4C around 2527 °C [100].

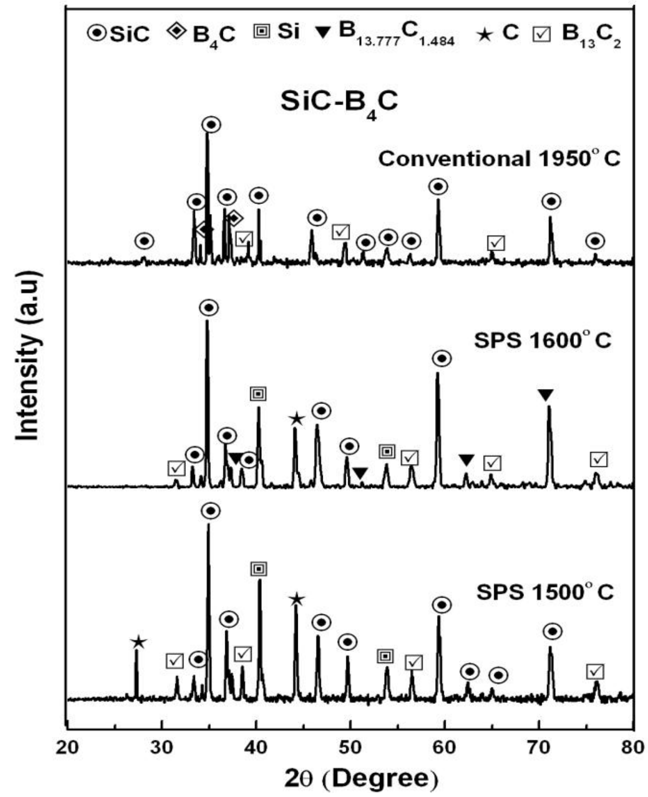

Figure 3.7 XRD spectra of $SiC_{60}(B_4C)_{40}$ sintered sample by conventional sintering and by SPS at different temperatures.

3.2b.2 Optical microscopy

Figure 3.8 depicts the optical microstructure of SiC-B_4C ceramic composite sample sintered at 1600 °C by SPS method. From the optical micrograph it is confirmed that, SiC and B_4C phases are uniformly distributed. Mechanical milling of the powder particles lead to grain refinement and the uniform distribution of all the phases present in the sintered product as shown in the figure. Uniform distribution of the particles is essential to obtain uniform physical and mechanical properties of the fabricated cermet samples.

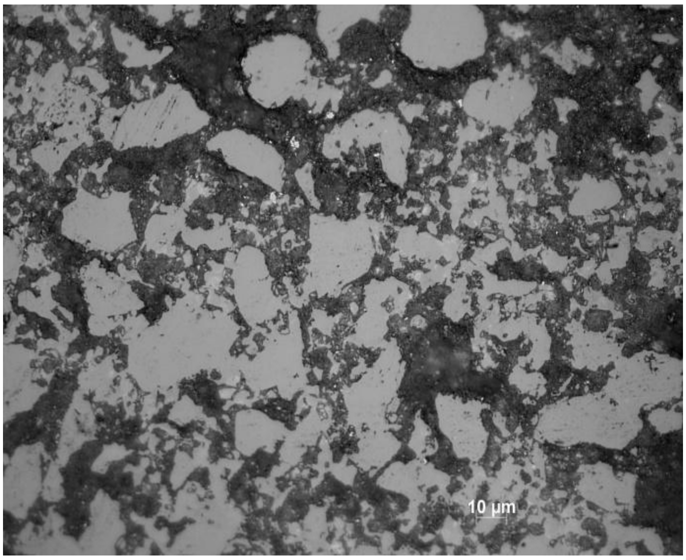

Figure 3.8 Optical microstructure of SiC-B4C ceramic composite sintered by SPS method at1600 °C.

3.2b.3 Field emission scanning electron microscopy (FESEM)

Figure 3.9 shows the microstructural evolution of SiC-B_4C sintered at different temperatures by conventional and SPS techniques. The black coloured B_4C and grey coloured SiC particles are marked in the micrographs. Large particle size with high porosity level is clearly visible in the samples consolidated by conventional sintering. As sintering was conducted at high temperature (1950 °C) for 30 min, grain growth is obvious. High temperature conventional pressure-less sintering is not sufficient to reduce porosity level of the consolidated product.

Microstructure of the spark plasma sintered specimen clearly shows very less amount of porosity level and less grain coarsening as compared to conventional sintered samples. This is also evident from the relative sintered density values, which is shown in Figure

3.10 (a) and Table 3.1. With increasing sintering temperature in SPS samples, sinterability increases with improved density and reduced porosity.

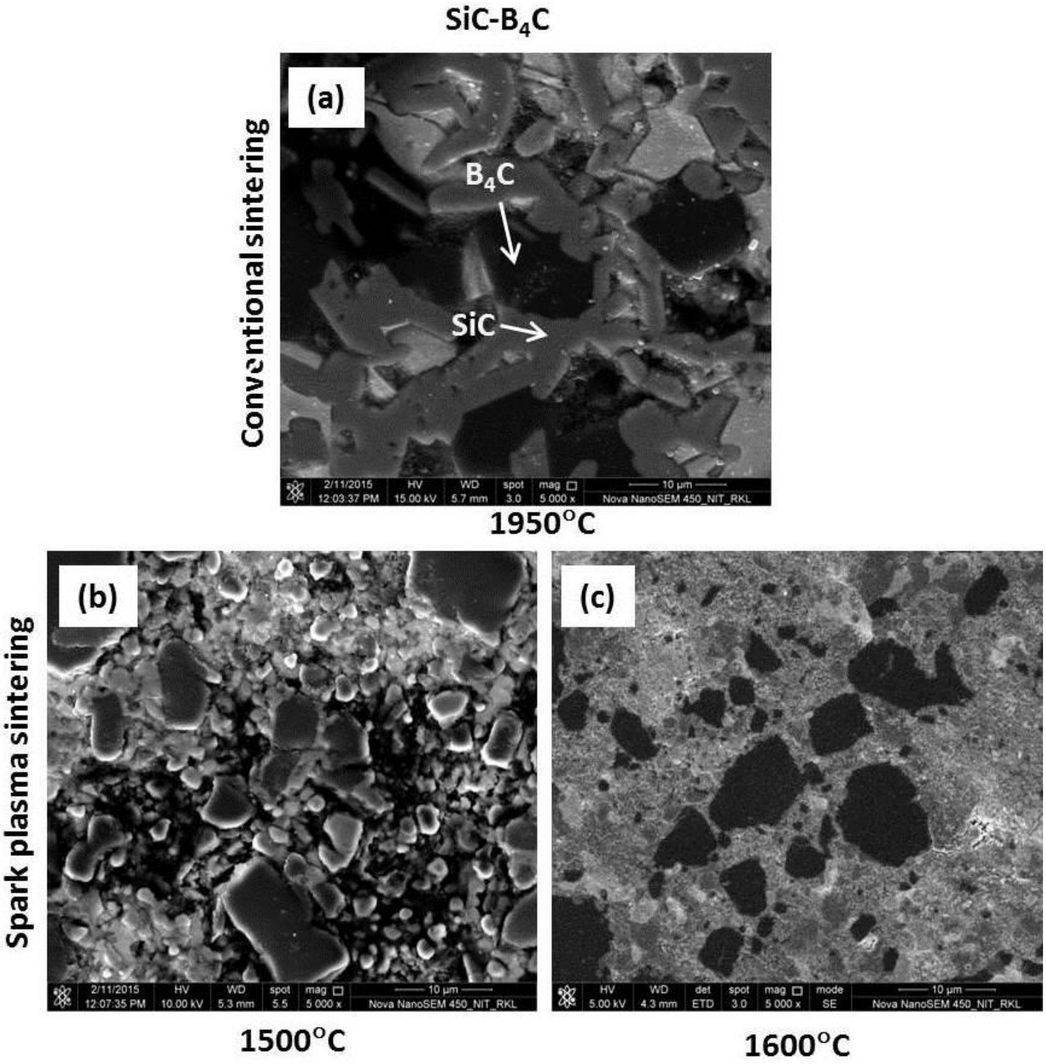

Figure 3.9 FESEM images of SiC-B$_4$C sintered by conventional sintering and SPS at different temperatures.

3.2b.4 Density and Microhardness study

Density and microhardness of SiC-B$_4$C ceramic composite were measured for the conventional and spark plasma sintered samples. Figure 3.10 (a) represents the effect of sintering temperature and sintering techniques on the relative density of SiC-B$_4$C as shown in bar diagram. SPS conducted at comparatively low temperature, exhibits higher density and hardness than conventionally consolidated samples due to simultaneous application of heat and pressure. Density of the sample increases with increase in sintering temperature from 1500 to 1600 °C. Sintered density increased by 1–4%, when SPS temperature was raised from 1500 to 1600 °C for SiC-B_4C sample. Maximum relative density of 96% is achieved for SiC-B_4C sample sintered at 1600 °C. At high temperature, the rate of diffusion increases and atoms within the composite rearrange themselves in a dense pattern. FESEM micrograph of SiC-B_4C in Figure 3.9 confirms that increase in sintering temperature decreases the number of pores and increases the density with increasing bond strength. The relative density was below 90% for the sample sintered by conventional sintering technique.

Figure 3.10 (b) shows the effect of sintering temperatures and sintering techniques on microhardness of SiC-B_4C ceramic composite. Vickers microhardness values are represented in bar diagram with error bar at different temperatures. The hardness value of SiC-B_4C was found to be increased from 24±2.27 to 27±2.11 GPa for variation of SPS temperature from 1500 to 1600 °C. It is to be noted that the hardness of SiC-B_4C sintered conventionally at 1950 °C was 19±3.17 GPa. The hardness was less in conventional sintered samples possibly due to low sintered density and coarsening of grains.

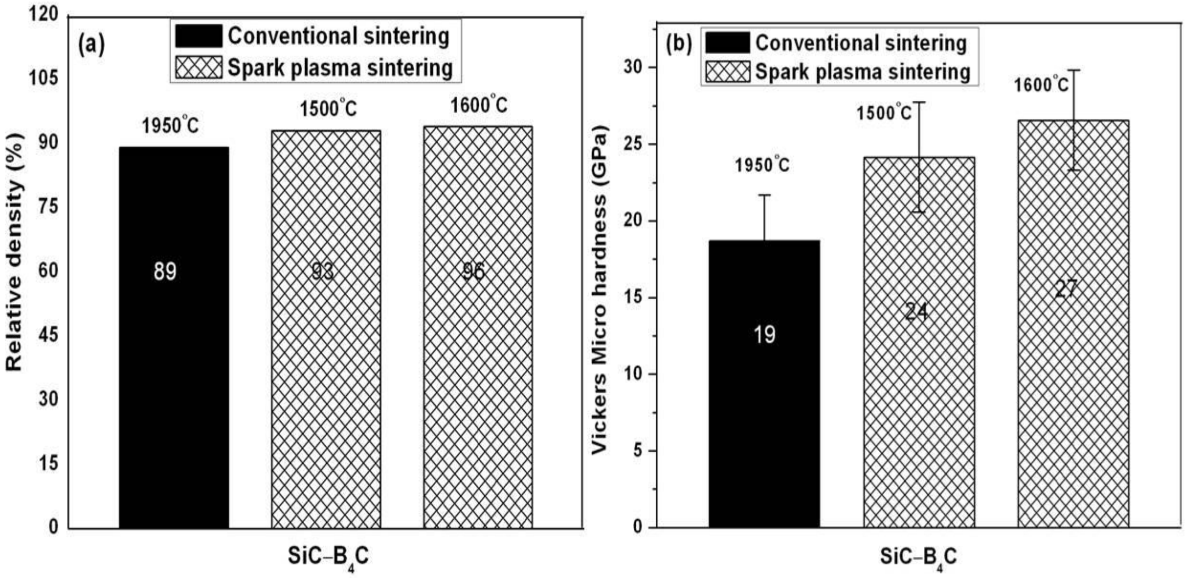

Figure 3.10 (a) shows the bar diagram of the relative sintered density of SiC-B_4C ceramic composite sintered by pressure-less sintering and SPS, and (b) bar chart showing the microhardness of pressure-less sintered and spark plasma sintered SiC-B_4C composite.

3.2b.5 Compression strength

Compression test was carried out on cylindrical specimens of diameter 10 mm and L/D = 0.8. Figure 3.11 shows the compressive stress-strain curve of SiC-B_4C ceramic composite consolidated by conventional pressure-less sintering at 1950 °C. The yield stress of 269

MPa was measured for the composite and failure occurred at little deformation. The density of conventional sintered SiC-B_4C sample was below ≤ 90% with hardness of 20 GPa. The covalent bonds of these ceramics make SiC and B_4C one of the stiffest materials but more sensitive to flaws. Figure 3.12 shows the compressive stress-strain curve of SiC-B_4C ceramic composite consolidated by SPS at 1350 °C. The yield stress of 449 MPa was observed for SPS sample. Higher yield stress in SPS sample is mainly due to the comparatively higher density (96%) and hardness (27 GPa) in SiC-B_4C ceramic composite.

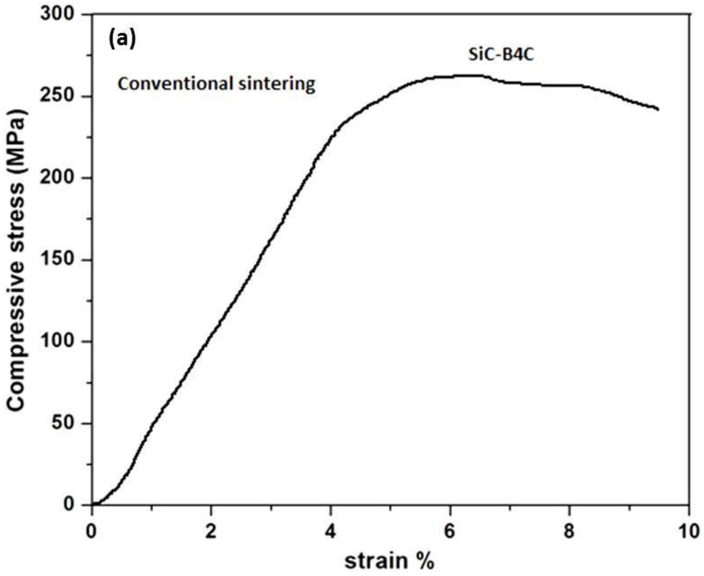

Figure 3.11 Compressive stress–strain curves of SiC-B_4C ceramic composite sintered by conventional sintering.

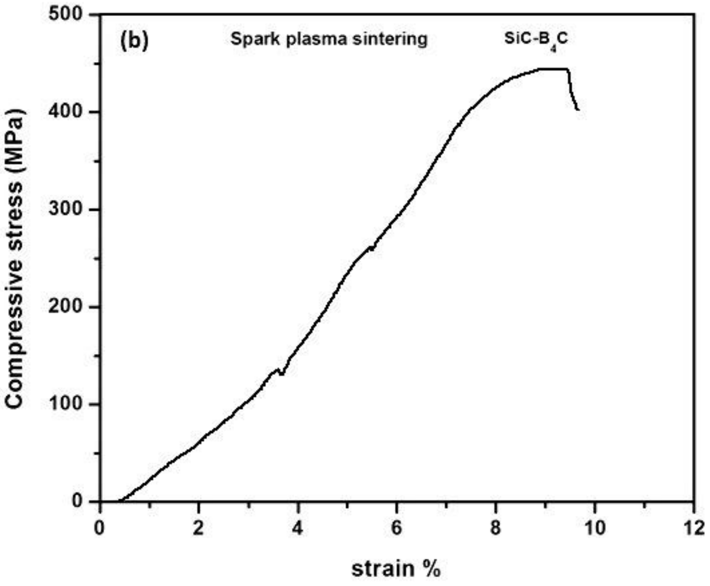

Figure 3.12 Compressive stress–strain curves of SiC-B_4C ceramic composite sintered by spark plasma sintering.

Fracture surface of compressive test sample of SiC-B_4C ceramic composite sintered by pressure-less sintering at 1950 °C is shown in Figure 3.13. The fracture surface shows brittle mode of fracture (transgranular), as both SiC and B_4C are covalently bonded hard and brittle ceramics. The ceramic composite shows voids and brittle facets on the material surface. Coarse cleavage fracture features are visible on many facets. Brittle facets are caused by transgranular crack propagation across the grains. Some voids are formed due to less closely packed particles of the composite and weak bonding between the carbide particles during sintering. These voids act as stress raisers and responsible for the reduction of overall strength of the material. Cleavage plates and river line marking are also visible on the facets, confirms the direction of crack propagation and the brittle fracture in the composite.

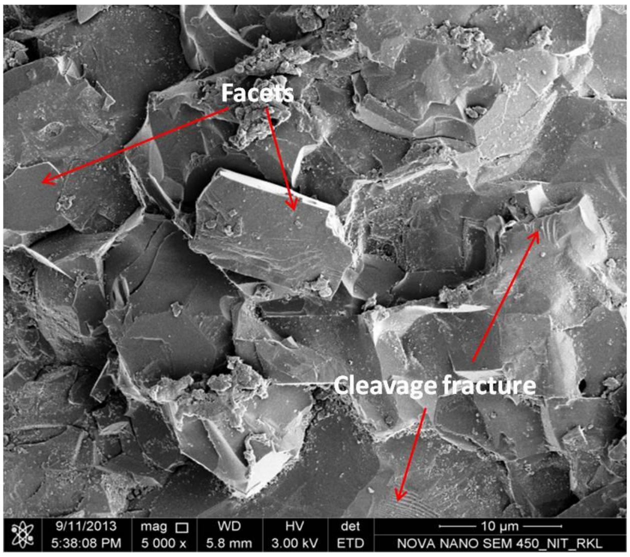

Figure 3.13 FESEM image of fracture surface of broken SiC-B_4C ceramic composite sample after compressive strength test sintered by conventional sintering.

3.2b.6 Flexural strength

Flexural strength of conventionally sintered SiC-B_4C ceramic composite was measured and presented in Table 3.1. Due to poor bonding in SiC and B_4C of conventional sintered sample, delivers porosity, poor density and hardness, and hence offers low flexural strength value of 78 MPa. Without any noticeable deformation grains got cut off. Due to unavailability of required dimension of SPS sample, flexural strength of SPS sample could not be done.

***Table 3.1** Physical and mechanical properties of SiC-B_4C ceramic composite fabricated by conventional sintering and spark plasma sintering methods.*

Properties	**SiC-B_4C**		
	Conventional pressure-less sintering	**Spark plasma sintering**	
	1950°C	***1500°C***	***1600°C***
Density (%)	89	93	96
Microhardness (GPa)	19.1±3.17	24±2.27	27±2.11
Fracture toughness ($MPa.m^{1/2}$)	1.1	1.36	1.87
Compressive strength (MPa)	269	-	449
Flexural strength (MPa)	78	-	-

3.2b.7 Fracture toughness

Figure 3.14 shows the FESEM micrograph of the Vickers indentation mark and crack propagation in SiC-B_4C composite for conventional and spark plasma sintered samples. Indentation fracture toughness (IFT) was calculated by Vickers indentation method using equation proposed by Niihara as shown in equation 2.4.

As SiC-B_4C is harder and brittle material, it gives lower fracture toughness values for conventional and spark plasma sintered samples as shown in Table 3.1. In case of SPS samples, the indentation toughness value increased from 1.36 to 1.87 $MPa.m^{½}$ with increase in sintering temperature from 1500 to 1600 °C. But for conventional sintered samples measured toughness value was 1.1 $MPa.m^{½}$.

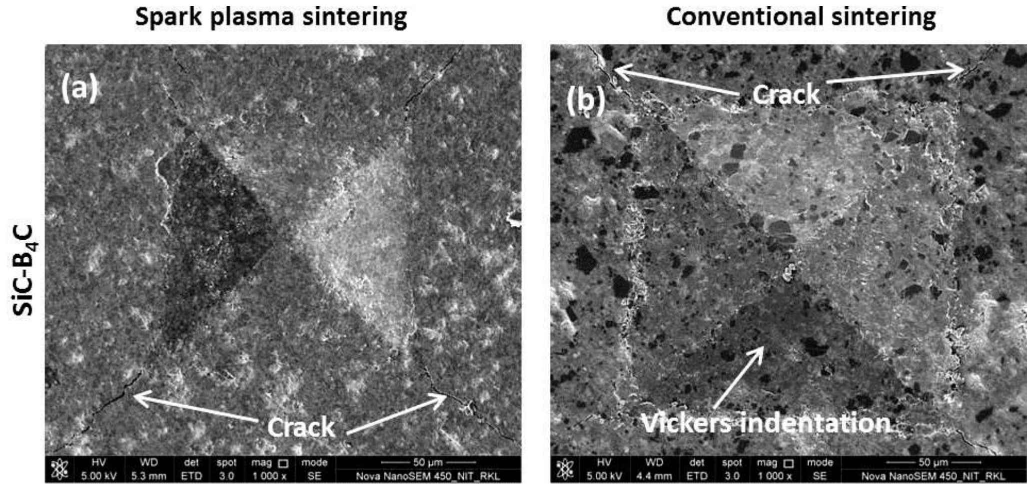

Figure 3.14 Vickers indentation marks and crack propagation of SiC-B_4C ceramic composite sintered by (a) SPS and (b) conventional sintering.

3.2c Characterization of SiC-B_4C–Si cermet

3.2c.1 X-ray diffraction (XRD)

Figure 3.15 (a) and (b, b’) shows the XRD patterns of 2, 5, 10, and 20 wt. % of Si added composites prepared by conventional sintering and spark plasma sintering techniques. XRD analysis has shown the presence of SiC, B_4C, Si and product phases for conventional as well as SPS sintered samples. During high-temperature conventional sintering at 1950 °C, free carbon is released from B_4C, reacts with molten Si and maintained the SiC content in the product [64]. When Si amount increased to 20 wt. % in SiC-B_4C composite, the product phase increased with SiC phase and minor residual Si phase is also observed. In the present study, XRD analysis confirmed the presence of minor SiO_2 and B_2O_3 in conventional sintered SiC-B_4C–Si samples. During sintering process the SiO_2 peaks were observed only on the surface of the pellets. This is because of some residual air or trace amount of oxygen was present in the argon atmosphere inside the furnace. It forms a glassy layer over the pellet and inhibits further oxidation.

Feng *et al.* [65] studied the solid solubility of Si in B_4C with increasing Si content. They reported the dissolution of Si in B_4C and found that the solid solubility increased from 1.38 at.% to 1.8 at.% with increasing the amount of Si from 4 wt. % to 8 wt. %. High Si content in the composition increased the residual Si amount and the SiC content also increased in the XRD spectra as shown in Figure 3.15 (b). In the SPS processing, sintering was conducted under vacuum. The pulsed current and activated sintering during SPS helps to breakdown the oxide layers on the surface of powder particles. The shorter sintering time and applied pressure during sintering on the surface reduced the porosity levels. There was no evidence of oxide peaks in SiC-B_4C–Si cermet compositions produced by SPS. XRD analysis confirmed the presence of SiC, B_4C and Si phases of the SPS sintered samples. Figure 3.15 (b’) shows the XRD analysis of the SPS samples containing 2 wt. % Si sintered at 1300 and 1350 °C. X-ray peaks confirm the presence of B_8C phase. With the increase in sintering temperature from 1300 to 1350 °C, added Si was consumed during reaction with carbon to produce SiC. For SPS samples, peak intensity increase as sintering temperature increased from 1100 to 1350 °C. This indicates the increase of SiC content in the composition and corroborates the reason behind the absence of Si in the pattern. The SiB_4 phase was identified from XRD pattern analysis in Si 10 wt. % composition sintered by SPS. The reaction product SiB_4 may be the results from the interaction between B_4C and SiC and/or between Si and B_4C [94].

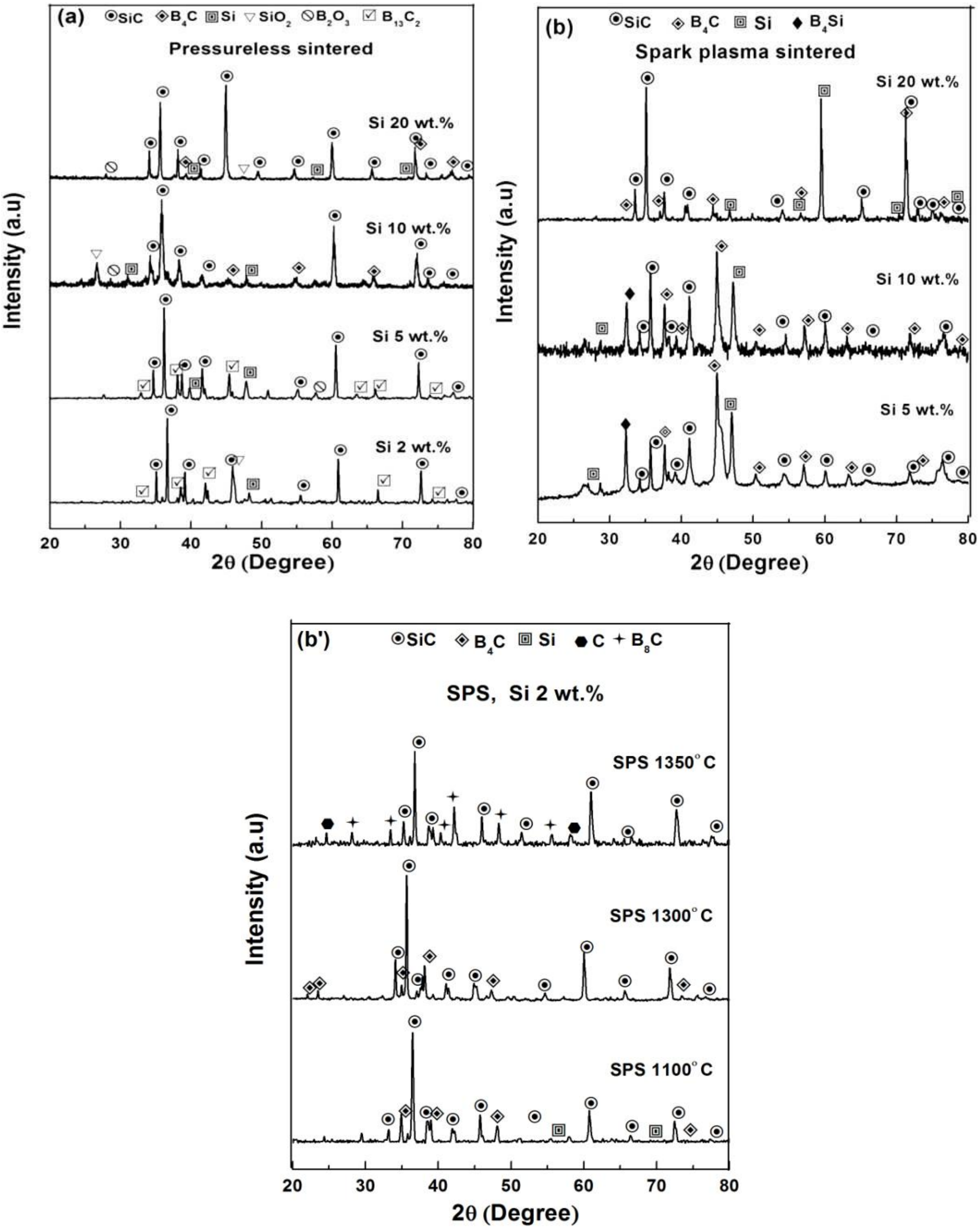

Figure 3.15 (a) XRD spectra of 2, 5, 10, and 20 wt. % Si cermet sintered by conventional sintering, (b) XRD spectra of 5, 10, and 20 wt. % Si cermet sintered by SPS, and (b') 2 wt. % Si samples sintered by SPS at 1100, 1300 and 1350 °C.

3.2c.2 Optical microscopy

Figure 3.16 shows the optical microstructure of 10 wt. % Si sample sintered at 1350 °C by SPS method. From the optical micrograph it is confirmed that, SiC, B_4C, and Si are uniformly distributed. At least 3 fields of view were considered and the average value was reported. In the micrograph, the grey, black and white regions are marked as SiC, B_4C and Si respectively. Optical micrograph conveys the compatibility of all the phases with good bonding in sintered sample. Mechanical milling of the powder particles lead to grain refinement and the uniform distribution of all the phases in the sintered product as shown in Figure 3.16. Uniform distribution of the particles is essential to obtain uniform physical and mechanical properties of the fabricated cermet samples.

The raw optical micrograph was also processed with Axio-vision image analysis software and these phases were represented with red, blue and yellow colour. Further, the quantities of different phases were calculated based on the volume fraction of each colour using an Axio Vision Release 4.8.2 SP3 (08-2013) software. The amount of different phases is also shown in the table and it is close to the original composition of cermet.

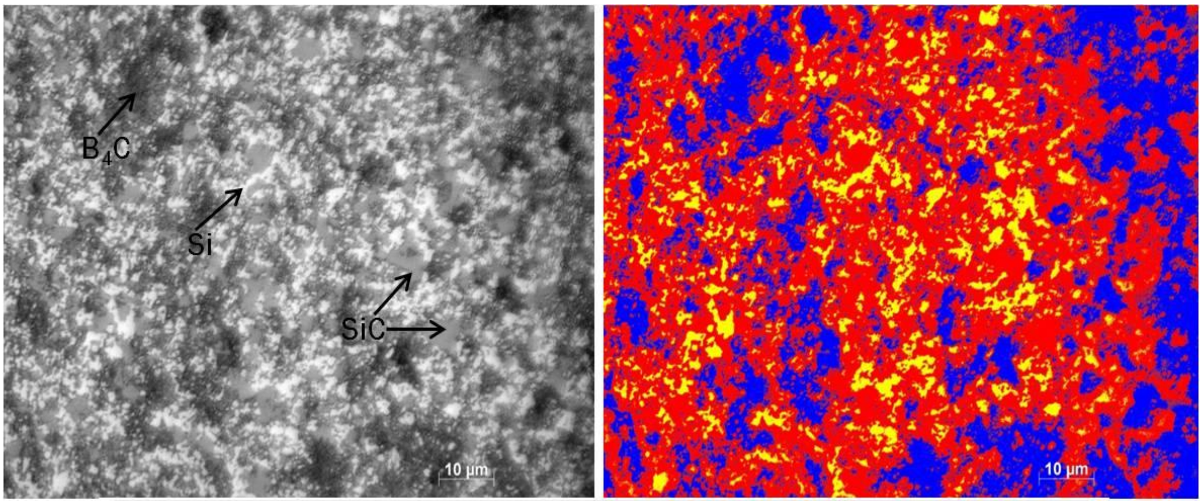

Phase name	Compositions	Volume percent (%)	Area percentage (%)
🟥 Phase 1	SiC	53.55	59±2
🟦 Phase 2	B_4C	34.10	27.6±0.4
🟨 Phase 3	Si	12.35	11.4±2

Figure 3.16 Optical image (left) of 10 wt. % Si cermet sample sintered by SPS at 1350 °C and phase distribution (right) with area percentage calculation.

3.2c.3 Field emission scanning electron microscopy (FESEM)

Figure 3.17 (a–d) represents the back scattered FESEM images of samples consolidated by SPS and Figure 3.17 (e–h) represents for the conventional sintered samples containing 2, 5, 10, and 20 wt. % Si respectively. Visible pores in the sample with 2 wt. % Si additive indicate the relatively low density. With increase of Si content to 10 wt. % the amount of pores in the composition decreases significantly. Large particle size with high porosity level is clearly visible in the samples consolidated by conventional sintering. Clearly, SPS samples showed less amount of porosity (3–4%) in 10 and 20 wt. % of Si contents in the compositions. Whereas, porosity value of around 8–10% are achieved for conventional sintered samples. As sintering was conducted at high temperature (1950 °C) for 30 minutes, grain growth is obvious. Large grain size in conventional sintered sample is due to prolong heating at high temperature. As per literature [47], α-SiC powders show much less grain growth and our results are consistent with this study and clear from FESEM micrographs. The presence of Si in the SiC-B_4C decreases the grain growth [68]. As the Si content increases, the microstructure of the cermet sample can be refined. The grey (B_4C) regions are uniformly distributed in white (SiC) regions and restrict the grain growth of the cermet. It has been observed that the average size of B_4C phase in SPS samples is < 5 µm, whereas, in case of pressure-less sintered samples, the average size of SiC and B_4C phases increases to ≥ 10 µm. The microstructural observation is also depicting the presence of molten Si in SPS samples as shown in Figure 3.17 (d’).

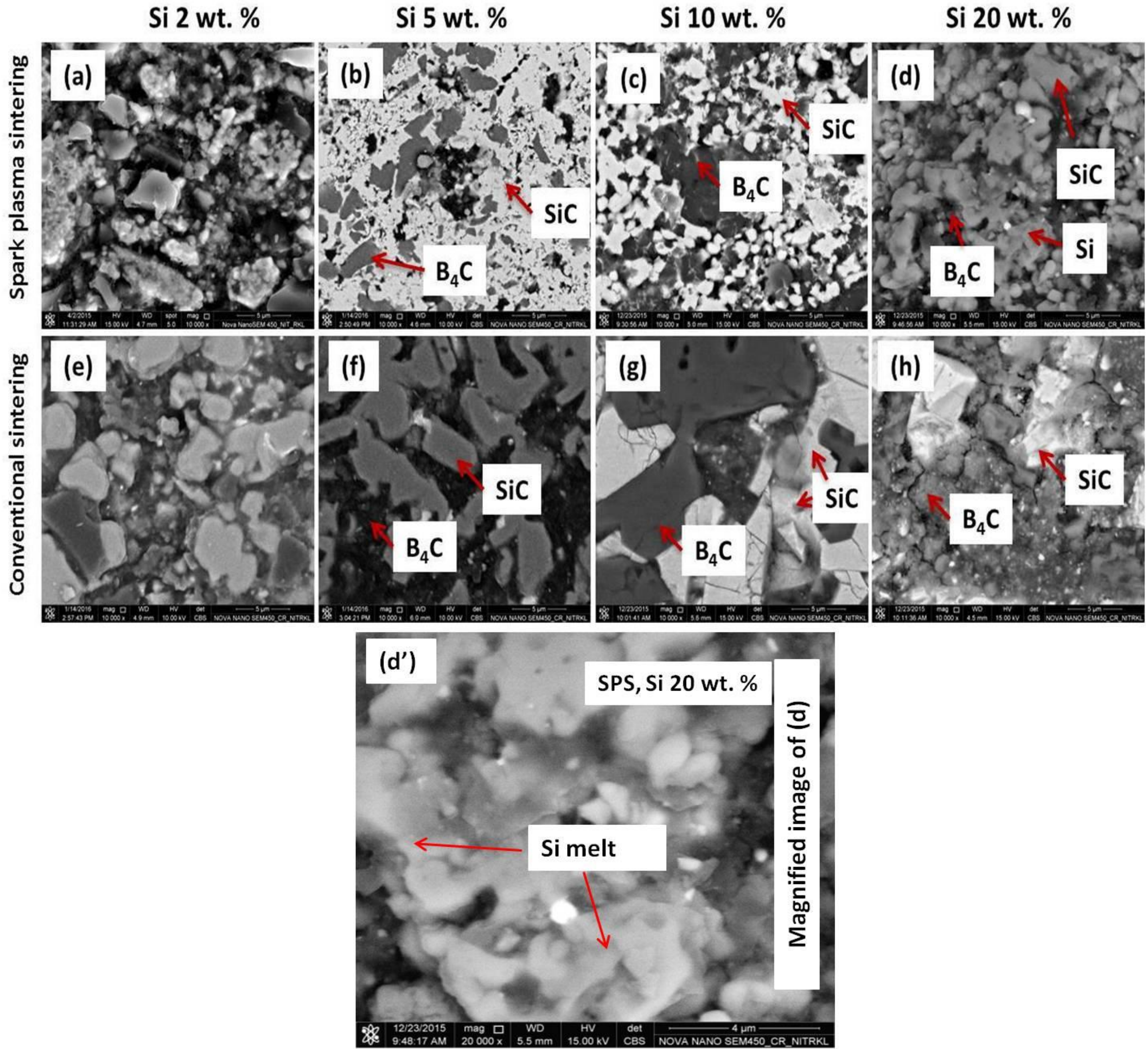

Figure 3.17 (a–d,d') FESEM micrographs of 2, 5, 10, and 20 wt. % Si cermets sintered by SPS and (e–h) FESEM micrographs of 2, 5, 10, and 20 wt. % Si cermets sintered by conventional sintering .

Grain size and morphology significantly depends on the sintering atmosphere, temperature and technique. Low temperature SPS samples showed less grain growth compared to conventional sintered samples since SPS was carried out for 5 minutes, whereas conventional sintering was conducted for 30 minutes. Figure 3.18 (a–c) shows the microstructural evolution of 2 wt. % Si samples sintered at 1100, 1300 and 1350 °C by SPS method. From the microstructure it has been observed that, number of pores decreases and relative density increases with increase in sintering temperature from 1100 to 1350 °C. Visible pores and cracks are observed in 1100 °C sintered sample. Interconnected pores with inter-particle necking are observed in 1100 °C sintered 2 wt. % Si sample as shown in Figure 3.18 (a). Pore radius decreases with increasing sintering temperature to1350 °C. At higher temperature, the rate of diffusion is more effective and the atoms rearrange themselves. Hence, for all the cermet samples with Si addition, SPS temperature was optimized to 1350 °C and properties evaluated. The deficiency in the Si content resulting improper bonding between particles as less amount of Si could not spread to cover all the hard solid particles during SPS and micro voids are observed as shown in Figure 3.18.

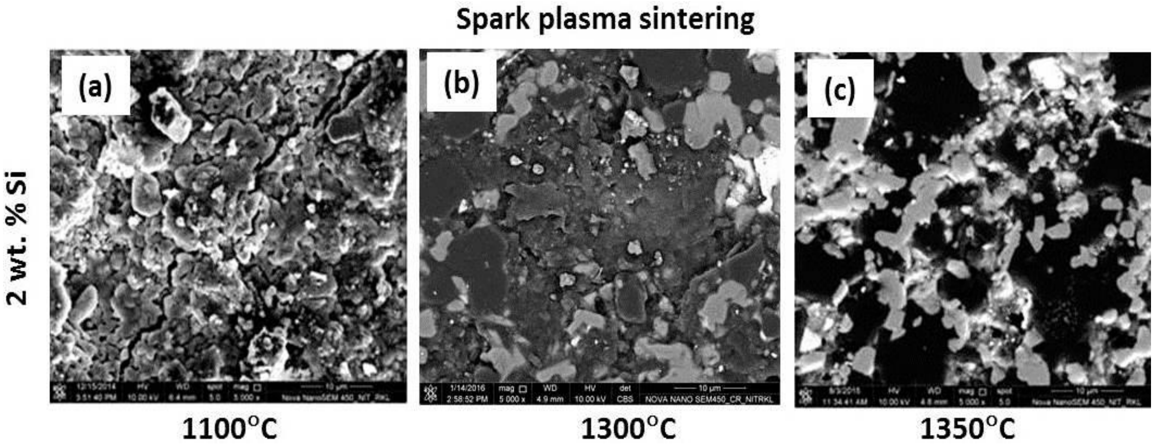

Figure 3.18 FESEM micrographs of 2 wt. % Si cermet sintered by SPS method at (a) 1100 °C, (b) 1300 °C, and (c) 1350 °C.

Figure 3.19 (a, b) shows the SEM micrographs of conventional sintered samples sintered at 1400 and 1600 °C. Conventional sintering of all samples carried out at 1400 and 1600 °C for 60 min holding time and at 1950 °C for 30 min holding time. At 1400 °C, interconnected pores are observed as shown in Figure 3.19 (a). With increasing sintering temperature to 1600 °C pore radius decreased. However, 1600 °C is not sufficient to increase densification due to high melting temperature of SiC and B_4C. Hence, conventional sintering was carried out at 1950 °C for all the cermet samples and properties evaluated. Conventional sintered samples of Si content at 1400 and 1600 °C exhibit poor relative density of 82 and 85% with hardness of 6 and 9 GPa respectively.

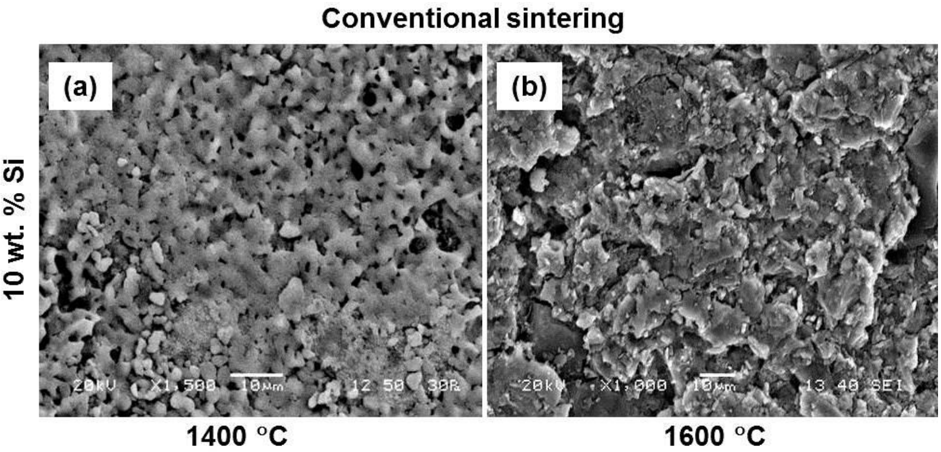

Figure 3.19 SEM micrographs of 10 wt. % Si cermet sintered by conventional sintering at (a) 1400 °C and (b) 1600 °C.

3.2c.4 Density and Microhardness study

The density of all the sintered samples was measured by using Archimedes' principle using distilled water as an immersion liquid. Figure 3.20 (a) shows the percentage of relative density with varying composition for both conventional as well as SPS samples. For SiC-B_4C–2 wt. % Si sample, sintered density increased by 1–4%, when SPS temperature was raised from 1100 to 1350 °C. SPS was found to be very much effective in densification of all the specimens. Relative density of SiC-B_4C–2 wt. % Si composites changes from 86.8 to 95.6% for variation of SPS temperature from 1100 to 1350 °C as shown in Table 3.2. At higher temperature, the level of porosity decreases and bond strength increases. The densities of sintered samples increases with increasing Si up to 10 wt. % and then slightly decreased with the further addition of Si (20 wt. %) for both cases. The highest relative density of 98% was obtained for sample containing 10 wt. % Si and sintered by SPS method. For conventional sintering, maximum density of 92% was achieved for 10 wt. % Si sample. The activation of powder particles during SPS and the liquid Si phase at the matrix interfaces of SiC-B_4C cermets are responsible to improve the wetting. On the other hand, in case of conventional sintered samples, the liquid or molten Si phase only helps in particles rearrangement but higher density can't be achieved as compared to the SPS products.

Microhardness was measured for all the conventional and spark plasma sintered samples. Figure 3.20 (b) shows the bar diagram of all the compositions versus microhardness values. SPS samples showed higher microhardness values than the conventional pressure-less sintered samples. It was observed that hardness values increases with increasing Si content for both sintering methods. Hardness values increases up to 10 wt. % of Si addition in to the matrix. Further addition of Si content to 20 wt. %, decreased the hardness value. The hardness of the cermets is directly related to the addition of Si in the main constituent and distribution of SiC, B_4C, and Si phases. It may be pointed out that B_4C is harder than SiC and Si. Increasing Si (softer phase) leads to the reduction in the proportion of B_4C. Microhardness value of 13±2.94 GPa was obtained for 2 wt. % Si sample consolidated by conventional sintering at 1950 °C. While the microhardness value of conventional pressure-less sintered samples varies from 15±2.24 to 18±2.23 GPa with increasing Si content from 5 wt. % to 10 wt. %., but decreased to 15 GPa in the case of Si 20 wt. %. For SiC-B_4C–2 wt. % Si composites, microhardness value changes from 12±1.81 to 22±1.02 GPa for the variation of SPS temperature from 1100 to 1350 °C as high temperature increases the atomic diffusion and bonding of particles. The microhardness value of SPS samples varies from 25±2.24 to 28±2.12 GPa with increasing Si content from 5 wt. % to 10 wt. %. But lower microhardness value of 24±2.25 GPa was obtained for 20 wt. % of Si sample, because of the increase in SiC content and residual Si in the product phase for Si (20 wt. %) cermets [68]. Addition of Si metal in SiC–B_4C composites has improved the density and mechanical properties of the sintered samples. It has been found that the hardness of the cermet containing 5 wt. % Si is lower than 10 wt. % of Si. The reason behind the low hardness is that the amount of molten Si required for proper diffusion and flowing around hard ceramic carbide particles is not sufficient. The deficiency in the Si content resulting micro voids as shown in the microstructure (Figure 3.17 and 3.18), which are responsible in increasing stress intensity at the tip. At that point, crack begins to form and deteriorates the mechanical properties. The decrease in pore size reduces the stress intensification. Hence, the addition of 10 wt. % Si is sufficient to reduce the pore size and refining the microstructure also account for the improvement in mechanical properties. While, 20 wt. % Si content is not advantageous as it decreases the hardness of the composition due to the presence of large amount of residual Si and increase of the SiC content in the composition (as the hardness of SiC is less than B_4C). Du *et al.* [64] studied the effect of Si addition on B_4C-SiC composites prepared from polycarbosilane-coated B_4C powder and found an enhancement of hardness, flexural strength and fracture toughness value by forming liquid phase at 11.4 wt. % Si. Feng *et al.* [65] also studied the effect of Si on densification and strengthening of B_4C consolidated by SPS. They observed maximum hardness, fracture toughness and flexural strength at 8 wt. % of Si. It should be mentioned here that all the density and hardness values of SPS samples were considerably higher than that of pressure-less sintered samples. The superior density and microhardness were supposed to be due to the finer microstructure of SPS sintered cermets.

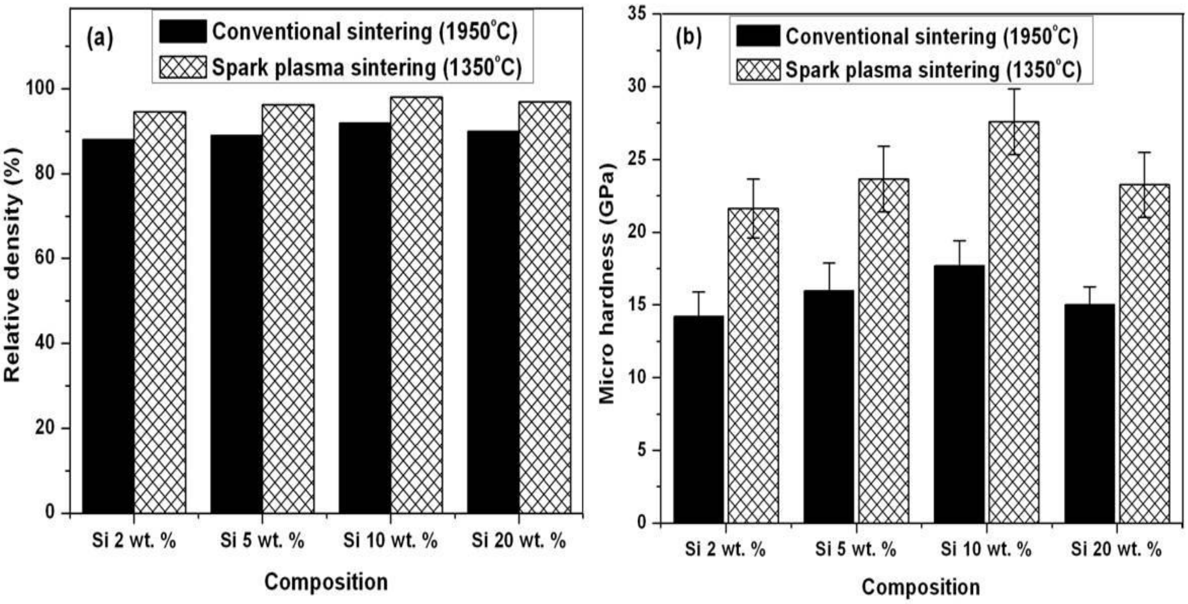

Figure 3.20 (a) Bar diagram of the relative sintered density of various compositions sintered by pressure-less sintering (1950 °C) and SPS (1350 °C), and (b) bar chart showing microhardness of pressure-less sintered and spark plasma sintered SiC-B_4C–Si cermets.

3.2c.5 Compression strength

Figure 3.21(a) shows the compressive stress-strain curves of 2, 5, 10, and 20 wt. % Si additions sintered by conventional sintering at 1950 °C. The cermet sample containing 10 wt. % Si shows maximum resistance to deformation as shown in the figure. The result reveals that the compressive strength increases with increase in Si content from 2 to 10 wt. % with exception for 20 wt. % Si sample. The compressive strength result with varying Si content was illustrated in Figure 3.21(b). As we know, 10 wt. % Si added composition exhibits maximum density and hardness and hence more stress is required to deform them. The 2 wt. % Si sample depicts low compressive strength 256 MPa indicating very little plasticity. It has also been observed that strain value increases from 8% to 19% with increasing Si content from 2 to 10 wt. % Si. This is due to the higher amount of plastic deformation during compressive stress for cermet containing higher amount of Si.

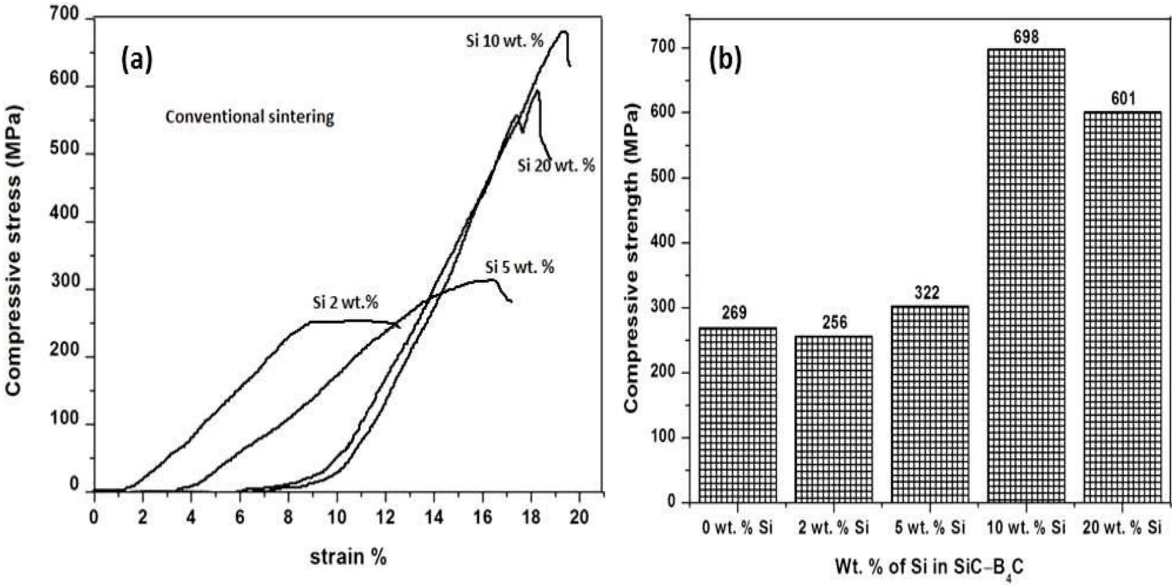

Figure 3.21 (a) Compressive stress–strain curves of SiC-B_4C−Si compositions sintered by conventional sintering and (b) bar diagram showing compressive strength vs. wt. % of Si addition in to SiC-B_4C.

Compressive strength test was carried out only for 10 wt. % Si cermet sample prepared by SPS method. Figure 3.22 represents the compressive stress-strain curve of 10 wt. % Si sample sintered by SPS method. SPS sample fractures more plastically than that of the conventional sintered samples. Due to better diffusion of particles during sintering, strong bond strength, and uniform particle distribution in SPS sample, provides higher strength to the cermet. Hence, 10 wt. % Si sample sintered by SPS method shows comparatively higher compressive strength of 1387 MPa than conventional sintered sample (698 MPa).

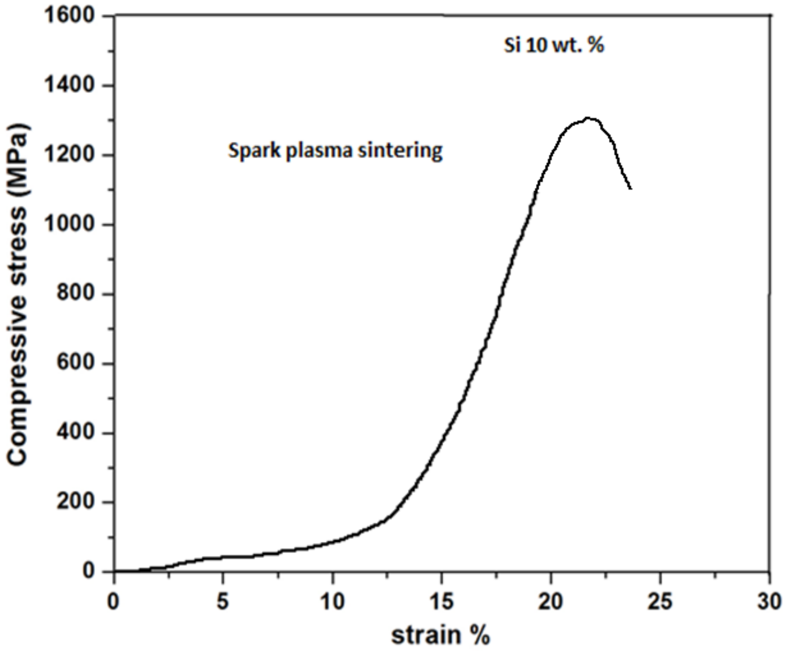

Figure 3.22 Compressive stress–strain curves of SiC-B_4C−10 wt. % Si compositions sintered by SPS method.

Figure 3.23 (a) illustrates the FESEM fractograph of SiC-B_4C–10 wt. % Si cermet sample sintered by pressure-less sintering at 1950 °C. Reinforcement of 10 wt. % Si in the ceramic matrix increase the fineness of fracture features. Fractograph plays the clear evidence of decreasing cleavage facets size as compared to SiC-B_4C composite (Figure 3.13). Here, two different modes of fractures are predominant, one is transgranular and other is intergranular fracture mode. Figure 3.23 (b and b') depicts the fractographs of SiC-B_4C–10 wt. % Si cermet sample sintered by SPS method. In contrast with previous case (SiC-B_4C ceramic composite, Figure 3.13), all the SiC and B_4C particles are not cut off as brittle mechanism. Instead, some of the SiC and B_4C grains are pulled out as observed in Figure 3.23 (b and b') with grooves. The observation reveals that, Si improves the bond strength in the cermet and hence breaks in a plastic manner as compared to ceramic composite.

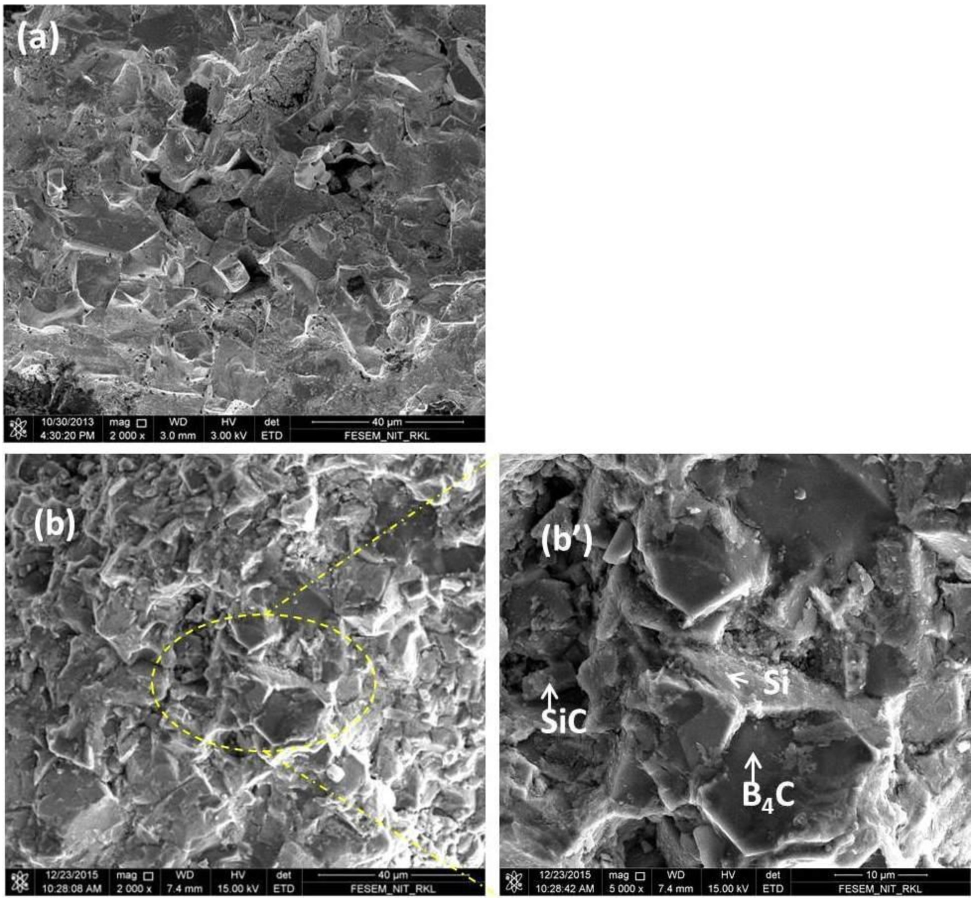

Figure 3.23 FESEM images of fracture surfaces of broken 10 wt. % Si sample after compressive strength test during sintering (a) conventionally at 1950 °C and (b, b') SPS at 1350 °C.

3.2c.6 Flexural strength

The flexural strength tests for conventional sintered samples were carried out and result is shown in Figure 3.24. Flexural strength of 10 wt. % Si reinforced cermet is highest among all the compositions. During flexural loading, the micro voids are formed in the vicinity of carbide particles leading to coalescence of the same. Due to enhanced bonding and relatively low porosity in SiC-B_4C–10 wt. % Si cermet sample, comparatively higher bend strength is obtained among all other compositions. As conventional sintered samples delivers poor density and hardness, it offers lower flexural strength for all the compositions. In the room temperature flexural strength test, the SiC and B_4C grains are cut off without any noticeable plastic deformation as shown in Figure 3.25. Flexural strength test could not be done for SPS samples as the required dimension (bar shape) for the test was not available.

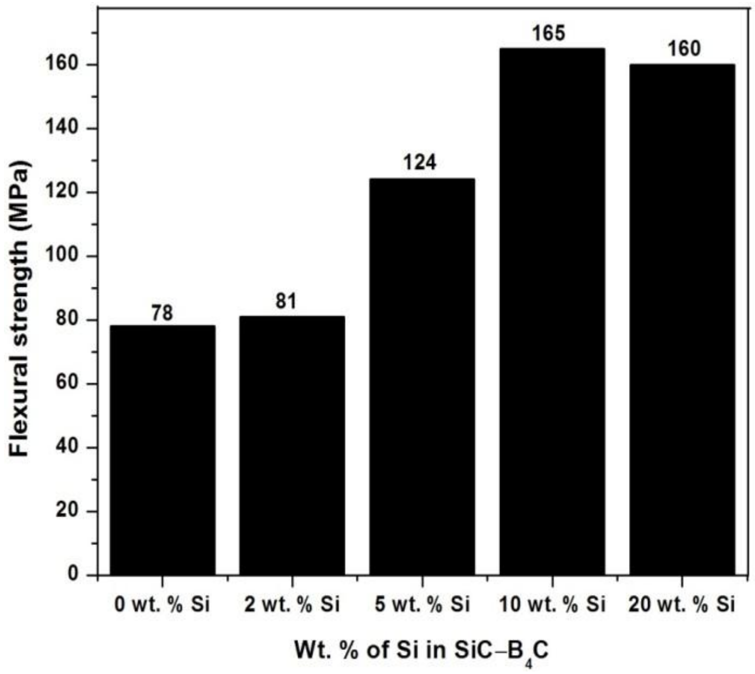

Figure 3.24 Flexural strength results with various compositions of SiC-B_4C−Si sample sintered by conventional sintering.

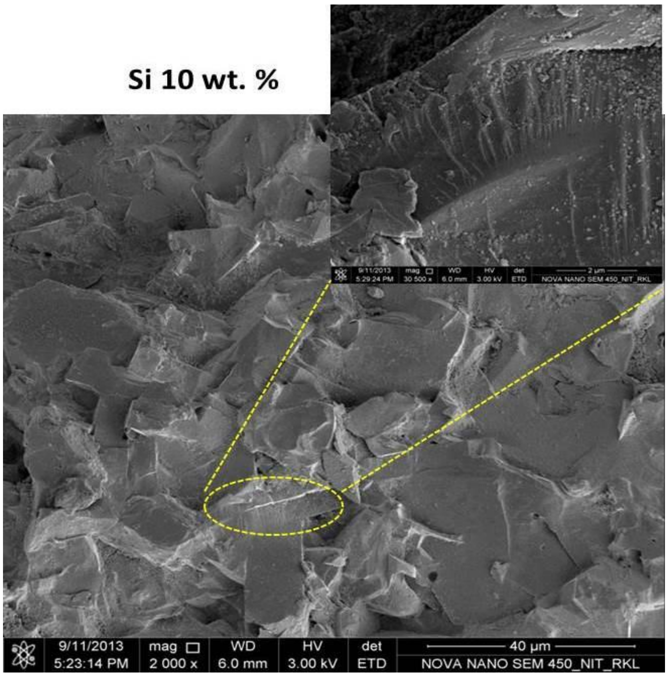

Figure 3.25 FESEM images of fracture surfaces of 10 wt. % Si sample after flexural strength test conventionally sintered at 1950 °C.

3.2c.7 Fracture toughness

Figure 3.26 (a, b) shows the FESEM micrograph of the Vickers indentation mark and crack propagation in SiC-B_4C–10 wt. % Si cermet for spark plasma sintered and conventional sintered samples. The propagation of crack length is comparatively less in case of SPS sintered samples than conventional sintered product. The increased fracture toughness values for the SPS samples could be explained by stronger bond strength and grain boundaries. Table 3.2 and 3.3 shows the indentation fracture toughness of the various investigated cermets developed by conventional and SPS methods. This data shows that with increasing Si content in SiC-B_4C, the indentation fracture toughness value is also increased. In the case of conventional pressure-less sintered samples, indentation fracture toughness values was calculated to be 1.2 MPa.m$^{1/2}$ for 2 wt. % Si addition in SiC-B_4C. The indentation toughness value is increased from 1.3 to 1.97 MPa.m$^{1/2}$ with the increase in Si content from 5 to 10 wt. %. However, the toughness value is reduced to 1.90 MPa.m$^{1/2}$ for 20 wt. % of Si addition. The similar trend of indentation fracture toughness also followed in case of SPS samples. When 2 wt. % Si added into SiC-B_4C, toughness value increased to 2.2 MPa.m$^{1/2}$ for SPS sintered at 1350 °C. For the SPS, indentation fracture toughness value has been improved from 2.9 to 3.8 MPa.m$^{1/2}$ with increasing Si content from 5 to 10 wt. %. The toughness value was reduced to 3.5 MPa.m$^{1/2}$ for the Si 20 wt. %. Internal stresses are developed due to the mismatch of thermal expansion co-efficient of SiC (2.56×10^{-6}/K), Si (2.77×10^{-6}/K) and B_4C (3.2×10^{-6}/K). The difference in thermal expansion co-efficient resulted in the generation of the micro-crack within the materials. The stresses that created these cracks were developed during cooling from higher temperature to room temperature because of the mismatch in thermal expansion co-efficient between SiC, B_4C, and Si sintered compacts. It is believed that the stress during cooling is responsible for lower fracture toughness values of the sample sintered at various temperatures [101].

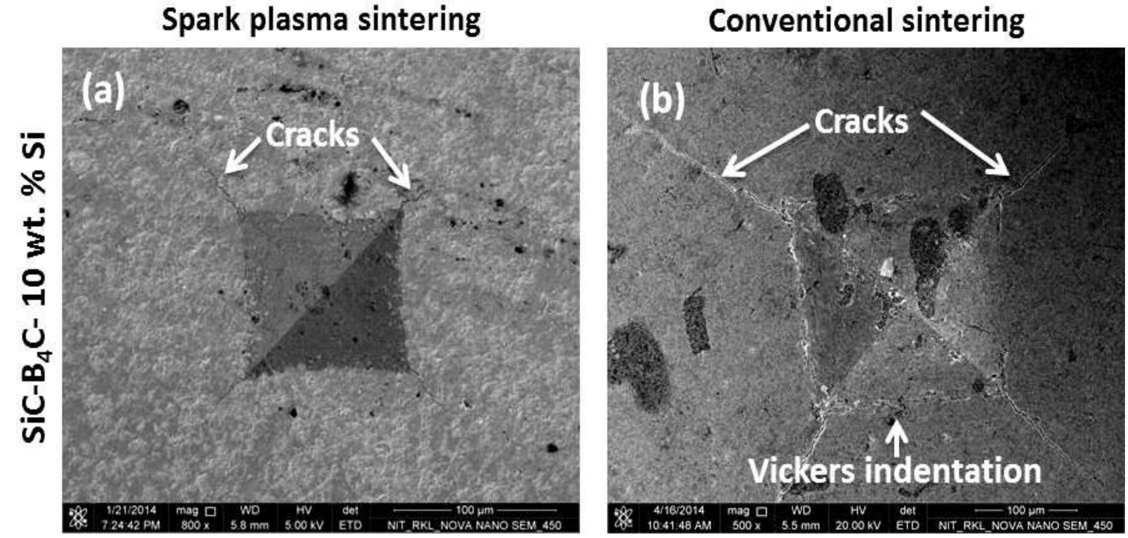

Figure 3.26 Vickers indentation marks and crack propagation of 10 wt. % Si samples sintered by (a) SPS and (b) conventional sintering.

Figure 3.26 shows the crack propagation by Vickers indentation method on the surface of the 10 wt. % Si sample sintered by SPS. The cracks generated for pure ceramic materials are deflection free and straight in nature. Transgranular fracture is the major fracture mode for carbide/ ceramic materials. While the SiC-B_4C–Si cermets, cracks are wavier and deflected due to the presence of SiC and re-solidified Si [63]. This leads to zigzag crack propagation between the particles and reduces the crack driving force in comparison to straight crack. The presence of molten Si at high temperature has improved the liquid phase sintering by flowing liquid Si through particle rearrangement and reducing pore amounts. With increasing Si addition, there is an improvement of interfacial bond strength of the sintered product with higher densification as the cohesive strength of carbides are weaker than that of interfacial bond of Si and carbide. The presence of Si leads to crack deflection, branching and bridging that is responsible for toughening of the cermet materials (Figure 3.27). The plastic deformation of Si above 1350 °C is an obvious candidate to increase the toughness with an increase in Si content. As SiC and Si do not have much difference in thermal co-efficient of expansion, the additional Si percentage in SiC-B_4C cermet is advantageous to increase the toughness up to certain level. The deflection of cracks occurs when the crack encounters different phases as shown in the circular region in the Figure 3.26. The interaction of indentation cracks in B_4C and Si particles leads to deflection and bridging, which in turn increases the toughening of the SiC-B_4C–Si cermet materials.

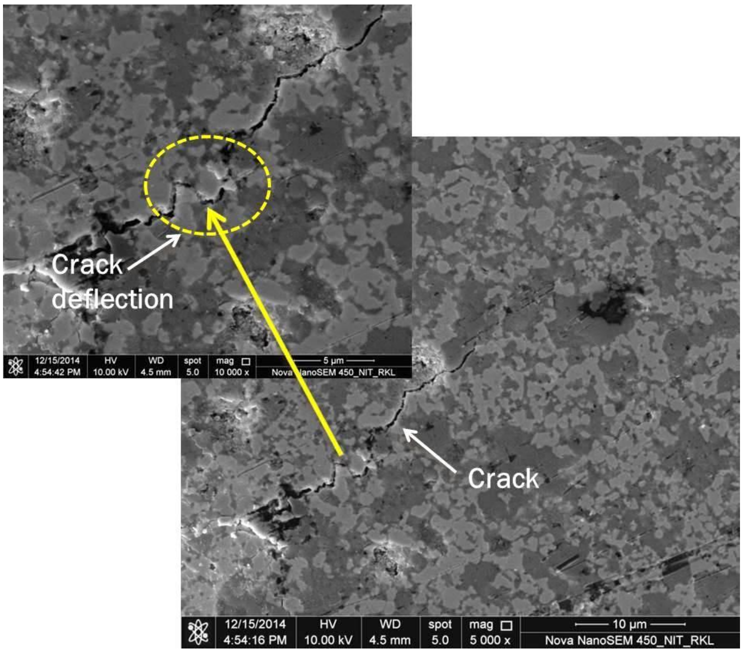

Figure 3.27 Crack path produced by Vickers indentation on the 10 wt. % Si sample surface.

Table 3.2 *Physical and mechanical properties of SiC-B$_4$C–2 wt. % Si ceramic composite fabricated by conventional sintering and spark plasma sintering at different temperatures.*

Properties	**SiC-B$_4$C–2 wt. % Si**			
	Conventional pressure-less sintering	**Spark plasma sintering**		
	1950°C	***1100°C***	***1300°C***	***1350°C***
Density (%)	89	86.8	94	95.6
Micro hardness (GPa)	13±2.94	12±1.81	20±1.92	22±1.02
Fracture toughness (MPa.m$^{1/2}$)	1.2	0.8	1.9	2.2
Compressive strength (MPa)	256	-	-	-
Flexural strength (MPa)	81	-	-	-

Table 3.3 *Physical and mechanical properties of 5, 10, and 20 wt. % Si contents in SiC-B$_4$C based cermets prepared by conventional sintering and spark plasma sintering methods*

Sample	**Conventional pressure-less sintering**					**Spark plasma sintering**			
	1950 °C					***1350 °C***			
	ρ^a (%)	*MH^b (GPa)*	*FT^c (MPa m$^{1/2}$)*	*CS^d (MPa)*	*FS^e (MPa)*	*ρ^a (%)*	*MH^b (GPa)*	*FT^c (MPa m$^{1/2}$)*	*CS^d (MPa)*
SiC$_{60}$(B$_4$C)$_{35}$Si$_5$	89.6	15±2.24	1.3	322	124	96.3	25±2.24	2.9	-
SiC$_{60}$(B$_4$C)$_{30}$Si$_{10}$	92	18±2.23	1.97	698	165	98	28±2.12	3.8	1387
SiC$_{60}$(B$_4$C)$_{20}$Si$_{20}$	90	15±1.72	1.90	601	160	97	24±2.25	3.5	-

a. Relative density (ρ) b. Microhardness (MH) c. Fracture toughness (FT) d. Compressive strength (CS) e. Flexural strength (FS)

3.2d Characterization of SiC-B$_4$C–Al cermet

3.2d.1 X-ray diffraction (XRD)

Figure 3.28 (a) and (b, b’) shows the XRD patterns of 2, 5, 10, and 20 wt. % of Al added compositions prepared by conventional sintering and spark plasma sintering techniques. XRD analysis shows the presence of parent phases like SiC, B$_4$C, and product phases of all samples sintered by conventional as well as SPS technique. In both techniques, Al melts and liquid Al reacts with SiC and B_4C as sintering is carried out above the melting point of Al. As Al melts and reacts with B_4C and SiC, it forms solid ceramic phases (Al_4SiC_4, $Al_8B_4C_7$, AlB_{12}, Al_8SiC_7, Al_4SiC_7 and $B_{13}C_2$) with reduced porosity and a considerable amount of shrinkage takes place. It has been reported that, Al_8SiC_7, Al_4SiC_7, $Al_8B_4C_7$, AlB_{12}, $Al_8B_{48}C_2$, and $Al_8B_{48}C_2$ phases have good oxidation resistance, high toughness and high hardness [14, 102–105]. In particular, $Al_8B_4C_7$ has good oxidation resistance applicable for carbon containing refractory materials and ultra-hard materials. $Al_8B_4C_7$ phase was found to be present for Al 10 and 20 wt. % samples sintered by conventional sintering. But for SPS samples, $Al_8B_4C_7$ was identified for Al 5, 10, and 20 wt. % compositions. Gao *et al.* [106] reported the formation of $Al_8B_4C_7$ ceramic phase above 1400 °C from a mixture of B_4C, C and Al via solid state reaction. AlB_{12} phase is formed in both conventional and SPS sintered samples for all the compositions. AlB_{12} phase is absent in 2 wt. % Al sample sintered by SPS at 1100 and 1200 °C as shown in Figure 3.28 (b). It is interesting to note that toughness of the composites increases rapidly as the AlB_{12} content increases [107]. According to Yamaguchi *et al.* [108], during sintering, Al melts at about 660 °C and form lowers contact angle with solid B_4C and SiC. With increasing temperature, Al become liquid and dispersed around the solid particles. The amount of free Al decreases above 800 °C and completely disappeared above 900 °C. Therefore, free Al peak was not observed in XRD patterns of all the sintered samples. Huang *et al.* [109] studied hot pressing of C-B_4C-SiC composites with Al additive and observed that the liquid Al to spread throughout the matrix. They also observed the decrease in surface area due to application of high pressure and accelerated sintering by shrinking of the particles. Hence, Al reinforcement increases the density and toughness of sintered samples [14]. $Al_4Si_4C_7$ and Al_8SiC_7 phases were identified in 2 wt. % Al sample sintered by both conventional sintering and SPS methods. An $Al_3B_{48}C_2$ phase was formed in conventional sintered sample containing 5 wt. % Al.

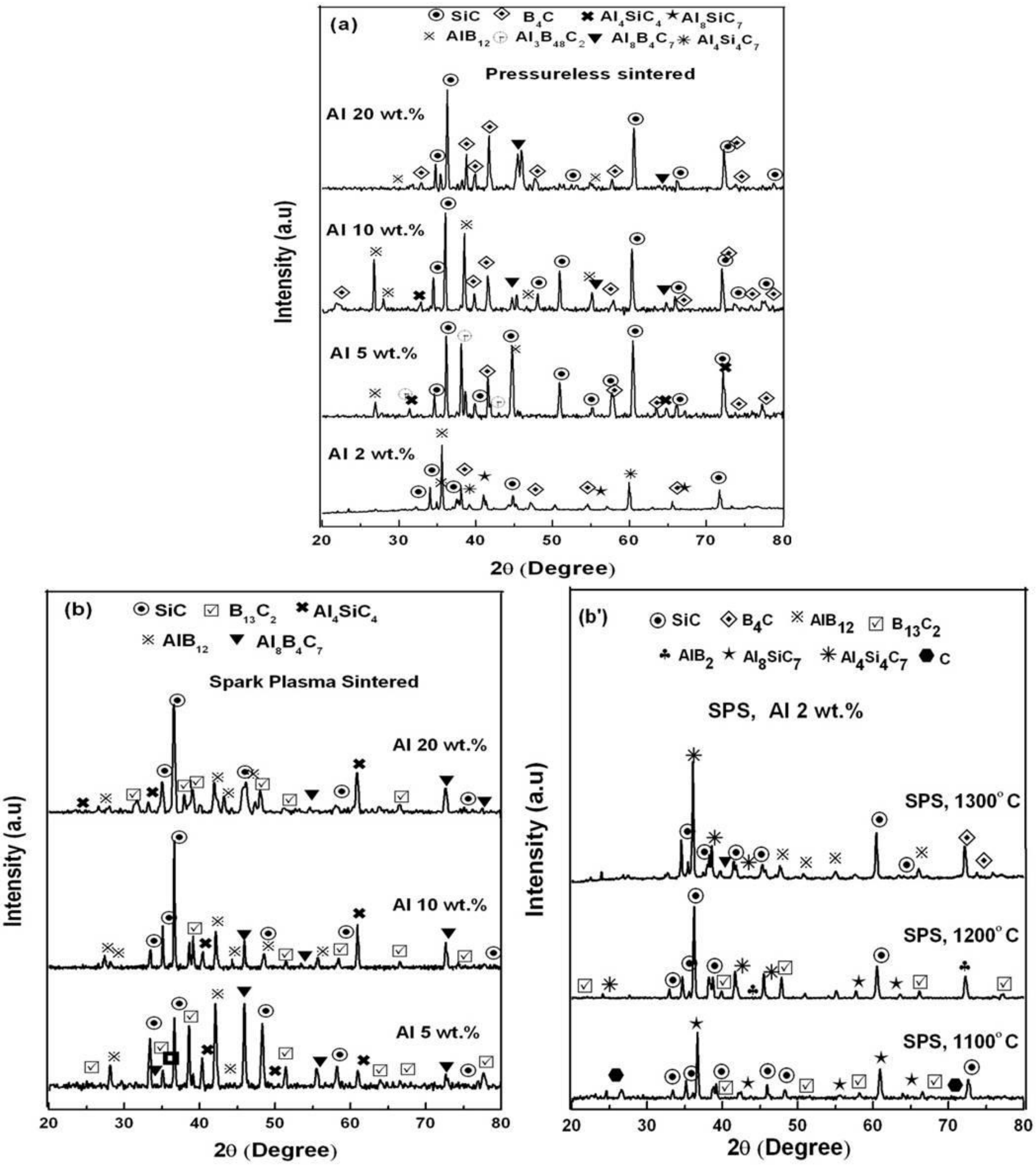

Figure 3.28 (a) XRD spectra of 2, 5, 10, and 20 wt. % Al cermet sintered samples by conventional sintering, (b) XRD spectra of 5, 10, and 20 wt. % Al cermet sintered by SPS, and (b’) 2 wt. % Al samples sintered by SPS at 1100, 1200 and 1300 °C.

3.2d.2 Optical microscopy

In order to know the distribution of different phases in sintered cermets, optical microscopy was carried out. The optical microstructure of 20 wt. % Al sample sintered at 1950 °C by conventional sintering and at 1300 °C by SPS is shown in Figure 3.29 (a, b). The micrograph shows the uniform distribution of white, grey and black regions corresponding to SiC, B_4C and product phases respectively.

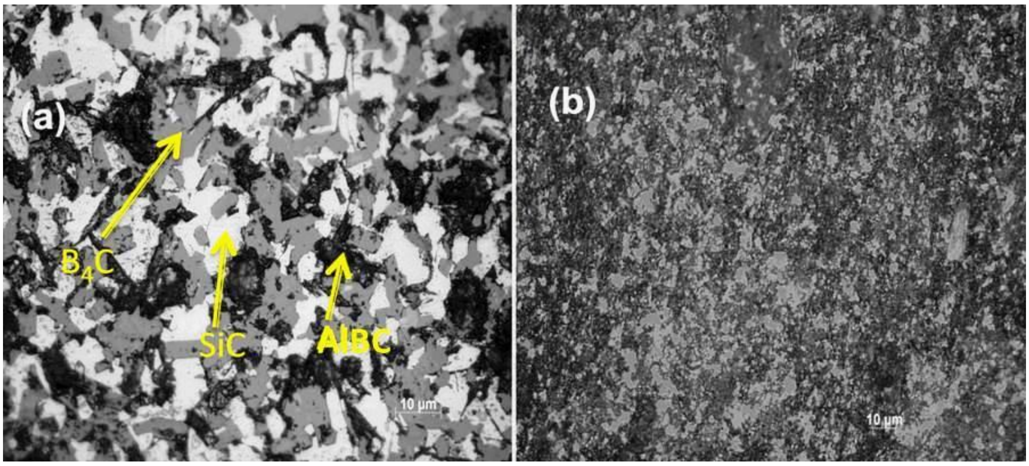

Figure 3.29 Optical micrographs of 20 wt. % Al cermet consolidated by (a) conventional sintered at 1950 °C for 30 min and (b) spark plasma sintered at 1300 °C for 5 min.

FESEM images in Figure 3.30 (a–e) shows the EDX mapping of 10 wt. % Al cermet sintered by conventional pressure-less sintering at 1950 °C for 30 min. Mapping confirmed the uniform distribution of Si, B, Al and C components over the field of analysis of the image.

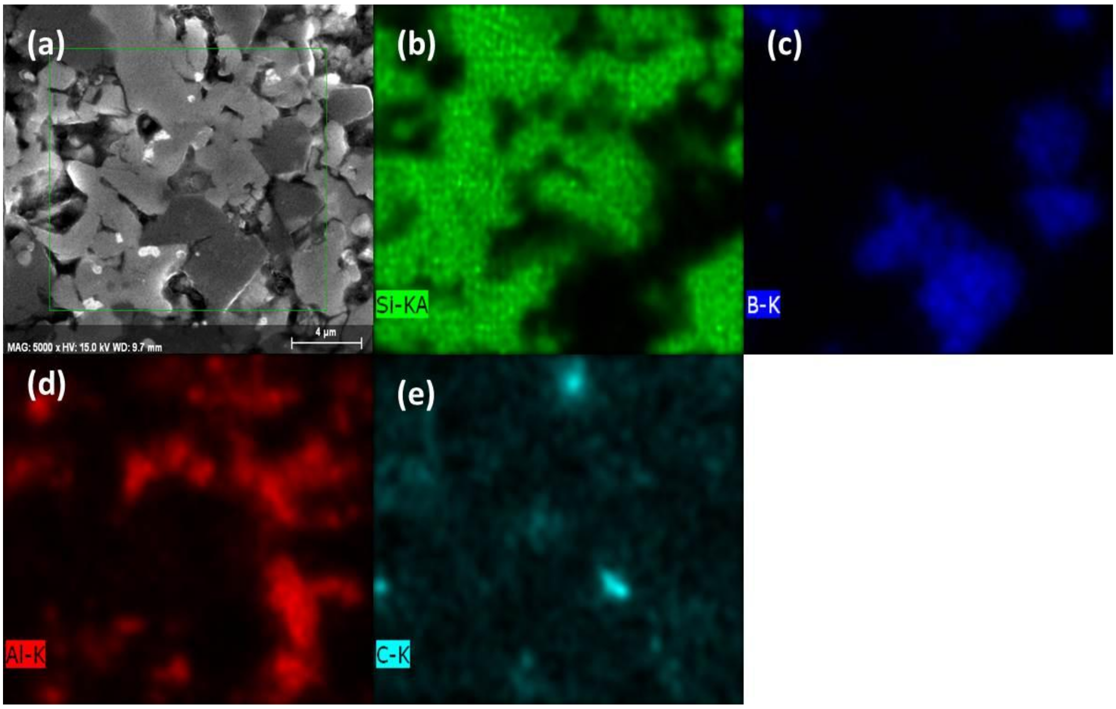

Figure 3.30 FESEM micrograph of (a) polished surface of 10 wt. % Al sintered at 1950 °C; (b) EDX mapping of silicon, (c) Boron, (d) Aluminium and (e) Carbon in 10 wt. % Al cermet.

3.2d.3 Field emission scanning electron microscopy (FESEM)

Figure 3.31 (a–d) represents the FESEM images of samples consolidated by SPS and Figure 3.30 (e–h) represents for the conventional sintered samples containing 2, 5, 10, and 20 wt. % Al respectively. Large grain size with high porosity level is clearly visible in the samples consolidated by conventional sintering. As sintering was conducted at high temperature (1950 °C) for 30 minutes, grain growth is obvious. It has been observed that addition of Al above 5 wt. % reduces average grain size of SiC-B_4C compact due to pinning at the grain boundaries. SPS samples show less porosity for all compositions. Mashhadi *et al.* [14] studied the effect of Al addition on B_4C by pressure-less sintering; they also observed increase in B_4C grain size with increasing Al content. They also observed that, the grain morphology depends significantly on the sintering atmosphere and temperature. It is evidenced by the relative density of SPS samples as shown in Tables 3.4 and 3.5. Although the sintering temperature for SPS is much lower than that of conventional sintering, it shows higher density which in turn yields samples with better mechanical properties. The plasma spark on the contact point and / or in the gap between the particles generates a local high-temperature of several thousand degrees of centigrade. This high-temperature causes melting of surface powder particles and neck formation around contact area between particles in SPS process. During sintering, the molten Al facilitates the wetting of SiC-B_4C cermet by forming a liquid phase at the matrix interfaces.

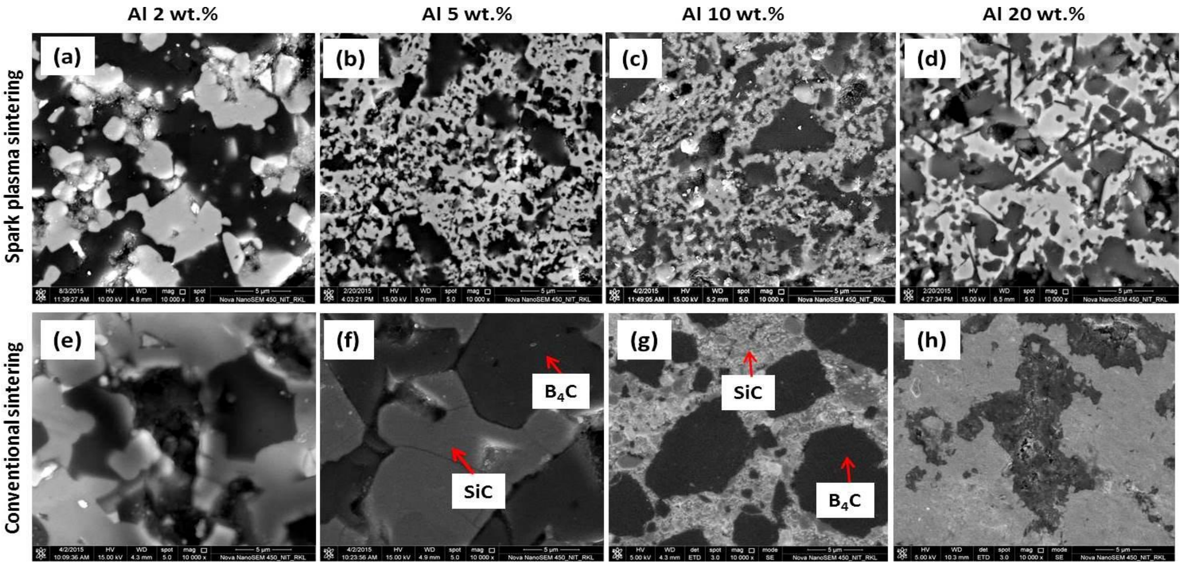

Figure 3.31 (a–d) FESEM micrographs of 2, 5, 10, and 20 wt. % Al cermets sintered by SPS at 1300 °C and (e–h) FESEM micrographs of 2, 5, 10, and 20 wt. % Al cermets sintered by conventional sintering at 1950 °C.

Figure 3.32 (a–c) shows the microstructural evolution of 2 wt. % Al samples sintered at 1100, 1200 and 1300 °C by SPS method. From the microstructure it has been observed that, number of pores decreases and relative density increases with increase in sintering temperature from 1100 to 1300 °C. With increasing sintering temperature in SPS samples, increase in sinterability results in improved density and reduced porosity. Addition of 2 wt. % Al into SiC-B_4C improve the compatibility between SiC and B_4C due to spreading of liquid and eventually there is reduction in porosity even when processed at low temperature (1300 °C). It may be noted that necking starts at 1100 °C for SPS samples of 2 wt. % Al composition as shown in Figure 3.32 (a). With increasing sintering temperature, gradually dense compacts are formed with uniform distribution of the phases. But micro voids are observed even at 1300 °C sintered samples.

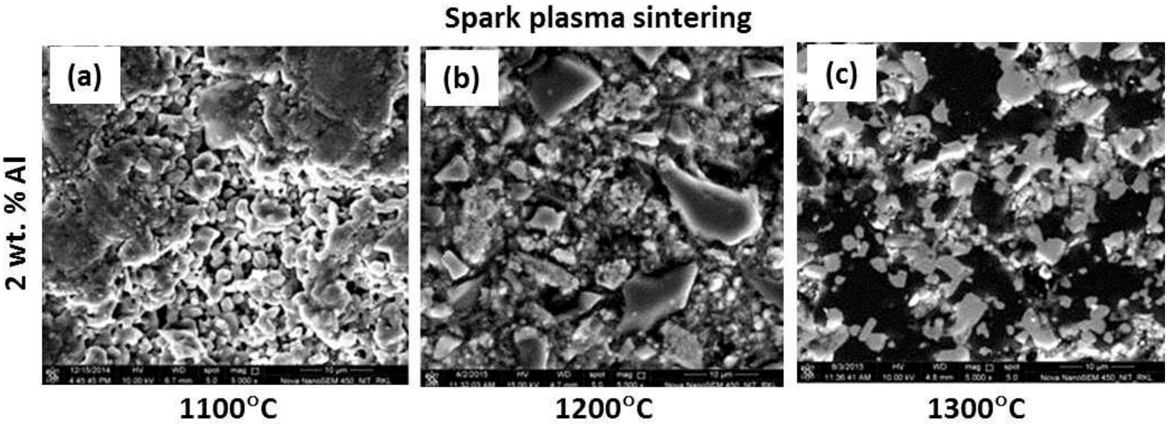

Figure 3.32 FESEM micrographs of 2 wt. % Al cermet sintered by SPS method at (a) 1100 °C, (b) 1200 °C, and (c) 1300 °C.

Figure 3.33 (a, b) shows the SEM micrographs of 10 wt. % Al sintered by conventional sintering at 1400 and 1600 °C for holding time of 60 min and at 1950 °C for holding time of 30 min. From the microstructure it is confirmed that, conventional sintering at 1400 and 1600 °C is not sufficient to densify high temperature resistance carbide materials. It is clearly observed that 1400 and 1600 °C could not provide better densification and large numbers of pores are present. Hence, conventional sintering was carried out at 1950 °C for all the compositions and also properties were evaluated. Conventional sintered samples at 1400 and 1600 °C exhibit poor relative density of 81 and 85% with hardness of 5 and 8 GPa respectively.

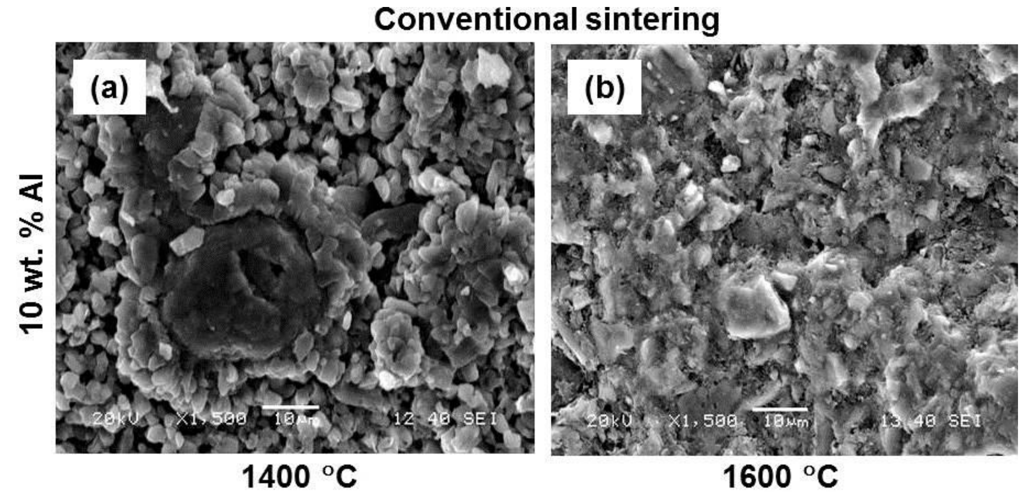

Figure 3.33 SEM micrographs of 10 wt. % Al cermet sintered by conventional sintering at (a) 1400 °C, (b) 1600 °C.

Figure 3.34 shows the EDS spectra and quantitative analysis of elements present in 20 wt. % Al sample sintered by SPS at 1300 °C. It reveals the presence of Si, B, Al and C with a negligible amount of Fe (0.07 wt. %). The presence of Fe peak is mainly from stainless steel milling media and vial during planetary milling.

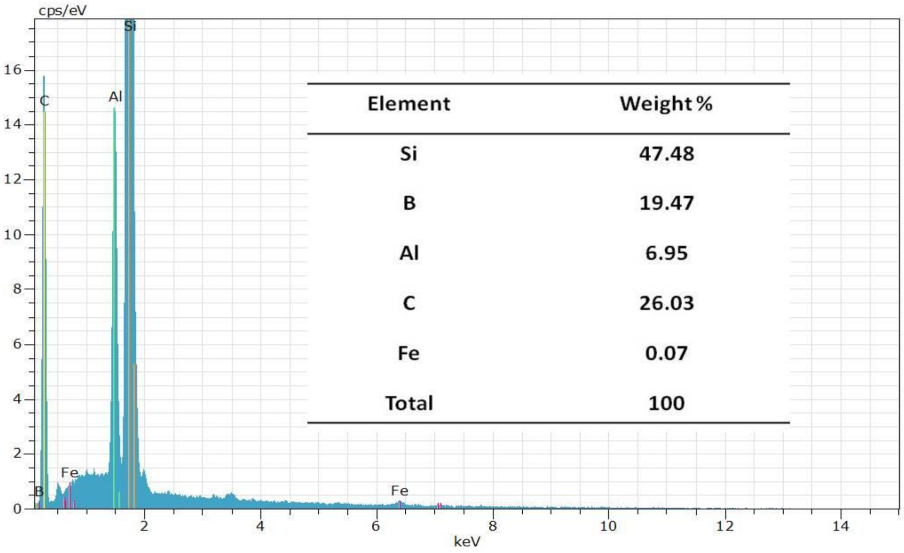

Element	Weight %
Si	47.48
B	19.47
Al	6.95
C	26.03
Fe	0.07
Total	100

Figure 3.34 EDS spectra of 20 wt. % Al cermet sintered by SPS at 1300 °C.

3.2d.4 Density and Microhardness study

Figure 3.35 (a) represents the percentage of relative density for both conventional as well as SPS SiC-B_4C–Al cermets. The samples sintered by SPS method exhibits higher density than the conventional sintered samples due to the simultaneous application of heat and pressure. On the other hand, conventional sintering uses only heat energy. SPS process reduces the sintering time and temperature. A high-temperature sputtering phenomena is generated by spark plasma, spark impact pressure is responsible for eliminating adsorptive gas and impurities existing on the surface of powder particles [110]. Eventually, the powder particles on the surface are easily purified and activated than in conventional sintering process. Density of all the samples increases with increasing Al content up to 10 wt. %. Density slightly drops down at 20 wt. % Al addition. With increasing Al addition, there is an improvement of interfacial bond strength of Al and carbides than that of the cohesive strength of carbides in the sintered product with higher densification. For SPS samples, the density values of 2 wt. % Al cermet changes from 92.7 to 95.7% for the variation of sintering temperature from 1100 to 1300 °C. High temperature sintering exhibits high speed diffusion and high-speed material transfer in micro and macro level which increases the density. The SPS sample of 10 wt. % of Al shows 97% of theoretical density which is the highest among all the compositions and superior to that of conventionally sintered samples (90%).

Figure 3.35 (b) represents the bar diagrams of Vickers microhardness values of all the conventional sintered and SPS samples containing 2 wt. % to 20 wt. % of Al. The hardness values of sintered samples show similar trends like densities. Vickers microhardness measurement was carried out at 300 gf indentation load. At least 10 trials of indentations were made and the average value was reported. Higher microhardness values are obtained for SPS samples than the conventional sintered samples. Hardness values increases with increasing Al content from 2 wt. % to 10 wt. % for both SPS and conventional sintered samples. The hardness value drops down at 20 wt. % of Al addition for both cases. The microhardness value of conventional sintered 2 wt. % Al cermet was 11±2.79 GPa. For 5 wt. % Al addition hardness value increases to 15±1.83 GPa, whereas it increases to 17 GPa with an addition of 10 wt. % Al. Finally, hardness value decreases to 14±1.59 GPa in 20 wt. % Al addition in SiC-B_4C. For SPS samples of 2 wt. % Al addition, the Vickers microhardness values changes from 12±2.98 to 15±1.83 GPa for the variation of sintering temperature from 1100 to 1300 °C. The microhardness value varies from 18±2.66 GPa in 5 wt. % Al to maximum microhardness value of 23±2.29 GPa for 10 wt. % Al addition. But slightly lower microhardness value of 19±2.23 GPa was obtained for the sample containing higher amount of soft phase (20 wt. % Al addition). The higher hardness values of SPS samples were supposed to be due to the finer grain size of SPS sintered cermets.

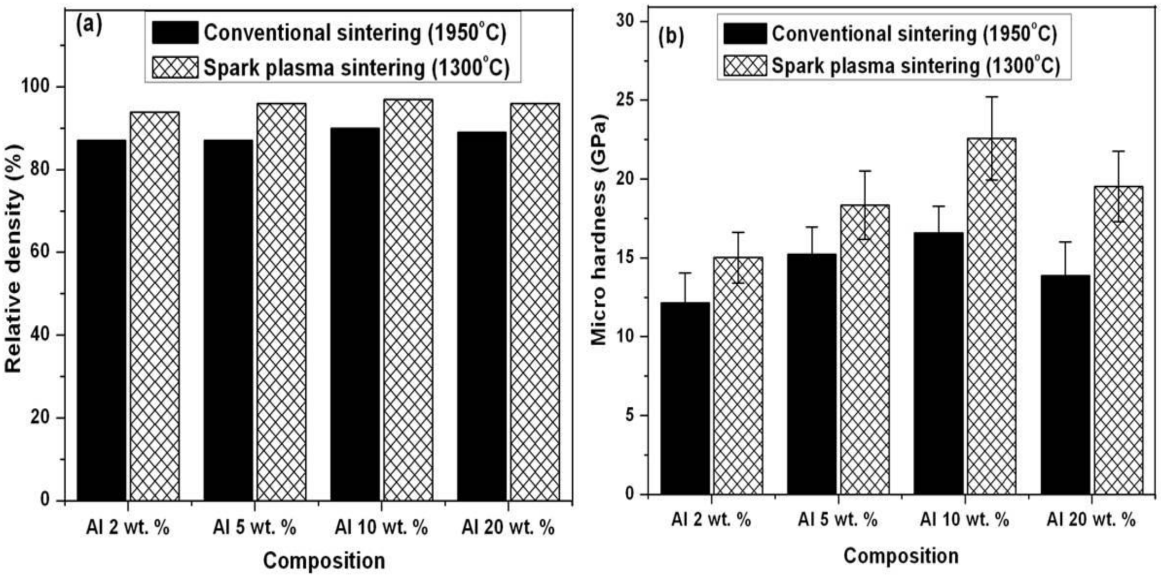

Figure 3.35 (a) Bar diagram of the relative sintered density of various compositions sintered by pressure-less sintering (1950 °C) and SPS (1300 °C), and (b) bar chart showing microhardness of pressure-less sintered and spark plasma sintered SiC-B_4C–Al cermets.

3.2d.5 Compression strength

Compressive yield stress of 2, 5, 10, and 20 wt. % of Al reinforced SiC-B_4C cermet samples sintered by conventional sintering at 1950 °C are studied. Figure 3.36 (a) represents the compressive stress-strain curves of all cermet samples. Sample with 20 wt. % Al addition exhibits higher yield strength than the other compositions with noticeable plastic deformation. The compressive strength result with varying Al content was illustrated in Figure 3.36 (b). As we have seen, 10 wt. % Al added composition exhibits maximum density and hardness and hence more stress is required to deform them. For 20 wt. % Al content, higher amount of AlB_{12} phase is formed as confirmed by XRD analysis, and hence the material strength increases. Bin et al [111] studied the compressive properties of Al-55% B_4C (volume fraction) particles at elevated temperature. They reported that, Al composite prepared by squeeze casting method shows the compressive strength nearly 480 MPa tested at strain rate of 5 Sec^{-1} and at 25 °C. The maximum compressive stress increases from 269 MPa to 512 MPa with increasing Al from 0 to 20 wt. %. It is also observed that strain value at maximum stress increases from 8% to 19% with increasing Al content from 2 to 20 wt. %. This is due to the presence of higher amount of Al, which is plastically deformed during compressive stress and generates high plastic strain.

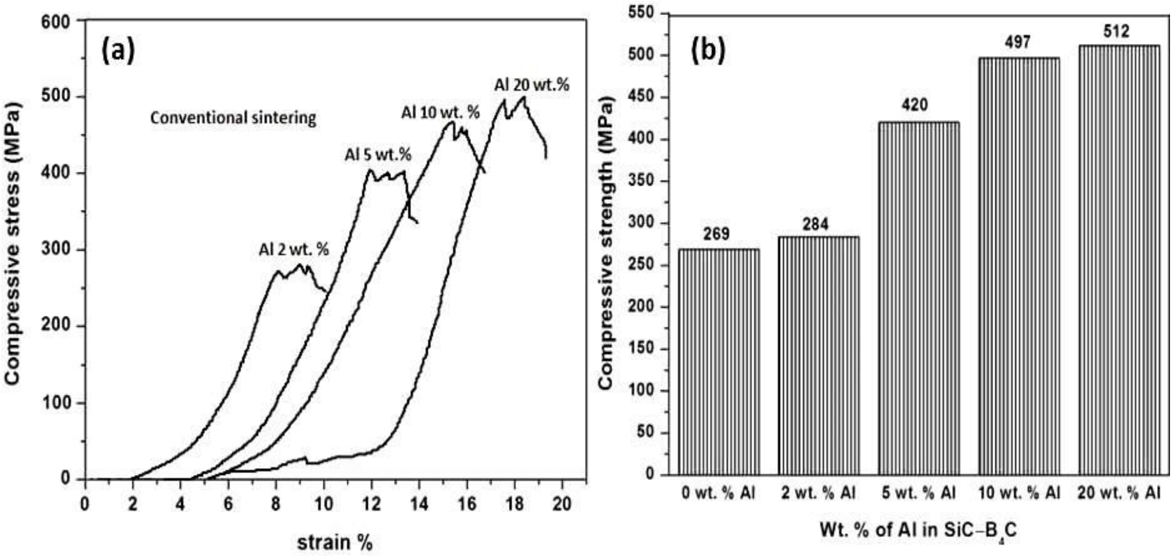

Figure 3.36 (a) Compressive stress–strain curves of SiC-B_4C−Al compositions sintered by conventional sintering and (b) bar diagram showing compressive strength vs. wt. % of Al addition in to SiC-B_4C.

Figure 3.37 shows the fractograph of 5 wt. % Al cermet. The figure indicates that, the mode of failure was mixed brittle and ductile nature. It shows transgranular brittle fracture with cleavage facets. Intergranular fracture with micro voids coalescence at the grain boundaries is observed. As a result, materials have reduced the fracture energy which endorses rapid crack propagation along the grain boundaries.

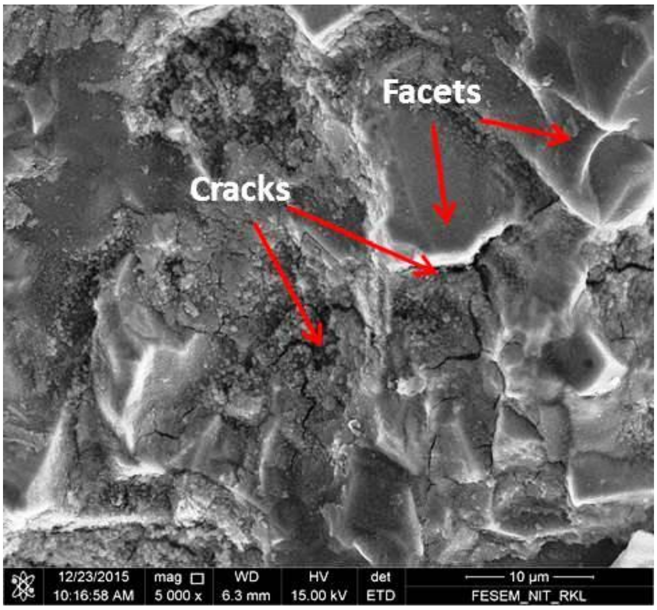

Figure 3.37 FESEM images of fracture surfaces of broken 5 wt. % Al sample after compressive strength test with sintering at 1950 °C.

3.2d.6 Flexural strength

Flexural strength test of conventional sintered SiC-B_4C−Al samples was carried out and result is shown in Figure 3.38. Flexural strength test could not be done for SPS samples as the required dimension (bar shape) for the test was not available. Figure shows that flexural strength of 20 wt. % Al reinforced cermet sample is highest among all the compositions. The flexural strength results shows similar trend like compressive strength values. As conventional sintered samples delivers poor density and hardness, it offers lower flexural strength for all the compositions. Due to relatively higher density and reduced porosity in 10 and 20 wt. % Al cermets, exhibits relatively higher bend strength than that of the SiC-B_4C ceramic composite.

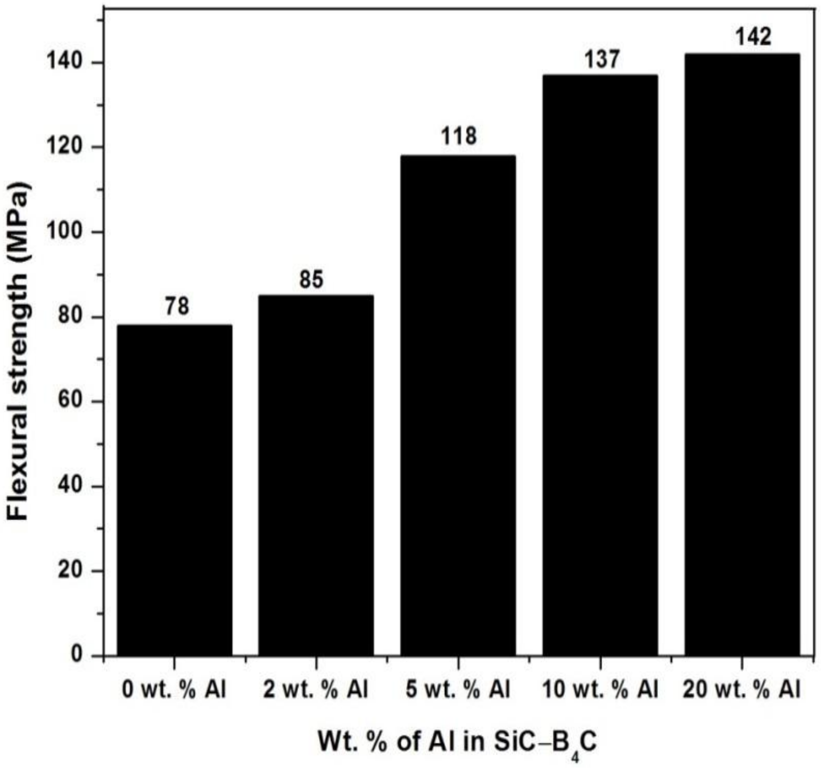

Figure 3.38 Flexural strength results with various compositions of SiC-B_4C−Al sample sintered by conventional sintering.

3.2d.7 Fracture toughness

Figure 3.39 (a–c) shows the schematic diagram and FESEM micrograph of the Vickers indentation mark with crack propagation in 10 wt. % Al cermet for conventional and spark plasma sintered samples. The propagation of crack length is comparatively less in SPS samples compared to conventional sintered samples, as shown in the figure. The increased fracture toughness values for the SPS samples could be explained by stronger bond strength and grain boundaries due to reactions between B_4C-Al phases. It is interesting to note that toughness of the composites increases rapidly as the AlB_{12} content increase [107]. From XRD analysis, higher amount of AlB_{12} phase was found in the SPS samples thereby increasing their toughness compared to the conventionally sintered samples, as shown in Figure 3.28. Table 3.4 and 3.5 shows the indentation fracture toughness of various cermets developed by conventional and SPS methods. The data clearly indicates an increase in indentation fracture toughness value with increase in Al content. For conventional pressure-less sintering, the indentation toughness value increases from 1.21 to 1.87 $MPa.m^{1/2}$ with increasing Al from 2 to 10 wt. %; however, it was found to decrease to 1.66 $MPa.m^{1/2}$ for 20 wt. % Al addition. A similar trend was observed for the SPS samples as well. For SPS samples, the indentation fracture toughness values of 2 wt. % Al increases from 1.23 to 2.19 $MPa.m^{1/2}$ for variation of sintering temperature from 1100 to 1300 °C. The toughness value improves from 2.89 to 3.28 $MPa.m^{1/2}$ with increasing Al from 5 to 10 wt. % and subsequently decreases to 3.19 $MPa.m^{1/2}$ for 20 wt. % Al. The presence of molten Al at high-temperature facilitate liquid phase sintering by flowing liquid Al, through filling pores and reducing porosity, and also by particle rearrangement. The presence of Al leads to crack deflection, branching and bridging. Hence, toughness of the cermet materials improves as shown in Figure 3.38. Internal stresses are developed due to the mismatch of thermal expansion co-efficient of SiC (2.56×10^{-6} / K), Al (22×10^{-6} / K) and B_4C (3.2×10^{-6} / K) resulting in the generation of micro-cracks within the materials. Stresses develop when the compacts cool from high temperature to room temperature after sintering due to the difference in thermal expansion co-efficient between SiC, B_4C, and Al. It leads to lower fracture toughness for the samples sintered conventionally at various temperatures [101]. The combined actions of pressure and thermal activation of powder particles under vacuum during SPS yield higher toughness values as compared to conventional sintering [112].

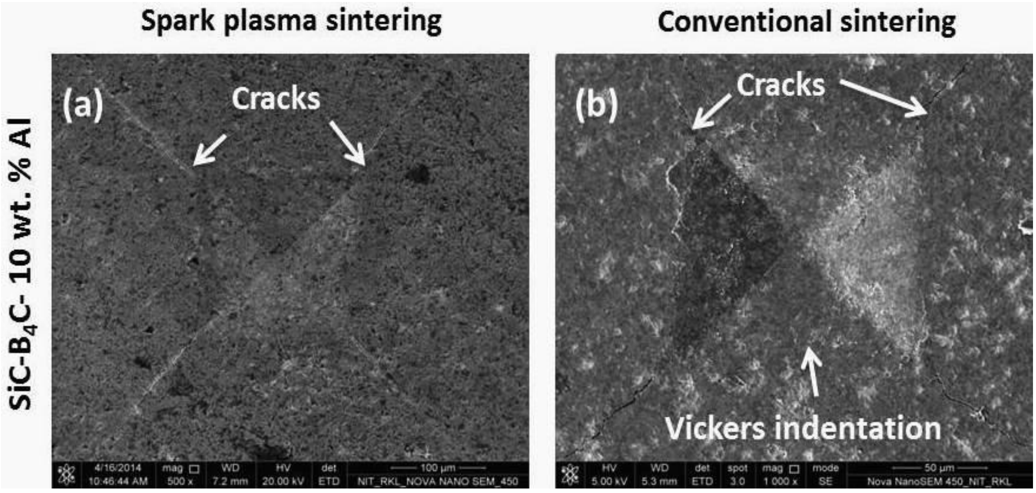

Figure 3.39 Vickers indentation mark and crack propagation of 10 wt. % Al samples sintered by (a) SPS and (b) conventional sintering.

Figure 3.40 shows the FESEM micrograph of crack propagation on the sample surface by Vickers indentation method. In general, cracks generated in pure ceramic materials are deflection free and straight. While in SiC-B_4C–Al cermets the cracks are wavy in nature and deflected due to the presence of SiC and re-solidified Al [63]. Hence, strong interfacial bonding for these SiC-B_4C–Al cermets was achieved by liquid phase sintering. As seen from the circle in Figure 3.40, when a crack propagates through different phases, deflection of cracks occurs.

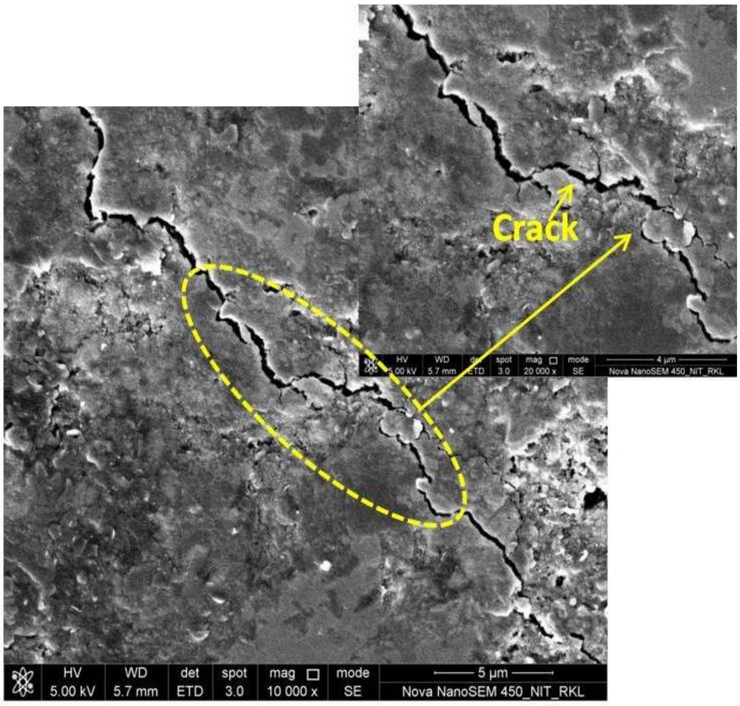

Figure 3.40 Crack path produced by Vickers indentation on the 10 wt. % Al sample surface.

Table 3.4 *Physical and mechanical properties of SiC-B$_4$C–2 wt. % Al ceramic composite fabricated by conventional sintering and spark plasma sintering at different temperatures.*

Properties	**SiC-B$_4$C–2 wt. % Al**			
	Conventional pressure-less sintering	**Spark plasma sintering**		
	1950°C	***1100°C***	***1200°C***	***1300°C***
Density (%)	87	92.7	93.2	95.7
Micro hardness (GPa)	11±2.79	12±2.98	14±2.12	15±1.83
Fracture toughness (MPa.m$^{1/2}$)	1.21	1.23	1.8	2.19
Compressive strength (MPa)	284	-	-	-
Flexural strength (MPa)	85	-	-	-

Table 3.5 *Physical and mechanical properties of 5, 10, and 20 wt. % Al contents in SiC-B$_4$C based cermets prepared by conventional sintering and spark plasma sintering methods*

Sample	**Conventional pressure-less sintering**					**Spark plasma sintering**		
	1950 °C					***1300 °C***		
	ρ [a] (%)	*M H [b] (GPa)*	*F T [c] (MPa m$^{1/2}$)*	*C S [d] (MPa)*	*F S [e] (MPa)*	*ρ [a] (%)*	*M H [b] (GPa)*	*F T [c] (MPam$^{1/2}$*
SiC$_{60}$(B$_4$C)$_{35}$Al$_5$	87	15±3.04	1.27	420	118	96	18±2.66	2.89
SiC$_{60}$(B$_4$C)$_{30}$Al$_{10}$	90	17±2.18	1.87	497	137	97	23±2.29	3.28
SiC$_{60}$(B$_4$C)$_{20}$Al$_{20}$	89	14±1.59	1.66	512	142	96	19±2.23	3.19

a. Relative density (ρ) b. Microhardness (MH) c. Fracture toughness (FT) d. Compressive strength (CS) e. Flexural strength (FS)

3.2e Summary

- Mechanically milled SiC-B$_4$C ceramic composite, SiC-B$_4$C–Si and SiC-B$_4$C–Al cermets with various compositions were successfully fabricated by conventional sintering and SPS methods. Higher density, microhardness, indentation fracture toughness, and compressive strength values were achieved for all the compositions consolidated by SPS than conventional sintering.

- Sintered density was increased by 1–4% with increasing sintering temperature from 1500 to 1600 °C for SiC-B_4C ceramic composite. Microhardness, indentation fracture toughness and compressive strength values of SiC-B_4C sample sintered by SPS at 1600 °C were found to be 27±2.11 GPa, 1.87 MPa $m^{1/2}$ and 449 MPa respectively.

- For SiC-B_4C–Si cermet samples, the highest physical and mechanical properties were obtained for 10 wt. % Si added composition consolidated by conventional sintering and SPS methods.

- The highest density of 92% and 98% are obtained for the composition containing 10 wt. % Si fabricated by conventional sintering at 1950 °C and SPS at 1350 °C respectively.

- With increasing the Si content from 5 to 10 wt. %, the density and the hardness value increases. Increase of Si content to 20 wt. %, the hardness of the cermet decreases due to the existence of large amount of residual Si and increase of the SiC phase in the composition.

- The microhardness, indentation fracture toughness and compressive strength of the SiC-B_4C–10 wt. % Si composition fabricated by SPS were 28±2.12 GPa, 3.8 MPa $m^{1/2}$ and 1387 MPa respectively, which is higher than the conventional sintered samples of same composition.

- Fractography study revealed mixed path of fracture (intergranular and transgranular) in SiC-B_4C–Si cermet samples.

- For SiC-B_4C–Al cermet samples, better physical and mechanical properties were obtained for 10 wt. % Al added composition for SPS as well as conventional sintering.

- XRD analysis confirmed the presence of $Al_8B_4C_7$ and AlB_{12} phases for SPS and conventional sintered samples and better toughness to the cermet samples are noticed.

- The maximum relative density, microhardness and indentation fracture toughness of SiC-B_4C–10 wt. % Al consolidated by SPS are 97%, 23±2.29 GPa and 3.28 MPa.$m^{1/2}$, respectively.

Chapter- 4

Un-lubricated sliding wear behavior and electrical conductivity study of SiC-B_4C, SiC-B_4C–Si and SiC-B_4C–Al cermets prepared by pressure-less sintering and spark plasma sintering methods

4.1 Scope and objectives of the work

Great efforts have been made by the researchers to reduce the wear of engineering materials. It is very important to study the wear properties of SiC-B_4C based cermet materials which are mostly used as abrasive media for grinding and lapping, polishing media for hard materials, wear resistance components as blast nozzles and wheels dressing tools, valve components and bearings, seal rings, and heat engine parts etc. [8, 9, 73, and 113]. During high speed application, heat generated from friction creates problems for metals. Metals get easily wear out and corrode. Improved wear resistance of the SiC-B_4C based ceramic composites can greatly overcome the worn out problem of most of the metals. Ceramic composites or cermets are recommended in a variety of harsh conditions. Chemically inert and high temperature resistant carbide materials are dimensionally and structurally stable for a wide range of temperature variation. Ceramic seal rings are recommended in situations where metal seals and glass seals fail to meet demanding performance. SiC and B_4C based ceramic composites can withstand vibration, high thermal and mechanical shock (generated for aircraft engine parts). Due to high hardness and corrosive resistance of SiC-B_4C based ceramic composites, it can increase the tool life of blast nozzles and water-jet nozzles. Carbides are the ideal materials to improve the cutting tool life compared to metal tools [114–117].

No reports are available till today on wear behaviour study of SiC-B_4C ceramic composites with metallic Si and Al reinforcement as discussed in section 1.2.6 (Literature review). Hence, we have focused un-lubricated sliding wear behavior study of SiC-B_4C–Si and SiC-B_4C–Al cermets fabricated by conventional pressure-less sintering and SPS techniques against a diamond indenter at different loads. The present study is divided into two sections. In the first section, we have discussed un-lubricated sliding wear bahaviour of SiC-B_4C–Si (0, 2, 5, 10, and 20 wt. %) cermets prepared by conventional sintering and SPS methods. The possible wear mechanisms, effects of sintering methods and applied loads on wear rate, volume and morphology of wear debris were investigated. In the second section, a detail study on un-lubricated sliding wear bahaviour of SiC-B_4C–Al (0, 2, 5, 10, and 20 wt. %) cermets prepared by conventional sintering and SPS methods are discussed.

4.2 Un-lubricated sliding wear behaviour study of SiC-B_4C and SiC-B_4C–Si cermet

4.2.1 Wear depth study

The variation of wear depth with sliding time for all the compositions consolidated by conventional sintering and SPS process are shown in Figure 4.1(a–d). The wear depth of the conventional sintered samples tested at 40N applied load is shown in Figure 4.1 (a) and SPS samples tested at 40, 60 and 80N applied load are shown in Figure 4.1 (b–d) respectively. Cermet samples sintered by SPS process possess maximum wear resistance than the conventional sintered samples. This is due to the increased density, hardness and decreased porosity ratios for SPS samples. It is known that wear depth is inversely proportional to the hardness of the materials and cermets with high hardness showed high wear resistance. The wear resistance increases with Si content up to 10 wt. % and minimum wear depth of 72 µm is obtained at 10 wt. % Si when tested at 60N. However, wear resistance decreases with further increase in Si content and maximum wear depth is obtained at 20 wt. %. Wear depth of 188 µm was observed for SiC-B_4C–20 wt. % Si. On the other hand, wear depth of conventional sintered samples containing 0, 2, 5, 10, and 20 wt. % Si tested at 40N applied load is found to be 742, 568, 281, 145, and 377 µm respectively.

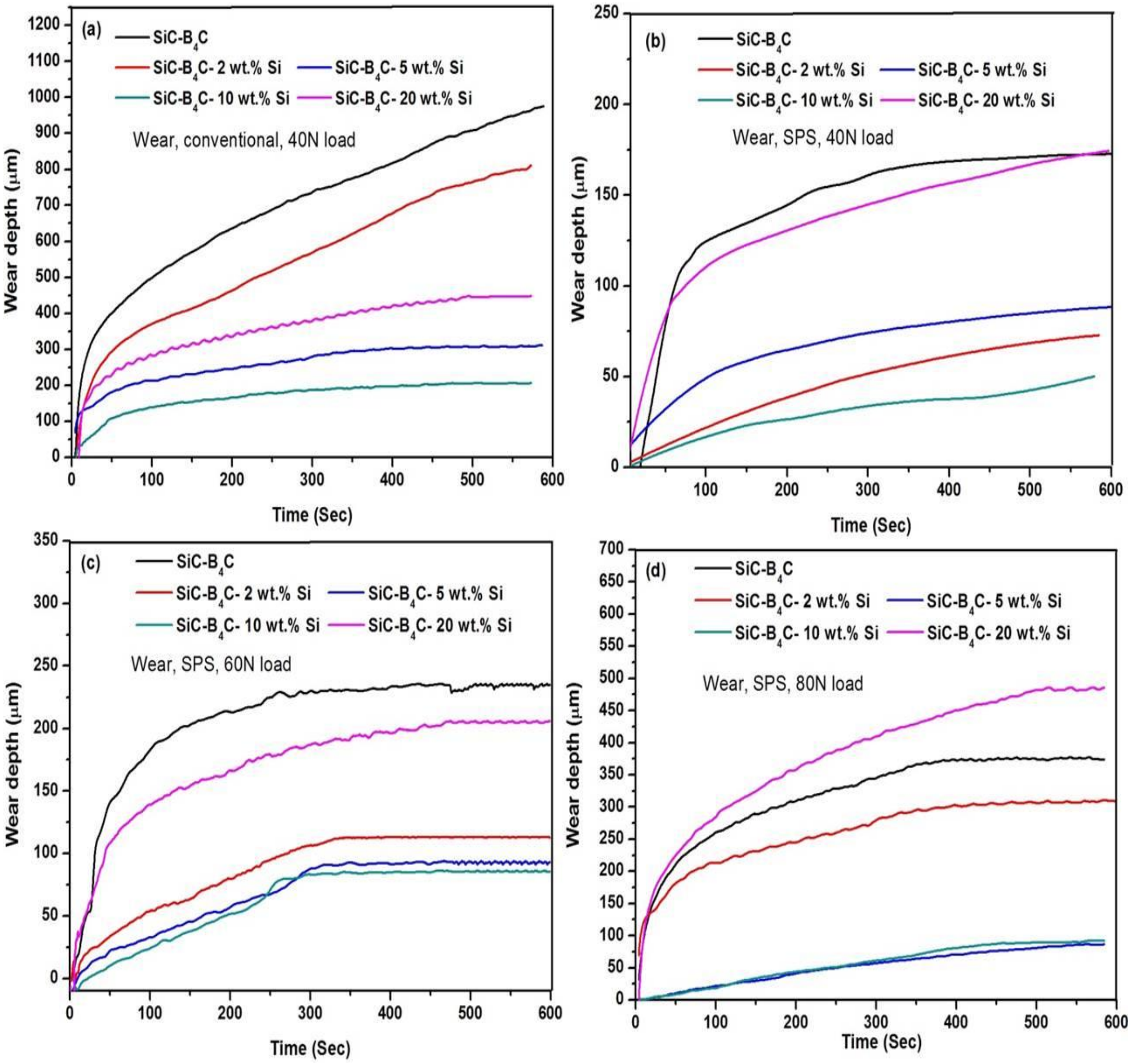

Figure 4.1 (a) Wear depth (µm) vs. sliding time (sec) plot for the conventional sintered samples (1950 °C) of SiC-B_4C–Si cermet at 40N loading condition and (b-d) SiC-B_4C–Si cermet samples consolidated by SPS (1350 °C) and tested at 40, 60, and 80N loading condition.

Figure 4.2 shows a typical depth profile of the worn region of the sample containing 10 wt. % of Si observed by stylus surface profilometer. Here, a diamond stylus is moved vertically in contact with sample and moved laterally across the sample for a specified distance and contact force. The stylus tracking force was fixed to 1mg. The wear depth value of conventional sintered sample containing 10 wt. % Si measured from surface profilometer is 128 µm (Figure 4.2 (a)). This value is in good agreement with the wear depth measured from graph of wear depth vs. sliding time as shown in Figure 4.1 (a). From surface profilometer study, the wear depth of sample containing 10 wt. % Si consolidated by SPS is found to be around 68 µm tested at 80N applied load as shown in Figure 4.2 (b).

This value is also corroborated the wear depth vs. sliding time plot (Figure 4.1 (d)) which shows wear depth of 70 µm for the same composition.

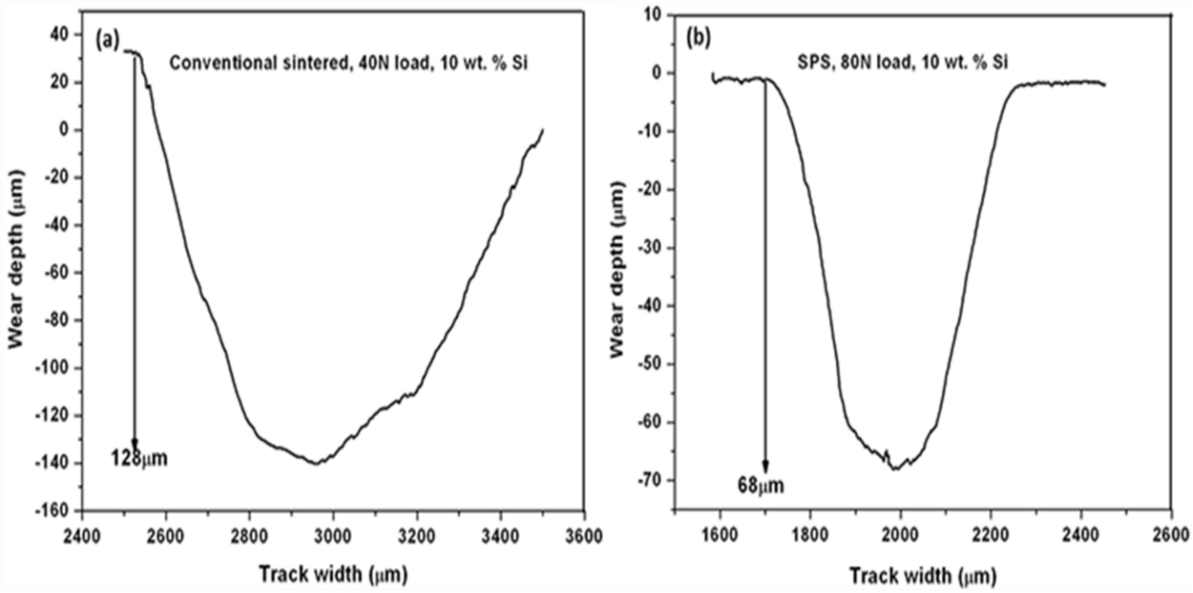

Figure 4.2 Surface profilometer data of depth of the worn region of (a) conventional sintered sample containing 10 wt. % Si using 40N applied load and (b) SPS sample using 80N applied load.

Figure 4.3 represents the wear track width of cermets consolidated by SPS method and wear test conducted at 60N applied load. It has been observed from the micrographs that track width gradually decreases with increasing Si content up to 10 wt. %. However, a higher track width of 817 µm was observed for 20 wt. % Si. In comparison, a minimum wear track width of 492 µm was achieved for the cermet containing 10 wt. % Si. The reason is increasing trend of hardness of cermets with Si (up to 10 wt. %) but decreasing trend of hardness at 20 wt. % Si. It has to be mentioned here that wear track width obtained from SEM micrographs (Figure 4.3) also support the trend obtained from wear depth in Figure 4.1 (c).

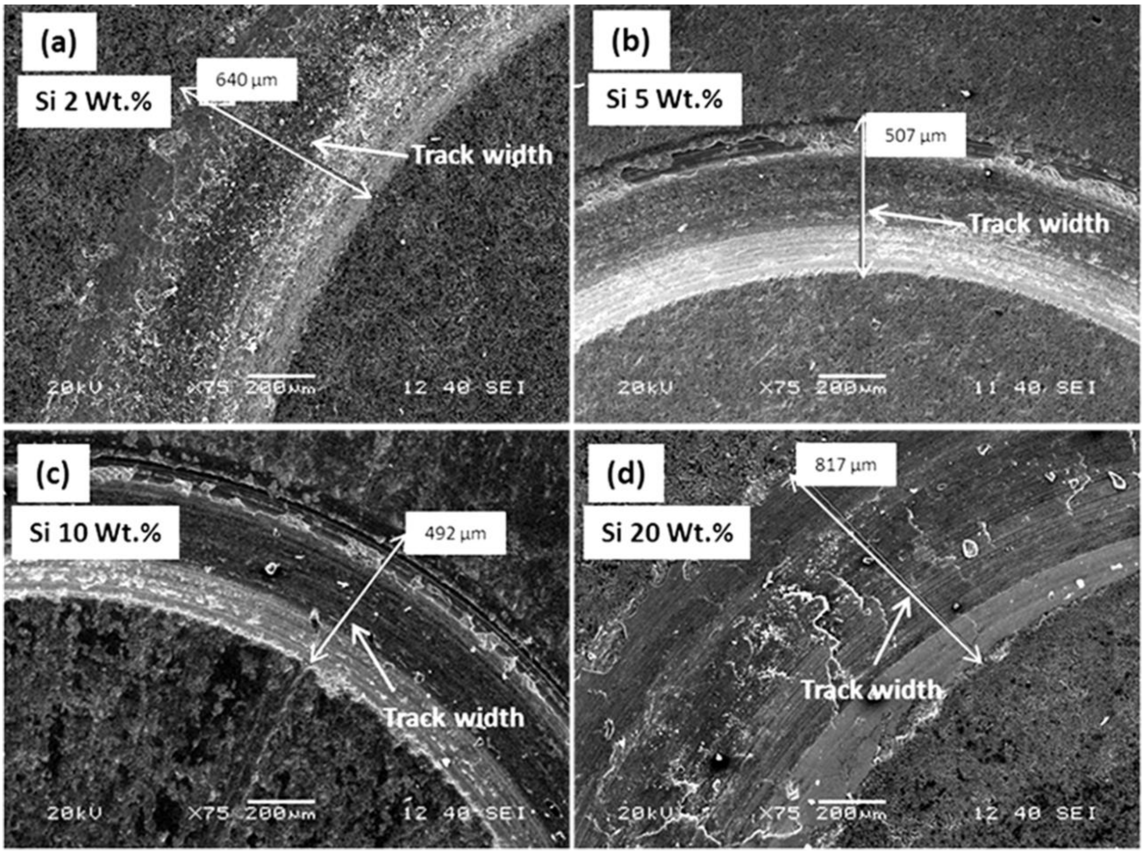

Figure 4.3 SEM micrographs of the SPS sintered samples at 60N applied load showing the value of wear track width for all the cermet samples.

4.2.2 Effect of Si content on wear behaviour

Figure 4.4 (a–d) represents the SEM images of worn surface of SPS samples containing 2, 5, 10, and 20 wt. % Si tested at 60N applied load. In Figure 4.4 (a), the magnified image of wear track is shown for 2 wt. % Si sample, which illustrates the existence of micro cracks on the surface of the wear track under the applied load of 60N. The surface cracks are believed to be caused by surface fatigue. This is called as fatigue cracks on the inter-granular boundaries which are followed by removal of carbide grains from the matrix [118]. However, with increasing Si content, such cracks are not visible (Figure 4.4 b–d). Wear loss is higher for 20 wt. % Si addition. Large amount of wear debris produced on the contact surface creates a film like structure on the contact surface due to the friction among the sample disk, wear debris and the diamond indenter as shown in Figure 4.4 (d).

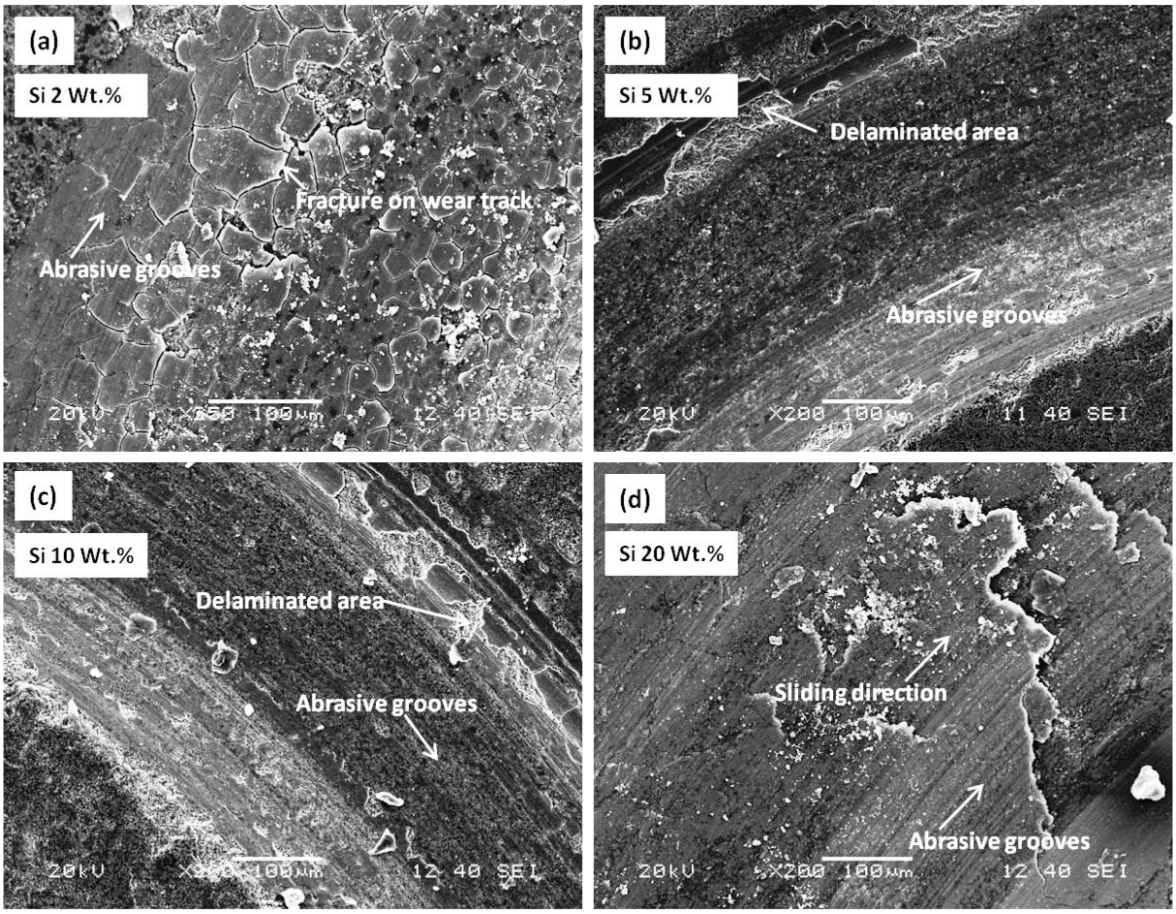

Figure 4.4 SEM micrographs of worn surfaces of SPS samples of 2, 5, 10, and 20 wt. % Si compositions after wear test at 60N load.

The wear phenomenon for the conventional pressure-less sintered samples is shown in Figure 4.5. Poor physical and mechanical properties of conventional sintered samples show poor wear resistance. Even at 40N applied load, wear is more severe compared to SPS samples, which results in production of large amount of wear debris, create deeper abrasive grooves, and delaminated area as shown in the micrographs. Ultrafine debris formed on the contact surface is responsible for the formation of friction films as shown in Figure 4.5.

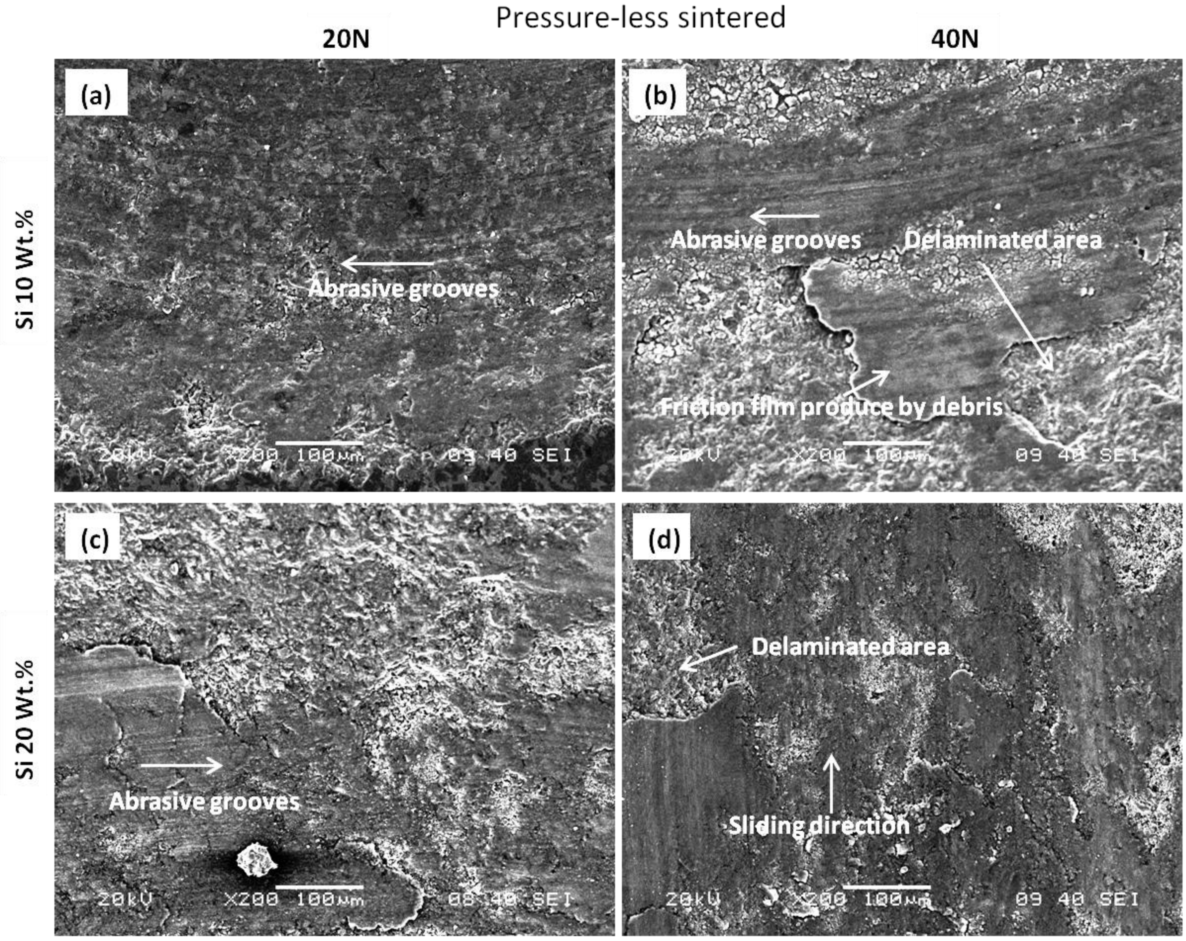

Figure 4.5 SEM micrographs of the conventional sintered samples of 10 and 20 wt. % Si compositions showing the wear behaviour.

4.2.3 Effect of load on a composition

Figure 4.6 shows the SEM micrographs of worn surfaces of sample containing 10 wt. % Si consolidated by SPS method and tested at various loads. It has been found that, mild abrasive wear was dominant with parallel grooves under the range of 20 to 40N load but severe wear with deeper abrasive grooves was observed for 60 and 80N applied load for SPS samples due to higher frictional force (Figure 4.6). From the SEM microstructures of the worn surface it is found that worn surface represents the abrasive wear mark along the sliding direction with ploughing mode (abrasive grooves). The degree of ploughing (grooves) depends on the strength of the materials. Stronger materials have lower ploughing mode of impression. It also depends on the amount of applied load, as load increases the grooves formed are also deeper as shown in Figure 4.6.

The impact of wear is comparatively less for Si 10 wt. % composition under repeated loading condition than other compositions. This is due to the higher hardness value of 10 wt. % Si sample. The track width for Si 2, 5, and 20 wt. % was higher which represents the more amount of materials removal from the surface for Si 2, 5, and 20 wt. % compositions.

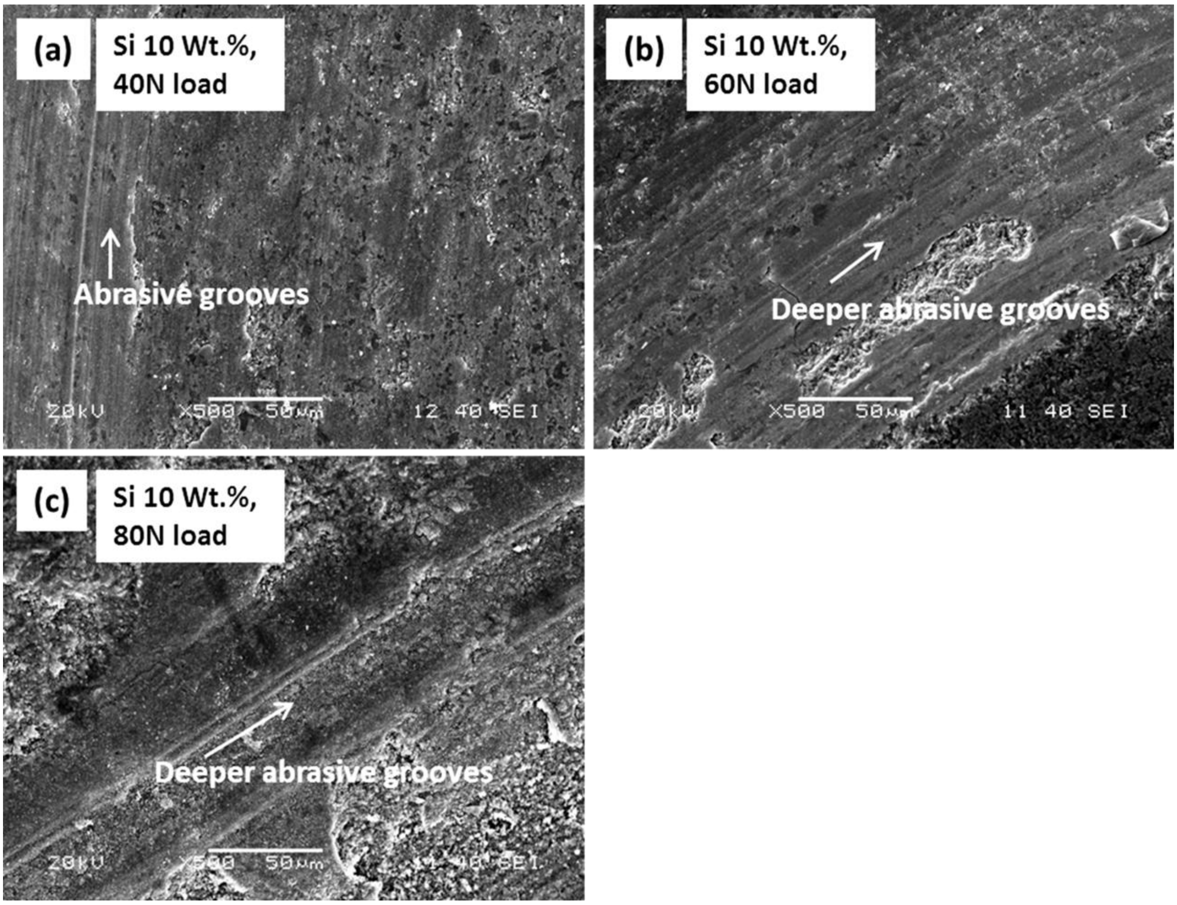

Figure 4.6 SEM micrographs of worn surfaces of sample containing 10 wt. % Si consolidated by SPS method and tested at 40, 60 and 80N applied load showing abrasive grooves.

4.2.4 Wear mechanism

The wear response of the material is influenced by some operating conditions i.e. normal load, sliding speed, temperature and environment. It also depends on the material conditions like hardness, microstructure, strength, surface finish, and fracture toughness. The fundamental wear mechanisms for surface damage in sliding contacts are mainly governed by surface fatigue, abrasion, adhesion and tribo-reaction. Figure 4.7 shows the schematic diagram of the possible wear mechanisms involved for the SiC-B_4C based ceramic composite. Wear resistance of the SiC-B_4C composite is mainly related to the hardness of the SiC and B_4C ceramics and the strength of the composites. For SiC-B_4C–10 wt. % Si sample, the SiC, B_4C and Si bear the major applied loads; thus, increase the abrasive and adhesive resistance of the cermets.

Porosity level reduced from 8% to 3% as sintering route changed from conventional sintering to SPS. The maximum pore size appears to be ≤ 1μm in diameter for the cermet processed at 1350 °C for SPS samples. Higher density with negligible porosity was observed in SPS samples with 10 wt. % Si and 10 wt. % Al added SiC-B_4C cermet. Highest porosity of 11% was obtained for conventional sintered and 6% was obtained for spark plasma sintered SiC-B_4C ceramic composite respectively, and showed highest wear depth (lowest wear resistance) and lowest wear rate. SiC-B_4C cermet showed wear depth of 742 µm and 162 µm for conventional sintered and SPS sample at 40N applied load. Whereas, 10 wt. % Si added sample showed wear depth of 145 µm and 33 µm for conventional sintered and SPS sample at 40N applied load. With increasing Si (2, 5, 10, 20 wt. %) in SiC-B_4C cermet as porosity level reduces and density increases; wear resistance and wear rate gradually increased. During wear test, the stress intensity is particularly high at irregular sharp corners of pores. Thus, the pore acts as a source of crack when the normal compressive load is applied during the wear test causing a transverse shear force to be imposed around pore. The stress intensity at these corners increases with an increasing applied load. Because of that, the area surrounding the pore becomes increasingly failure-prone with the increase in the applied load. The nearly dense 10 wt. % Si sample represents the true wear behaviour with minimum pore.

At higher applied load, cermet with high Si content, materials transfer from one contacting surface to another. As the load increases, the contact force between the sample disk and the diamond indenter pin increases. When the applied load increases from 40 to 80N, it produces stresses higher than the fracture resistance of the SiC and B_4C due to their brittle nature. As a result, these materials loss their ability to support the load and pulling out of SiC and B_4C particles in the form of worn materials are observed. The pulled out fragment particles entrap between the composite sample disc and the friction material pin and hence third-body abrasion come into picture. It produces abrasive grooves on the worn particle surface and the friction materials. Under high pressure, the ultrafine debris produces the friction film on the contact surface. At higher load, surface delamination occurred by the removal of the friction film which causes crack formation on the contact surface. Continuous wear give rise to crack nucleation and propagation in the sample disk and wear debris detached from the contact sample surface. In addition to this, due to the abrasive action of pulled out hard carbide particles, microgrooves are formed on the surface of the material as shown in Figure 4.4.

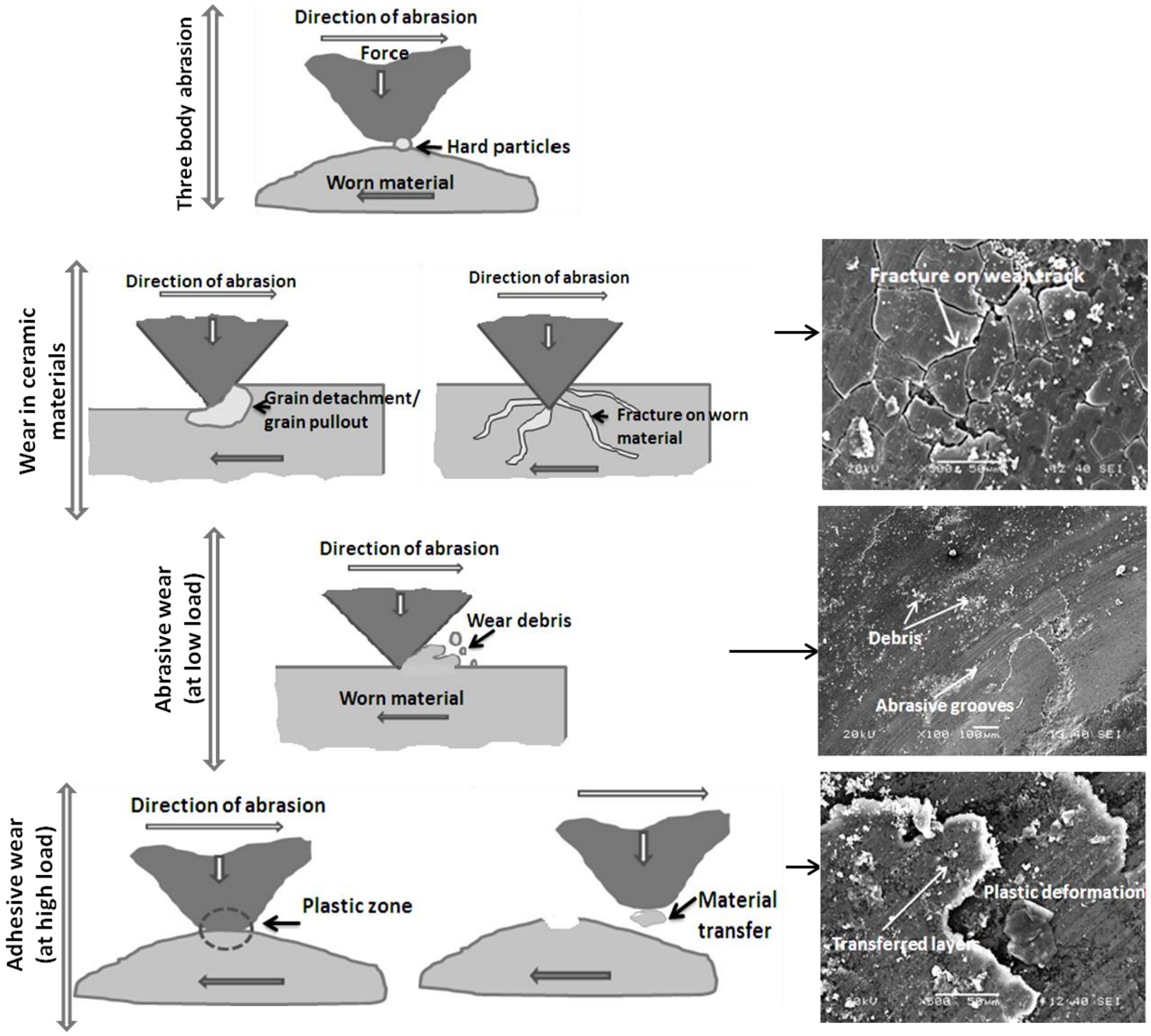

Figure 4.7 Schematic diagram of various wear mechanisms involved in SiC-B_4C based ceramic composites.

4.2.5 Effects of load and composition on wear rate

Figure 4.8 (a) and (b) shows the variation of wear rate for conventional pressure-less sintered samples and SPS samples respectively. It is observed that wear rate is higher for the SiC-B_4C ceramic composite (without Si content) and SiC-B_4C–20 wt. % Si cermets for all the loading conditions. The lowest wear rate was calculated for SiC-B_4C–10 wt. % Si composition. It is also observed in Figure 4.8 that, wear rate increases with increasing applied load from 20 to 80N for SPS samples and 20 to 40N for conventional sintered samples. The wear rate is higher for the conventional sintered samples than the SPS samples. In the present study, the SiC-B_4C ceramic have poor bond strength and low hardness compared to SiC-B_4C–Si cermets due to solid state sintering. On the other hand, higher hardness and density is achieved for SiC-B_4C–Si cermet due to wetting of SiC and

B_4C by molten Si during liquid state sintering. It prevents abrasion between the contact surfaces and hence reduces the amount of wear. Highest wear rate was obtained for 20 wt. % Si sample for the maximum load applied to conventional sintered as well as SPS samples. In 20 wt. % Si sample, the material properties deteriorate due to the formation of residual Si phases [119]. The presence of residual Si in the 20 wt. % Si sample is unable to bear the excessive load and increased the wear rate with increasing applied load.

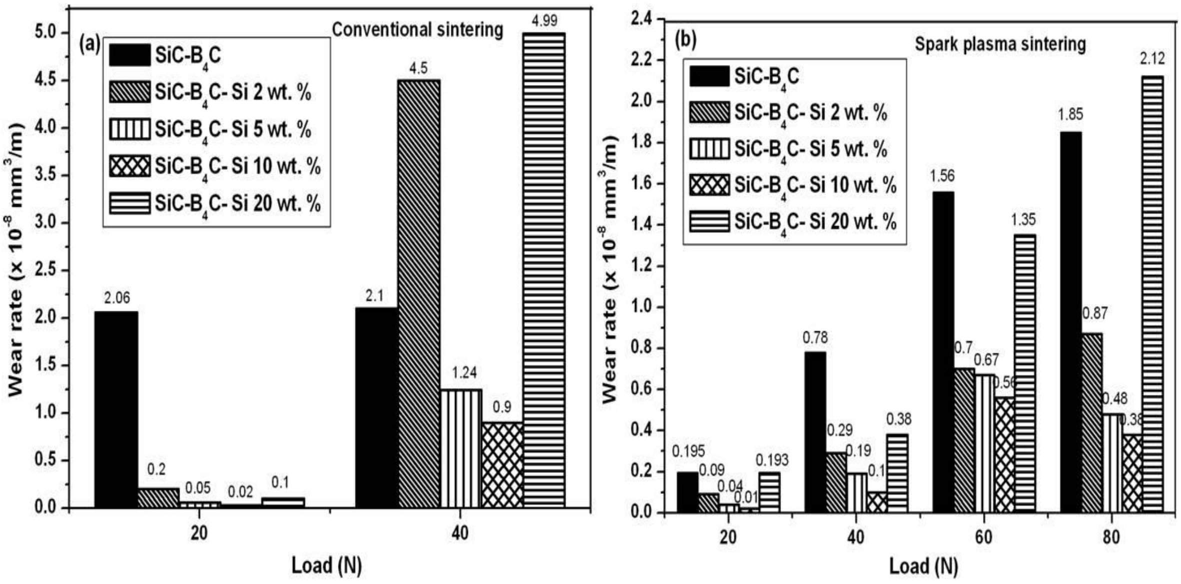

Figure 4.8 Effect of applied load on wear rate of all the (a) conventional sintered and (b) SPS of SiC-B_4C–Si cermet samples.

4.2.6 Microstructure of worn surface and volume of the wear debris

Figure 4.9 (a–d) represents SEM micrographs of wear debris of SPS samples containing 10 wt. % Si tested at 20, 40, 60, and 80N applied load respectively. At low load, the wear debris produced is in the form of small particles but the particles are compacted and form flakes at higher loads. The small particle shape wear debris is evident at 20N loads. On the other hand, at 40, 60 and 80N loads the morphology of debris changes from particle shape to flake shape. It should be mentioned here that SiC and B_4C particles are hard and brittle. Application of higher amount of loads (60 and 80N) fractures the particles. These fracture particles are cold welded with soft Si metal and form laminates at higher load.

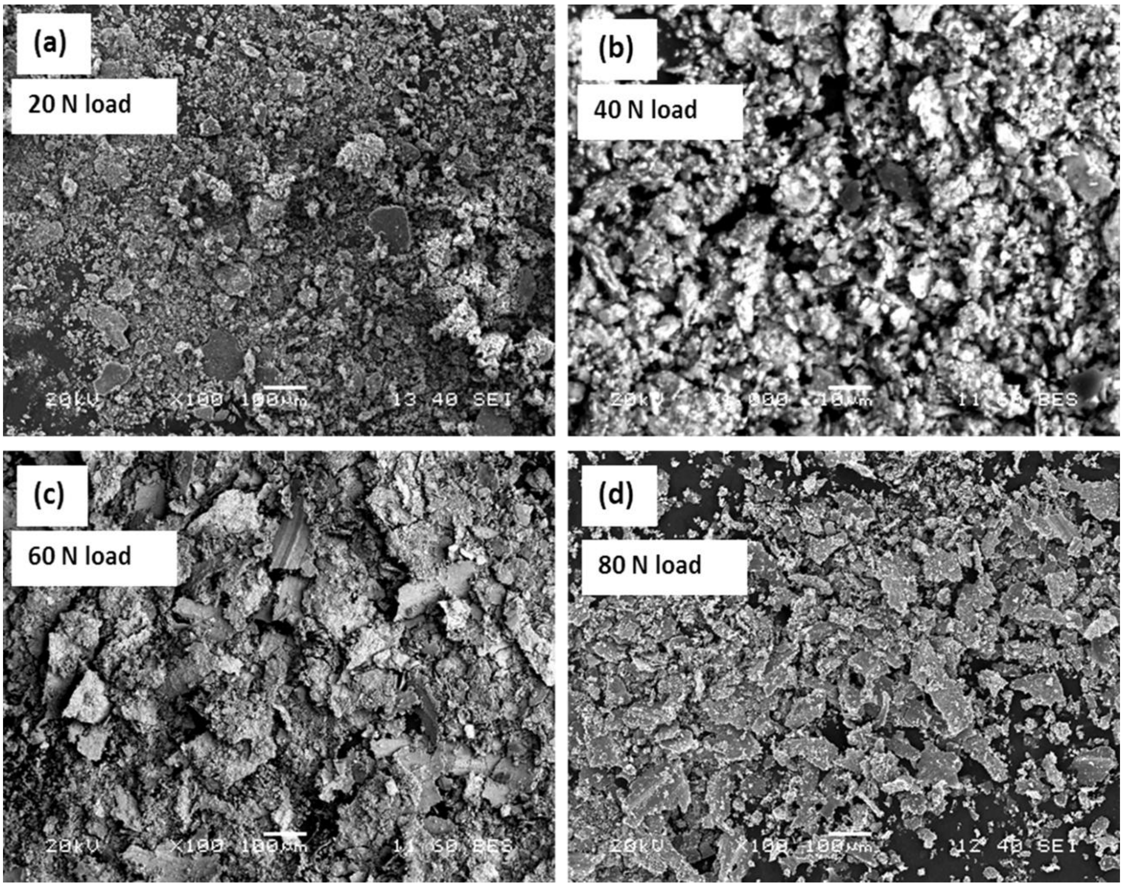

Figure 4.9 (a–d) SEM images of wear debris of SPS samples containing 10 wt. % Si tested at 20, 40, 60, and 80N applied load respectively.

The XRD pattern of wear debris produced by 80N applied load for the cermet containing 20 wt. % Si sintered by SPS process is shown in Figure 4.10. The XRD pattern shows the peaks of SiC and $B_{13}C_2$. Boron carbide can exist as one phase with a large variation in carbon concentrations. The existence of C-B-C chains in $B_{13}C_2$, instead of C-C-C chain in B_4C is the only difference [51, 53, 99]. With increasing sintering temperature, B_4C changes to $B_{13}C_2$ as C eliminates. There is no phase transformation until it reaches the melting point around 2527 °C [100]. It can be deduced that the materials found in the debris completely come from composites. There was no oxidation peaks observed in the wear debris of Si 20 wt. % composition.

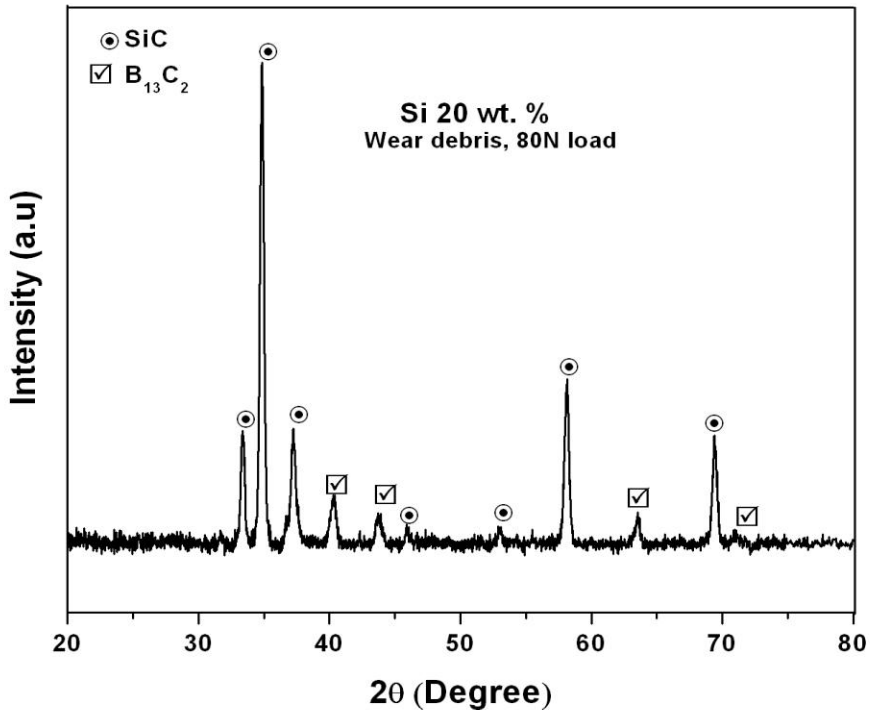

Figure 4.10 XRD analysis of the wear debris produced for Si 20 wt. % sample sintered by SPS process at an applied load of 80N.

Figure 4.11 (a, b) represents the volume of wear debris produced for pressure-less sintered and SPS samples respectively of all the composites at all applied loads. Volume of the wear debris depends upon the hardness of the cermet material; higher the hardness lower will be the volume of wear debris. Volume of wear debris of all the conventional and SPS samples were calculated theoretically using Archard equation as depicted in Table 4.1. The wear depth, wear volume, wear rate produced at different sintering methods and different applied load are tabulated in Table 4.1. Volume of wear loss was also measured experimentally from the weight of wear debris and density of the respective cermet sample as shown in Figure 4.11. Wear study of all the cermet samples at 20N applied load produce less wear debris than the cermet samples at 40, 60, and 80N applied load. From the figure it is confirmed that the volume of the wear debris increased with the increase in applied from 20 to 40N for conventional sintered samples and 20 to 80N for SPS samples. It is clearly observed that the cermet without Si reinforcement produced high amount of wear debris. It has been found that with increasing Si content from 0 to 10 wt. %, volume of wear debris gradually decreased. But in the case of 20 wt. % Si sample again the volume of wear debris increased. Volume of wear debris is lowest for the SiC-B_4C–10 wt. % Si sample sintered by conventional sintered as well as SPS methods. In case of conventional sintered sample containing 10 wt. % Si, the volume of wear debris was increases from 0.07

x 10^{-6} mm^3 to 3.4 x 10^{-6} mm^3 when applied load increases from 20 to 40N. Wear volume increases from 0.39 x 10^{-6} mm^3 to 10.2 x 10^{-6} mm^3 with increase in applied load from 20 to 40N for 20 wt. % Si sample. Wear loss was highest for SiC-B_4C sample (18.5 x 10^{-6} mm^3) at 40N applied load. Similarly, highest wear loss was obtained for SPS samples at maximum applied load of 80N. At 40N applied load, wear loss was 0.3 x 10^{-6} mm^3 for 10 wt. % Si. But at 80N loads, wear loss for 10 wt. % Si was found to be 1.4 x 10^{-6} mm^3.

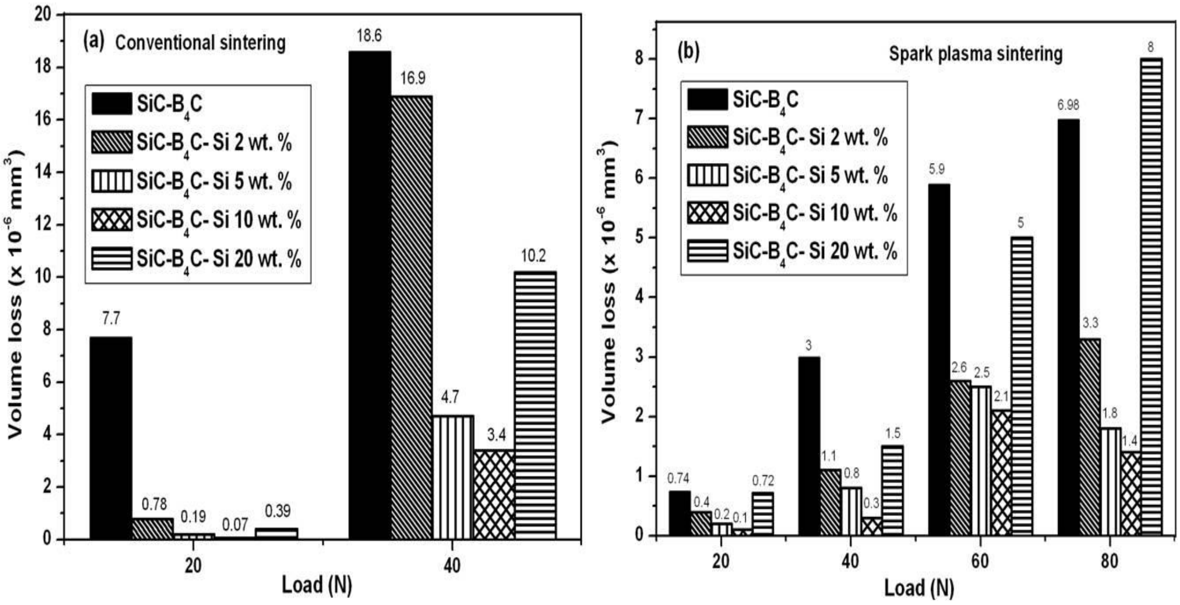

Figure 4.11 Bar diagram showing volume loss vs. applied load of (a) conventional sintered samples and (b) SPS samples.

Table 4.1 *Values of wear depth, wear volume and wear rate at different applied loads for the SPS and conventional sintered SiC-B$_4$C–Si samples.*

Compositions	**Applied load (N)**	**Wear depth (µm)**	**Wear rate (x 10^{-8} mm^3/m)**	**Wear Volume (x 10^{-6} mm^3)**	
				Archard equation	**Experiment**
Spark plasma sintering					
SiC-B$_4$C	20	26 ± 4%	0.195	0.27	0.74
	40	162 ± 3%	0.78	0.54	3
	60	230 ± 4%	1.56	0.8	5.9
	80	373 ± 2%	1.85	1.07	6.98
SiC-B$_4$C–2 wt. % Si	20	19 ± 3%	0.09	0.34	0.4
	40	52 ± 2%	0.29	0.7	1.1
	60	104 ± 3%	0.7	1.02	2.6
	80	306 ± 4%	0.87	1.3	3.3
SiC-B$_4$C–5 wt. % Si	20	10 ± 5%	0.04	0.3	0.2
	40	74 ± 3%	0.19	0.6	0.8
	60	76 ± 4%	0.67	0.92	2.5
	80	69 ± 3%	0.48	1.2	1.8
SiC-B$_4$C–10 wt. % Si	20	5 ± 5%	0.01	0.27	0.1
	40	33 ± 3%	0.1	0.5	0.3
	60	72 ± 3%	0.56	0.8	2.1
	80	70 ± 4%	0.36	1.08	1.4
SiC-B$_4$C–20 wt. % Si	20	18 ± 5%	0.193	0.3	0.72
	40	145 ± 4%	0.38	0.63	1.5
	60	188 ± 4%	1.35	0.94	5
	80	470 ± 3%	2.12	1.26	8
Conventional sintering					
SiC-B$_4$C	20	256 ± 5%	2.06	0.37	7.7
	40	742 ± 4%	2.1	0.75	18.6
SiC-B$_4$C–2 wt. % Si	20	195 ± 6%	0.2	0.5	0.78
	40	568 ± 5%	4.5	1.07	16.9
SiC-B$_4$C–5 wt. % Si	20	121 ± 7%	0.05	0.45	0.19
	40	281 ± 5%	1.24	0.93	4.7
SiC-B$_4$C–10 wt. % Si	20	68 ± 6%	0.02	0.41	0.07
	40	145 ± 5%	0.9	0.83	3.4
SiC-B$_4$C–20 wt. % Si	20	168 ± 5%	0.1	0.5	0.39
	40	377 ± 5%	4.99	1	10.2

4.3 Un-lubricated sliding wear behaviour study of SiC-B_4C–Al cermet

4.3.1 Wear depth study

The variation of wear depth with sliding time for all the SiC-B_4C–Al compositions consolidated by conventional sintering and SPS process are shown in Figure 4.12 (a–d). Figure 4.12 (a) represents the variation of wear depth with sliding time for the conventional sintered samples containing 2, 5, 10, and 20 wt. % Al at 40N applied load. Minimum wear depth of 139 µm was obtained for 10 wt. % Al sample. Figure 4.12 (b–d) depicts the variation of wear depth with sliding time for SPS of all the SiC-B_4C–Al compositions at 40, 60, and 80N applied load respectively. Wear depth value increases with increasing applied load for all the samples as revealed in figure. That indicates resistance of wear decreases as applied load increases from 40 to 80N. For all the applied loads, 10 wt. % Al sample possess lowest wear depth (higher wear resistance) compared to other compositions. Cermet of 2 wt. % Al composition shows highest wear depth (lowest wear resistance). From the FESEM micrograph of Figure 3.31 (e–h) it is confirmed that, large grain size with high porosity level was obtained for the samples consolidated by conventional sintering. With increasing Al content porosity ratio decreases and bond strength increases. For SPS samples, less porosity with high density was obtained as shown in Figure 3.31 (a–d) and Tables (3.4 and 3.5). Al content above 5 wt. % can reduce the average grain size of SiC-B_4C compact due to pinning at the grain boundaries. Better density with high hardness was obtained for 10 wt. % Al sample sintered by SPS method. Therefore, 10 wt. % Al sample shows better wear resistance compared to 2, 5, and 20 wt. % Al samples.

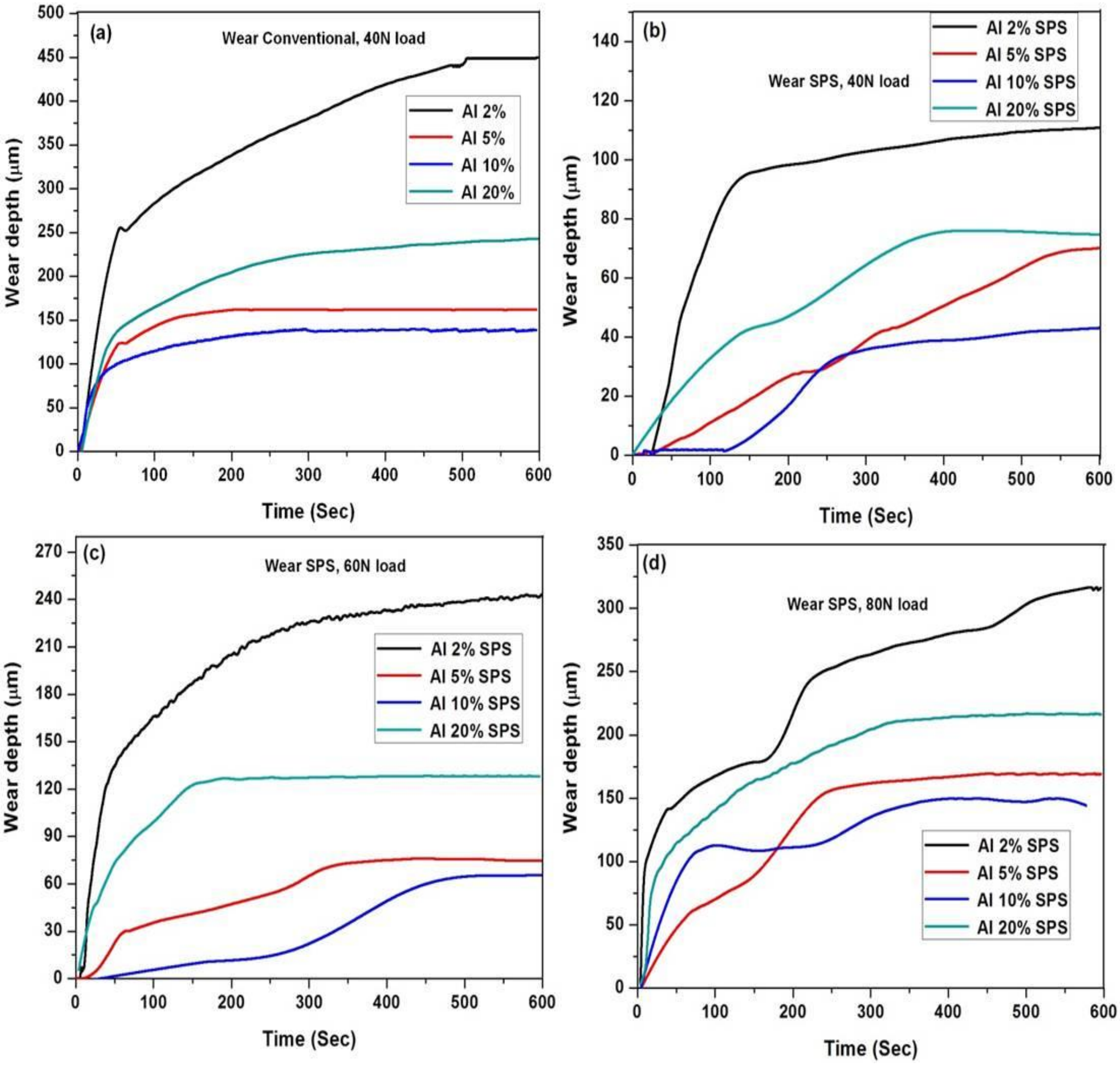

Figure 4.12 (a) Wear depth (μm) vs. sliding time (sec) plot for the conventional sintered (1950 °C) SiC-B_4C–Al samples at 40N applied load and (b-d) SiC-B_4C–Al samples consolidated by SPS (1300 °C) and tested at 40, 60, and 80N applied load.

Figure 4.13 (a–d) shows a typical front view of worn region of 10 wt. % Al added sample sintered by conventional sintering and SPS at various applied load. Wear depth of 10 wt. % Al sample consolidated by conventional sintering at 20 and 40N applied load are depicted in Figure 4.13 (a, b). Wear depth of 81.5 µm and 138 µm were obtained for 20 and 40N applied load respectively. These values are good agreement with the wear depth values measured from graph of wear depth vs. sliding time for 40N applied load as shown in Figure 4.12 (a) and Table 4.2. From the surface profilometer study, the wear depth of 10 wt. % Al sample sintered by SPS method is found to be 39. 4 µm at 40N applied load; whereas the wear depth is around 144.4 µm at 80N applied load as shown in Figure 4.13

(c, d). These wear depths values also support wear depth vs. sliding time plot (Figure 4.12 (a, b, and d)) which shows wear depth of 39 and 144 µm for the same composition at 40 and 80N applied load.

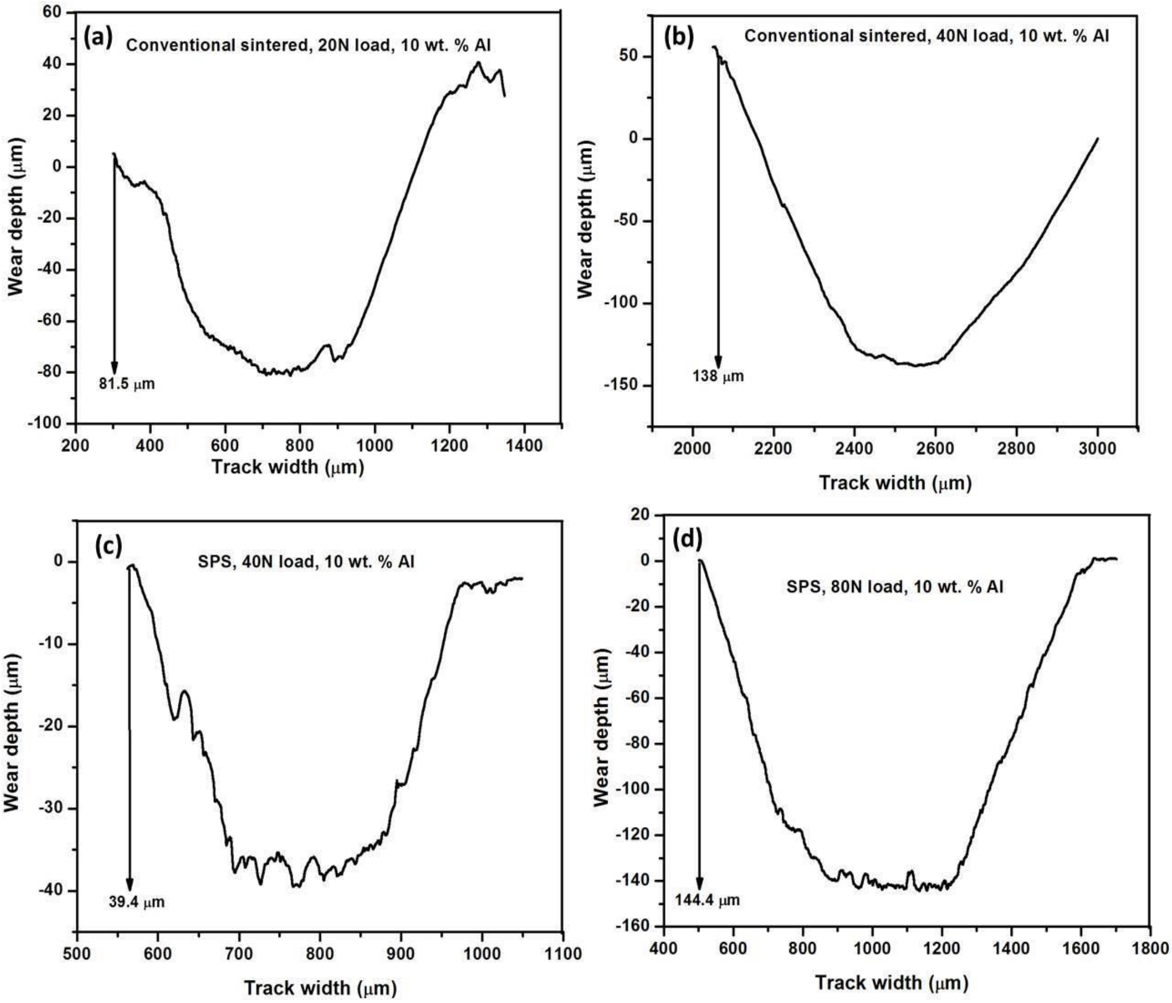

Figure 4.13 Surface profilometer data of depth of the worn region of (a, b) conventional sintered sample containing 10 wt. % Al using 20 and 40N applied load and (c, d) SPS sample using 40 and 80N applied load.

4.3.2 Effect of Al content on wear behaviour

Figure 4.14 (a–d) shows the effect of applied load (80N) on the variation of Al from 2 to 20 wt. % for the cermets sintered by SPS method. It has been observed that wear mechanism varies with the variation in composition. For 2 and 20 wt. % Al content, large numbers of fractures with abrasive grooves are observed at 80N load. At higher applied load, large amount of wear debris is produced on the contact surface. These wear debris get entrapped between the contact sample surface and pin during wear test, and hence produced films or sheets like structures on the contact surface. These cracks nucleate in the continuous contact with the indenter pin and material removes by delamination. As higher density and hardness are obtained for 10 wt. % Al sample, it has better wear resistance compared to other compositions as confirmed in Figures 4.12 and 4.13. Hence, smaller wear depth with less amount of wear debris are produced. Abrasive wear is the main wear mechanism in the sample. Since small amount of wear debris get entrapped into the contact surface, creates less cracks with trivial delaminated areas which confirms the higher wear resistance of 10 wt. % Al content sample. Larger delaminated areas with abrasive grooves confirmed the poor wear resistance (by removal of excess worn materials) in 20 wt. % Al sample.

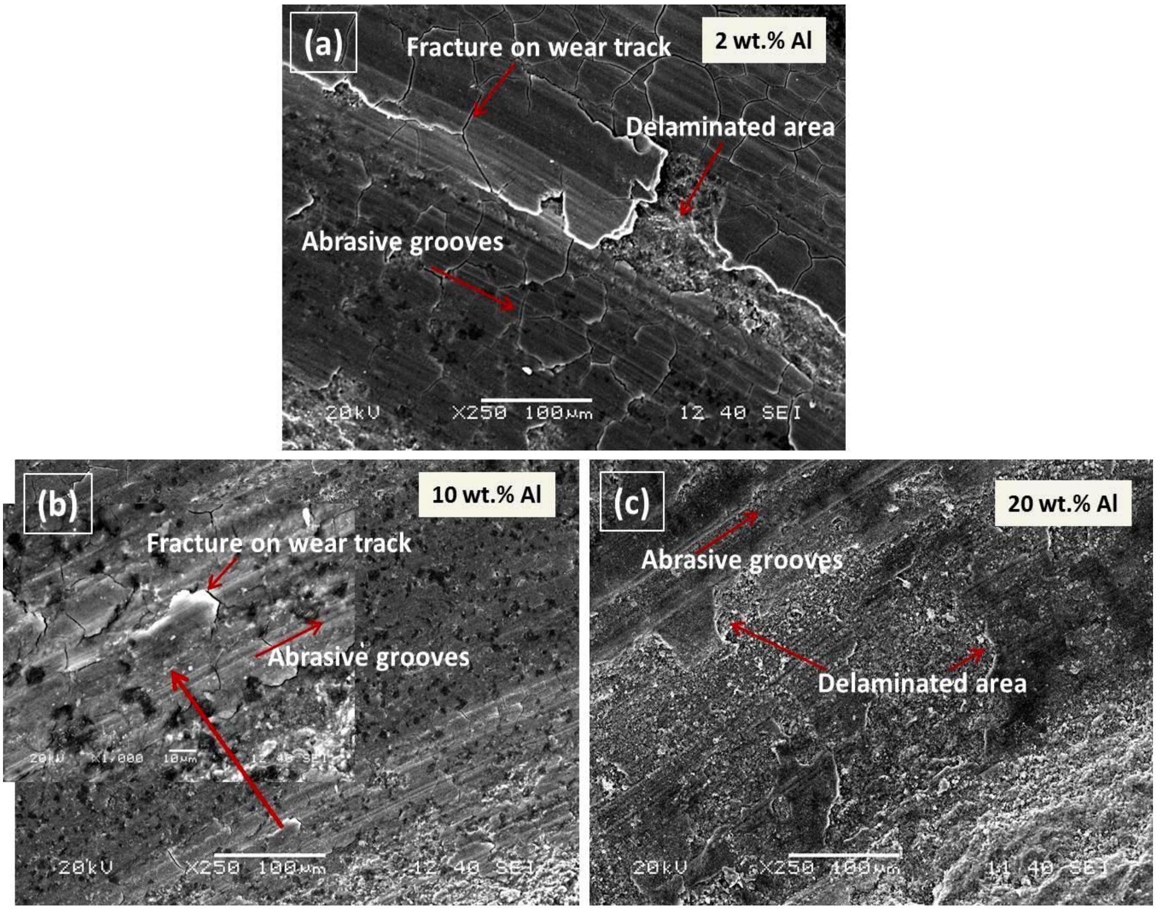

Figure 4.14 SEM micrographs of worn surfaces of SPS samples of 2, 5, 10, and 20 wt. % Al compositions after wear test at 80N applied load.

4.3.3 Effect of load on a composition

It can be observed from the SEM micrographs (Figure 4.15 (a–c)) of the worn surface of 2 wt. % Al sample that, the abrasive grooves are less distinct in 40N applied load. Small cracks on the worn surface are also visible. For 60N applied load, some distinct grooves with obvious cracks on the wear track was observed. Under high pressure, the ultrafine debris produced friction films or sheets on the contact surface. Cracks on the wear surface are originated at various points and propagate along the direction of indenter movement. These nucleated cracks get accumulated at one point which results in the removal of wear debris in the form of films or sheets. Figure 4.15 shows removal of wear debris in the forms of friction films causes delamination on the wear surface at higher applied loads. At the maximum applied load of 80N, the abrasive grooves become deeper and hence relatively more amount of materials removed as revealed in Figure 4.15 (c). The micrograph shows deeper grooves with bigger fracture surface and removal of large amount of materials in the form of bigger delaminated area.

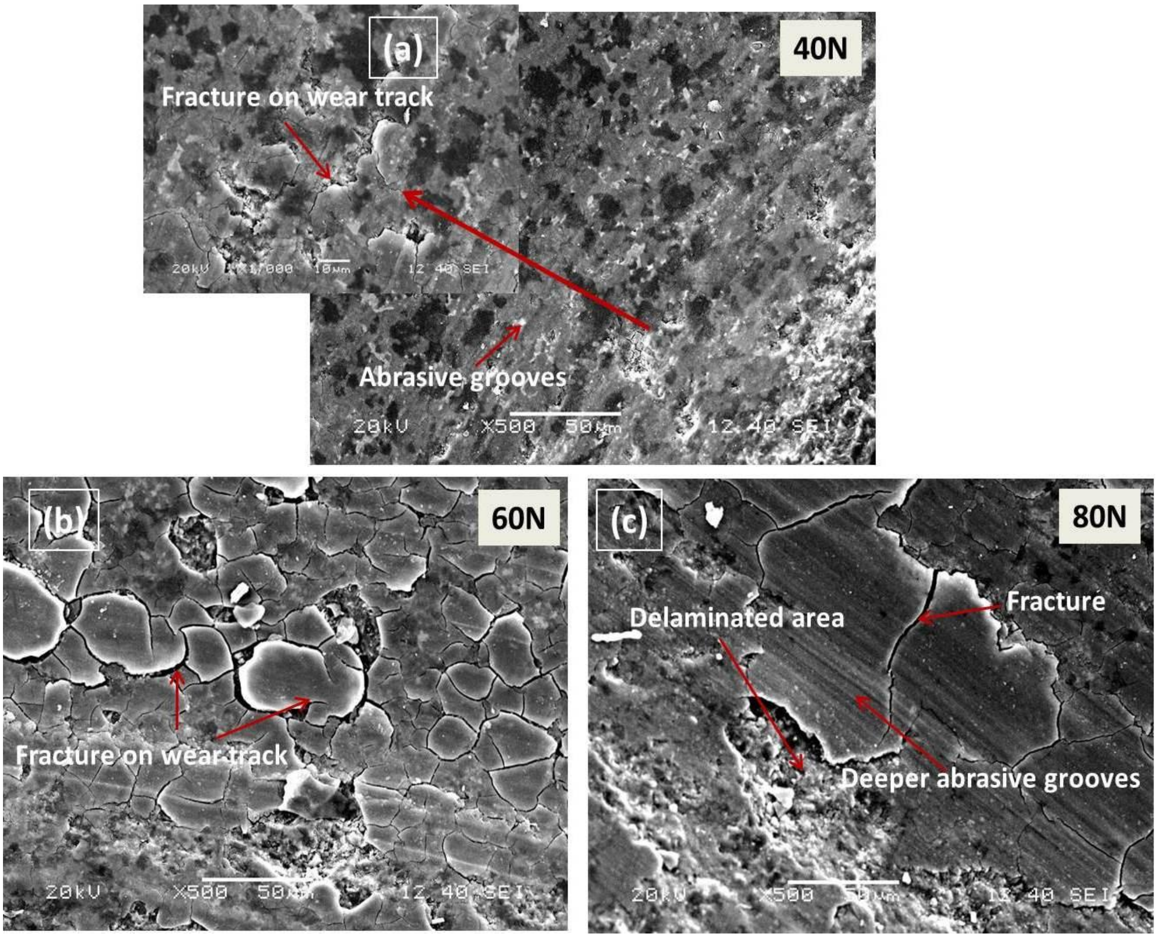

Figure 4.15 SEM micrographs of worn surfaces of sample containing 2 wt. % Al consolidated by SPS method and tested at 40, 60 and 80N applied load.

4.3.4 Effects of load and composition on wear rate

Figure 4.16 (a) and (b) shows the variation of wear rate for conventional sintered and SPS samples as a function of applied load. Wear rate is higher for SiC-B_4C–20 wt. % Al cermets for all the loading conditions. At a load of 80N, the wear rate shows an increasing trend in the bar diagram, which indicates more amount of materials removal from the surface. The micrograph in Figure 4.15 (c) reveals the removal of materials by delamination. Higher hardness and density is achieved for SiC-B_4C–Al cermet due to wetting of SiC and B_4C by molten Al during liquid state sintering. It prevents abrasion between the contact surfaces and hence reduces the amount of wear. The wear depth, wear rate, volume of wear debris obtained from experimental and Archard equation at different sintering methods and different loads are tabulated in Table 4.2.

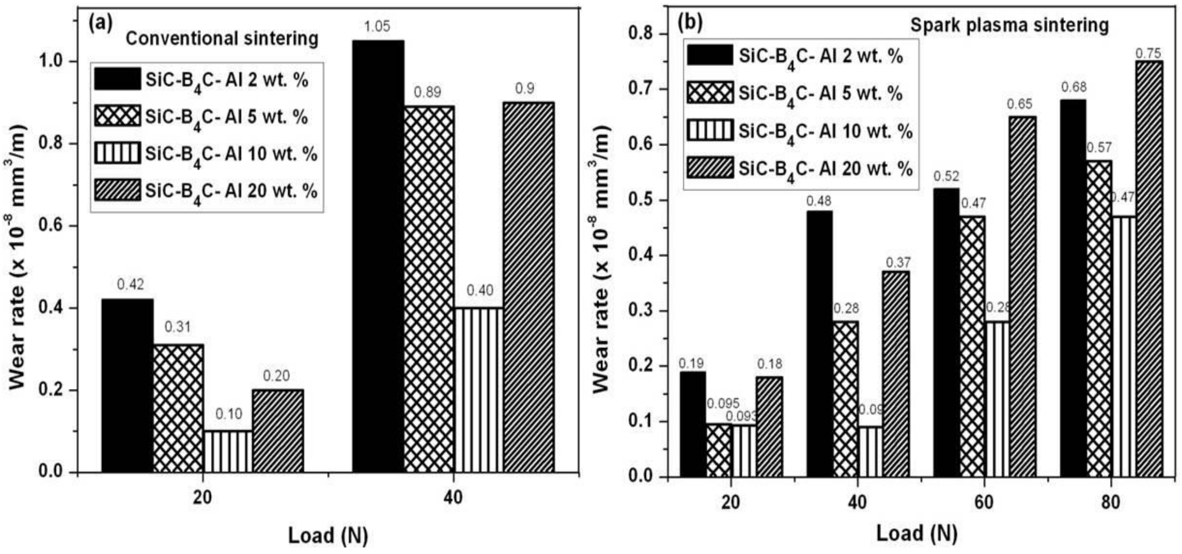

Figure 4.16 Effect of applied load on wear rate of all the (a) conventional sintered and (b) SPS samples.

4.3.5 Microstructure of worn surface and volume of the wear debris

Figure 4.17 (a–d) represents SEM micrographs and EDS spectra of wear debris of SPS samples containing 2, 10 and 20 wt. % Al tested at 80N applied load respectively. EDS spectra in Figure 4.17 (b) reveals the presence of SiC in the wear debris. Boron could not be identified from EDS analysis due to low atomic number. Smaller particle shape of wear debris with maximum surface area was produced for 10 wt. % Al sample. As 10 wt. % Al sample shows high hardness and high wear resistance and hence produced limited amount of wear debris with smaller size. Bigger flake (sheets) shape wear debris was evident for 2 and 20 wt. % Al samples. The delaminated area in the micrograph (Figure 4.14) confirms that, the larger amount of materials removes in the form of wear debris and provides poor wear resistance.

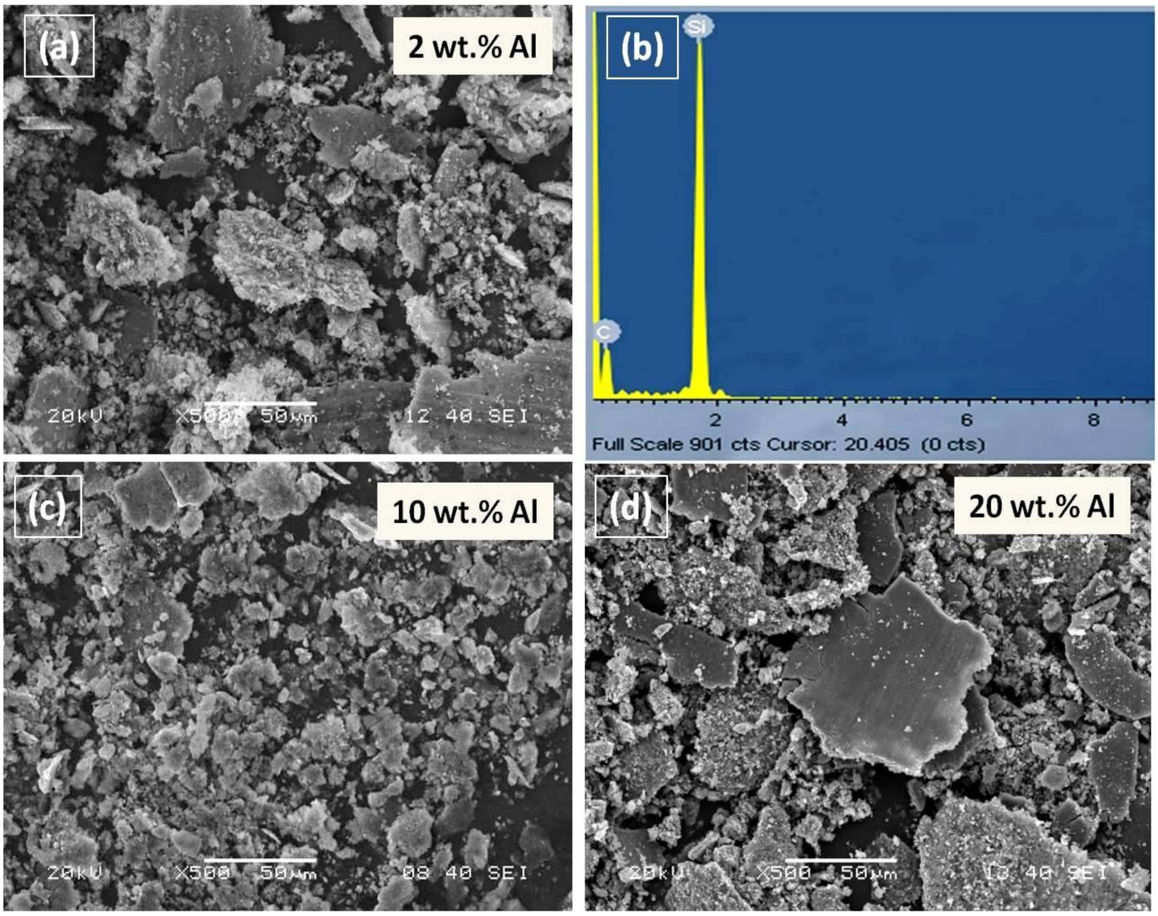

Figure 4.17 (a, c, d) SEM images of wear debris of SPS samples containing 2, 10 and 20 wt. % Al tested at 80N applied load and (b) EDS spectra of wear debris obtained for 10 wt. % Al sample.

Figure 4.18 (a, b) shows the bar diagram of volume of wear debris produced for conventional sintered and SPS samples for the variation of applied load and compositions respectively. Volume of wear loss for SiC-B_4C–Al cermets was measured experimentally from the weight of wear debris and density of the respective cermet sample as shown in Figure 4.18. Volume of wear debris of all the conventional and SPS samples were also calculated theoretically using Archard equation as depicted in Table 4.2. The experimentally produced wear volume follows the linear trend as that of Archard equation. Wear of the material is less at lower applied loads and increases with increasing applied loads. Wear volume increases from 0.38×10^{-6} to 1.52×10^{-6} mm^3 with increases in applied load from 20 to 40N in case of 10 wt. % Al sample consolidated by conventional sintering. Similarly, it increases from 1.58 x 10^{-6} to 3.96 x 10^{-6} mm^3 in case of 2 wt. % Al sample. For SPS sample of 10 wt. % Al composition, wear loss of 0.35 x 10^{-6} and 0.353 x 10^{-6} mm^3 was measured for 20 and 40N applied loads; whereas, it increases from 1.06 x 10^{-6} to 1.76 x 10^{-6} mm^3 for 60 and 80N applied loads. However, wear debris formed is found to be less for SPS samples than the conventional sintered samples. It has been found that 10 wt. % Al sample sintered by SPS and conventional sintering produced less wear debris than the other compositions. Volume of wear debris depends upon the hardness of the materials; higher hardness shows lower volume of wear debris. Hence, SPS samples produced less wear debris due to higher density, hardness and wear resistance compared to conventional sintered samples. Natarajan *et al.* [120] also calculated volume of wear debris of A356/25SiCp aluminium matrix composites using Archard equation and reported that, with increase in applied load volume of wear debris increases.

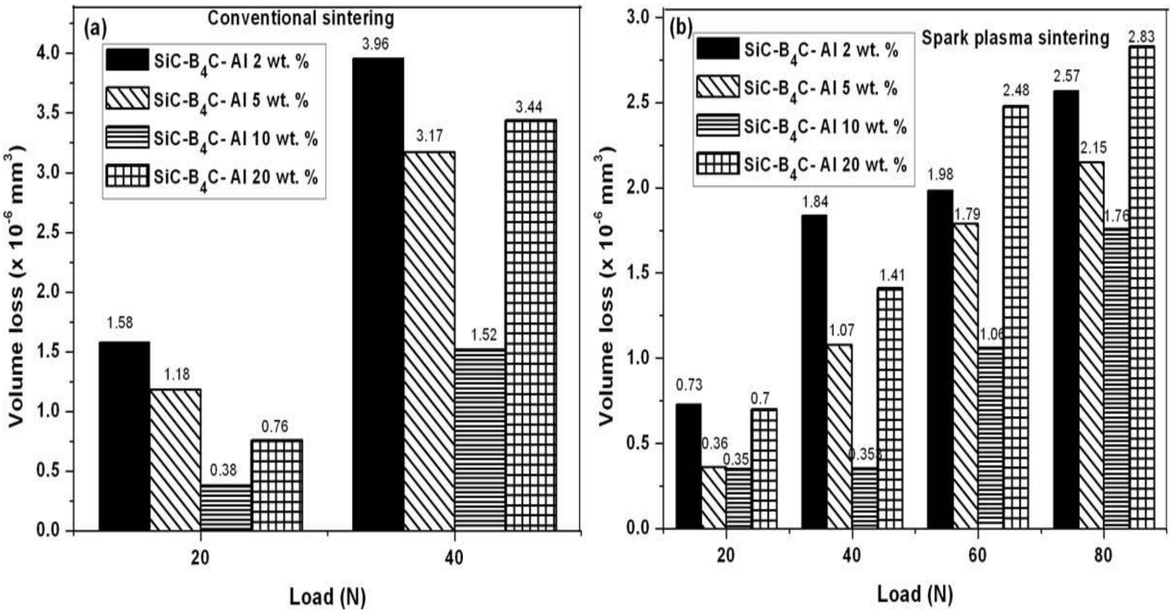

Figure 4.18 Bar diagram showing wear volume loss vs. applied load of (a) conventional sintered samples and (b) SPS samples.

Table 4.2 *Values of wear depth, wear volume and wear rate produced at different applied loads for the SPS and conventional sintered SiC-B$_4$C–Al samples.*

Spark plasma sintering					
Compositions	**Applied load (N)**	**Wear depth (μm)**	**Wear rate (x 10 $^{-8}$ mm^3/m)**	**Wear Volume (x 10 $^{-6}$ mm^3)**	
				Archard equation	**Experiment**
SiC-B$_4$C	20	26 ± 4%	0.195	0.27	0.74
	40	162 ± 3%	0.78	0.54	3
	60	230 ± 4%	1.56	0.8	5.9
	80	373 ± 2%	1.85	1.07	6.98
SiC-B$_4$C–2 wt. % Al	20	23 ± 3%	0.19	0.57	0.73
	40	107 ± 3%	0.48	1.15	1.83
	60	235 ± 4%	0.52	1.73	1.98
	80	309 ± 4%	0.68	2.31	2.57
SiC-B$_4$C–5 wt. % Al	20	13 ± 5%	0.093	0.38	0.36
	40	66 ± 4%	0.28	0.76	1.07
	60	76 ± 2%	0.47	1.15	1.79
	80	164 ± 3%	0.57	1.53	2.15
SiC-B$_4$C–10 wt. % Al	20	7 ± 6%	0.095	0.31	0.35
	40	39 ± 5%	0.093	0.63	0.353
	60	61 ± 3%	0.28	0.94	1.06
	80	144 ± 5%	0.47	1.26	1.76
SiC-B$_4$C–20 wt. % Al	20	19 ± 6%	0.18	0.35	0.7
	40	75 ± 5%	0.37	0.71	1.41
	60	128 ± 4%	0.65	1.07	2.48
	80	213 ± 4%	0.75	1.43	2.83
Conventional sintering					
SiC-B$_4$C	20	256 ± 5%	2.06	0.37	7.7
	40	742 ± 4%	2.1	0.75	18.6
SiC-B$_4$C–2 wt. % Al	20	194 ± 5%	0.42	0.50	1.58
	40	443 ± 6%	1.05	1	3.96
SiC-B$_4$C–5 wt. % Al	20	106 ± 6%	0.31	0.47	1.18
	40	163 ± 6%	0.84	0.94	3.17
SiC-B$_4$C–10 wt. % Al	20	81 ± 6%	0.10	0.44	0.38
	40	138 ± 5%	0.40	0.88	1.52
SiC-B$_4$C–20 wt. % Al	20	158 ± 5%	0.20	0.50	0.76
	40	235 ± 6%	0.90	1.02	3.44

4.4 Electrical conductivity study

Carbide ceramics (SiC and B_4C) are widely used in many advanced applications due to their excellent mechanical properties. Materials working at high temperatures in harsh environment, operating at high power and frequency are of great technological interest [121]. Electrically conductive ceramics (ECC) with high wear and corrosive resistance are very interesting as electrically conductive components, complex shape with small precision parts as in electrodes, sensors, electronic devices. The ECCs could be prepared by insulating ceramics (SiC, B_4C, ZrO_2, Al_2O_3, Si_3N_4) with electrically conducting phases (Al, Mo, TiB_2, ZrB_2, W, $MoSi_2$) [122–124].

Figure 4.19 (a) shows the electrical conductivity of SiC-B_4C–Si cermet with increasing Si content. The variation of electrical conductivity with wt. % of Si was measured experimentally using four-point probe electrical resistance measurement system as explained in section 2.7. For conventional sintered samples, conductivity decreased from 13.59 $S.m^{-1}$ to 7.3 $S.m^{-1}$ with increasing Si content from 0 to 20 wt. %. Similarly, for SPS samples also same trend in conductivity was observed. SPS samples exhibit comparatively higher conductivity than conventional sintered samples due to higher density values. These helps in improving bonding among particles in SPS samples and make easier pathways for electron flow with higher electrical conductivity [125]. For SPS samples, conductivity decreased from 35.32 $S.m^{-1}$ to 26.65 $S.m^{-1}$ with increasing Si content from 0 to 20 wt. %. As Si (1.54×10^{-3} $S.m^{-1}$) [126] has lower electrical conductivity than α-SiC (6H) (10 $S.m^{-1}$) [127] and B_4C (140 $S.m^{-1}$) [128], addition of higher amount of Si might be reduced the conductivity value.

Figure 4.19 (b) shows the electrical conductivity of SiC-B_4C–Al cermet with increasing Al content. As Al has high electrical conductivity (3.5×10^{7} $S.m^{-1}$) [126], hence, the compositions with Al addition shows higher electrical conductivity than the compositions with Si addition. With increasing Al wt. %, electrical conductivity continuously increased. For conventional sintered samples, conductivity increased from 6.58×10^{3} $S.m^{-1}$ to 1.15×10^{4} $S.m^{-1}$ with increasing Al content from 0 to 20 wt. %. For SPS samples, conductivity increased from 9.36×10^{3} $S.m^{-1}$ to 1.29×10^{4} $S.m^{-1}$ with increasing Al content from 0 to 20 wt. %. The electrical conductivity of SiC and B_4C semiconductor was significantly enhanced by the presence of electrically conductive Al phase at grain boundaries [129, 130].

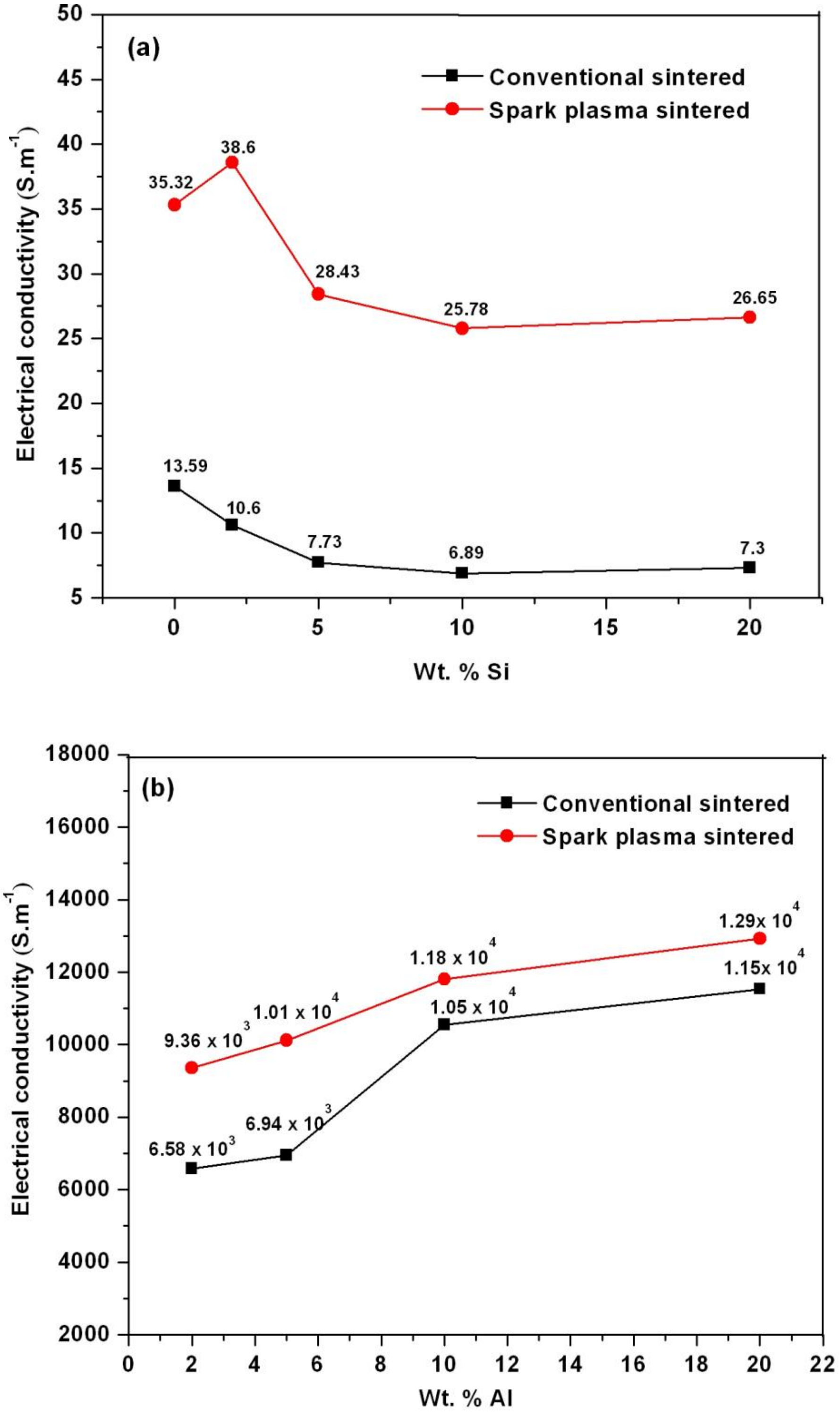

Figure 4.19 (a) Variation in electrical conductivity with weight percent of Si (b) Variation in electrical conductivity with weight percent of Al.

4.5 Summary

Following summary can be made from the present investigation:

- The present investigation shows that, wear depth and wear rate increases with increase in applied load from 20 to 80N for all the SPS samples and also for conventional sintered samples tested at 20 and 40N.
- The wear resistance increases with Si content up to 10 wt. %. With further increase in Si content to 20 wt. % wear resistance decreases. The higher wear depth (low wear resistance) is found for SiC-B_4C ceramic system as compared to SiC-B_4C-Si cermets.
- Volume of wear debris increases with increase in applied load. The possible wear mechanisms are abrasive grooves, delamination and formation of crack.
- Similar results are also obtained for SiC-B_4C–Al based cermets as SiC-B_4C–Si based cermets.
- Addition of 10 wt. % Al makes it a better wear resistant material as compared to other compositions.
- Electrical conductivity decreased with increasing Si addition in the compositions as Si has low electrical conductivity than SiC and B_4C. Whereas, conductivity increased with increasing Al, as Al is more electrically conductive than SiC and B_4C.

Chapter 5

Oxidation behaviour studies of SiC-B_4C, and SiC-B_4C–Si cermets prepared by pressure-less sintering and spark plasma sintering methods

5.1 Scope and objectives of the work

SiC-B_4C based composites are very interesting engineering materials due to its high hardness, low bulk density and high oxidation resistance; used as refractories, wear resistant and abrasive media [8, 9, 73]. Oxidation resistance study of SiC-B_4C composite is an important subject for its practical application at high temperatures. The main objectives of this chapter is to study the high temperature oxidation behavior of the SiC-B_4C ceramic composite, and SiC-B_4C–Si cermets containing 2, 5, 10, and 20 wt. % Si prepared by both SPS and conventional sintering methods. Isothermal oxidation studies were performed at 800, 1000 and 1200 °C for all the compositions. This study was executed to understand the effect of added Si amount (0–20 wt. %) in SiC-B_4C ceramic matrix and temperature on oxidation behaviour.

5.2 Analysis of isothermal oxidation behavior at elevated temperatures

5.2.1 Oxidation mechanism of SiC-B_4C ceramic composites

SiC is generally used for lining on blast furnaces due to good alkali resistance property [86]. The SiO_2 phase formed on the SiC based materials by thermal oxidation can act as an excellent protective layer against oxidation. Liquid B_2O_3 and borosilicate is the main oxide product formed by the thermal oxidation of B_4C and SiC. High temperature oxidation of SiC can be found in the form of active and passive oxidation. Passive oxidation starts when oxygen partial pressure closes to one bar. From the thermodynamic point of view, the most probable oxidation reactions of SiC for passive and active oxidation are shown below:

$$2SiC\ (S) + 3O_2\ (g) \rightarrow 2SiO_2\ (S) + 2CO\ (g)\ \text{(Passive oxidation)} \quad (5.1)$$

$$SiC\ (S) + O_2\ (g) \rightarrow SiO\ (S) + CO\ (g)\ \text{(Active oxidation)} \quad (5.2)$$

According to Schneider *et al.* [131] and Ogura and Morimoto [132], when the total pressure at the interface crosses the ambient pressure, bubbles are generated. They have showed the passive to bubble transition and then passive to active transition. The SiO phase formation leads to vaporization and loss of mass. During passive oxidation, SiO_2 forms a dense layer and deposited on the SiC surface. This layer acts as an anti-oxidation protective layer or termed as barrier for the oxygen penetration.

The most probable reactions responsible for oxidation in SiC-B_4C composites from 800 °C to 1200 °C are as follows:

$$2SiC\ (s) + 3O_2\ (g) \xrightarrow{800^\circ C} 2SiO_2\ (s) + 2CO\ (g) \quad (5.3)$$

$$4B\ (s) + 3O_2\ (g) \xrightarrow{500^\circ C} B_2O_3\ (l) \quad (5.4)$$

$$B_4C\ (s) + 4O_2\ (g) \xrightarrow{450-600^\circ C} 2B_2O_3\ (l) + CO_2\ (g) \quad (5.5)$$

$$2B_2O_3\ (l) \xrightarrow{500-1000^\circ C} B_2O_3\ (g) \quad (5.6)$$

$$SiO_2\ (g) + B_2O_3\ (l) \xrightarrow{1000^\circ C} B_2O_3.xSiO_2\ (l) \quad (5.7)$$

$$B_2O_3.xSiO_2\ (l) \xrightarrow{\geq 1000^\circ C} B_2O_3\ (g) + xSiO_2\ (s) \quad (5.8)$$

Liquid B_2O_3 and solid SiO_2 phase formed due to the oxidation of B_4C and SiC in the composites during the oxidation temperature from 600 to 800 °C. The liquid borosilicate formed by the dissolution of SiO_2 phase in the liquid B_2O_3 in the temperature range of 800 to 1000 °C. The formation and stability of B_2O_3 phase decreases the formation of SiO_2 phase intensity, can be detected by XRD analysis. When the oxidation temperature increases above 1000 °C, the mass loss can be observed in the SiC-B_4C composite at 1000 °C. The mass loss might be higher above the temperature of 1000 °C due to vaporization of B_2O_3 phase in liquid borosilicate. But prolong heating above 1200 °C, a thin SiO_2 film formed over the surface of SiC grains and protect it from further oxidation. Such protective action of SiO_2 continued up to 1500 °C [91, 133].

5.2.2 Mass change during oxidation

Figure 5.1 shows the weight changes of conventional sintered SiC-B_4C–Si cermets oxidized at (a) 800 °C, (b) 1000 °C and (c) 1200 °C for 10 h. Weight of the sample before and after oxidation were taken with the help of electro balance with accuracy 0.01 mg. The weight gain of the SiC-B_4C composite and SiC-B_4C–Si cermets containing 2, and 5 wt. % Si was nearly 13–14% after oxidation at 800 °C, 12–13% after 1000 °C and 13–16% after 1200 °C. The weight gain increased linearly with the oxidation time for the initial 1 h, then kept almost constant for remaining last 9 h. The initial weight gain may be due to the oxidation of B_4C in air at 800 °C. Oxidation of B_4C normally starts near 500 °C in the presence of air [134]. However, the weight gain of SiC-B_4C–Si cermets containing 10 and 20 wt. % Si was nearly 0–1% after oxidation at 800 and 1200 °C. But no weight change (0–0.2%) was observed after oxidation at 1000 °C. Experimental results reveal that addition of Si content above 10 wt. % significantly increased the oxidation resistance. During oxidation of SiC, the surface layer of silica (SiO_2) developed above 600 °C [135, 136]. SiO_2 content increased with increasing Si content in the SiC-B_4C composite. During initial stage of oxidation above 600 °C, the protective layer of SiO_2 was formed on the surface of the samples and prevents the oxidative weight change during high temperature oxidation for 10 and 20 wt. % Si samples. The surface protective layer of SiO_2 was responsible for prevention of further oxidation of all the samples when oxidation temperature increased from 800 to 1200 °C.

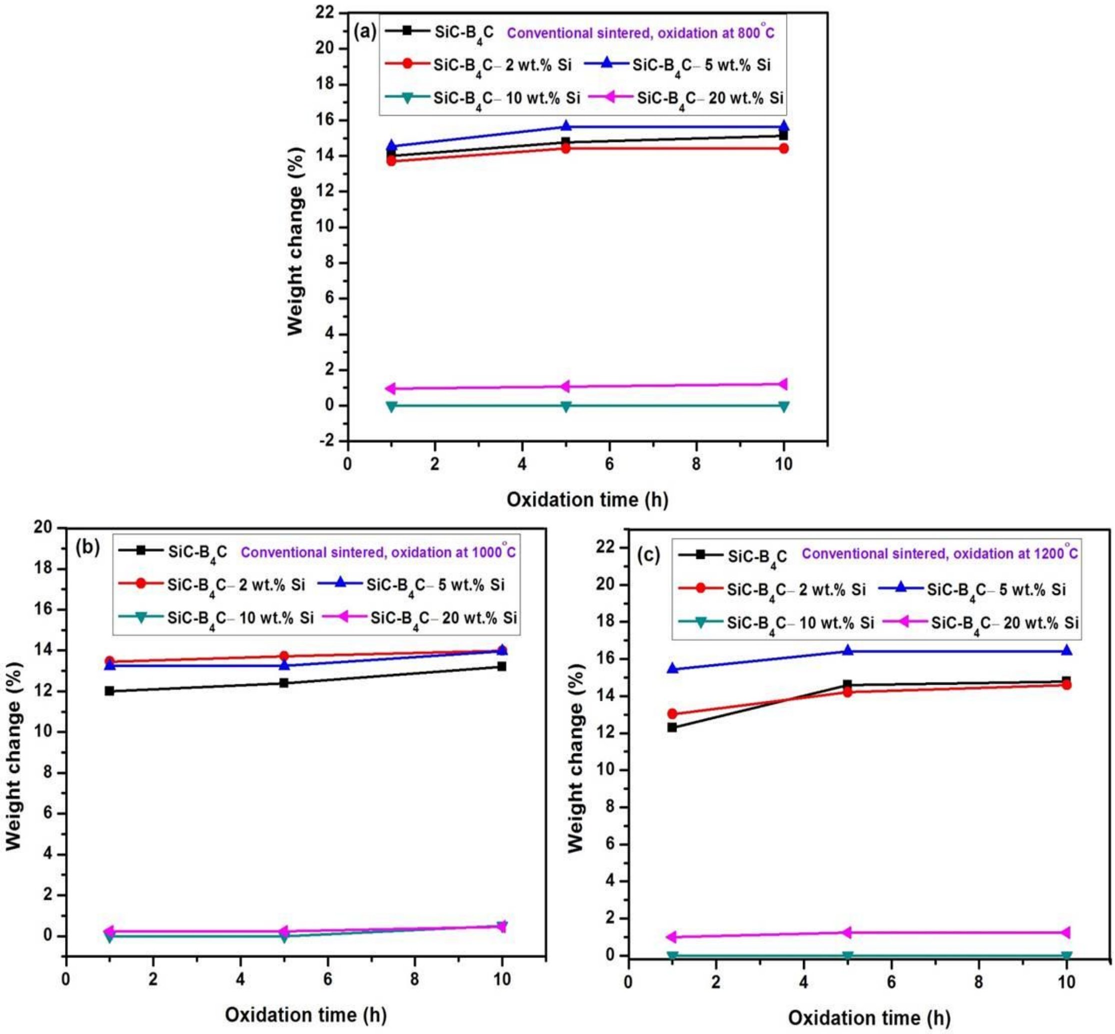

Figure 5.1 Weight change versus oxidation time plots of conventional sintered SiC-B$_4$C, SiC-B$_4$C–Si (2, 5, 10, and 20 wt. % Si) cermets during oxidation at (a) 800 °C, (b) 1000 °C and (c) 1200 °C respectively.

The weight change of spark plasma sintered SiC-B$_4$C–Si cermets oxidized at (a) 800 °C, (b) 1000 °C and (c) 1200 °C for 10 h is shown in Figure 5.2. There was a decrease in mass for SiC-B$_4$C and SiC-B$_4$C– 2 wt. % Si samples during initial stage of oxidation. After 1 h of oxidation, no change in mass was observed for remaining time periods. The reason may be due to the ablation of surface carbon from SiC and B$_4$C was faster during initial stage of oxidation in SPS samples of SiC-B$_4$C ceramic matrix without Si addition and 2 wt. % Si addition. Fewer amounts of Si and SiC content in these compositions could not prevent B$_4$C and SiC to oxidize. But after 1 h of oxidation at 800, 1000 and 1200 °C, the surface of all the samples were protected from further oxidation by the formation of surface protective layer of SiO$_2$. The higher amount of Si content in the composites improved the oxidation resistance even during initial stage of oxidation temperature (there was no weight change during oxidation) as shown in Figure 5.2. The weight change of the SiC-B_4C–Si cermets containing 5, 10, and 20 wt. % Si was very less nearly 0–0.004% after oxidation at 800 °C, 0–0.3% after oxidation at 1000 and 1200 °C. There was no weight change of 20 wt. % Si sample even at 1200 °C. But for SiC-B_4C composite, weight loss was nearly 1%, 1.2% and 2% at 800, 1000 and 1200 °C respectively. For SiC-B_4C– 2 wt. % Si sample, the weight loss varied from 0.2 to 0.6% when oxidation temperature varies from 800 to1200 °C. The spark plasma sintered cermets show higher density and improved mechanical properties with better wear resistance compared to conventional sintered samples as discussed in previous chapter 3 and chapter 4. The highly dense SPS sample also shows better wear resistance and oxidation resistance during thermal oxidation than the conventional sintered samples.

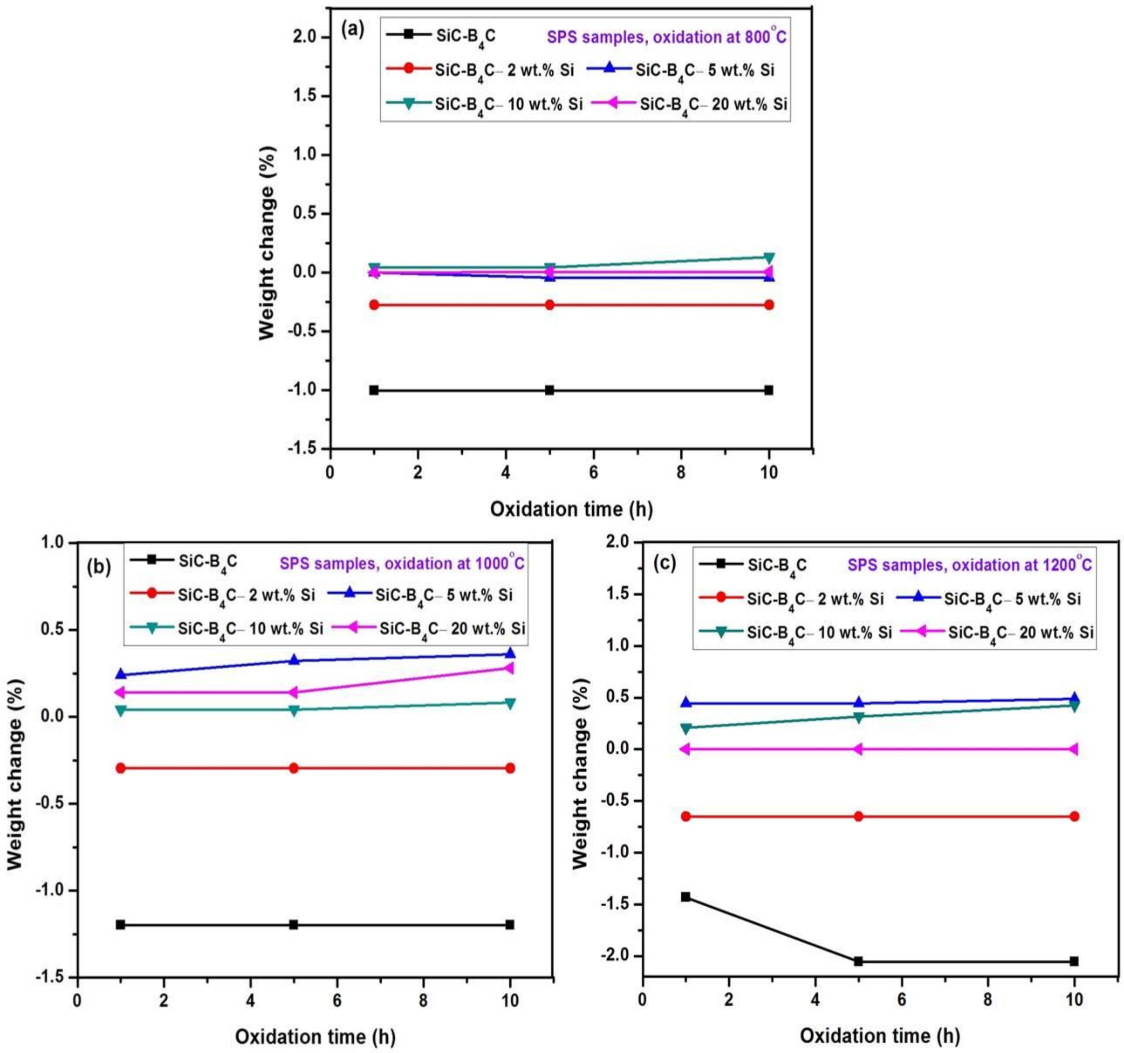

Figure 5.2 Weight change versus oxidation time plots of spark plasma sintered SiC-B_4C, SiC-B_4C–Si (2, 5, 10, and 20 wt. % Si) cermets during oxidation at (a) 800 °C, (b) 1000 °C and (c) 1200 °C respectively.

5.2.3 Oxidation behavior from XRD analysis

To investigate the effect of temperature on oxidation behavior, XRD analysis of all the cermets after oxidation was carried out. Figure 5.3 (a, b), 5.4 (a, b) and 5.5 (a, b) shows the influence of oxidation temperatures of SiC-B_4C based cermets samples prepared by both SPS and conventional sintering methods. From XRD spectra, B_2O_3, SiO_2 and SiC phases were identified after oxidation at 800 °C for conventional sintered SiC-B_4C composites as shown in Figure 5.3 (b). For 10 and 20 wt. % Si samples B_2O_3 was not detected for conventional sintered samples. Cermets containing 10 and 20 wt. % Si provide the protective layer during oxidation at 800 °C and prevent the expose of B_4C in the oxygen medium during oxidation. The excess SiO_2 phase suppresses the formation of B_2O_3 phase in the compositions during oxidation [24]. Hence, it restricts oxidation of B_4C even in the oxidative media and improves the efficiency of the oxidation resistance property of the material. For all the SPS samples, minor oxide peak of B_2O_3 was detected from the XRD analysis of SiC-B_4C ceramic composite. The product phases of SiC and SiO_2 were also detected as shown in the Figure 5.3 (a). Low carbon content phase $B_{25}C$ was detected in spark plasma sintered 10 wt. % Si sample. XRD peak also shows the presence of carbon in conventional sintered sample containing 5 and 10 wt. % Si. According to Narushima *et al.* [91], SiC-B_4C composites after oxidation of at 800 °C showed a carbon peak at oxide/composite interface. They confirmed that, the carbon phase is thermodynamically stable when carbon monoxide (CO) partial pressure > 10^{-1} Pa at 800 °C.

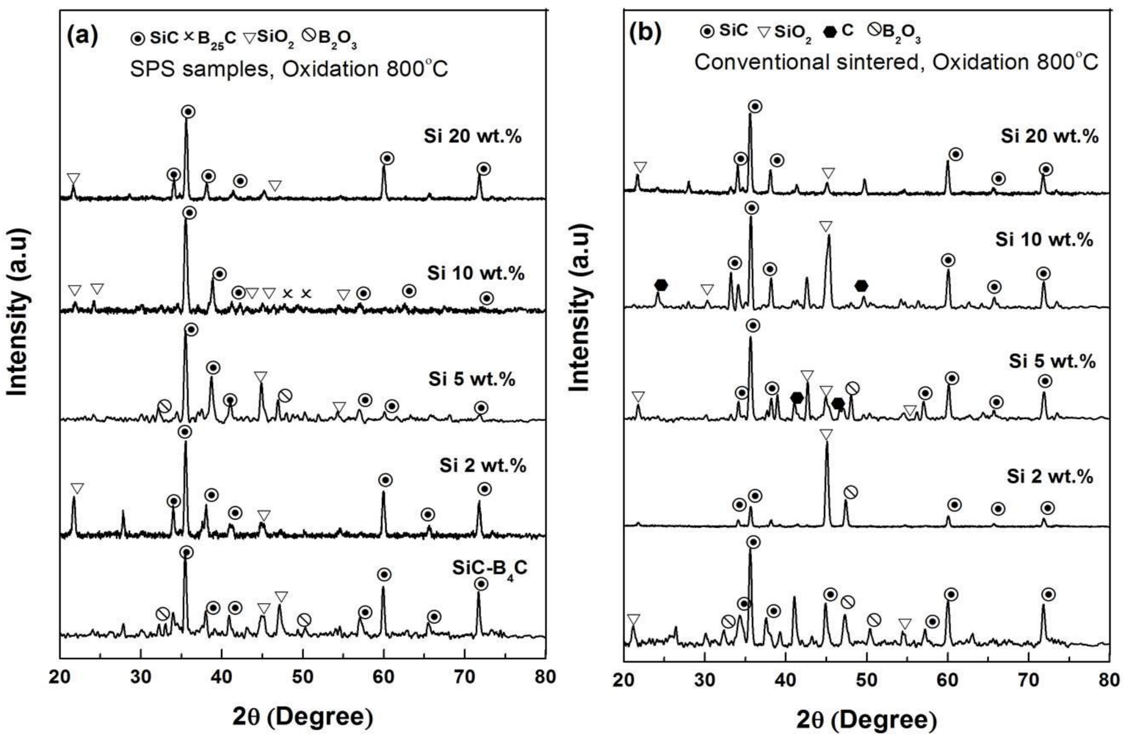

Figure 5.3 (a) XRD spectra of spark plasma sintered SiC-B_4C ceramic composite, SiC-B_4C–Si cermets (2, 5, 10, and 20 wt. % Si) and (b) conventional sintered samples after oxidation at 800 °C.

XRD analysis showed no peaks of B_2O_3 in conventional sintered samples when heated at 1000 °C. The less increase in mass might be due to the vaporization of boron oxide at 1000 °C. Narushima *et al.* [91] observed that, the weight gain in SiC-B_4C composites at 800 °C was due to the formation of less viscous liquid B_2O_3 phase, generated from the oxidation of B_4C. There was slight decrease in weight gain (1.5–2%) at 1000 °C compared to weight gain at 800 °C (Figure 5.1 (a, b)), may be due to the vaporization of B_2O_3 in the liquid borosilicate. Therefore, no B_2O_3 phase was observed at 1000 °C of conventional sintered and SPS samples. SPS samples of 5 and 10 wt. % Si content depicted the presence of $B_{25}C$ and B_8C phases (low carbon content) on the surface after oxidation at 1000 °C as shown in Figure 5.4 (a).

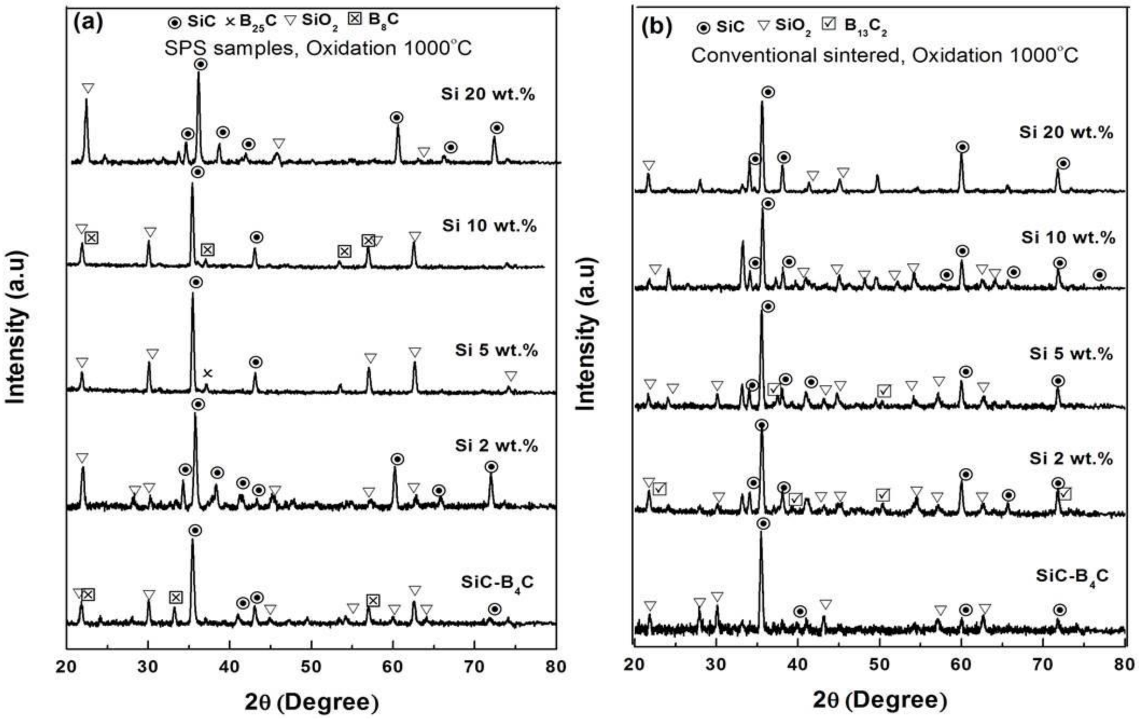

Figure 5.4 (a) XRD spectra of spark plasma sintered SiC-B_4C ceramic composite, SiC-B_4C–Si cermets (2, 5, 10, and 20 wt. % Si) and (b) conventional sintered samples after oxidation at 1000 °C.

Similar trend of XRD phase analysis as that of 1000 °C was observed for all the cermet samples after oxidation at 1200 °C as shown in Figure 5.5 (a, b). A very negligible weight change (Figure 5.1 and 5.2) of all the compositions after oxidation at 1000 and 1200 °C is also corroborated from the XRD analysis.

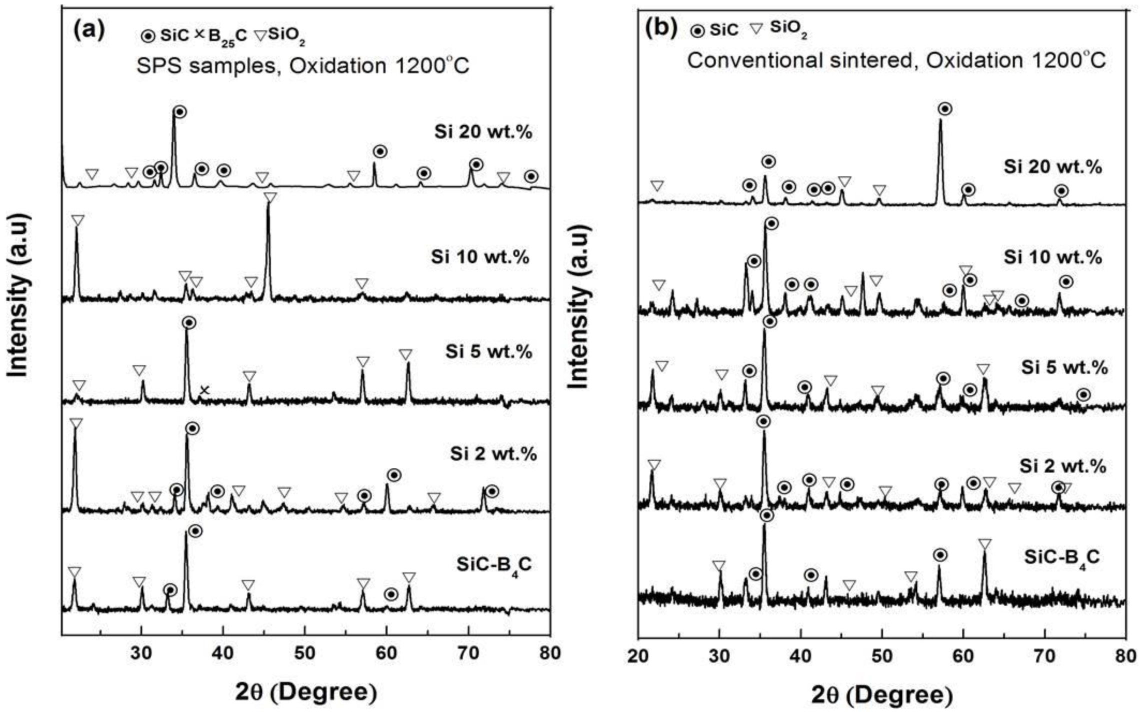

Figure 5.5 (a) XRD spectra of spark plasma sintered SiC-B_4C ceramic composite, SiC-B_4C–Si cermets (2, 5, 10, and 20 wt. % Si) and (b) conventional sintered samples after oxidation at 1200 °C.

5.2.4 Surface morphology analysis

Figure 5.6 represents the SEM images of the oxide surfaces of the spark plasma sintered SiC-B_4C composite after oxidation at 800 °C (a, a’), 1000 °C (b, b’) and 1200 °C (c, c’) respectively. Figure 5.6 (a, a’) indicates the presence of small size pores ($\leq$ 3 µm) with crack formation on the oxide surface of SiC-B_4C composite after oxidation at 800 °C. The crack formation during oxidation led the diffusion channel of oxygen and resulted in the weight loss due to oxidation. A comparatively big cavity (nearly 10–40 µm) was found on the surface of SiC-B_4C composite after oxidation at 1000 °C, led to a relatively higher weight loss of the composition. Cavity on the oxide surface indicates the evaporation of oxides in the form of gas. This was also confirmed from the weight change versus oxidation time plot as shown in Figure 5.2 (a, b). The irregular shape pores on the surface of SiC-B_4C composite after oxidation at 1200 °C indicates the evaporation of oxides is higher.

Weight loss in spark plasma sintered 2 wt. % Si sample after oxidation at 800 °C was also identified from the FESEM analysis as shown in Figure 5.7 (a, a’). Surface cracks on the oxide surface with pore size $\leq$ 2 µm were found on the micrograph. The weight loss was comparatively less for 2 wt. % Si sample than the SiC-B_4C composite as smaller pore size in 2 wt. % Si sample.

Surface morphology of spark plasma sintered 20 wt. % Si added compositions found without any cracks and presence of small size pore on the oxide surface after oxidation at 800 °C as shown in Figure 5.8 (a–c). SEM analysis confirms the oxidation resistance of 20 wt. % Si sample is better than the oxidation resistance of SiC-B_4C composite. EDS spectra also confirms the presence of SiC and SiO_2 protective layer on the surface of the cermet sample. Some platinum peaks were identified on the EDS spectra due to the platinum coating on the sample surface for SEM analysis.

Figure 5.9 shows the SEM micrograph of spark plasma sintered SiC-B_4C– 20 wt. % Si cermet after oxidation at 1200 °C. As the cermet sample was oxidized at higher temperature, SiO_2 glassy phase layer was found without presence of any cavity on the surface. This indicates the self-protection against oxidation after oxidation at 1200 °C for SiC-B_4C– 20 wt. % Si cermet. This was also confirmed from the weight loss versus oxidation time plot as shown in Figure 5.2 (c). There was no weight change when the sample was exposed to air at high temperature. Addition of 10 and 20 wt. % Si was effective to decrease the mass loss or gain by oxidation for conventional and SPS samples.

Oxide surface of conventional sintered 5 wt. % Si sample after oxidation at 1000 and 1200 °C was shown in Figure 5.10 (a, b). Circular shape cavity indicates the formation of less viscous B_2O_3-SiO_2 glass film to cover the surface for further diffusion of oxygen [137]. There was no crack formation on the oxide surface of conventional sintered sample as shown in Figure 5.10 (a, b). Whereas after oxidation at 1200 °C, a glassy phase layer was found on the oxide surface without any visible cavity. This indicates oxidation at 1200 °C protects the sample from further diffusion of oxygen by forming self-protecting SiO_2 phase. Figure 5.10 (a’, b’) shows the EDS spectra, confirms the presence of SiO_2 phase on the oxidized surface of the sample.

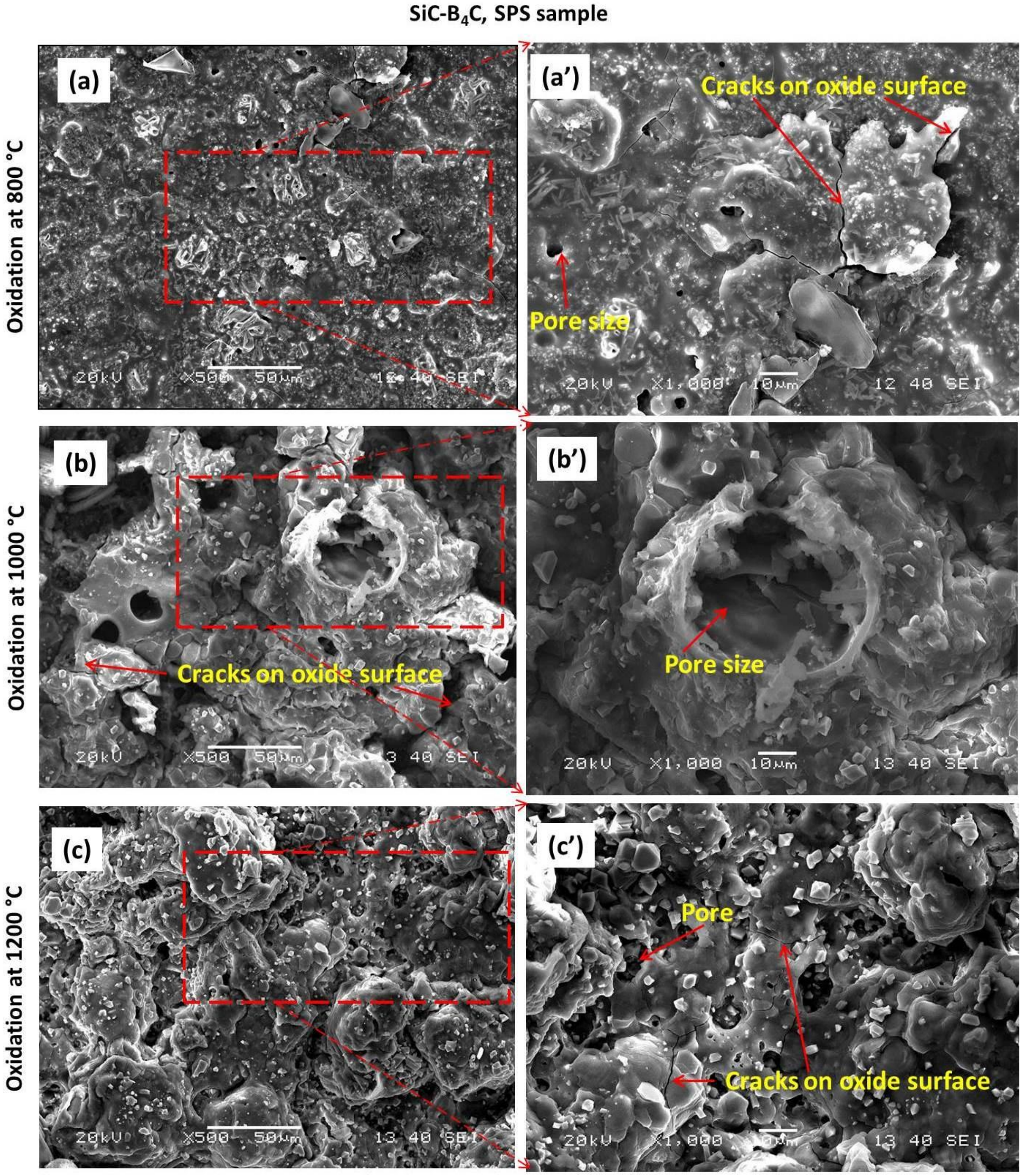

Figure 5.6 SEM image of (a, a'), (b, b') and (c, c') shows spark plasma sintered SiC-B$_4$C ceramic composite after oxidation test at 800, 1000, and 1200 °C respectively.

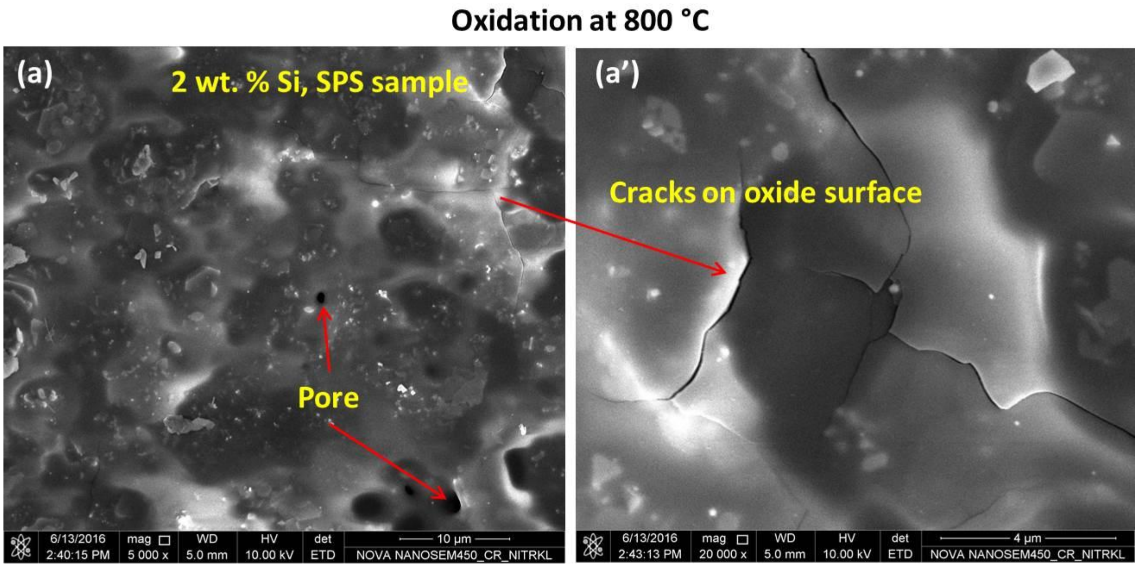

Figure 5.7 (a, a') Surface morphology of spark plasma sintered SiC-B$_4$C– 2 wt. % Si cermet after oxidation at 800 °C.

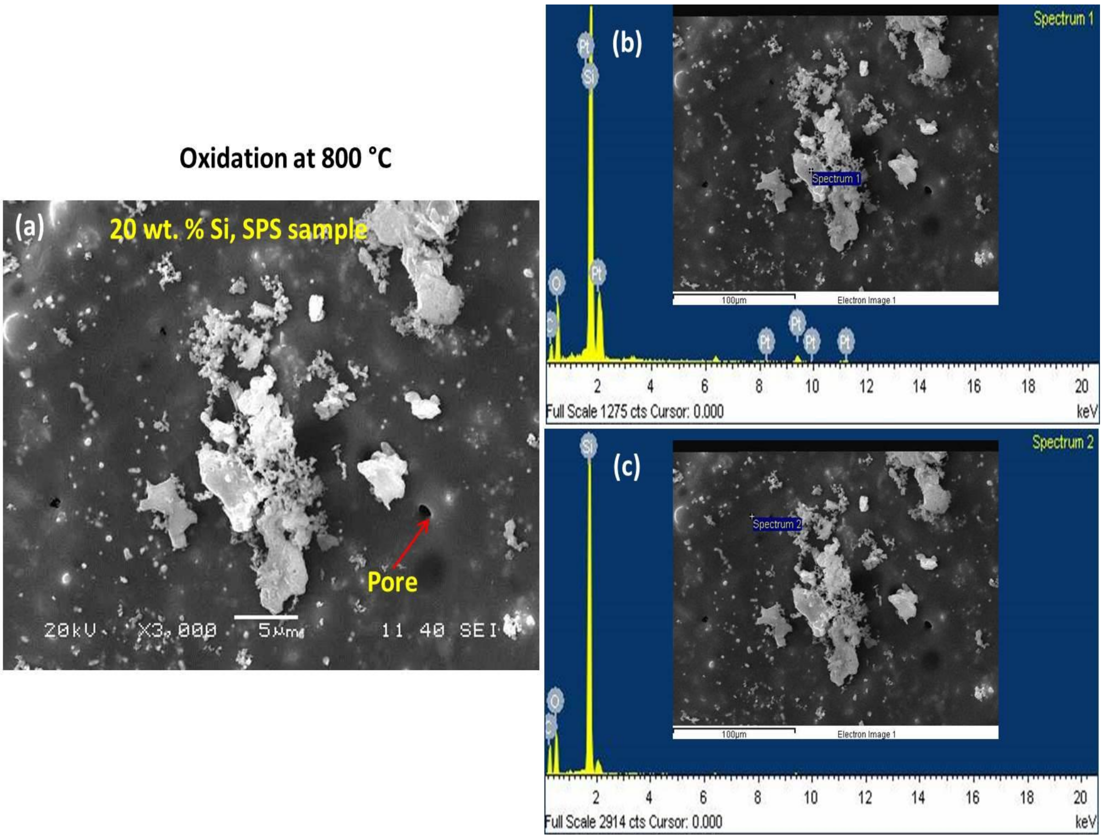

Figure 5.8 Surface morphology and EDS spectra analysis of spark plasma sintered SiC-B$_4$C– 20 wt. % Si cermet after oxidation at 800 °C.

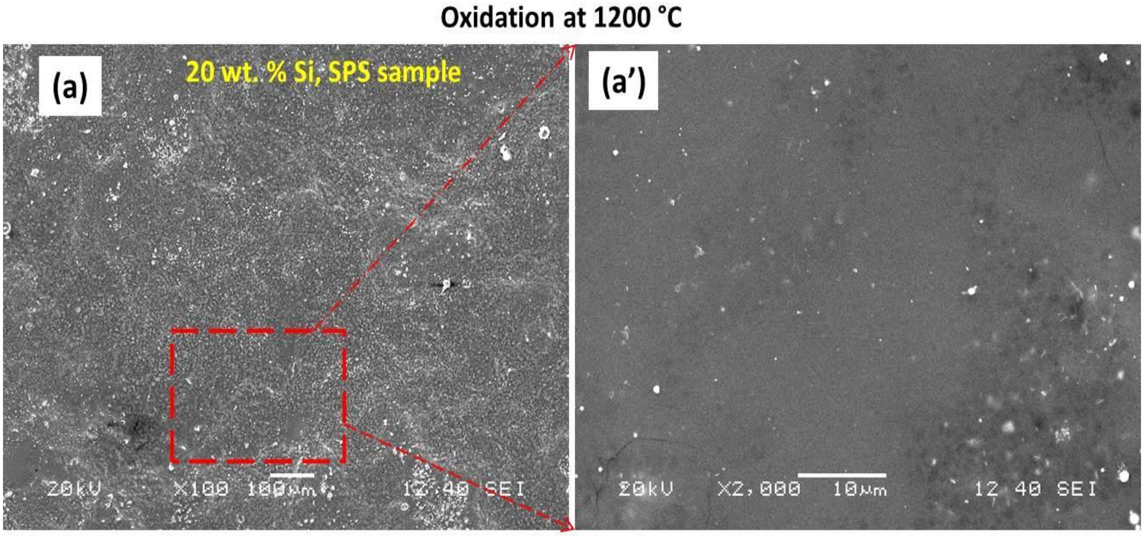

Figure 5.9 (a, a') Surface morphology of spark plasma sintered SiC-B_4C– 20 wt. % Si cermet after oxidation at 1200 °C.

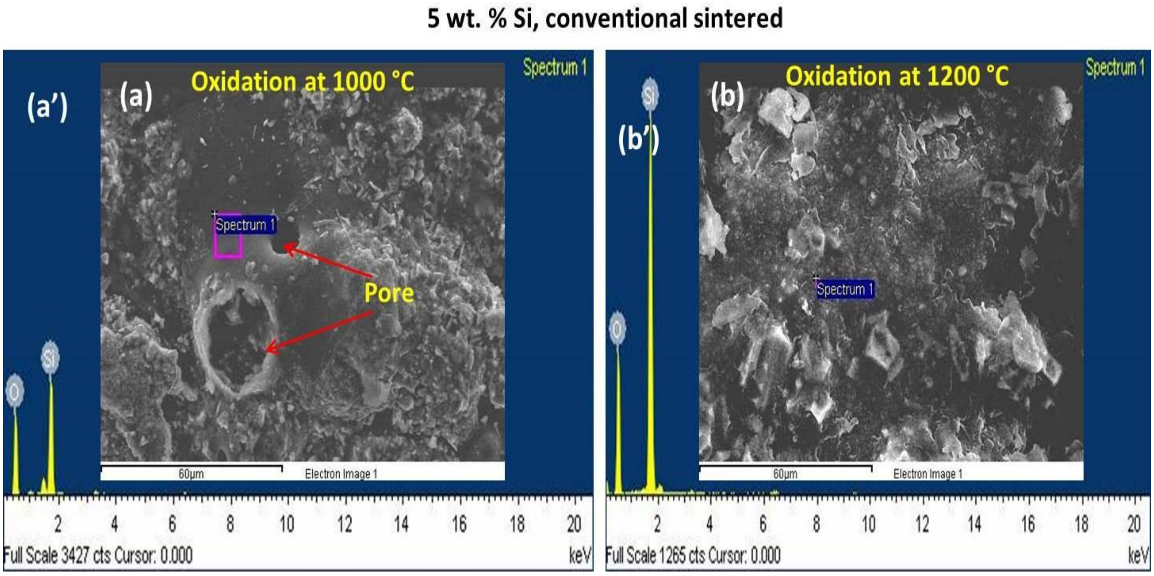

Figure 5.10 Surface morphology of conventional sintered SiC-B_4C– 5 wt. % Si cermet after oxidation at (a, a') 1000 °C and (b, b') 1200 °C.

5.3 Summary

- The oxidation behavior of SiC-B_4C ceramic composite and SiC-B_4C–Si cermets containing 2, 5, 10, and 20 wt. % Si were investigated at 800, 1000, and 1200 °C.

- XRD analysis detected the SiC, B_2O_3, SiO_2 and carbon phases on the oxidation surface of the SPS and conventional sintered samples.

- Oxidation at 800 °C for conventional sintered samples with low Si addition show weight gain due to formation of B_2O_3 by the oxidation of B_4C with oxygen.

- There was no weight change in10 and 20 wt. % Si added composition for conventional and SPS samples due to the formation of SiO_2 glass phase as barrier for oxygen diffusion. The higher amount of Si content in the composites improved the oxidation resistance from 800 to 1200 °C.

Chapter 6

Conclusions

In the present thesis, systematic attempts were made to prepare SiC-B_4C (60:40 wt. %) ceramic composite powder, SiC-B_4C–Si (2, 5, 10 and 20 wt. % of Si) and SiC-B_4C–Al (2, 5, 10 and 20 wt. % of Al) cermet powders of various compositions separately by mechanical milling for 10 h in a planetary mill. Then the powders were consolidated by both conventional sintering and spark plasma sintering (SPS) techniques. The effect of sintering methods and temperatures on microstructure, density, hardness, compressive strength, flexural strength and fracture toughness of all the cermets were evaluated. We also studied the un-lubricated sliding wear behaviour of all the cermet samples against diamond indenter at different loads. Oxidation behaviour of the SiC-B_4C, SiC-B_4C–Si based cermets was carried out by isothermal oxidation at different temperatures.

Major outcomes of the present study are summarized as follows:

- Milling reduces the average particle size of all the compositions to 3–4 µm from 40 µm. XRD, SEM and particle size analysis reveal the particle size reduction and homogeneous distribution of Si, Al, in the respective SiC-B_4C composite matrix. XRD spectrum of milled powder shows no phase transformation during milling. It is also found that cermet powders are irregular after milling as shown in SEM micrographs.

- Thermal analysis of SiC-B_4C–Al cermet powders shows the exothermic peak, which represent crystalline phase transition and lattice strain release during heating. The exothermic peaks at around 700 and 1100 °C indicate the formation of $Al_8B_4C_7$ and AlB_{12} phases respectively in the Al added cermet samples.

- For SiC-B_4C ceramic composite, sintered density was increased by 1–4% with increasing sintering temperature from 1500 to 1600 °C. Microhardness, indentation fracture toughness and compressive strength values of SiC-B_4C sample sintered by SPS at 1600 °C were found to be 27±2.11 GPa, 1.87 MPa $m^{1/2}$ and 449 MPa respectively.

- Conventional sintering of SiC-B_4C composite is not much effective as it produced larger grain size with high porosity in sintered sample as confirmed by FESEM analysis, and hence degrades the properties of the composite material.

- Mechanically milled SiC-B_4C–Si cermet with varying Si (2, 5, 10, and 20 wt. %) content were consolidated by conventional sintering and SPS route. The effects of wider composition range and consolidation methods on physical and mechanical properties of the cermet samples were studied. The highest physical and mechanical properties were obtained for 10 wt. % Si added composition consolidated by conventional sintering and SPS methods. The highest density of 92% and 98% are obtained for the composition containing 10 wt. % Si fabricated by conventional sintering at 1950 °C and SPS at 1350 °C respectively. In conventional sintered samples, weak peaks of SiO_2 and B_2O_3 are observed from XRD analysis and may be responsible for comparatively lesser improved properties than SPS samples. There are no glassy phases and reaction phases are observed in sintered products for SPS specimens with Si contents. Hence, better mechanical and physical properties were found. With increasing the Si content from 5 to 10 wt. %, the density and the hardness value increases. Increase of Si content to 20 wt. %, the hardness of the composition decreases due to the existence of large amount of residual Si and increase of the SiC phase in the composition. There is an enhancement of Vickers microhardness from 18±2.23 to 28±2.12 GPa for the cermet sample containing 10 wt. % Si when the sintering condition was changed from conventional sintering to SPS. The indentation fracture toughness and compressive strength of the SiC-B_4C–10 wt. % Si composition fabricated by SPS were 3.8 MPa $m^{1/2}$ and 1387 MPa, respectively which is higher than the conventional sintered sample of same composition. Fractography study revealed mixed mode of fracture in SiC-B_4C–Si cermet samples. Flexural strength study was carried out only for conventional sintered samples. Maximum flexural strength of 165 MPa was measured for SiC-B_4C–10 wt. % Si composition. The novelty of this present study is that, the wettability, ductility and properties got improved with reduced porosity in the cermet by the addition of Si into the SiC-B_4C matrix.

- For SiC-B_4C–Al cermet samples, better physical and mechanical properties were obtained for 10 wt. % Al added composition for SPS as well as conventional sintering. XRD analysis confirmed the presence of $Al_8B_4C_7$ and AlB_{12} phases for SPS and conventional sintered samples provide better oxidation resistance and toughness to the cermet samples. The maximum relative density, microhardness and indentation fracture toughness of SiC-B_4C–10 wt. % Al consolidated by SPS are 97%, 23±2.29 GPa and 3.28 MPa.$m^{1/2}$, respectively. There was an enhancement of Vickers microhardness from 17±2.18 to 23±2.29 GPa for the cermet sample containing 10 wt. % Al when the sintering condition was changed from conventional sintering to SPS. SPS is more efficient for fabrication of SiC-B_4C–Al cermet even at much lower temperature than pressure-less conventional sintering.

- We have studied un-lubricated sliding wear behavior of SiC-B_4C–Si and SiC-B_4C–Al cermets fabricated by conventional pressure-less sintering and SPS techniques against a diamond indenter at different loads. There as an increase in wear resistance of SiC-B_4C–Si based cermets when sintering method change from conventional sintering to spark plasma sintering. Wear depth and wear rate increases with increase in applied load from 20 to 80N for all the SPS samples and also for conventional sintered samples tested at 20 and 40N. The wear resistance increases with Si content up to 10 wt. %. With further increase in Si content to 20 wt. % wear resistance decreases. The higher wear depth (low wear resistance) is found for SiC-B_4C ceramic system as compared to SiC-B_4C-Si cermets. The morphology and size of wear debris changes with change in applied load. Volume of wear debris increases with increase in applied load. The possible wear mechanisms are abrasive grooves, delamination, and formation of crack.

- Similar results are also obtained from the wear behavior study of SiC-B_4C–Al based cermets as SiC-B_4C–Si based cermets. Wear depth, wear rate and wear volume increases with increase in applied load for conventional sintered as well as SPS samples. There is an increase in density; high hardness with minimum porosity level and improved mechanical properties in 10 wt. % Al sample; makes it a better wear resistant material as compared to other compositions. The possible wear mechanisms are abrasion, delamination, and crack formation, similar to that of SiC-B_4C–Si based cermet.

- The oxidation behavior of SiC-B_4C ceramic composite and SiC-B_4C–Si cermets containing 2, 5, 10, and 20 wt. % Si were investigated at 800, 1000, and 1200 °C. XRD analysis detected the SiC, B_2O_3, SiO_2 and carbon phases on the oxidation surface of the

SPS and conventional sintered samples. Oxidation at 800 °C for conventional sintered samples with low Si addition shown weight gain due to formation of B_2O_3 by the oxidation of B_4C with oxygen. There was no weight change in 10 and 20 wt. % Si added composition for conventional and SPS samples due to the formation of SiO_2 glassy phase as barrier for oxygen diffusion. The higher amount of Si content in the composites improved the oxidation resistance from initial temperature of oxidation to higher temperature at 1200 °C. There were no weight change in all the compositions for conventional and SPS samples after 1 h of oxidation at 800, 1000 and 1200 °C due to the formation of SiO_2 glassy phase over the surface. At 1200 °C, the SiO_2 glassy phase acted as oxidation protective layer over the sample surface and prevented from further oxidation.

After investigating all the above mentioned points, characterizations, and results it can be summarized that mechanical milling is effective for refining all the composite powders. Higher density, microhardness, indentation fracture toughness, and compressive strength values were achieved for all the compositions consolidated by SPS than conventional sintering. There was not much grain growth of the cermets after consolidated by SPS as compared to conventional sintered cermets. It was also found that SiC-B_4C based cermets with 10 wt. % Si and 10 wt. % Al addition helps in enhancing all the physical, mechanical, wear and oxidation resistance properties required for practical applications.

Scope for Further Research

Following studies can be carried out in future for better understanding of the SiC-B_4C based cermets for its structural applications:

- Varying percentage of SiC and B_4C to understand the response of the material to varying composition.

- Adding different other metals to receive the response of materials to toughness and wettability of the composite.

- TEM analysis of SPS and Conventional sintered SiC-B_4C–Si and SiC-B_4C–Al cermets for detail investigation of effect of Si and Al reinforcement.

- Performing conventional sintering above 1950 °C to investigate the densification and mechanical properties.

- To carry out high temperature wear and electrical conductivity test for high temperature behavior of such high temperature resistant cermet materials.

References

[1] Ellis JL, Goetzel CG. Cermets, metals hand-book-properties and selection: nonferrous alIoys and special-purpose materials. American society for Metals, Metals Park, OH, USA, 10th ed., 1990;2.

[2] Johnson WC. Advanced materials and powders. Am Ceram Soc Bull 2001;80:64–66.

[3] Weimer AW. Carbide, nitride and boride materials synthesis and processing. London: Chapmann & Hall, 1st ed., 1997.

[4] Zhang S. Titanium carbonitride-based cermets: processes and properties.Mater Sci Eng A.1993;163:141–148.

[5] Prochazka S. Hot pressed silicon carbide. Patent No. US3853566; 1974.

[6] Ying TN, Shen M.C., Wang YS, Hsu SM. Tribology of Si-Based Ceramics: Wear Mechanisms. Tribol Trans 1997; 40:685–693.

[7] Ersoy DA, Mcnallan MJ, Gogotsi Y, Erdemir A. Tribological properties of carbon coatings produced by high temperature chlorination of Silicon carbide. Tribol Trans 2000; 43:809–815.

[8] Thevenot F. Boron Carbide-A comprehensive review. J Eur Cer Sot 1990;6:205.

[9] Lee H, Speyer RF. Pressureless sintering of boron carbide. J Am Cer Sot 2003;86:1468–1473.

[10] Deng J, Zhou J, Feng Y, Ding Z. Microstructure and mechanical properties of hot-pressed B_4C/(W,Ti)C ceramic composites. Ceram Inter 2002;28:425–30.

[11] Sigl LS. Processing and mechanical properties of boron carbide sintered with TiC. J Eur Ceram Soc 1998;18:1521–29.

[12] Suri AK, Subramanian C, Sonber JK, Murthy TSR Ch. Synthesis and consolidation of boron carbide: A review. Int Mater Rev 2010;55:4–40.

[13] Glasson DR, Jones JA. Formation and reactivity of borides, carbides and silicides. I Review and introduction. J appl Chem 1969;19:125–37.

[14] Mashhadi M, Taheri-Nassaj E, Sglavo VM. Effect of Al addition on pressureless sintering of B_4C. Ceram Inter 2009;35:831–837.

[15] Cho K, Munir ZA, Lee H.Microstructure of spark plasma sintered silicon carbide with Al-B-C. J Ceram Process Res 2008;9:500–505.

[16] Yamada S, Hirao K, Yamauch Y, Kanzaki S. Mechanical and electrical properties of B_4C–CrB_2 ceramics fabricated by liquid phase sintering. Cer Inter 2003;29:299–304.

[17] Levin L, Frage N, Dariel MP. A novel approach for the preparation of B_4C-based cermets. Int J Ref Met Hard Mat 2000;18:131–135.

[18] Shi XL, Xu FM, Tan Y, Wang L. Mechanical properties of hot-pressed B_4C–SiC composites. In: Bansal NP, Singh JP, editors. Processing and properties of advanced ceramics and composites II, America, 2012, p. 189–196.

[19] Gilbert CJ, Cao JJ, MoberlyChan WJ, De Jonghe LC, Ritchie RO. Cyclic fatigue and resistance-curve behavior of an in situ toughened silicon carbide with Al-B-C Additions. Acta Metall Mater 1996;44:3199–214.

[20] Cao JJ, MoberlyChan WJ, De Jonghe LC, Gilbert CJ, Ritchie RO. In situ toughened silicon carbide with Al-B-C additions. J Am Ceram Soc 1996;79:461–69.

[21] Wei H, Zhang Y, Deng X. Effect of silicon additions on the hot pressing of B_4C. J Ceram Process Res 2011;12:599–601.

[22] Schwetz KA, Sigl LS, Pfau. Mechanical properties of injection molded B_4C–C ceramics. J Solid State Chem 1997;133:68–76.

[23] Ling Y, Li J, Ge C, Bai X. Fabrication and evaluation of SiC/Cu functionally graded material used for plasma facing components in a fusion reactor. J Nucl Mater 2002; 303:188–95.

[24] Magnani G, Beltrami G, Minoccari GL, Pilotti L. Pressureless sintering and properties of αSiC–B_4C composite. J Eur Ceram Soc 2001; 21:633–638.

[25] Zurnachyan AR, Kharatyan SL, Khachatryan HL, Kirakosyan AGh. Self-propagating high-temperature synthesis of SiC–Cu and SiC–Al cermets:Role of chemical activation. Int J Refra Metal Hard Mater 2011;29:250–55.

[26] Suryanarayana C. Mechanical alloying and milling. Prog Mater Sci 2001; 46:1–184.

[27] Omori M, Takei H. Composite silicon carbide sintered shapes and its manufacturing,U.S. Pat. No. 4502983, Mar. 5, 1985.

[28] Omori M, Takei H. Method for preparing sintered shapes of silicon sarbide, U.S. Pat. No. 4564490, Jan. 14, 1986.

[29] Hulbert DM, Jiang D, Dudina DV, Mukherjee AK. The synthesis and consolidation of hard materials by spark plasma sintering. Int J Refract Met Hard Mater 2009;27: 367–75.

[30] Hayun S, Kalabukhov S, Ezersky V, Dariel MP, Frage N. Microstructural characterization of spark plasma sintered boron carbide ceramics. Ceram Int 2010;36:451–57.

[31] Munir ZA, Anselmi-Tamburini U, Ohyanagi M. The effect of electric field and pressure on the synthesis and consolidation of materials: a review of the spark plasma sintering method. J Mater Sci 2006;41:763–77.

[32] Sairam K, Sonber JK, Murthy TSR Ch, Subramanian C, Fotedar RK, Nanekar P, Hubli RC. Influence of spark plasma sintering parameters on densification and mechanical properties of boron carbide. Int J Ref Met Hard Mater 2014;42:185–92.

[33] German RM. Powder metallurgy science. 2nd ed. Metal powder industries federation, Princeton, New Jersey 1994:83–123.

[34] Rahaman N Mohamed. Ceramic processing. Taylor & Francis group. 2006. 1–440.

[35] Richarson W David. Modern ceramic engineering: properties, processing, and use in design. 3rd ed. Taylor & Francis group, London, New York 2005:1–728.

[36] German RM, Powder Metallurgy. John Wiley and Sons, Inc., New York, 2nd ed. 1994.

[37] Coble RL, Cannon RM. Current paradigms in powder metallurgy. Mater Sci Res 1978;11:151–170.

[38] Greenwood GW. The growth of dispersed precipitates in solutions. Acta Metall 1956;4:243–248.

[39] Wagner C. Theory of Ostwald ripening. Z Electrochem 1961;65:581–591.

[40] Lifshitsz IM, Slyozov VV. The kinetics of precipitation from supersaturated solutions. Phy Chem Solids 1961;19:35–50.

[41] Cahn JW. The impurity drag effect in grain boundary motion. Acta Metall 1962;10:789–798.

[42] Stearns LC, Harmer MP. Particle-inhibited grain growth in Al_2O_3-SiC: I, Experimental results. J Am Cer Soc 1996;79:3013–3019.

[43] Stearns LC, Harmer MP. Particle-inhibited grain growth in Al_2O_3-SiC: II, Equilibrium and kinetic analysis. J Am Cer Soc 1996;79:3020–3028.

[44] LaSalvia JC. Advances in ceramic armor IX. Cer Engg Sci Proceed 2013;34 issue 5.

[45] Sahin FC, Apak B, Akin I, Kanbur HE, Genckan DH, Turan A, Goller G, Yucel O. Spark plasma sintering of B_4C–SiC composites. Sol Stat Sci 2012;14:1660–1663.

[46] Suzuki K, Sasaki M. Effects of sintering atmosphere on grain morphology of liquid-phase-sintered SiC with Al_2O_3 additions. J Eur Cer Soc 2005;25:1611–1618.

[47] Gomez E, Echeberria J, Iturriza I, Castro F. Liquid phase sintering of SiC with additions of Y_2O_3, Al_2O_3 and SiO_2. J Eur Cer Soc 2004;24:2895–2903.

[48] Kackell P and Wenzien B, Bechstedt F. Influence of atomic relaxations on the structural properties of SiC polytypes from abinitio calculations. Phys Rev B 1994;50:10761–10768.

[49] Melinon,P. and Masenelli B., From Small Fullerenes to Superlattices: Science and Applications, PanStanford Publishing Pte Ltd (2011).

[50] Dolloff RT. Research study to determine the phase equilibrium relations of selected metal carbides at high temperatures. Research Laboratory of National Carbon Company, Division of Union Carbide Corporation, Parma, Ohio, Contract No: AF 33(616)-6286, Project No: 5370, July 1960.

[51] Widom M, Huhn WP. Prediction of orientational phase transition in boron carbide. Solid Stat Sci 2012;14:1648–1652.

[52] Will G, Kossobutzki KH. An X-ray diffraction analysis of boron carbide, $B_{13}C_2$. J Less Comm Metal 1976;47:43–48.

[53] Zhang S, Lu W, Wang C, Shen Q, Zhang L. Synthesis and characterization of $B_{13}C_2$ boron carbide ceramic by pulsed electric current sintering. Ceram Inter 2012;38:895–900.

[54] Okamoto H. Boron-Carbon phase diagram. In: Baker H, editors. ASM Handbook, ASM International: Materials Park, OH, USA: 1992, p. 422.

[55] Emin D. Structure and single-phase regime of boron carbides. Phys Rev B 1988;38:6041–6055.

[56] Mallick PK. Composites Engineering Handbook, Marcel Dekker, Inc., 1997.

[57] Jianxin D, Jun Z, Yihua F, Zeliang D. Microstructure and mechanical properties of hot-pressed B_4C/(W,Ti)C ceramic composites. Cer Intern 2002;28:425–430.

[58] Sigl LS. Processing and mechanical properties of boron carbide sintered with TiC. J Eur Cer Soc 1998;18:1521–1529.

[59] Shinozaki SS, Hangas J, Carduner KR., Rokosz MJ, Suzuki K, and Shinohana N. Correlation between microstructure and mechanical properties in silicon carbide with alumina addition. J Mater Res 1993;8:1635–43.

[60] Mulla MA, Krstic VD. Pressure-less sintering of β-SiC with Al_2O_3 additions. J Mater Sci 1994;29:34–38.

[61] Mulla MA, Krstic VD. Low-temperature pressureless sintering of β-silicon carbide with aluminum oxide and yttrium oxide additions. Am Ceram Soc Bull 1991;70:439–43.

[62] Padture NP. In situ-toughened silicon carbide. J Am Ceram Soc 1994;77:519–23.

[63] Moshtaghioun BM, Ortiz AL, Gomez-Garcia D, Rodriguez AD. Toughening of super-hard ultra-fine grained B_4C densified by spark-plasma sintering via SiC addition. J Eur Ceram Soc 2013;33:1395–1401.

[64] Du X, Wang Y, Zhang Z, Zhang F, Wang W, Fu Z. Effects of Si addition on the microstructure and properties of B_4C-SiC composite prepared with polycarbosilane- coated B_4C powder. J Mater Sci Eng A 2015;636:133–137.

[65] Feng Y, Hou WZ, Zhang H, Liu L. Densification and mechanical properties of spark plasma sintered B_4C with Si as a sintering aid. J Am Ceram Soc 2010;93:2956–2959.

[66] Han IS, Lee KS, Seo DW, Woo SK. Improvement of mechanical properties in RBSC by boron carbide addition. J Mater Sci Lett 2002;21:703–706.

[67] Hayun, S., N. Frage, and M. P. Dariel. The morphology of ceramic phases in BxC–SiC–Si infiltrated composites. J Sol Stat Chem 2006;179:2875–2879.

[68] Telle R, Petzow G. Reaction sintering of boron carbide with silicon and titanium. Horizon Powd Metall Part II. 1986;2:1155–1158.

[69] Zhou Y, Tanaka H, Otani S, Bando Y. Low-Temperature Pressureless Sintering of alpha-SiC with Al_4C_3-B_4C-C Additions. J Am Ceram Soc 1999;82:1959–64.

[70] Viala JC, Fortier P, Bouix J. Stable and metastable phase equilibria in the chemical interaction between aluminium and silicon carbide. J Mater Sci 1990;25:1842–50.

[71] Viala J C, Peronnet M, Bosselet F, Bouix J. Chemical compatibility between Al base matrices and light refractory carbide reinforcements, ICCM12 proceedings, 1999, paper no:739.

[72] Nelmes RJ, Loveday JS, Wilson RM, Marshall WG. Observation of inverted-molecular compression in boron carbide. Phy Rev Lett 1995;29:2268–2271.

[73] Lee H, Speyer RF, Hackenberger WS. Sintering of boron carbide heat treated with hydrogen. J Am Cer Sot 2002;85:2131–2133.

[74] Gee MG, Matharu CS, Almond EA, Eyre TS. The measurement of sliding friction and wear of ceramics at high temperature. Wear 1990;138:169-187.

[75] Miyoshi K, Buckley DH, Srinivasan M. Tribological properties of sintered polycrystalline and single-crystal silicon carbide. Am Cer. Sot Bull 1983;62:494–500.

[76] Derby J, MacBet J, Seshadri S. Tribological behaviour of alpha silicon carbide engine components, IMechE 1985;65:133–137.

[77] Adewoye OO, Page TF. Frictional deformation and fracture in polycrystalline SiC and Si_3N_4. Wear 1981;70:37–51.

[78] Larsson P, Axen N, Hogmark S. Tribofilm formation on boron carbide in sliding wear. Wear 1999; 236:73-80.

[79] Skopp, A, Woydt M, Ceramic and ceramic composite materials with improved friction and wear properties. Tribol Tran 1995; 38:233–242.

[80] Kato K, Adachi K. Wear of advanced ceramics. Wear 2002;253:1097–1104.

[81] Zum Gahr KH. Microstructure and wear of materials. Elsevier, Amsterdam, The Netherlands, 1987.

[82] Tkachenko YG, Yulyugin VK, Bovkun GA, Yurchenko DZ. High-temperature friction of borides of group IV–VI metals. Sovt Pow Metall Met Cer 1984;23:85–88.

[83] Yang Q, Senda T, Kotani N, Hirose A. Sliding wears behavior and tribofilm formation of ceramics at high temperatures. Sur Coat Tech 2004;184:270–277.

[84] Daoud A, Abou El-khair MT. Wear and friction behavior of sand cast brake rotor made of A359–20 vol% SiC particle composites sliding against automobile friction material. Tribol Int 2010;43:544–553.

[85] Zorzi, JE, Perottoni CA, da Jornada JAH. Hardness and wear resistance of B_4C ceramics prepared with several additives. Mater Lett 2005;59:2932–2935.

[86] Hirohata Y, Kobayasi M, Maeda S, Nakamura K, Mohri M, Watanabe D, Yamashina T. SiC coatings for first-wall candidate materials by RF sputtering. Thin Solid Film 1979;63:237.

[87] Krawiec P, Kaskel S. Thermal stability of high surface area silicon carbide materials. J Solid Stat Chem. 2006;179:2281–2289.

[88] Levine SR, Opila EJ, Halbig MC, Kiser JD, Singh M, Salem JA. Evaluation of ultra-high temperature ceramics foraeropropulsion use. J Euro Cer Soc 2002;22:2757–2767.

[89] Fan Z, Song Y, Li J, Liu L, Song J, Chen J, Zhai G, Shi J. Oxidation behaviour of fine-grained SiC–B_4C/C composites up to 1400 °C. Carbon 2003;41:429–436.

[90] The effects of nanoparticulate SiC upon the oxidation behavior of C-SiC-B_4C composites. Carbon 1998;36:1591–1595.

[91] Narushima T, Goto T, Maruyama M, Arashi H, Iguchi Y. Oxidation of boron carbide–silicon carbide composite at 1073 to 1773 K. Mater Trans 2003;44:401–406.

[92] Antonov M, Hussainova I. Cermets surface transformation under erosive and abrasive wear. Tribol Int 2010;43:1566–75.

[93] Klaasen H, Kubarsepp J. Abrasive wear performance of carbide composites. Wear 2006;261:520–6.

[94] Zhang M, Zhang W, Zhang Y, Gao L. Fabrication, microstructure and mechanical behavior of SiCw-B_4C–Si composite. Mat Sci Engg A 2012;552:410–414.

[95] Niihara K, Morena R, Hasselman DPH. Evaluation of KIc of brittle solids by the indentations method with low crack-to-indent ratios. J Mater Sci Lett 1982;1:13–16.

[96] Archard JF, Hirst W. The wear of metals under un-lubricated conditions. Proceedings of the Royal Society of London. Series A, Mathematical and Physical Sciences, 1956;236:397–410.

[97] Zmitrowicz A. Wear patterns and laws of wear - a review. J Theor Appl Mech 2006;44:219–253.

[98] Arslan G, Kara F, Turan S. Quantitative X-ray diffraction analysis of reactive infiltrated boron carbide–aluminium composites. J Eur Ceram Soc 23;2003:1243–55.

[99] Will G, Kossobutzki KH. An X-ray structure analysis of boron carbide ($B_{13}C_2$). J Less Common Met 1976;44:87–97.

[100] Okamoto H. Boron-Carbon phase diagram. In: Baker H, editors. ASM Handbook, ASM International: Materials Park, OH, USA: 1992, p. 422.

[101] Blanda M, Balko J, Duszova A, Hvizdos P, Dusza J, Reveron H. Hardness and indentation fracture toughness of alumina-silicon carbide nanocomposites. Acta Met Slov Conf 2013;3:270–275.

[102] Kubota M, Cizek P. Synthesis of Al_3BC from mechanically milled and spark plasma sintered Al–MgB_2 composite materials. J Alloy Comp 2008;457:209–15.

[103] Tsuchida T, Kan T. Synthesis of Al_3BC in Air from mechanically activated Al/B/C powder mixtures. J Eur Ceram Soc 1999;19:1795–99.

[104] Viala JC, Bouix J, Gonzalez G, Esnouf C. Chemical reactivity of aluminium with boron carbide. J Mater Sci 1997;32:4559–73.

[105] Lee SH, Kim HD, Choi SC, Nishimura T, Lee JS, Tanaka H. Chemical composition and microstructure of Al_3BC_3 prepared by different densification methods. J Eur Ceram Soc 2010;30:1015–20.

[106] Gao Y, Huang Z, Fang M, Liu Y, Huang S, Ouyang X. Synthesis of $Al_8B_4C_7$ ceramic powder from Al/B_4C/C mixtures. Powd Tech 2012;226:269–73.

[107] Du W, Watanabe T. High-toughness B_4C-AlB_{12} composites prepared by Al infiltration. J Eur Ceram Soc 1997;17:879–884.

[108] Yamaguchi A. Effects of oxygen and nitrogen partial pressures on the stability of metals, carbides, nitrides and oxides in refractories which contain carbn, Refract. 1986;38:2.

[109] Huang, Tan Q, Yang P, Huang Q, Lu B, Yu H, Guowen. Realationship of properties of hot pressing C-B_4C-SiC composite with the content of additive Al. Transaction of NFsoc 1995;5:93–96.

[110] Suarez M, Fernandez A, Menendez JL, Torrecillas R, Kessel HU, Hennicke J, Kirchner R, Kessel T. Sintering applications. InTech 2013;319–342.

[111] Bin Liu, Wen-mao Huang, Hao-wei Wang, Ming-liang Wang, Xian-feng Li. Compressive behavior of high particle content B_4C/Al composite at elevated temperature. Trans Nonferrous Met Soc China 2013;23:2826−2832.

[112] Sahani P, Karak SK, Mishra B, Chakravarty D, Chaira D. Effect of Al addition on SiC-B_4C cermet prepared by pressureless sintering and spark plasma sintering methods. Inter J Refract Metal Hard Mater 2016;57:31–41.

[113] Nelmes RJ, Loveday JS, Wilson RM, Marshall WG. Observation of inverted-molecular compression in boron carbide. Phy Rev Lett 1995;29:2268–2271.

[114] Eber M. Method of making ceramic metal seal, Patent no: US 2848801 A; 1958.

[115] Dong X, Jahanmir S, Ives LK, Wear transition diagram for silicon carbide. Tribol Int 1995; 28:559–572.

[116] Deng J, Zhang X, Niu P, Liu L, Wang J. Wear of ceramic nozzles by dry sand blasting. Tribol Int 2006; 39:274–280.

[117] Antonov M, Hussainova I, Veinthal R, Pirso J. Effect of temperature and load on three-body abrasion of cermets and steel. Tribol Int 2012; 46:261–268.

[118] Farrokhzad MA, Saha GC, Khan TI. Wear performance of co-electrodeposited cermet coatings. Surf Coat Tech 2013; 235:75–85.

[119] Sahani P, Karak SK, Mishra B, Chakravarty D, Chaira D. A comparative study on SiC-B_4C-Si cermet prepared by pressure-less sintering and spark plasma sintering methods. Metall Mater Trans A 2016;57:31–41.

[120] Natarajan N, Vijayarangan S, Rajendran I. Wear behaviour of A356/25SiCp aluminium matrix composites sliding against automobile friction material. Wear 2006;261:812–822.

[121] Christoph H, Christine E, Ralf R. Silicon carbonitride ceramics derived from polysilazanes Part II. Investigation of electrical properties. J Euro Cer Soc 2000;20:1365–1374.

[122] Hillig WB. Making ceramic composites by melt infiltration. Am. C eram. Soc. Bull., 1994;73:56–62.

[123] Claussen N, Knechtel M, Prielipp H, Rodel J. Metcers—A strong variant of cermets. Cfi/Ber. DKG 1994;71:301–304.

[124] Gianpietro van de G, Peter S, Karl B. Electrically conductive ceramic composites. Solid Stat Ionic 1997;101–103:1163–1170.

[125] Rajkovic V, Bozic D, Jovanovic MT. Properties of copper matrix reinforced with various size and amount of Al_2O_3 particles. J Mater Process Tech 2008;200:106–114.

[126] Raymond A. Serway (1998). *Principles of Physics* (2nd ed.). Fort Worth, Texas; London: Saunders College Pub. p. 602. ISBN 0-03-020457-7.

[127] Neuberger N. Electronic properties information center (EPIC), Silicon Carbide data sheet-Defense Technical Information. 1965:21.

[128] http://www.azom.com/article.aspx?ArticleID=75.

[129] Balog M, Kovac J, Satka A, Hasko D, Zhang J, Crimp MA, Vavra O, Vavra I. SiC-based cermet with electrically conductive grain boundaries. Mater Charact 61;2010:420–426.

[130] Kusunose T, Sekino T, Niihara K. Production of a grain boundary phase as conducting pathway in insulating AlN ceramics. Acta Mater 2007;55:6170–5.

[131] Schneider B, Guette A, Naslain R, Cataldi M, Costecalde A. A theoretical and experimental approach to the active-to-passive transition in the oxidation of silicon carbide: experiments at high temperatures and low total pressures. J Mater Sci 1998;33:535–547.

[132] Ogura Y, Morimoto T. Mass spectrometric study of oxidation of SiC in low-pressure oxygen. J Electrocheml Soc 2002;149:J47–52.

[133] Liu Y, Cheng L, Zhang L, Wu S, Li D, Xu Y. Oxidation protection of multilayer CVD SiC/B/SiC coatings for 3D C/SiC composite. Mater Sci Engg A 2007;466:172–177.

[134] Litz LM, Mercuri RA. Oxidation of boron carbide by air, water and air-water mixtures at elevated temperatures. J Electro Soc 1963;110:921–925.

[135] Song Y, Dhar S, Feldman LC, Chung G, Williams JR. Modified Deal Grove model for the thermal oxidation of silicon carbide. J Appl Phys 2004;95:4953–4957.

[136] Heuer AH, Ogbuji LU, Mitchell TE. The microstructure of oxide scales on oxidized Si and SiC single crystals. J Amer Cer Soc 1980;63:354-355.

[137] Zhang WG, Cheng HM, Sano H, Uchiyama CY, Kobayashi CK, Zhou LJ, Shena BZH, Zhoua BL. The effects of nanoparticulate sic upon the oxidation behavior of C-SiC-B_4C composites. Carbon 1998;36:1591–1595.

[138] Uehara M, Shiraishi R, Nogami A, Enomoto N, Hojo J. SiC–B_4C composites for synergistic enhancement of thermoelectric property. J Euro Cer Soc 2004;24:409–412.

[139] Zhang Z, Du X, Wang J, Wang W, Wang Y, Fu Z. Synthesis and structural evolution of B_4C–SiC nano-composite powders by mechanochemical processing and subsequent heat treatment. Powd Tech 2014;254:131–136.

[140] Izhevskyi VA, Genova LA, Bressiani AHA, Bressiani JC. Microstructure and properties tailoring of liquid-phase sintered SiC. Int J Refract Met Hard Mater 2001;19:409–17.

[141] Rehman SS, Ji W, Khan SA, Asif M, Fu Z, Wang W, H Wang, J Zhang, Y Wang. Microstructure and mechanical properties of B_4C based ceramics with Fe_3Al as sintering aid by spark plasma sintering. J Eur Ceram Soc 2014;34:2169–75.

[142] Hulbert DM, Jiang D, Anselmi-Tamburini U, Unuvar C, Mukherjee AK. Continuous functionally graded boron carbide-aluminum nano-composites by spark plasma sintering. Mater Sci Engg A 2008;493:251–55.

Appendix 1

Table 1 A brief summaries on processing and mechanical properties of SiC-B_4C–Si cermets from literatures and comparison with present work.

	Composition	**Method**	**Temp. (°C), pressure (MPa)**	**Relative density (%)**	**Hardness (GPa)**	**Toughness (MPa $m^{1/2}$)**
Zhang *et al.* [94]	B_4C–5 wt% SiC–10 wt% Si	Ball milling + reaction hot pressing	1577, 30	96.5	~19	5.78
Sahin *et al.* [45]	B_4C–10 wt% SiC	SPS	1750, 40	98.8	33	-
Moshtaghioun *et al.* [63]	B_4C–15 wt% SiC	SPS	1700, 75	99	36	5.7
Uehara *et al.* [137]	SiC–30 wt% B_4C, SiC–70 wt% B_4C	Hot pressing	2000, 50	99	~ 15 (for 30wt%B_4C) 30 (for 70wt%B_4C)	-
Du *et al.* [64]	B_4C–11 wt% Si– 15 wt% (SiC+C)PCS	Hot pressing	1950, 30	99	33.1	5.64
Feng *et al.* [65]	B_4C–8 wt% Si	SPS	1800, 50	99	41.8	6.1
Zhang *et al.* [139]	SiC–B_4C (1:1)	Mechanochemical alloying+ hot pressing	1950, 30	96	24	4.6
Magnani *et al.* [24]	SiC–5 vol% B_4C	Mixing+ conventional sintering	2150	96	30	4.19
Present work	SiC-B_4C– 10 wt% Si	Ball milling+Pressure-less sintering	1950	92	18±2.23	1.97
		Ball milling+ SPS	1350, 50	98	28±2.12	3.8

Appendix 2

Table 2 A brief summaries on processing and mechanical properties of SiC-B_4C–Al cermets from literatures and comparison with present work.

	Composition	**Method**	**Temp. (°C), pressure (MPa)**	**Relative density (%)**	**Hardness (GPa)**	**Toughness (MPa $m^{1/2}$)**
Mashhadi *et al.* [14]	B_4C–1 to 5 wt% Al	planetary milling + pressure-less sintering	2050 and 2150	96	-	-
Izhevskyi *et al.* [140]	SiC–10 vol% (AlN-Y_2O_3)	Attrition milling + Sintering	1950	98.8	≤ 24	3.6–5.9
Rehman *et al.* [141]	B_4C– 0 to 9 wt% Fe_3Al	SPS	1700, 50	98	32.46	4.1
Hulbert *et al.* [142]	B_4C– Al	SPS+ melt infiltration	1600, 53 1180	91	32.3	5.7
Present work	SiC-B_4C– 10 wt% Al	planetary milling+ Pressure-less sintering	1950	90	17±2.18	1.87
		planetary milling+ SPS	1300, 50	97	23±2.29	3.28

Thesis Dissemination

International Journals

1. **P. Sahani**, S. K. Karak, B. Mishra, D. Chakravarty and D. Chaira**.** ***"Effect of Al addition on SiC-B$_4$C cermet prepared by pressureless sintering and spark plasma sintering methods"***, *International Journal of Refractory Metals and Hard Materials, 2016, Volume 57, PP. 31–41.*

2. **P. Sahani**, S. K. Karak, B. Mishra, D. Chakravarty and D. Chaira. ***"A comparative study on SiC-B$_4$C-Si cermet prepared by pressureless sintering and spark plasma sintering methods"***, *Metallurgical and Materials Transactions A, 2016, Volume 47, Issue 6, pp. 3065–3076.*

3. **P. Sahani** and D. Chaira. ***"Un-lubricated sliding wear behaviour study of SiC-B$_4$C based cermet with different weight percent of Si additions"***, *Journal of Tribology, 2016, (Accepted).*

4. **P. Sahani,** S. K. Karak and D. Chaira. ***"Oxidation behavior and electrical conductivity study of SiC-B$_4$C-Si cermet prepared by powder metallurgy route"***. *(Under review).*

Manuscript under preparation

1. **P. Sahani** and D. Chaira. ***"Un-lubricated sliding wear behaviour study of SiC-B$_4$C based cermet with different weight percent of Al additions".***

2. **P. Sahani**, S. K. Karak, B. Mishra, P. Das and D. Chaira. ***"Effect of small addition of Si and Al into SiC-B$_4$C during fabrication of cermets through conventional and spark plasma sintering assisted by mechanical milling"***,

International & National conferences / Proceedings

1. **P. Sahani,** B. Mishra, S. K. Karak and D. Chaira. ***"Mechanical and Electrical Properties of SiC-B$_4$C-Si Cermets Prepared Via Spark Plasma Sintering"***, PM-15- International conference on powder metallurgy and particulate materials + exhibition & 41st annual technical meeting, **IIT Bombay, 19–21 Jan. 2015 (**Oral presentation**).**

2. **P. Sahani**, B. Mishra, S. K. Karak and D. Chaira, "***Processing and mechanical characterizations of SiC-B$_4$C-Al Cermet prepared by pressure-less sintering and spark plasma sintering method***", NMD ATM 2014, COEP, Pune, 12–15 Nov. 2014 (Poster presentation).

3. **P. Sahani,** B. Mishra, S. K. Karak, D. Chakravarty and D. Chaira, ***"Effect of Si on SiC-B4C based cermet prepared by pressureless sintering and spark plasma sintering methods"***,

International conference on emerging materials and process (ICEMP), 26–28 Feb. 2014, IMMT Bhubaneswar, ISBN: 978-81-928552-1-9, CSIR-IMMT, Bhubaneswar (Oral presentation) **(Proceeding)**.

4. **P. Sahani**, B. Mishra, S. K. Karak and D. Chaira, *"Powder metallurgy short term course (PMSC-13)",* organized by (Powder Metallurgy Association of India) PMAI & ARCI, ARCI Hyderabad, 18–21 Nov. 2013.

5. **P. Sahani**, B. Mishra, S. K. Karak and D. Chaira. ***"Synthesis and characterization of SiC-B_4C-Al & SiC-B_4C-Si cermets prepared by pressureless sintering and Hot Pressing"***, National Symposium for Materials Research Scholars, MR–13, IIT Bombay, 8–10 May 2013, (Oral presentation).

6. **Pankajini Sahani**, and Debasis Chaira. ***"Synthesis and characterization of SiC-B4C based cermets"***, NMDATM 2012, XLRI Campus, Jamshedpur, Jharkhand, 16–19 Nov. 2012 (Poster presentation).

Biography of the scholar

Pankajini Sahani was born in Rourkela, Sundargarh district, Odisha, India on 20th June 1986. She finished her schooling from REC Campus High School, Rourkela (OBSE board) in 2001. She obtained her intermediate degree from Sushilavati Govt. Women's Jr. College, Rourkela (CHSE board) in 2003, one of the premier science colleges in Rourkela. She completed her Bachelors in science (B.Sc) from Neelasaila Mahavidyalay, Rourkela under Sambalpur University, Odisha with Physics as honors subject in 2006. She pursued her Master in science (M.Sc Physics) from National institute of Technology, Rourkela in 2008. She did her final year M.Sc project on superconducting materials with the title of "effects of fine particles of $BaZrO_3$ *inclusions on the growth and microstructure of YBCO"* under *Dr. D. Behera in National Institute of Technology, Rourkela. During her M.Sc days, she was attracted a lot towards Materials Science and Engineering. Hence, she pursued her master in technology (M.Tech) in Metallurgical and Materials Engineering Department, National Institute of Technology, Rourkela in 2010. She secured third position in her M.Tech and was awarded by Director, National Institute of Technology, Rourkela. She completed her final year M.Tech project on "synthesis and characterizations of copper based nanostructures developed by mechanical milling". She was awarded third position in an International conference on ICON-2010, Coimbatore, Tamilnadu for full paper presentation during her M.Tech. She has published international journal papers in Material science and Engineering A and proceedings in IEEE Xplore. She enrolled herself for pursuing PhD degree in the department of Metallurgical and Materials Engineering, National Institute of Technology, Rourkela as a full time Institute scholar with fellowship under the supervision of Dr. Debasis Chaira, Assistant Professor, NIT Rourkela. She was involved in research titled "fabrication of* $SiC\text{-}B_4C\text{–}Si$ *and* $SiC\text{-}B_4C\text{–}Al$ *cermets by powder metallurgy route" (mechanical milling followed by consolidation with conventional sintering and spark plasma sintering techniques) in 2012. She worked with spark plasma sintering in ARCI, Hyderabad and CGCRI, Kolkata, India. She worked with high temperature conventional sintering (1950 °C) in CSIR-NML, Jamshedpur. Materials (SiC,* B_4C*, and Si) for her research work were supplied by DISIR, Rajgangpur, Odisha and she worked with conventional sintering in DISIR, Rajgangpur. She has published papers in frontier journals such as Metallurgical and Materials Transactions A, International Journal of Refractory Metals and Hard Materials, and many more. Her research interests comprises of powder metallurgy, ceramic matrix composite, nano-structured metal matrix composite, mechanical behavior of materials etc. She is interested to pursue post-doctoral research in an internationally renowned university in the line of core materials engineering to unravel the science of interface behind the powder metallurgy, wetting and toughness of cermet materials.*